UNIVERSITAT DE BARCELONA

Linear and nonlinear approaches to unravel dynamics and connectivity in neuronal cultures

Elisenda Tibau Martorell

Linear and nonlinear approaches to unravel dynamics and connectivity in neuronal cultures

Elisenda Tibau Martorell

PhD Advisor
Jordi Soriano Fradera
PhD Tutor
Jaume Casademunt Viader

Barcelona, April 2017
Doctorat Program in Physics
Department of Condensed Matter Physics
Faculty of Physics

Als meus pares

"The brain is a world consisting of a number of unexplored continents and great stretches of unknown territory."

Santiago Ramón y Cajal

Resum

La capacitat dels teixits neuronals de processar i transmetre la informació de forma eficient depèn de les propietats dinàmiques intrínseques de les neurones i de la connectivitat entre elles. Un dels pocs sistemes experimentals que permet de forma controlada monotoritzar l'activitat individual de cada neurona i de la seva població i moldejar la seva conectivitat són els cultius neuronals. L'objectiu principal de la tesi ha estat explorar les diferents estratègies experimentals i de simulació a fi i efecte de caracteritzar la relació entre l'activitat i la connectivitat de xarxes corticals de rata embrionària cultivades en el Laboratori del Dr. Jordi Soriano.

El sistema experimental amb el qual s'ha treballat ha consistit en mesurar l'activitat espontànea d'una població de neurones corticals embrionàries en cultiu, mitjançant una càmera ràpida i tècniques de flourescència. Mitjançant tècniques d'encapsulament físic i confinament químic, s'ha lograt obtenir diferents distribucions espaials de les neuornes, desde cultius amb topològies molt homogènies a més agregades. Durant el desenvolupament de la tesis ens hem centrat a explorar dues línes experimentals diferents: *desenvolupament* i *desintegració*. En el primer cas s'ha investigat els canvis en el comportament de la xarxa a mesura que els cultius maduraven durant el primer més gestació. En el segon cas, s'han aplicat diferents fàrmacs que ens han permès reduir la interconnectivitat neuronal. Tots els anàlisis posteriors i modelat al llarg de la tesi s'han basat en l'anàlisis d'aquestes dades experimentals.

A fi i efecte de reproduir els patrons observats en el Laboratori s'han desenvolupat els dos models de simulació que s'exponen a continuació. Per simular la xarxa física o topològica s'usa un model mètric aleatori de creixement neuronal. En aquest model s'implementen diferents patrons geomètrics bicolors com a subracte, on en sols un color es permet el posicionament i creixement neuronal. Per simular la dinàmica neuronal somàtica s'utilitza un model quadrtic d'integració i dispar amb adaptació i depressió. Aquest model permet simular un ampli espectre de dinàmiques neuornals i al presentar un baix cost comutacional permet la simulació raonable de xarxes de 1000 a 10.000 neuornes. En el nostre cas s'implementa el model dinàmic més simple possible (de dispar regular) amb la finalitat d'analitzar com el canvi de la topologia de la xarxa afecta a la dinàmica col·lectiva.

Es caracteritza la dinàmica global i individual de la població de neurones i es correlaciona amb l'estructura subjacent mitjanant tècniques lineal i no–lineals de series temporals.

En un primer estudi, per la caracterització de la dinàmica i estudi de les seves correlacions, tant temporals com topológiques es modelitza cada seria temporal com un procès estocàstic lineal autoregressiu (ARIMA) i ens focalitzem a estudiar la seva distribuci energètica i espectral. En particular, ens centrem en l'anàlisis mitjançant l'espectre de potència (PSD), amb la carcaterització del seu exponent frequencial (α). S'observa que en la primera setmana de creixement, els canvis són abruptes i molt ràpids, que a partir del dia 7 in vitro (DIV$\sim 7 \pm 2$) apareix la corrent inhibidora (GABA switch) i que quan arriba a estats més madurs (DIV $> 10 \pm 2$), s'estabilitza l'estat d'energia, en condiciona

amb excitació i inibició treballant ([E+I]). Així mateix s'observa que la dinàmica del sistema evoluciona d'estats més homogènis a heterogènis, a mesura que els cultius maduren. En efecte, en aquests estadis (DIV $\leq 21 \pm 2$) s'observa que tots els espectres col·lapsen a una llei de potència $P \sim f^{-\alpha}$, tal que $2.3 \leq \alpha \leq 2.8$. Paral·lelament, l'anàlisis espaial de la densitat espectral, ens revela, l'existència de comunitats fortament connectades, que pulsen en oscil·lacions quasi sincròniques, la frequencia de la qual està fortament correlacionada amb el grau de desintegració de la xarxa. Al degradar–se la xarxa, clarament podem identificar la dinàmica col·lectiva i individual de la xarxa.

Seguint aquesta linea de desenvolupament, es procedeix a ampliar l'estudi usant tènciques no–lineals d'incrustació ('embedding') per tal de reconstruir la dinàmica subjacent en l'espai de fases i d'aquesta forma estudiar les recurrències internes que emergeixen en el sistema col·lectiu i individual. En concret ens centrem amb el mètode dels vectors amb retard i especial èmfasis es posa per determinar els dos paràmetres característics d'aques mètode: la dimensió d'incrustació (m) que ens indica el nombres de variables independents que necessitem per descriure el sistema i el temps de retard (δ), que ens caracteritza els dos processos linealment independent o descorrelacionats de la serie temporal. Per tal determinació es testegen diferents mètodes i per posteriors anàlisis ens quedem amb el proposat per Gautama et al., 2003. Seguidament es procedeix a calcular la matriu de distància entre els respectius estats, anomenat gràfic de recurrència, i a estudiar els diferents patrons dinàmics subjacents que van emergint. S'observa que malgrat que la dinàmica individual de cada neurona és altament estocàstica ($m >$8 y $\delta >$ 6 s), a partir del DIV= (5 ± 2) comença a emergir un règim col·lectiu coherent, baix dimensional (m $\in$ [3-4] i $\delta \sim 1$ s). En efecte, a partir de la primera setmana apareixen clarament òrbites periòdiques amb aparició d'un cercle límit (m $\in$ [3-4] i $\delta \sim 1$ s), on la sincronisitat augmenta considerablement a partir de DIV=(8 ± 2) i va decreixent a partir del DIV=(13 ± 2). Efectivament, a mesura que els cultius van madurant (DIV $>15 \pm 2$), s'observa un increment en la dimensionalitat (m $\in$ [5-12]) del sistema, la complexitat augmenta, l'interior de les orbites col·lectives es poblen amb majors microestats, i els gràfics de recurrències presenten rics patrons dinàmics. Aquests patrons de major riquesa dinàmica observats en les xarxes madures [E+I], es veuen lleugerament empobrits al bloquejar les corrents inhibidores i al analitzar les xarxes [E], les quals presenten estats altament sincrónics i periòdics mostrant comportament semblants als típics estats epilèptics. En particular, durant el desenvolupament i desintegració s'observen diferents transicions dinàmiques en correspondència al guany o pèrdua de complexitat dinàmica dels cultius.

L'estudi del règim dinàmic col·lectiu amb diferents tamany de xarxa i de fortalesa sinàptica, tant per topologies homogènies i agregades mitjantant les simulacions, indican que només una fina regió es correspon a l'observada al Laboratori. Per xarxes homogènies sols amb tamanys superiors a N $> 10^4$, s'observen comportament col·lectius clarament oscil·latoris, comportament similars als ritmes del cervell. Tanmateix, tal dinàmica no s'ha pogut observar en el Laboratori, segurament perquè treballem amb xarxes de tamanys inferiors. En les simulacions, per xarxes homogènies i de tamanys inferiors (N $= [10^3 - 10^4]$) el règim col·lectiu coherent és impossible assolir-l'ho, a menys que se li afegeixin petits agregats. En efecte, al afegir petites agrupacions de diferents densitats neuronals, es facilita que s'assoleixi el règim col·lectiu amb un nombre inferior de connexions, promovent la activitat, augmentant el coeficient de clustering i generant re-

gions la topologia de la qual facilita i amplifica tal activitat. És de notar, tan mateix, que si bé aquestes agregacions promouen l'activitat, tenen molt baixa probabilitat d'iniciar-la.

A fi i efecte de reconstruir la conectivitat de la xarxa es tasteja mitjanant simulacions quatre mètodes diferents. Per construcció, considerem que dues neurones es troben conectades, si i només si, presenten un comportament dinàmic similar al llarg de totes les mesures, altrament dit, si presenten un coeficient (i) de correlació creuada, (ii) o de correlació parcial, (iii) o de mútua informació (iii) o de transferència d'entropia generalitzada (TEG) superior al 85% de la xarxa. Es van testejar aquestes quatre metodologies a través de simulacions, i es conclou que s'obtent millor reconstruccions a través de TEG. Sobre aquesta base, TEG–reconstruccions s'han aplicat amb les diferents dades experimentals a fi de determinar la connectivitat física de les xarxes, o almenys una descripció global a través de paràmetres estadístics clau com la connectivitat mitjana $\overline{k}$ o el grau de asortatividad. S'observa que cultius joves exhibeixen valors baixos de $\overline{k}$ en l'interval de 3–5 per a xarxes homogènies i de 7 – 20 per als agregats, respectivament. En cultius madurs, TEG–reconstruccions han proporcionat valors de $\overline{k}$ entre 15 – 150 per cultius homogenis i entre 20–180 per cultius agregats. Malgrat presentar certs tres de xarxes tipus 'petit món', els nostres cultius mostren una distribució de grau 'exponencial' o 'esbiaixada' per, respectivament, cultius joves i madurs. Addicionalment, hem observat que les xarxes homogènies presenten la propietat de disassortativitat, mentre que xarxes amb un creixent nivell d'agregació espaial presenten assortativitat. En efecte, les xarxes amb major grau d'agregació pressenten, un nivell d'assortativitat intermitja ($p \sim 0.6$), propietat que impacta fortament en la transmissió, resistència i sincronització de la xarxa.

Contents

Introduction

0.1 Overview of the Research

Brain computation emerges as result of electrical and chemical signals flowing through the complex network of connected brain regions. Despite tremendous advances in Neuroscience, we still poorly understand the basic principles of how signal flow is routed through neuronal networks to generate appropriate behavior. Understanding how information is transmitted and processed in the neuronal networks requires the measurement of not only single–cell dynamics but also of collective spatio–temporal activity patterns. In other words, the ability of a neuronal tissue to efficiently process and transmit information crucially depends on both the intrinsic dynamical properties of the neurons and their interconnectivity.

The interplay between neuronal dynamics and connectivity then becomes the cornerstone in the understanding of information flow in neuronal tissues and its optimization throughout evolution. To tackle this problem, neuronal network dynamics at the mesoscopic scale offers a tradeoff between the microscopic scale, dominated by individual behavior and molecular processes, and the macroscopic organization of the brain, where its structural intricacy and complexity at multiple spatial and temporal scales hinder its analysis and comprehension.

In the present work, we propose to explore the meso–scale connectome of *in vitro* cortical networks, both experimentally and theoretically, by adopting a fresh perspective centered on the application of concepts from dynamical systems. Experimentally, the usage of *in vitro* cortical culture of embryonic rats, combined with different strategies and techniques to *act* on them, will offer us a practical and agile platform for measuring and manipulating neuronal spontaneous activity across a broad range of spatial and temporal scales. In addition, fluorescence calcium image will provide us a suitable tool to track the activity of either individual or multiple neurons with high detail. Theoretically, recent advances in computer science, mathematical analysis and processing techniques will help us to reconstruct the underlying dynamics of the neuronal population and their respective connectivity under diverse experimental conditions.

0.2 Conceptual Framework

Complexity theory, which is the study of interacting nonlinear dynamical systems, provides a useful conceptual framework that reconciles the essential behavior of neurons with the emergence of self–organized dynamical patterns of neuronal populations. Complex system science is the study of large population of couple entities, and where the global

behavior is a non–trivial outcome of the interaction between individual elements [566]. The inference of how such collective behavior emerges as a result of these interactions is a fundamental yet elusive scientific issue. Interestingly, even though single neuronal cells are highly sophisticated devices, a cortical population can be modeled as a system of many interacting particles exhibiting complex behavior.

The interactions between individuals entities is often modeled as a signaling (or communication) process. A signaling process in turn refers to the ability of sharing and transferring meaningful information among two or more entities. Thus, emergent complex behavior has often been described from the perspective of biological computation [491] and has been postulated to be associated with the ability to support universal computation [137]. Indeed, living systems can be viewed as fundamentally computational in nature. In particular, neuronal systems emerge as one of the finest examples of 'biological computation' [407], even in the absence of stimuli. In these sense, *Information* and *Complexity* are two concepts closely linked. Although the theory of Complexity and the theory of Computation are frameworks that are treated separately, one cannot understand one without the other.

The term 'complexity' encompasses different areas, with *Chaos Theory* and *Network Theory* two of its pillars. Chaos theory [441] deals with systems in which the recursive application of nonlinear deterministic functions can give rise to apparent random behavior and subtle patterns. Recursion is one of the main ingredient that distinguishes complex behavior. It can be viewed as an optimized processor of resources, and therefore 'recursion' is presented as a procedure that calls itself (a loop), and that can be extended indefinitely to create unbounded sequences or structures. Local patterns of neural activity can be addressed by looking at the 'reverberatory activity' of the environment, which is maintained by circulation in synaptic feedback loops [575, 173, 439]. Indeed, depending on the the network topology chosen, interactions are mediated in one form or another through simple rules. On the other hand, whereas Chaos Theory generally attempts to model the outcome of interactions, Network Theory mainly focuses on modeling such interactions. Indeed, network models capture the essence of the interaction among many agents in a system.

Hence, in the context of this thesis, each area brings powerful tools to comprehend systems as enigmatic as living neuronal networks.

0.3 Hypotesis of the research

The hypothesis of this thesis is the following: *if we can describe and quantify how information flow is routed in neuronal cultures, then we will be closer to understand the evolution and development of neuronal tissues in Nature.*

0.4 Objectives of the research

The analysis of how information flows along an anatomical neuronal circuitry is a basic requirement to reveal fundamental aspects on functional computation in neuronal tissues. In turn, such analysis offers the possibility to tackle a very difficult *inverse problem*: given the flow information, can we reveal the underlying structure of the network?

We must note that *Network Information* flow, which describes the dynamic utilization of the network as a transportation or communication environment, can be usually characterized by direct empirical observation of the system. In contrast, *Network Connectivity*, which describes the physical architecture of a network (i.e. structural or anatomical connectivity), is inaccessible and unknown to us. In turn, during the development of neuronal cultures, both structural and functional connectivities are continuously reshaped on a reciprocal basis. In the present study, the overall goal of the research was aimed at investigating the **interplay between connectivity and dynamics** in embryonic neuronal cultures upon different experimental conditions.

To achieve this goal, we break it down into two parts. Below, we detail the established partial objectives to accomplish. In line with these objectives, the different associated questions are also raised.

A) Characterization of the dynamics in neuronal cultures

- Can we reconstruct the underlying dynamics of a neuronal population with only partial information, namely the neurons' fluorescence traces?

If yes, then the following questions arise:

- What kind of dynamics does the neuronal population present?
  - *Periodic, quasi–periodic or chaotic?*
  - *Linear or nonlinear?*
  - *Low dimensional or high dimensional?*
  - *Deterministic* [1] *or stochastic?*
- Given a specific dynamics, is it possible to characterize it?
  - *How many degree of freedom (variables) do we need to describe the neuronal population?*
  - *Is it possible to determine the predictability distance of system?*
  - *Is it possible distinguish recurrent patterns or dynamical motifs, in a qualitative and quantitative way?*
- What is the impact of the population dynamics in its functionality?

B) Characterization of connectivity in neuronal cultures

- Is it possible to reconstruct the underlying anatomical connectivity of a neuronal culture from solely the activity of their neurons?

If yes, then the following questions arise:

- What connectivity description do we obtain?

[1] In the present work, the term deterministic is used following the definition in the terminology of embedding theory (see Chapter 5).

  - *Anatomical, functional or effective?*
    * *What is the interrelation between them?*
    * *Do physical constraints in the preparation of the cultures translate into characteristic dynamical features?*

- What kind of connectivity map present the neuronal cultures?
  - *Random, small–world, scale–free, other?*
  - *What other network measures can be quantify?*

- What impact has the observed connectivity on network functionality?

In both parts (A) and (B), if the answers are negative, we then proceed as follows:

- What are the obstacles that prevent obtaining a good reconstruction of dynamics and connectivity?
  - *Are they grounded on the experimental technique used?*
  - *Are our analysis tools insufficient?*
  - *Are there alternative approaches to close the gap?*

0.5 Review of the methodology

The thesis combines diverse concepts at both experimental and simulation levels. They are briefly revised next.

From an experimental perspective, different techniques and strategies were considered to achieve the above–mentioned objectives. First, we chose embryonic neuronal cultures since they are a simple yet powerful platform to investigate living neuronal networks during development. Versatile and highly–resilient, neuronal cultures are one of the few experimental systems where one can vary the connectivity of neuronal networks in a control manner via chemical or mechanical perturbations. Second, we used calcium fluorescence imaging to ensure the simultaneous monitoring of hundreds to thousands of neurons *in vitro* with sufficiently good spatial and temporal resolution.

From a simulation perspective, several approaches were implemented in order to model neuronal networks in a biologically plausible and computationally efficient way. The structural connectivity of the network was modeled by a metric model that accounts for spatial embedding and heterogeneities in neuronal distribution. This models describes well neuronal cultures at the mesoscopic level. The dynamics of individual neuron was simulated through a quadratic integrate–and–fire model with adaptation and depression (QIFAD). This model allowed us to simulate the rich variety of individual neurons' dynamics. However, as we focused on analyzing the interplay between connectivity and dynamics, the simplest model of neuronal dynamics was chosen. Thus, the singular neurons in our models consisted of regular spikers (RS type) and, hence, bursting activity during neuronal discharges was a network phenomenon.

In line with simulations, Linear and Nonlinear Time Series Analysis was implemented in order to characterize the underlying dynamics and connectivity of neuronal networks.

Our starting point was the experimental and simulated fluorescence traces corresponding to a population of neurons (network) and their constituting single–cells (neurons). Then, with the help of different data processing techniques, we studied whether fluorescence data sufficed to decode the functional circuitry of the network and its associated dynamics.

0.6 Outline of the research

The structure of thesis is organized in seven chapters, arranged according to the presented objectives and with the goal of addressing all the aspects relevant to the comprehension of the issues covered. Broadly, the thesis is divided into four thematic blocks.

Block 1 represents the Introduction (Chapter 1) and describes in detail and the problem and ideas that gave rise to this thesis. It constitutes the framework of the problem to be dealt with and is the starting point for orienting the development of the research. It presents the state of the art, together with theories and other studies related to our work. **Block 2** covers the methodological frameworks (Chapters 2 and 3) applied along this thesis, i.e. it describes the methods, techniques, procedures and basics tools implemented within the domains of both experiments and computational simulations. **Block 3** encompasses the Results (Chapters 4, 5 and 6) obtained from the analysis of the experiments carried out along 4 years. These findings are in turn contrasted with the simulations. Finally, **Block 4** summarizes the work, its conclusions and pinpoints future directions of work (Chapter 7).

The detailed content of each chapter is as follows.

Chapter 1 introduces an overview of the cortical mammalian brain. First, we briefly describe its organization and structure. Next, its corresponding functionality is exposed, together with an overview of theoretical models proposed in the literature. Likewise, all the spectrum of dynamics associated to cortical networks is exposed, in particular the interplay between dynamics and connectivity. Finally, we show the motivation of our research and the justification for using cortical cultures as a first step towards the understanding of more complex circuits.

Chapter 2 describes the technical and experimental frameworks used in this thesis. First, an introduction of neuronal cultures is given. Next, the different protocols for dissociation, isolation, plating and maintenance of primary, rat embryonic cortical cultures is outlined. Then, we introduce the calcium image fluorescence technique to monitor spontaneous activity in cultures. Finally, we expose the different experimental lines explored in this thesis.

Chapter 3 exposes the mathematical and computational model that we employed in order to simulate neuronal cultures at the mesoscopic level. First, a metric model is explained with the aim to simulate the connectivity of the networks. Next, a quadratic integrate–and–fire model with adaptation and depression (QIFAD) is detailed to simulate the dynamics of individual neurons.

Chapter 4 presents the results centered in the characterization of the dynamics of neuronal populations, along different experimental conditions, and using *linear* time series analysis. The usage of spectral analysis provides a first estimator to characterize global

dynamical and structural traits of the measured neuronal cultures.

Chapter 5 brings to light the characterization of the experimental data using *nonlinear* time series analysis. Embedding techniques are developed in order to reconstruct the underlying dynamics of the system in the state space. Once the orbits are drawn, we proceed to analyze their characterization. The distance matrix of states is computed and evaluated with the aim of elucidating the emergence of recurrent patterns. We end the chapter by exposing nonlinear test of our physiological data.

Chapter 6 approaches connectivity reconstruction, and considers different methodologies. The usage of simulations provides us a reference and testing framework. Next, different networks are reconstructed and analyzed using the most appropriate methods previously tested.

Chapter 7 concludes the thesis with a summary of the obtained results, an analysis of the limitations of the investigation, and possible future lines of research.

Chapter 1

Cortical connectivity and dynamics

Understanding the organization, function, and development of the mammal brain is perhaps one of mankind's greatest challenges in the present days. Indeed, the brain emerges as one of the most complicated organ in Nature [531, 575]. In spite of significant advances from the scientific community, the studies elucidating the *modus operandi* and key mechanisms of the mammalian brain are far from providing a complete picture. In this Chapter, a global vision of mammalian brain in the macro–scale level will be exposed. In particular, special emphasis will be placed on explaining cortical structures, as well as the relationship between topology and dynamics and its impact in brain's functionality. The different advances, studies and models proposed in the literature will be described in order to contextualize the different strategies and perspectives adopted in our research. As we shall see, the analysis of the whole brain and its inherent cortical structures at a global level is extremely difficult. In view of these difficulties, and with the aim at simplifying, a meso–scale approach is proposed as the starting point of our research.

1.1 The Mammalian Brain

The mammalian brain is composed of 100 billion cells, with up to 100.000 inter–cellular connections. This high interconnectivity supports complex interactions between different units and regions to form sophisticated information processing networks. In a highly changing environment, the brain provides us with an a agile and adaptive system of communication which receives, codes, stores, transforms and retrieves the information, producing an accurate and fast response. Indeed, similar to a computer's central processing unit (CPU), all the tasks of the human body are coordinated and managed by this extremely complex organ. Intriguing is the question of how Nature has given rise to this extraordinary organ and that becomes the coordinating center of our behavior.

The brain consists of electrical circuits formed through the interconnection of a vast number of highly specialized cells termed neurons. By way of a fine and refined morphology [111, 444, 753], nerve cells communicate to each other by acting as 'transducers', converting electrical cues into chemical ones and vice versa. In response to the input of certain chemical compounds called neurotransmitters, the neurons create electrical signals which are converted into chemical messages that are 'transmitted' from a neuron to another. Individual neurons, however, are small components that need substantial time to operate. Indeed, as Von Neumann already pointed out [739], neurons present a slow

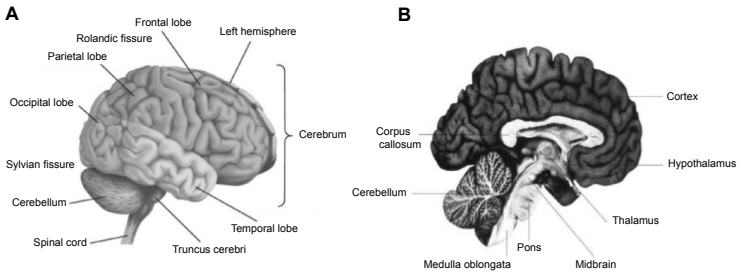

Figure 1.1: **Anatomy of the mammalian brain.** Lateral view of the right hemisphere of the brain, showing (A) its sagittal section and, (B) some of its most important parts.

dynamics, 10^5 times slower than the typical time for electrical components to complete a basic logic operation. Hence, taking into account the speed of decision–making in the brain, information is certainly processed quickly, so other features must be at play. It is thought that the brain compensates this 'slowness' through massive parallel processing and that computational tasks seem to emerge as a result of a collective phenomena of an interacting population. Indeed, it seems that the capacity to process, store and retrieve information is centered in the brain's networking ability rather than in the precise behavior of its individuals elements. A pivotal example of this ability lays in the cerebral cortex, specifically the *neocortex*.

1.2 The Cerebral Cortex

The cerebral cortex is the outer layer of the cerebral hemispheres, the 0.5 cm thick *gray matter*. it is crumpled and folded, forming numerous convolutions (gyri) and crevices (sulci). The cortex is divided into four different lobes (areas), namely the frontal, parietal, temporal, and occipital, each one responsible for processing different types of sensory information (Fig. 1.1).

Depending on its phylogenetic origin, the cerebral cortex is divided into the *neocortex* (or *isocortex*) and the *allocortex*. The *neocortex* is the most recent part of the cerebral cortex in terms of the evolutionary history of mammals. It represents the great majority of the cerebral cortex and is responsible for carrying out the highest levels of mental functioning. In contrast, the *allocortex* represents the older areas of cerebral cortex. These more primitive areas are located in the medial temporal lobes and deal with olfaction and survival functions such as visceral and emotional reactions.

Certain cortical regions have somehow simpler functions, termed the primary cortices. These include areas that directly receive sensory input (such as vision, hearing, or somatic sensation) or that are directly involved in the production of limb or eye movements. In contrast, the association cortices mediate more complex functions, including memory, language, abstraction, creativity, judgment, emotion and attention. But, how can it efficiently carry out all these functions? Different hypothesis have been proposed in the light of the experiments, and most of the data seem to indicate that the combined action of network topology and dynamics is the key aspect to understand this riddle.

1.2.1 Architecture and function

In the study of neuronal connectivity and its topology, a crucial aspect to analyze is how neuronal networks have evolved to perform information processing functions. In order to carry out such computational tasks, the organization of anatomical and functional cortical networks is guided by two basic principles: *segregation* and *integration* [709, 708, 246]. Anatomical and functional segregation refers to the existence of a specialized set of neuronal cells, organized into distinct neuronal populations (groups or columns) which selectively respond to specific input features (such as orientation, special frequency or wavelength) or conjunctions of features (such as faces). However, these segregated and specialized groups do not operate in isolation. Indeed, several studies [97, 669] evince that coherent perceptual and cognitive states require the coordinated activation, i.e. the functional integration, of very large numbers of neurons within the distributed system of the cerebral cortex. As will be see, the detailed balance between segregation and integration in the cortical circuitry allows the generation of information that is concurrently highly diversified and highly integrated, giving rise to patterns of high complexity.

The cortex is a strikingly ordered structure, but its vertical and horizontal arrangements obey very different schemes. The *neocortex* is differentiated into six horizontal layers while the *allocortex* has at most three cellular layers. Each cortical layer, also termed *laminae*, contains different neuronal shapes, sizes and density as well as different organizations of nerve fibers. The relative thickness of each layer varies in accordance to its functions. The six layers of this part of the cortex are numbered with Roman numerals from superficial to deep ($I - VI$ or $I - III$). In turn, neurons in various layers connect vertically to form small micro–circuits, termed *cortical columns* [438, 440, 503, 504, 338]. Columns only vary from 300 to 600 μm in diameter, even between species whose brains differ in volume by a factor of 10^3. Additionally, such columns contain $\simeq 80$ mini–columns of $50 - 60$ μm in diameter. Each mini–column in primates contain $\simeq 80 - 100$ neurons, except for the striate cortex where the number is about 2.5 times larger. Mini–columns contain the major cortical neural cell phenotypes, and emerge from the iterative division of a small cluster of progenitors cells.

Form a functional point of view, cortical columns are usually called *modules*, because these local neural circuits are repeated iteratively within each cortical area. And mini–columns are considered as the elementary functional units (information–processing units), i.e. the building blocks of the cortex. Studies of Mountcastle and coworkers [505, 503] demonstrated that the functional properties of the cortex change abruptly between laterally adjacent points, whilst they kept continuous in the direction perpendicular to the surface. Elementary function and columnar organization seem to be link in some way. For example, in the primary visual cortex of mammals, columns are specialized for different stimulus orientation [341, 60], direction of motion [752] and spatial frequency [640]. Studies of the auditory cortex of mammals unveiled that sound frequencies are mapped in a orderly and tonotopic manner to different cortical areas, constituting isofrequency bands [765, 103, 482, 23, 498]. In the cat, these bands are stacked in linear arrays from low to high frequencies in the posterior to anterior direction in auditory sensory areas. In the motor cortex, different studies suggest that the frequency of discharge of columnar cells varied in an orderly fashion with the direction of the movement (‘directionally tuned

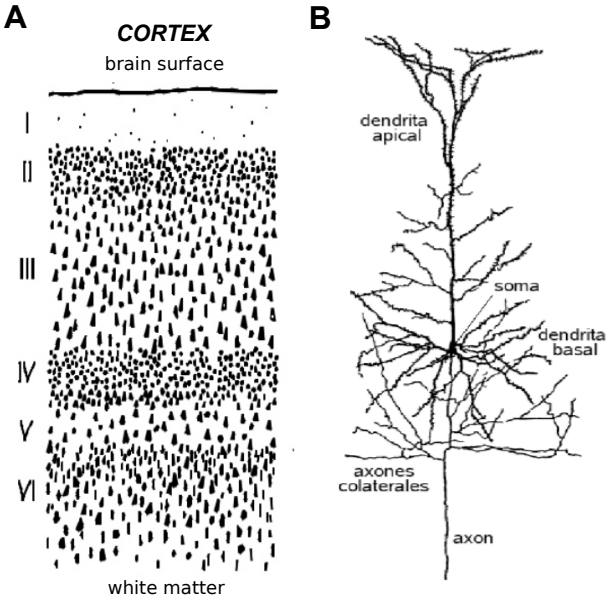

Figure 1.2: **Cortical columns and pyramidals neurons.** (A) Cortical column: distribution of the different layers of neurons observed in the human cortex (only the somas of neurons are pictured). (B) Cortical pyramidal neuron, prototype of excitatory neuron in the cerebral cortex. They have axons that branch locally by sending collaterals to neighboring neurons and others more distal that reach other regions of the nervous system.

cells') [266, 450, 267]. However, the functionality of those columnar structures is yet an elusive issue and we are still far from understanding its precise organization and behavior.

Comparative analysis of cortical organization between different species may help to understand certain unknown aspects. The laminar and columnar organization of primitive cortex such as the one of the reptiles is much less pronounced than for the mammals. Indeed, evidences shown that, throughout the evolutionary process, the brain networks have increased in size and level of complexity [359, 106, 369]. However, this cortical expansion is achieved by expanding cortical surface area, with little change in thickness. Hence, larger brains might involve larger or more neurons, or both. However, larger neurons introduce problems of maintaining the same conduction time over longer axons and the same passive electrical properties over longer dendrites. Indeed, a small increase in dendrites and axon lengths can be very costly in total brain size. Following the Cajal's laws of optimization of neuron morphology this option is ruled out[1].

Bigger neurons indeed leads to a disproportionate increase in dendrites and axons thicknesses, producing the so–called *wiring catastrophe* [678]. For example, an axon that

[1]In the Chapt.V (pag.115-125 in [111]) Cajal already described three biological laws of neuronal architecture: optimization principles for conservation of space, cytoplasm and conduction time in the neural circuitry. The usage of these principles allowed him to postulate a wide variety of theories of functionality and directionality of signal flow in various brain areas. Consequently, in such a way, this brilliant pathologist, histologist and neuroscientist already pointed out the inference of functional tasks from just the cells' morphology.

doubles in length would require its cross sections area to increase by a factor 4 in order to double its conduction velocity and maintain the same conduction delay. [585]. Such change would also cause strong alterations in the functionality of the circuits [69]. On the other hand, Ringo *et al.* [585] compared the diameters of axons connecting the two cerebral hemispheres in mice and humans, and found that the mean axonal diameter in humans was only 26% larger than in mice. Interestingly, a mean increase in diameter of about 1500% would be required to maintain the conduction times in both brains. In conclusion, actual axons' size is much smaller than one would expect from just a simple rescaling and, effectively, an increase in the size of dendrites and axons cannot explain the larger cortical areas in higher mammals and humans.

If neurons do not increase in size, then the only option is that the number of neurons and glia augment. Given that, a larger number of neurons would imply a higher density of connections. However, although the human brain is larger and contains more neurons than other mammals, different experiments evidence [677, 94] that the number of connections per neuron is similar to other brains. Empirical results [677] show that cortical neurons in mammalian brains are sparsely interconnected, with each neuron receiving direct synaptic inputs from less than 3% of its neighbors (underlying the surrounding square millimeter of cortex), and that the extent of connectedness hardly changes in brains that range in size over about four orders of magnitude. Moreover, experimental observations [20, 43, 154, 155, 620, 366, 527, 571, 740] show that the density of synapses in the cortex of mammals is constant ($s \simeq 6 \times 10^8$ synapses/mm^3) across cortical layers, regions ans species. Likewise, empirical works [563, 588] expose that the number of neurons that underline a square millimeter of cortical surface ($\rho \simeq 1.48 \times 10^5$ neurons/mm^2) is also constant across cortical regions and species [2].

In light of these results, theoretical studies [678, 136] suggest that the physiological properties of axons and dendrites frame an optimal wiring fraction of 3/5 (wiring volume / total volume). [136]. Indeed, it seems that evolution optimized neural circuits to minimize conduction delays in axons, passive cable attenuation in dendrites, and the 'wiring' length to construct circuits, leading to a maximization of the density of synapses [111, 136, 130]. In this regard, the general principles that minimize wiring cost would shape neuronal architecture by establishing a structure–function relationship [111, 130]. These ideas seem in accordance with experimental observations [94] that indeed evidence a cortical *wiring fraction* of 3/5, with typically a microliter of cortex containing approximately 10^5 neurons and 10^9 synapses.

Furthermore, an additional strategy to solve the problem of large cortical areas consists in shaping the brains more modular. More specifically, studies showed that the expansion of cortical brain is generated by an increase in the number of cortical columns, and by an increase in size [570]. Lund *et al.* [448] suggested that the correlation between column size and dendritic spread is a fundamental property maintained throughout various cortical areas and species. In addition, in mammals, the increase of cortical brain leads to the general scaling of brain moduli to total brain size [223], probably to maintenance the functional inter–relationship of the parts acquired over time. Indeed, modularity through cortical columns implies not only the hierarchical organization of components from one level of complexity to the next, but also the capacity to reuse those

[2]The density of neurons of primate area 17 differs in magnitude from other cortical areas, but it is also constant across species ($\rho \sim 3.57 \times 10^5$ neurons/mm^2).

components. From an evolutionary point of view, the segregation by modules provide a flexible and versatile reusing of resources.

However, this well known parcellation of the mammalian cerebral cortex into a large number of functional units present a problem when addressing the complex cortical integration to achieve higher functions. Several studies [115, 654, 37] showed that these columns are connected within individual cortical areas via tangential or horizontal connections, forming functionally segregated networks spanning several millimeters. In turn, neuronal groups in different cortical regions are connected via inter–regional pathways, linking areas over several millimeters and centimeters of cortical space. These inter–regional pathways form extended cortical systems such as the cortical visual, auditory and somatosensory areas that are in turn connected between each other through additional long–range pathways [220]. Anatomical studies [270, 280] have indeed revealed that large–scale cortical networks are made up of a widely distributed subnetworks of interconnected different areas, providing an anatomical substrate for large–scale parallel processing of information in the cerebral cortex. Neurophysiological studies [167, 165, 166, 168] demonstrated the functional co–activation of multiple areas in large–scale networks. And neuropsychological studies [281, 279, 483, 561] confirmed that coordinated large–scale networks mediate several different complex cognitive functions. Hence, even if elementary functions seem localized in discrete cortical areas [341], high cortical functions require the integrated action of many areas distributed throughout both cerebral hemispheres [449]. As a whole, large–scale cortical networks exhibit highly heterogeneous structures as well as distinct clusters [318, 319], hierarchical organization [320], a specific composition of of structural and functional motifs [664], short wiring lengths [133] and an overall high complexity [666, 665]. In addition, several studies demonstrated that functional cortical network also present small–world attributes [749] with highly clustering and short path lengths [666, 318, 667, 603, 17], as well as scale–free properties [208].

1.2.2 Dynamics and function

In order to characterize cortical dynamics, three major aspects must be taken into account. Firstly, the overall dynamics can only be understood on the basis of the physical structure of the network that supports it. Indeed, the relationship between a fixed topology and its dynamics is crucial to understand the optimal functionality of cortical networks. However, what solutions has Evolution found? Secondly, the ultimate goal of mature neocortical networks is to support complex higher functions, as well as memory, language, abstraction, creativity, judgment, emotion and attention. But, how it is achieved? What models have been proposed? Although in this thesis we studied embryonic–derived networks, it is important to comprehend the purposes the system has been designed for. And, thirdly, given a specific topology, it is possible to obtain different dynamics depending on the behavior of the neurons. Thus, what types of dynamics can arise? And, is it possible that each one of these dynamics can be enhanced depending on the task to be developed, the mental state acquired or some associated pathology? Can a specific dynamical regime be associated to a functional mode (*modus operandi*) of the network?

The topology–dynamics paradigm

The interplay between network topology and functional dynamics in a neuronal tissue is a quite old idea that goes back to the 20th century, when Donald Hebb in 1949 suggested the concept of *cell assembly* [311]. In Hebbian theory, a *cell assembly* refers to a combination of neurons that can be grouped together as a processing unit [311]. D. Hebb is considered the father of neurophysiology and was the first one to inquire the mechanisms underlying neuronal communication. He also settled the relationship between a specific function and its physiological counterparts. His work indeed encompasses the link between the dynamics and the structure of a neuronal network, which can be synthesized in the following way: "When an axon of cell A is close enough to excite cell B, and A repeatedly or persistently takes part in the firing B, then some growth process or metabolic change takes place in one or both cells such that A's efficiency, as one of the cells firing B, is increased" [311]. This is commonly referred to as Hebb's Law, which can be summarized as "cells that fire together, wire together" [443]. And in this sense, "two cells or systems of cells that are repeatedly active at the same time will tend to become 'associated', so that activity in one facilitates activity in the other" [311]. A new and fresh idea fully involved is the Hebb hypothesis, which consists in that a discrete, strongly interconnected group of active neurons, represents a distinct cognitive process that performs a given action or is associated to a given concept in the brain. The idea of ongoing (or reverberating) activity becomes central to Hebb's thinking and breaks away from the traditional Pavlovian paradigm of stimulus–response associations. As R. Lorente de Nó remarked, the ongoing activity in the cortex is a process distinct of a simple response from the arrival of sensory inputs; and that signaling through cortical neurons is not a strictly hierarchical and serial progression of information [173, 439]. Then, due to this 'reverberatory activity', local patterns of neural activity can be maintained by circulation in synaptic feedback loops. Although Hebb postulated that short–term memory is represented in reverberatory circuits, this postulate has also been applied to situations involving long–term modification in synaptic strength [179, 247, 322], including those occuring during cortical development [684].

In 1911, Santiago Ramón y Cajal [111] also suggested that it would be possible to understand the functions of the brain with an analysis of the functional architecture of the nervous system. Shape–function paradigm were already underlined in his writings as a key element for the understanding of brain's operation, not only at the micro–scale level but also at the macro–scale organization. At the micro–scale, Cajal already pointed out that the morphology of neurons arises as a result of their specialization for neural functions. Certainly, for example, the specific branching morphologies —in particular axonal and dendritic trees— provide immense benefits not only at the geometrical and structural level [111], but also for reception, propagation, integration and emission of electrical signals [111, 391]. Indeed, dendrite and axonal trees present fractal morphologies [444, 753], which allow the maximization of the number of synaptic contacts with the same presynaptic neurons, amplifying the surface of area available for absorption, distribution or collection of information processing. In the same way, these self–similar geometries, and despite their redundancy and irregularities, provide robustness and resilience to damage. In addition, thanks to its self–complementarity, such geometric structures would be capable of operating with good–to–exceptional performance at many different frequencies

simultaneously, giving rise to outstanding designs for wideband and multiband application [326]. In turn, the detailed description of morphologies of neuronal cells enabled Cajal to postulate a wide variety of theories of functionality and directionality of signal flow in various brain areas.

The relationship between network structure and dynamics has been extensively considered in theoretical studies [28, 516, 82, 252]. Since small–world networks present short average distances (like random graphs) and a high clustering coefficient (like regular lattices), these networks have a high vale of global and local efficiency [749]. Then, small–world networks are extremely efficient in exchanging information both at a global and at a local scale [82, 410, 411]. On the other hand, scale–free network [28] procure a dynamic scenario at the edge between order and disorder, thus maximizing the repertoire of dynamical regimes that a system can exhibit as well as the information diversity in the system [82, 462].

Functional cortical networks: Associative Memory

Different models have attempted to explain the functioning of cortical structures. Bressler and Freeman in 1980 [98] developed a model of olfactory discrimination, and proposed that odor information is carried through spatio-temporal patterns of amplitude of electrical activity (carrier wave)[98, 236, 244, 237, 239, 240, 245]. Like a self–organized system, spatio–temporal structures that have some degree of stability are created to'store' the information, but that can reconstruct themselves when a small external perturbation (stimulus) is applied. Indeed, when the same stimulus is applied the same structures are observed.

In the same years, such ideas became popular in the scientific community. In this spirit, Little [432, 431, 433] and Hopfield [330, 331] formulated the theoretical model of associative memory. This model was described as a network representing a dynamical system for which a global function called 'energy' could be defined. Actually, this 'energy' can be viewed as a Liapunov function for the autonomous system describing the state of the network. Like Bressler and Freeman's model [98, 244], the state space flow was apparently dominated by attractors that represented the nominally assigned memories. When the flow was not entirely deterministic and small stochastic effects were incorporated, a general physical content–addressable memory emerged. It is noteworthy mentioning that the classical associative memory is an abstraction of the assembly concept [759, 538, 539]. Since cortical structures are the natural system for associative memory, let us consider this model more carefully.

Firstly, the concept of associative memory is based on understanding the information as a semantic representation of knowledge, usually in terms of relational structures. In particular, the term content–addressable memory is understood as the ability to retrieve previously stored information on the basis of its contents rather than by the specific address and location. This means that *addressing* is based on semantic content represented by dynamical patterns in the phase space associated to nominally memory, and not on the specific index in the hardware storage. In these models, the phase space can be divided into different semantic zones and its selection (redirection) spontaneously emerges through the coupling between the applied stimulus and the specific properties of the network. Along this process, and as a result of an external perturbation, the popula-

tion reaches a locally stable limit point, offering the information required and the search process finalizes.

A remarkable feature is that the searching process is very efficient and robust. Indeed, as Aristotle already remarked in his book entitled *On Memory and Reminiscence*, brain's recollection is a synthesis of memorized information, and not necessary an identical copy of the original occurrence. We note that our standard computer memories require complete knowledge of specific addresses for retrieval, whereas associative memory allows the recall based only on partial information. In computers, sequential access or random access are used to access any item of data from a population of addressable elements. Both addressing methods are based on an indexation mechanism, i.e. a serial mechanism. By contrast, a 'genuine' content–addressable memory or content–associative memory always performs all comparisons in parallel and a solution is provided when an attractor is reached. This leads to a significant change in the accessing speed. Indeed, for example, the speed of the random–access memory is proportional to $\sqrt{n}\log_2(n)$, where n is the number of elements stored [24], whereas the speed of content–associative memory is independent of n and of the amount of information present in the elements [414].

Secondly, associative memory implicitly involves the use of relational structures which provide the recollection of information. As Hanlon pointed out [307] on content–addressable memories, the correct meaning of 'associative' refers to interrelationships between data, and not on the information storage mechanism. Indeed, it is usually considered that mental items are connected fulfilling the following laws: (i) simultaneous occurrence ("spatial contact"), (ii) occurrence in close succession ("temporal contact"), (iii) similar meaning, or (iv) opposed meaning. We note that the first two premises are suitable for writing or encoding processes, creating recurrent spatio–temporal patterns in the network, or generating functional dynamics. In contrast, the last two premises are well suited for reading or decoding processes and implicitly require a comparison process. Traditionally, accessing data on the basis of their content always requires a comparison of an external desired argument with part or all of the information stored in the cells. In general, a high positive correlation (similarity) or a negative one (contrast) can be used as the input key or search argument. In this sense, 'association rule mining' aims at discovering spatio–temporal patterns using interrelations or cross–references between pieces of information only. However, there is a subtle nuance between a content–addressable memory and a content–associative memory. Both represent the information semantically and compute in parallel, but the relational structures are completely different. With a content–addressable memory, the implemented relational structures are based on a comparison between a binary classical logic and the content of each of the cells. In contrast, in a content–associative memory, associative learning is based on the distribution of the strength of the link between every pair of cells. Then, the strength of each link is set to a value proportional to the similarity (or dissimilarity) of the respective activity values of the cells. Hence, the memory traces correspond to changes in these links (its corresponding strengths), and not to changes in the cells themselves. It is the result of a network effect grounded on the inter–relationships between nodes. Such a functioning implies an increase in the memory capacity since the number of interconnections scales as 2^n in comparison to the number of cells n.

A third and crucial point, already sketched, is that computation emerges as a spontaneous process of a self–organized system. But, what requirements are needed? The

studies of C.R.Langton [408] focused on understanding the conditions under which computation might emerge spontaneously in Nature. In particular, he analyzed under what conditions the class of formal abstraction, so–called cellular automata (CA), support the basic operation of information transmission, storage and modification. Just like the previous investigations, the study of Ref. [408] reported the formation of similar spatio–temporal structures, but with the incorporation of a new idea. The author suggested that computation may emerge spontaneously and come to dominate the dynamics of physical systems when those systems are at (or near to) a transition between highly ordered and highly disordered dynamics, in analogy to a second–order or 'critical' transition between the solid and fluid states of matter. In this way, such a description falls within the class IV of classification of Wolfran's CA [763]. Then, this CA whose dynamics is said to drive near *the edge of order and chaos*, arises with *extensive computational capabilities* [536, 535, 408, 73, 454].

At this point, one may ask, when speaking about *computational capabilities*, what are we referring to? Different properties must be taken into account in the definition of computational capabilities of an information processing system. Firstly, this system needs to be highly sensitive to detect external stimuli (inputs). It is somewhat curious that the nervous system is immersed in a highly noise environment. As we shall see later, working nearby a nonlinear region (and in certain conditions) increases the resonance capacity of the brain and hence, the sensitivity of incoming signal. Secondly, the propagation of information (transmission) hmust be highly efficient and robust, over short and long distances. We note that class IV CA present large transients with large correlation lengths that provide an efficient propagation of complex dynamical patterns. Thirdly, these systems should exhibit an extremely high–capacity for storing information. Since class IV CA work near a transition point, a substantial number of metastable states arise, increasing the system access to memories while preserving efficient information management, i.e. stored and transmitted information interact with one and other.

The notion of metastability implies that system's global activity enters into different states of coordination of its constituent domains without becoming trapped in any particular state. This, in turn, allows the system to adopt swiftly to environmental changes and supports flexible processes, and with an efficient and fast information search mechanisms.

A fourth property worth addressing is that these systems have to transform any specific input to a corresponding *desired* output. We note that, by construction, the neuronal model proposed above is intrinsically *computable* [3] and neuronal circuits act as Turning Machines (TMs). However, we note that in the neuronal system the classical notion of computability introduced by the thesis of Church–Turing [137] must be extended. Effectively, this is mainly due to the fact that neuronal networks present themselves as intrinsically interacting and concurrent [4] system [278] and, hence, a neuronal network in

[3] A problem is computable if it can be solved in principle by a computing device, usually called Turing Machine (TM) [137]. Usually, the computability of a problem is closely linked to the existence of an algorithm to solve the considered issue. In turn, the term computability implies an "effective calculability" and, hence, the existence of a well–defined function. From a mathematical viewpoint, the assumption of computable problems involve a function–based framework. Throughout history a wide range of models of computability have been proposed, as well as Turing–computable [137], μ–recursive functions [386, 387] and λ–calculus [137]. However, all these models exclude interaction and concurrency.

[4] Concurrency and parallelism are two terms that are often interchanged although they represent different concepts. Indeed, *concurrency* regards operations that appear overlap in an unforeseeable

general represents formal models of interaction machines (extended TMs). We note that these two ingredients are always excluded in the theory of computation and, in this sense, a neuronal network also represents a natural platforms that changes our comprehension of what is computation and how it is modeled.

We note that the concept of CA [763] and the model of C. Langton [408] are related to classical models of statistical mechanics, in particular percolation and Ising models [384]. Indeed, numerical simulations suggested that there is a sharp transition between the ordered and chaotic regimes [186]. These studies used ideas from statistical physics to develop an accurate mean–field theory for random Boolean networks [186] and for Ising–spin models [184, 185] which allows to determine the critical parameters analytically. Since the transition is abrupt, the search mechanism is fast, but unfortunately this makes difficult its detection. However, experimentally, several studies suggested that cortical brain might operate at criticality [52, 51], a conjecture supported by the recent observation of neuronal avalanches in cortex *in vitro* [558, 679, 67], in anesthetized rats [272] awake primates [548], and in neuronal models [131, 215, 170, 13, 693]. A neuronal avalanche is a cascade of burst of activity where a local group of neurons triggers the activity of other neurons. This pattern of activity reflects fast propagation of local synchrony, by cumulative local interaction, where the size and life–time distribution of it can be approximated by a power law, which in turn can be linked to the structure of the local neuronal circuits. Several authors suggested that the establishment of a detailed tuning of the balance between excitation and inhibition [679, 67], as well as an optimal concentration of dopamine [679], then the *size of avalanches* follow the power law behavior with an exponent of $-3/2$, while the *duration of avalanches* exhibit an exponent of -2. This characteristic exponent can be 'appropriately' tunned by modifying the excitatory-inhibitory balance [67] and the neuronal networks go trough the different states of subcritical, critical and supercritical.

Despite the elegance of all these ideas, their detailed experimental assessment is very difficult when considering the whole brain. Indeed, cerebral cortex give rise to a bewildering variety of dynamics, with frequent overlap of dynamical states or strong synchrony. Despite technological advances, the characterization of the dynamics turns out to be very difficult in a system with several actors at play. We note that the characterization of the cortical dynamics (and topology) is of utmost importance to understand its functionality, but it is clearly a difficult task.

manner, and it consists in the right management and control of a non–deterministic flow. In concurrent computation, two process advance independently of each other and they are scheduled by the system operative to run on a single-core. Concurrency is usually referred to as a property of software, sharing the same resources, and it is framed in a non–function model. In contrast,*parallel operations* consider that concurrent parts are executed at the same time on a multi–core, multi–processor or distributed systems. Hence, parallel execution is a property of the machine (topological network), and not of the software (dynamics). However, according to a language–based approach, by definition, parallelism is about the dependencies among the subcomputations of a deterministic computation and, therefore, it is treated in a function–model framework. Indeed, concurrency is the management of sequential content that changes to unpredictable stimuli. In contrast, parallelism consists in analyzing the parts of the code that are independent, and the different dependencies established among them.

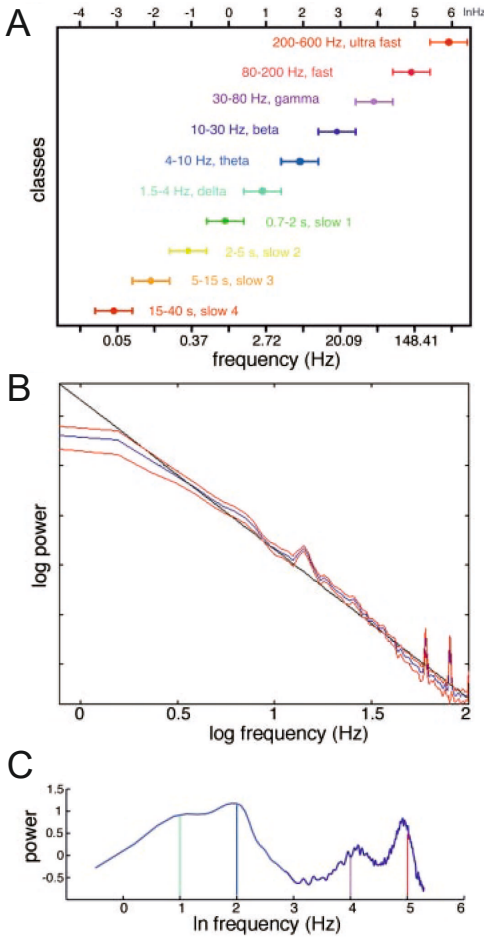

Figure 1.3: **Power spectrum of EEG recordings.** (A) Distribution of bands in EEG rat recordings. For each band, the range of frequencies is shown, together with its commonly used terminology. Adapted from Refs. [547, 108]. (B) Power spectrum of EEG from the right temporal lobe in a sleeping human subject. Adapted from Ref. [243]. (C) Illustrative power spectrum of hippocampal EEG recordings in mice. Adapted from Refs. [547, 108].

Cortical dynamics and functional modes

A plethora of dynamic regimes has been observed in the cerebral cortex. Below, we expose some of the most remarkable ones together with their associated functionality.

A) Linear description of dynamics

In 1929, Hans Berger identified oscillatory behavior in cortical human EEG–recordings [71]. They were initially termed Berger rhythms and, later, classified as α rhythms. These oscillations form part of a series of cortical signals whose frequency values fall in the range $f \in [0.5 - 500]$ Hz (Fig. 1.3A). The power spectrum of these physiological signals exhibit an interesting feature, and is that the power is inversely proportional to the frequency f (Fig. 1.3B). This $1/f$ trends indicates that perturbations at low frequencies can cause energy dissipation at higher frequencies, i.e. that extensive (spatial) oscillations at slow frequencies can modulate faster local events. All these properties are a consequence of the

architecture of the networks of neurons, besides the limitation in the speed of transmission (due to axon conductivity and synaptic delays). Since most connections are local, the oscillation period would be limited by the number of neurons recruited by the rhythm. High frequency oscillations would be confined in spatially reduced networks, whereas the recruitment of larger networks require slower oscillations.

On the other hand, it has been observed that there are regions of the spectrum that are enhanced during the performance of certain tasks, specific mental states or when some pathologies take place. These portions of the spectrum comprise regions whose frequencies determine what is known as the EEG bands, as illustrated in Fig. 1.3C). They are:

- **Delta band**, δ $(0.5-3.5$ Hz). It is characteristic of deep sleep states, but may also be associated with certain pathologies when it appears with certain rhythmicity or morphologies, or at specific locations.

- **Theta band**, θ $(3.5-7.5$ Hz). It appears augmented during sleep and plays a very important role during infancy and childhood. In the adults, its presence at high amplitude during the waking state is considered abnormal, reflecting some pathologies.

- **Alpha band**, α $(7.5-12.5$ Hz). It arises spontaneously in healthy, awake adults, particularly in states of relaxation or mental inactivity. This band is better detected when the eyes remain closed and, specifically, over the occipital region.

- **Beta band**, β $(12.5-30$ Hz). Before expectation or tension states it is strengthened and traditionally subdivided into two bands, the β_1 and β_2. Of lower amplitude than α band, it is much better captured in central and frontal positions.

- **Gamma band**, γ $(30-60$ Hz). Initially this band did not capture much attention, but it the last years its role was ascribed to the integration of information.

This classification according to different bands is motivated by the fact that, experimentally, the central frequency of these oscillations fits a straight line when the power is plotted as a function of the frequency on a natural logarithmic scale (Fig. 1.3B). Moreover, if adjacent frequency bands are compared, it can be seen how there is a constant relation between them.

Associated to the term *band* there is also the term *rhythm*. While the former refers to the region of the spectrum in which the oscillations take place, the latter determines the location and functionality of the oscillatory activity. This is the case for example of the μ rhythm, which appears on the motor region, sharing the same frequencies as the α rhythm. Although both rhythms fall within the α band, they perform very different functionalities.

In spite of the advances and the time elapsed since the discovery of these rhythms, their precise functional role remains elusive. A first reason is that, traditionally, there has been more interest in studying the 'spatial' coding of information (the activation of each brain area or neuronal group according to its anatomical location) rather than in identifying the temporal pattern of the information. A second reason is that, for years, any cognitive activity has been considered to be linked to 'desynchronized' states.

For instance, waking states present patterns of small amplitude, and for this reason the associated oscillatory activity was considered synonymous of brain at rest. This apparent inverse relationship between cognitive activity and the strength of cerebral rhythms was further strengthened when epileptic patterns were investigated; or during anesthesia, inherently associated with the loss of consciousness.

This view has been substantially revised in the last years. Recent advances suggest that the synchronization between different oscillatory networks could reflect a bridge between the dynamics at the cellular level and the global behavior of the network. In certain pathologies, for instance, brain rhythms are modified [102, 614], and in the development of cognitive tasks, interrelations between the rhythms of different regions are established [730]. Evidences also shown that, in certain motor tasks, the oscillatory activity presents well defined patterns [30, 31]. As a result, it was suggested that both perception, memory and even consciousness could result from the synchronization of different neuronal populations.

Nonlinear description of dynamics

The idea that 'chaotic' activities may exist in physiological system is not a new one. Several studies seem to indicate that chaos plays a relevant role in the physiological brain and may be even a necessary ingredient for normal functioning. Nonlinear time series analyses have suggested that the human electroencephalogram (EEG) may share statistical and dynamical properties with chaotic systems [212, 396, 413, 583, 608, 672]. Studies by Rapp *et al.* [578, 579] showed that low–dimensional chaos could occur in the spontaneous activity of motor cortex of anesthetized monkey. Analysis of EEG data by Babloyantz *et al.* [50] from the human brain during the sleep cycle revealed also the existence of low–dimensional chaotic dynamics. After the pioneering studies of Rapp and Babloyantz, a plethora of studies showed the importance of using nonlinear descriptions [26, 46, 47, 48, 49, 61, 201, 211, 284, 412, 451, 452, 476, 477, 478, 495, 580, 602, 649, 659, 747, 746, 511, 39].

For instance, experimental and theoretical studies of chaos in EEG were carried out by Freeman to investigate the perceptive events in the olfactory system of the conscious rabbit [235, 231, 236, 238, 239, 235, 234, 244, 647, 734] and in the visual system of the monkeys [240, 232, 244]. The authors suggested that the bulbar background activity is chaotic, and pointed at the existence of an attractor in the phase space that acted as point repellor. They also showed that the PSD was distributed as $1/f$, with an autocorrelation function that decayed rapidly, and with time series markedly aperiodic [239]. They concluded that the dynamical processes in the olfactory system of a motived rabbit was characterized, in absence of any significant odor, by a spatially and temporally unpatterned chaotic state. However, immediately after the application of a learned odor, the rabbit's brain briefly switched to a global odor–specific chaotic state characterized by a single near–limit cycle attractor. In line with these results, studies in the respiratory cycles of olfactory bulb of the conscious rabbit also evidenced a fast shift in the dimension of correlation, from $6-7$ during expiration to $1-2$ during inspiration [492].

The change of dimension from a higher value to a lower one, which occurs during the evaluation of a set of environmental inputs, may be an important part of sensory processes. In the same way, dimension evaluation for EEG recordings of cortical structures

in adult cats [594, 595, 596], indicated the presence of various attractors with correlation dimensions in the range $3.8 - 5.6$ during slow–wave sleep ($1 - 3$ Hz). In contrast, higher dimension measurements in the range $8 - 9$ were obtained in spontaneous activity recordings of the auditory cortex of an awakened cat, with activity frequencies in the window $100 - 1000$ Hz [597, 62].

States of wakefulness and attention may be also associated to high–dimensional dynamics, which are perhaps analogs to a stochastic system [90]. For instance, the studies of Goldberger and West [277, 276] suggested that the dynamics of a healthy physiological system would produce apparently highly irregular and highly complex types of variability and fluctuations, whereas disease and even aging would result in less complexity and more regularity. The authors argued that chaos should be healthy because it provides the organism with an 'information–rich (broadband) state' and 'spectral reserve', while that periodic behavior can foreshadow disease [276]. Indeed, the notion complexity loss appears to be a characteristic feature in many mental disorders. The term 'dynamical disease' [273, 274, 275, 458, 459, 488] captures the notion of abnormal rhythms, which could be either more irregular or more regular than normal, and are associated with pathological physiological functioning.

It is still unclear, however, the role of chaotic dynamics and the dimensional switch on the functionality of cortical structures. Several hypotheses were provided. Indeed, chaotic dynamics can offer many functional advantages. Adaptable and flexible, this dynamics operates under a wide range of conditions allowing the system to cope with the demands of an unpredictable and changing environment. Chaotic systems are more flexible than non–chaotic ones since the attractor spans a large volume of the state space. With proper control, the system can rapidly switch from a state to another.

The inherent instability of chaotic motions facilitates the ability of neuronal systems to quickly adapt, and to make transitions from a pattern to another when the environment is altered [567]. Effectively, the presence of continuous aperiodic activity allows neurons to stay fit and to rapidly transit to other states. It also procures broad spectrum carrier waves, minimizes tendencies to parasitic phase locking, and provides a source of unstructured activity for driving Hebbian synapses during learning. The latter ensures the creation of new basins of attraction instead of reinforcing existing attractors in complex landscapes [241, 242, 233].

Although, at a first look, irregular behavior might appear devastating for the system, it is an essential ingredient that also provides mechanisms for noise filtering. Additionally, cognitive functions such as searching in memory for a concept, or the creative solution of a problem, cannot be described in a linear fashion. Hence, models that involve simple oscillations without ensuring enough flexibility may fail at procuring a correct description of cortical functioning.

Other hypothesis has been raised in line the previous ones. It was suggested, for instance, that lower–dimensional attractors are associated with the evaluation of familiar and expected stimuli, while higher–dimensional attractors arise when new or conditional stimulus emerge [769]. Indeed, dimensional complexity increases over those brain areas with little involvement in a specific task, whereas it reduces in those regions in which networks become actively engaged. Theoretical studies [169, 662] exposed that a synaptic evolution, either via spike–timing dependent plasticity (STDP) or via Hebbian learning, leads to a reduction of chaos towards a less complex dynamics, permitting the association

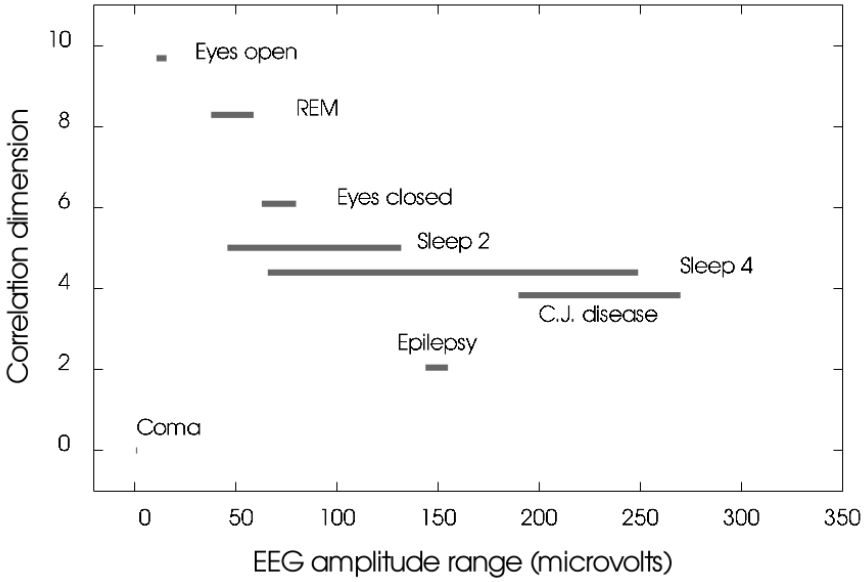

Figure 1.4: **Correlation between dimension and amplitude for different human brain states.** The correlation dimension of EEG signals is shown as a function of the amplitude range (maximal amplitude deflection calculated over 1 second periods). Plot adapted from Refs. [90, 187]

of a specific pattern to simple orbits.

The correlation dimension obtained for different brain states are represented in the Fig. 1.4, and according to Refs. [90, 187]. Interestingly, this representation reveal a 'hierarchy' of dimensionality as a function of activity, as previously described.

On the other hand, random noise in linear information theory has been traditionally seen as harmful for signal reception. However, in regard of stochastic dynamics, noise can be beneficial in the sense that it can increase the sensitivity to detect external stimuli. Several studies indeed suggest that signal detection is enhanced by noise, for instance in *in vitro* preparation [194], in animal experiments [148, 292], and in human perception [147, 646, 584]. Additionally, although noise presents an unpredictable behavior and lacks any structure in the state space, it is extremely important for information processing. Noise could be able to organize the irregular behavior of individual neurons or neuronal assemblies. T. Mäki–Marttunen and coworkers showed that networks with Poisson degree distributions could be tuned to a regime of maximal complexity by adding a suitable amount of noise to a deterministic Boolean dynamics [463]. In addition, the authors demonstrated that the presence of noise helps retaining the system in a state with high information content.

Since our research is focused on the analysis of *spontaneous activity* in dissociated embryonic cortices, it is important to contextualize the importance of this spontaneous activity for neuronal circuits and the brain in particular. First, a broad body of experimental work has shown that spontaneous brain activity is not random, but structured in both time and space. At the level of large-scale neural systems, measures with functional

MRI (fMRI) evidenced that spontaneous activity is linked to a series of highly coherent functional networks. Second, ongoing cortical activity has been shown to play a critical role in development [81] and is essential for processing sensory perception [379, 306]. A.G. Blankenship *et al.* [81] showed that, despite differences in architecture and output across various circuits, the source of spontaneous correlated activity and the mechanisms that generate it are remarkably similar. And, third, in recent years, a variety of studies across multiple *in vivo* and *in vitro* systems showed that spontaneous activity is essential for processing sensory perception, for modulating of stimulus–evoked activity, and for accessing internal representation [379, 221, 494, 735, 717, 225]. Interestingly, A. Luczak et al. [445] speculated that cortical architecture imposes common constraints on spontaneous and evoked activity flow, which may result in a similarity of the patterns. These 'default patterns' would then be strongly conserved under a variety of conditions. G. Deco *et al.* suggested that the formation and dissolution of these resting–state patterns could reflect the exploration of possible functional network configurations around a stable anatomical skeleton [180]. Functionally, it was also proposed that cortical spontaneous activity underlies processes such as mental imagery [399, 397, 398], cognition [601], and the consolidation of memories [107, 325, 89].

1.3 From the brain to neuronal cultures

The interplay between single cell dynamics and network topology is tremendously complex, particularly when addressing to the comprehension of the human brain [135, 32, 12]. To advance in this quest, the last two decades have witnessed the emergence of a large of techniques to investigate the brain. This includes brain functional and mapping techniques such as fMRI, EEG, MEG, or DTI, together with resources from graph theory and signal processing [104, 219]. As a whole, they have provided unprecedented details on brain functional interactions and their dependence with the underlying circuitry.

Current research has also opened new perspectives in our comprehension of dysfunctional circuits. Indeed, severe neurological disorders and behavioral deficits are associated to alterations of the neuronal circuitry [623], abnormal neuronal activity coordination [721], or deficient neuronal machinery [456]. Autism, for instance, has been ascribed to an underconnectivity or overconnectivity of local brain circuits combined with long-distance disconnection. Schizophrenia has been associated with an imbalance of the excitatory and inhibitory circuits, among other factors [453, 771]. Epileptic brains, compared to those of healthy subjects, display a richer functional connectivity with a clear modular structure [127], while brain networks in Alzheimer's disease patients are characterized by a loss of the small–world network feature [670].

In line with these studies, dynamical analysis from different states of human EEG reveal evidences for low–dimensional chaos for pathological states such as Epilepsy[47, 348, 229, 550, 345, 698, 418, 642, 346, 551, 417], Parkinson's disease [710], manic–depressive illness [512, 710], the terminal state of Creutzfeldt–Jakob disease [189] or Huntington's disease [310]. For epileptic seizures, it was shown that the degree of chaos significantly changes just before and during a seizure [47, 284, 600]. Epileptic seizures could be classified according to their degree of coherence. For instance, epileptiform bursts are char-

acteristic of uniform and stereotypical events [556, 715] [5]. On the other hand, Nandrino *et al.* [512] reported a decrease of complexity in EEG as a sign of depression. The authors argued that this diminished complexity of brain function in depression could be associated to a low level of environmental interaction.

All these advances have provided novel clinical prognosis tools by linking specific functional failures to topological traits of the anatomical network. They have evidenced that the information obtained from functional and anatomical techniques contain several signatures that reveal the properties of brain functions, both in normal and disease states. Nevertheless, a major difficulty in analyzing this information has been the sheer size and complexity of the human brain. The activity recorded from the intact brain results from the occurrence of several, simultaneous processes involving a huge number of interacting cells, thus complicating the understanding of the ultimate mechanisms that regulate neural activity. These difficulties have called for more controlled, accessible and simplified systems that would allow to investigate the basis of brain operation.

Neuronal cultures have emerged as one of those systems. These *in vitro* preparations are typically derived from dissociated rat cortical or hippocampal tissues, can be maintained for several months, and their activity monitored by a number of recording techniques that are able to track single cell behavior [204]. The flexibility of neuronal cultures to fit diverse experimental platforms, as well as the ability of the experimentalist to act on them by chemical, electrical or other means, have made them very attractive for a large number of investigations, most notably the emergence and richness of spontaneous activity patterns [742, 530], the interplay activity–connectivity [738], the network's self–organizing potential [544], and criticality [695].

The importance of neuronal cultures is that they provide a suitable environment to study important features in living neuronal circuits, in particular collective phenomena. The accessibility of the cultures make then also very useful to explore some of the linear and nonlinear studies outlined above, and clearly in a much easier way than in the entire brain. Although the neuronal cultures have lost the connectivity layout of the original tissue, their retain the neuronal type and exhibit similar dynamics. Hence, neuronal cultures serve as a true *living lab* to investigate universal phenomena in neuronal systems, their physical modeling, and the sensitivity of network behavior to failure at a circuitry or neuronal level.

Here we propose to use analytical tools based on linear and nonlinear time series analysis to investigate the functional and structural topology of neural cultures under different experimental conditions. We will use fluorescence calcium imaging to monitor the spontaneous activity of the neuronal network with single cell resolution. In a first set of experiments, we will investigate the development of the network along the first 3 weeks of maturation, a period in which the average neuronal connectivity, circuitry topology, and the excitatory–inhibitory balance change significantly. In a second set of measurements, we will perturb the topology of mature cultures by gradually weakening the excitatory connections. This action results in a gradual decay of collective spontaneous activity until it is fully disrupted. The analysis carried out in these different scenarios shows that fluorescence data can capture changes in the dynamical features of the neuronal network, providing a means for decoding the internal circuitry of the network.

[5] For more information about the different types of epilepsy, with a focal or generalized nature, one can consult Ref. [522].

Our study is a modest investigation that, although it requires a thorough exploration and modeling, may help understanding the use of statistical descriptors to detect and quantify distinct topological and dynamical traits in neuronal networks.

The developments presented here are still in their infancy, without any doubt. However, they bring to light or deepen in exciting fields of research. We believe that the detailed study of neuronal cultures is an important and helpful step towards the understanding of the functioning of living neuronal networks and the brain.,

Chapter 2

Experimental Setup and Procedure

The aim of this Chapter is to describe the experimental tools, strategies and procedures that were carried out to culture neuronal tissue, monitor its activity, as well as to provide the collection of experiments that shaped the core of this thesis. In the first section we give a brief overview of neuronal cell culturing. Next, we describe the different protocols for preparation, isolation, plating and maintenance of primary, rat embryonic cortical cultures. We then introduce the calcium image fluorescence technique to record spontaneous activity in the culture's neuronal population. We finally expose the different experimental lines explored in this thesis along its four years.

2.1 Mammalian brain and neuronal cultures

Neuronal cultures in general [146, 204] constitute one of the most fascinating experimental tools for the Neuroscience and Physics communities alike. Cultures are typically prepared by isolating neurons from specific neuronal tissues (in our case, brain cortices of embryonic rats), and platting them in biocompatible substrates. As a standard procedure, prior to plaiting, the tissue under interest is dissociated, either mechanically or enzymatically, to break the inter–neuronal connections created during embryonic development. Upon plating, and with adequate culturing conditions, neurons quickly connect to one another in a self–organizing process to form a new neuronal network within days [204, 140, 660]. Connections are formed, grown and refined in a complex morphological and functional manner. Surprisingly, the ultimate *de novo* network is characterized by a rich spontaneous activity that exhibits complex spatio–temporal dynamical patterns.

Neuronal cultures are usually prepared from embryonic animals for various reasons. Firstly, like skeletal muscle, neurons are highly specialized cell types that do not divide after the perinatal period[1] and therefore it is very difficult to maintain primary cell cultures of adult brains. Indeed, a major problem in culturing mature neuronal cells is their lack of proliferation, compromising their survival. For this reason it is customary to use a specific time point of embryonic development, in the range $18 - 21$ (typically indicated as E18 − E21). At these embryonic stages, neuronal tissue is formed by a mixed population of cells capable of dividing, the so–called *neuroblasts* and *glioblasts*. Neuroblasts

[1] In humans, for instance, the perinatal period commences at 22 completed weeks (154 days) of gestation and ends seven completed days after birth.

are neuronal cells able to proliferate and differentiate, developing into mature neurons[2]. We note that neuroblasts have not yet extensively developed axons and dendrites (collectively called *neurites*) and are not highly innervated. Hence, during dissociation of the neuronal tissue, the cells become less susceptible to damage. Similarly, glioblasts are early cells able to differentiate into several different types of neuroglia, specifically astrocytes and oligodendrocytes. It is generally accepted that neurons in culture require glial–conditioned medium to survive and grow, and a balanced ratio between these two populations is needed [196]. The glia to neuron ratio differs not only from species to species, but also from a brain region to another. Different cell–counting studies concluded that the glia to neuron ratio in the adult rat cortex is approximately $2:1$ [582], whereas in the human brain there easily exist 10 glia per neuron. To maintain this ratio in rat cortical cultures, the excessive glia cell proliferation is stopped at five days *in vitro* (DIV 5) through the incorporation of cell division inhibitors in the culture medium.

Regarding the selection of the embryonic age, at $\mathrm{E}18-21$ a sufficiently mixed neuron cell type has already long migrated from proliferative zones to cortical plates [480, 524]. In rats, the formation of the cortex (corticogenesis) starts around E14 and ends in the fetal stage ($\sim$E21). From proliferative zones, neuroblasts are generated and migrated in an orderly progression, with cells of the deepest cortical layers born first, followed by cells of the middle and finally the upper layers [568, 569, 479]. This inside–out pattern of neurogenesis produces neuroblasts within a given layer with similar functional properties and connectivity. Despite the complexity of this organization (which ultimately leads to an overlay of six different layers) cortical tissue mainly presents the same neuron cell type and, at this embryonic age, two main phenotypes are expressed [395, 66, 249, 65]. Indeed, cortical cultures usually contain a mixed of excitatory pyramidal neurons ($\approx 75-80\%$) and inhibitory non–pyramidal neurons ($\approx 15-20\%$), sufficient for complex synaptgenesis and electrophysiological behavior.

Upon plating, the process of aggregation, differentiation and arealization of immature cortical neurons takes place quickly as the synaptic connections are established. Hence, dissociated cortical cultures offer a useful framework to study the formation of neuronal circuits at the first stages of development [296, 553]. Diverse studies have shown that the cells grow fibers during the first 48 h, constituting a fiber network within 5 days with electrophysiological behavior. Neurons then become assembled into functional networks by growing out neurites that connect synaptically to other neurons. In general, after plating and along three weeks, the network experiences several changes [254, 70, 724, 728, 660]. Many of them are still unknown or are poorly understood.

Regarding the formation and typology of the connections, some consideration are worth mentioning. On the one hand, neurons predominantly communicate in the mature cortex via chemical synapses while glia cells interact mainly via electrical junctions (*gap junctions*). In the early stages of neocortical development, chemical synapses between neurons are scarce and therefore non–synaptic communication is predominant

[2]Although neuroblasts are mainly present as precursors of neurons during embryonic development, they also constitute one of the cell types involved in adult neurogenesis [251]. Neuroblasts are therefore being studied extensively as they have the potential to be used therapeutically to fight against cell loss due to brain injury or disease. Indeed, some studies evidence that fetal tissue grafted in damaged adult brains and spinal cords can survive and differentiate [80]. Moreover, this grafted cells may also receive and project connections, as well as to release neurotransmitters in a behavior–dependent manner in the adult damaged brain [199].

[496, 593, 590, 685], and both neuroblast and neuroglia aggregate into clusters (also called *neurospheres*) with cells coupled to each other via gap junctions. This packaging mechanism is very useful during the migration process to transport the cells from the proliferative zones to the cortex. In cultures, this aggregation occurs spontaneously when the cells do not have any mobility restrictions over the substrate, and different studies suggest that this structure can offer a favorable environment for neuronal maturation [502, 260]. Cells within the aggregates extend process, form synapses, synthesize neurotransmitters and express appropriate receptors [622, 34, 333]. In addition, the conditions within the small aggregates also appear to be favorable for the division of neuronal precursors, which do not proliferate well in dissociated cell cultures [259]. Interestingly, with ongoing development, these cell clusters have the ability to gradually disaggregate.

On the other hand, in cortical cultures, several of the above communication structures are retained, although with important differences [625, 562]. Studies showed that morphological differentiation of cortical pyramidal neurons in culture appear intrinsic in the development of the cell and may not require a highly organized environment for their formation [400, 653]. Indeed, the morphological and physiological properties of neuronal connections closely resemble those in their *in vivo* counterparts [400]. Furthermore, the distribution of cell types in culture is also similar [343]. From the functional point of view, cultured neurons display activity–dependent, path–specific synaptic modifications [76, 361] that closely resemble the long–term potentiation and depression observed *in vivo*. Nevertheless, the process of dissociation and platting erases the information on the wiring architecture of the native tissue. Cells' environment indeed shifts from the highly organized cortical environment to a planar substrate. Plating therefore induces a mono–layer of cells that tend to connect with their closest neighbors in a random manner, with axons and dendrites growing in a two–dimensional space. The *connectome* of the network that arises may therefore substantially differ from the native circuit. This aspect is the major criticism to neuronal cultures. In studies with brain slices [606], for instance, the connectivity is preserved along the plane of the slice, making these preparations more appealing for investigations in which the circuitry is crucial, such as in the understanding of rhythmic activity in the visual cortex [606].

The relative simplicity of the connectivity diagram in a neuronal culture can be viewed, however, as a positive aspect. First, the biochemical environment is much simpler, which provides an excellent platform to investigate the role of specific neurotransmitters and other agents. Second, the connectivity can be dictated at some extent through patterning, providing a very valuable tool to study the interplay activity–connectivity, adaptability, and network resilience. Third, the processes of self–organization, growth, maturation, and stabilization can be neatly monitored and modeled. And fourth, cultures emerge as a unique laboratory in the quest for identifying general mechanisms governing the dynamics in neuronal tissues, such as synchronization or the emergence and robustness of spontaneous activity patterns.

2.2 Culturing rat cortical cultures

In all the experiments along this thesis we used rat cortical neurons from 18 to 19–day–old Sprague–Dawley embryos. All the procedures were approved by the Ethical Committee

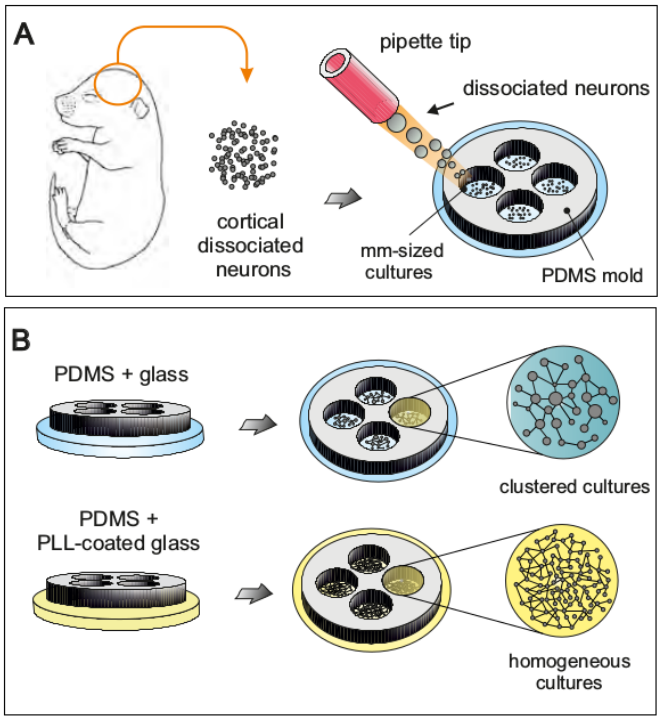

Figure 2.1: **Culture preparation.** (A) Cortices from embryonic rat brains were dissected and neurons dissociated by pipetting. Neurons were then suspended in plating medium and seeded onto previously prepared PDMS–glass structures 13 mm in diameter, and containing 4 cavities, each 3 mm in diameter. (B) Each cultures well contained 4 networks (*mini–cultures*), which developed independently from one another by setting the PDMS walls sufficiently high, above 2 mm. In the absence of adhesive proteins such as Poly–L–lysine, PLL (top), neurons moved and an aggregated configuration emerged. The coating of the glasses with PLL (bottom) gave rise to homogeneous networks.

for Animal Experimentation of the University of Barcelona, under order DMAH-5461. Culture preparation and actual experiments were carried out in Soriano's laboratory.

Every week, a batch of 24 wells of cortical tissue was prepared and cultured along the next 3 weeks. Cultures were combined with perforated molds to prepare different culture sizes. Cultures were typically designed as circular preparations with a diameter of either 3 or 13 mm. In general, neuronal density ranged in these cultures from 200 to 400 neurons/mm^2, with $70-80\%$ excitatory connections and $20-30\%$ inhibitory ones [660]. Fig. 2.1 illustrates the procedures involved in the preparation of the cultures. Along the thesis, different experimental techniques have been also tested to dictate the connectivity of the network in an effort to shape different connectivity blueprints, as detailed later. All the protocols and strategies that we applied are described in detail in Refs. [96, 142, 660].

2.2.1 Culture substrate preparation

Prior cell culturing, the physical substrate where neurons would sit had to be prepared for seeding. The substrate must ensure correct adhesion, growth, morphology and differentiation of the neuronal cells. In general, primary cells do not adhere to factory–ready

plastic or glass surfaces, since they have a net negative charge that conflicts with the glycoproteins and glycolipids present in the cells' membrane. These proteins and lipids contain several anionic groups that are repelled by the negative surface charge. Hence, substrates are usually treated with radiation, chemicals or electrical ion discharges to increase positive charges and while facilitating a hydrophilic behavior. Additionally, one can use biomolecules present in the extracellular matrix to coat the substrate, therefore enhancing cell adhesion and survival. In all our experiments we used borosilicate cover glasses 13 mm of diameter and 100 μm thick (#1 Marienfeld–Superior) coated with Poly–L–lisine (PLL, Sigma). The advantage of the borosilicate substrate is that it offers optimal optical clarity with a minimal autofluorescence.

The cleaning process of the cover glasses was as follows. First, cover glasses were placed into a custom–made carrier and immersed for 2h in nitric acid ($> 96\%$ HNO_3) which dissolves all organic material present in the surface. Glasses were next rinsed 10 times with double distilled water (DDW) and then immersed in $> 96\%$ ethanol for additional cleaning. After filling the Ultrasonic Cleaner with pure water and 1% Micro-90 soap, the loaded carrier in the presence of ethanol was sonicated at 60°C for 20 min. Glasses were then flamed and stored in sterile glass petri dishes for further usage.

Additional preparations were required in order to, ultimately, restrict the size of the cultures or to obtain different connectivity patterns. Although there are several strategies to control the connectivity of a neuronal culture through patterning, two of the most successful methods that we used were physical trapping and chemical confinement. The first one consisted in using topographical molds or hollow masks shaped on the silicon–based organic polymer known as polydimethylsiloxane (PDMS). The second one consisted in imprinting adhesive proteins in specific localizations of the substrate, creating areas for cell adhesion. The following sections briefly summarize the techniques and protocols implemented along the thesis.

Glass–PDMS structure preparation

Simple small–sized cultures (*mini–cultures*) were obtained by plating neurons onto a glass attached to a pierced PDMS mold, as shown in Fig. 2.1A. Although there are several strategies for manufacturing structures in PDMS, we focused in the most common approach and the most common PDMS in the market. We took the PDMS Sylgard 184 Silicone Elastomer Kit provided by Dow Corning (Midland, MI, USA). This kit consists of two components: a resin (base or cross–linker) and a hardener (curing agent). Both components were briskly mixed in a small beaker at a ratio of 10:1 (typically 30 mg of the resin with 3 mg of the hardener) until they were completely merged. The viscous mixture was carefully spreat over a 100 mm diameter petri dish to achieve a large area and a homogeneous layer. The amount of PDMS poured depended on the desired thickness of the mold, typically in the range $2 - 4$ mm. The PDMS dish was either left overnight at room temperature or heated at 80°C during 2 h in an oven. Once the PDMS film hardened, it was pierced with a stainless steel puncher of 13 mm in diameter, the same diameter as the cover glasses used for culturing.

Small cavities were next implemented by piercing the PDMS film with a puncher (Integra Miltex) of 3 mm in diameter. The reason to restrict the cultures to 3 mm in diameter was primarily to fit $2 - 4$ mini–cultures (depending on the study) in the field

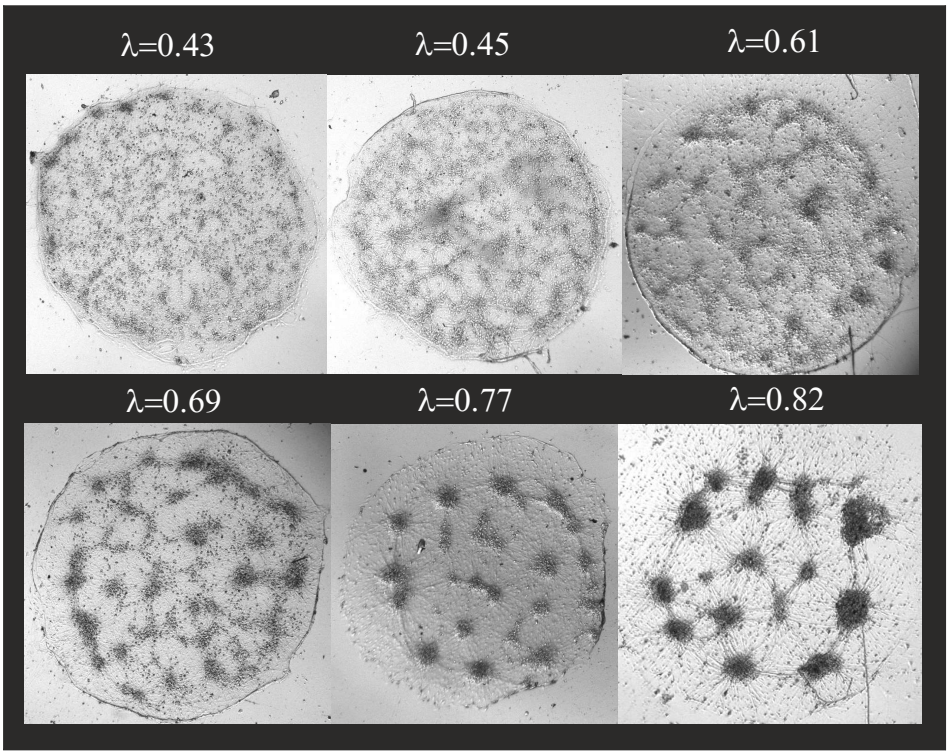

Figure 2.2: **Neuronal cultures with different topology.** Examples of cultures with different degree of aggregation: homogeneous ($\lambda = 0.43, 0.45$), semi–aggregated ($\lambda = 0.61, 0.69$) and aggregated ($\lambda = 0.77, 0.82$). The degree of aggregation is measured through the Gini coefficient (Fig. 2.3).

of view under optimal recording conditions, as described later. Finally, the PDMS molds were attached to the glass coverslips and autoclaved at $105°C$. This process both sterilized the PDMS and strongly bond it to the glass. Fig. 2.1B sketches a typical preparation. Final culture substrates were allocated in a 24–well culture plate for easy manipulation in the incubator.

Controlling neuronal connectivity with PLL

Different degrees of neuronal aggregation, and therefore circuit connectivity, can be achieved by treating the PDMS–glass structures overnight with the adhesive protein PLL [457, 770, 419]. To obtain homogeneous topologies, we prepared a solution of 1 ml PLL-4832 (0.1 mg/ml stock concentration) and 12 ml Borate Buffer (pH 8.40), and placed 1 ml of the solution in each well. By reducing the concentration of PLL we could then obtain cultures with a gradually higher degree of aggregation. Indeed, a lower concentration of adhesive protein facilitated cell motility and aggregation. At the extreme of a total absence of PLL, neurons formed highly compact three–dimensional neuronal assemblies or clusters [661, 349], usually termed *neurospheres* in the literature.

After PLL application, culture wells were carefully inspected for air bubbles. Air bubbles were undesirable since coating would fail in some areas. Air can also transport

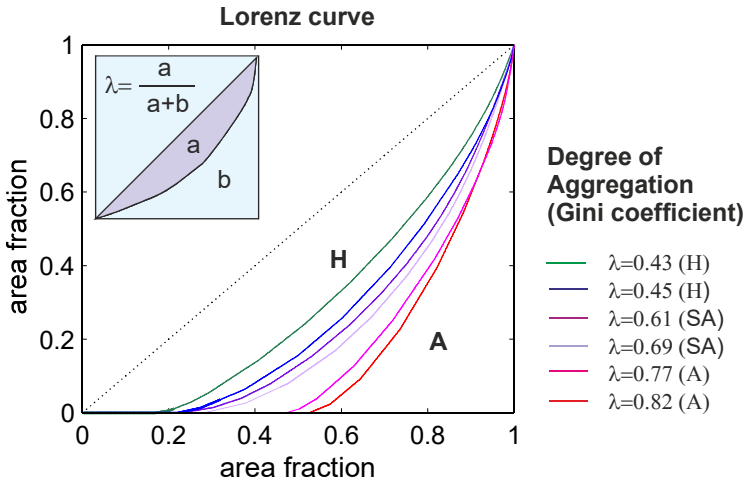

Figure 2.3: **Determination of the degree of aggregation through Lorenz curves.** The plot shows a graphical representation of the degree of aggregation λ corresponding to different Lorenz curves. These curves plot the number of neurons per unit area in cumulative percentages up to 100%. A straight diagonal line represents a perfectly homogeneous neuronal distribution. The difference between the straight line and the curved line accounts for heterogeneity (spatial aggreagation) in neuronal distribution. The Gini coefficient (inset) is calculated as the discrepancy between the diagonal line and the Lorenz curve. **H** means homogeneous; **SA** semi–aggregated; and **A** aggregated.

contaminants and oxidize neurons. Existing air bubbles were removed by gentle pipetting.

The glasses, or the combined PDMS–glasses structures, containing PLL were placed overnight in the culture incubator for PLL to bind the surface. The glasses were rinsed the next day twice with DDW and, finally, neural basal media, supplemented with B27 and glutamax, was added to the substrates, making them ready for seeding.

Fig. 2.2 shows examples of cultures with different *degree of aggregation*, which is quantified as the 'area under the Lorenz curves' (Fig. 2.3). These curves quantify the divergence of spatial coverage respect to a homogeneous scenario. In the graph, a straight line along the diagonal represents a perfect homogeneous distribution. The Lorenz curve for each experimental case lies beneath it. The difference between the straight line and the curve is termed *Gini coefficient* λ. It varies between 0 (perfectly homogeneous network) and 1 (extremely aggregated network), and provides a measure of the degree of aggregation.

We must note that, experimentally, there is always some degree of aggregation. The best homogeneous cultures typically exhibit $\lambda \simeq 0.3 - 04$ (Fig. 2.2). For sake of classification of the experimental data, we considered as homogeneous networks those with $\lambda \leq 0.50$, semi–aggregated for $0.50 < \lambda \leq 0.75$, and aggregated for $\lambda > 0.75$.

2.2.2 Dissociation and seeding

Pregnant rats were deceased with CO_2 at the animal farm of the University of Barcelona. Embryos were manipulated under sterile conditions, and their heads transferred to a large

culture dish containing ice–cold L-15 medium (Life) enriched with 0.6% glucose and 0.5% gentamicin (Sigma-Aldrich). After whole–brain extraction, the meninges were removed from each hemisphere to reveal the cerebral cortex. The frontal lobe was finally isolated from the rest of the brain and stored in a separate bath of enriched ice–cold L-15 medium.

After dissecting all embryos, the isolated cortices were aspired from the petri dish and mixed with 1 ml of plating medium [90% Eagle's MEM (Life) —supplemented with 0.6% glucose, 1% 100X glutamax (Gibco), and 20μg/ml gentamicin— with 5% heat–inactivated horse serum (Life), 5% heat–inactivated fetal calf serum, and 1μl/ml B-27]. Mechanical dissociation was then carried out by pipetting the solution in and out about $30-40$ times with a fire–polished Pasteur pipette until all fragments of tissue were homogeneously dispersed. Finally, additional plating medium was added to the suspension in order to achieve the desired neuronal concentration, typically in the range $(90-110)\times 10^3$ cells/ml. The final suspension volume delivered to each well was 1 ml, and each well contained approximately a number of cells equivalent to half cortex. Although the plating procedure led to a nominal density of about 0.1 million cells/well ($5,000$ neurons/mm^2), the final density measured upon recording (at day *in vitro* $6-21$) was around $200-400$ neurons/mm^2.

2.2.3 Cultures maintenance

Cultures were incubated at 37°C, 95% humidity, and 5% CO_2 for 4 day in plaiting medium. The medium was next switched to changing medium [90% supplemented MEM, 9.5% heat–inactivated horse serum, and 0.5% 5–fluoro–deoxy–uridine (FUDR, Sigma-Aldrich)] for 3 days to limit glia growth, and thereafter to final medium [90% supplemented MEM and 10% heat–inactivated horse serum]. The final medium was refreshed every 3 days by replacing half of the culture well volume. For clarity, in Tab. 2.1 we summarize the contents of the culture media and their role.

2.3 Neuronal activity monitoring

2.3.1 Introducing recording techniques

Various technologies have been introduced for neuronal recordings of the mammalian brain *in vivo* and *in vitro*. The devised technologies have their advantages and limitations, but the final choice for one or another depends on the constraints of the experimental system and the particular aspect that one is interest to explore. The understanding of information transmission in a neuronal circuit, for instance, requires methods for simultaneously tracking the activity of a large population of neurons with sufficient precision. Fluorescence Calcium Imaging [587, 651] and Multi–Electrode Arrays (MEAs) [703, 761, 296] are the two main approaches used to simultaneously monitor neuronal activity *in vitro*. The optical, calcium fluorescence imaging approach is the one used in our experiments given its versatility and affordable price.

Product Name	Description	Provider	Role
L15+2G	L15 enriched with 0.6% glucose and gentamicin	Sigma-Aldrich	Maintains physiological pH conditions before plating
MEM+3G	Essential Medium Eagle's-L-glutamate enriched with gentamicin, glutamate and glucose	Sigma-Aldrich	Main buffer for cell culturing and development
Plating medium	MEM+3G with 5% of foetal calf serum (FCS), 5% of horse serum (HS), and 0.1% B27	FCS and HS, Invitrogen B27, Sigma-Aldrich	Neuronal growth
Changing medium	MEM+3G with 0.5% FUDR, 0.5% Uridine, and 10% HS	FUDR and Uridine, Sigma-Aldrich	Limits glia cell division
Final medium	MEM+3Gwith 10% HS	HS Invitrogen	Maintains a proper environment to keep cultures healthy for long time
EM	500ml DDW with 128mM NaCl, 1mM CaCl2, 1mM MgCL2, 45 mM sucrose, 10mM glucose, and 0.01M Hepes; pH 7.4	--	Recording solutions i.e. pH-stable buffer for actual experiments

Table 2.1: **Cell culture and recording solutions.** The table summarizes the different culture media used for preparation and maintenance of the cultures, as well as for recording activity. We also include the manufacturer of the product and the role of the different products.

2.3.2 Calcium fluorescence imaging

Calcium fluorescence imaging allows for the simultaneous monitoring of hundreds to thousands of cells both *in vivo* and *in vitro* with sufficiently good spatial and temporal resolution [293, 680]. This technique allows for the detection of neuronal firings by the indirect monitoring of calcium transients through a calcium sensitive probe, as described in detail in the review of Grienberger *et al.* [293].

Calcium indicators are molecules that can respond to the binding of Ca^{2+} ions by changing their conformation and, ultimately, fluorescence properties. There are in general two classes of Ca^{2+} indicators, *genetically encoded* fluorescent proteins [390] and *chemically engineered* fluorophores [490]. In this thesis we used chemical indicators. Their major advantage over genetically encoded ones is that do not require transfection into the cells, greatly simplifying the biochemical protocols. Chemical calcium indicators simply require the incubation of the culture with the fluorescence probe prior measurement.

Chemical indicators allow for intracellular Ca^{2+} detection over a very large range (< 50 nM to > 50 μM). In our studies we used the Fluo-4 calcium probe (F14201, Life) available as cell–permeant AM ester in packages of 50 μg, and prepared as aliquots of 1 $\mu g/\mu l$ in DMSO (F14217, Life). Fluo–4 is a tricarboxylate compound in the form of an ester derivative which penetrates the cell membrane. Then it is enzymatically split

to release tetracarboxylate ions which are impermeable to the cell membrane, therefore remaining into the cell soma. The calcium indicator incorporates a green fluorescent protein that, at binding to calcium ions upon neuronal firing, experiences conformational changes that enable the fluorescence emission. Specifically, Fluo–4 is excited in the blue range ($\simeq$ 485 nm) and emits in the green range ($\simeq$ 506 nm).

It is important to mention that not only the spectral characteristics are important, but also the binding properties (*affinity*) of the probe. The majority of Ca^{2+} within cells is not free to diffuse but tightly bound to various cellular buffers. The bound to free ratio of Ca^{2+} within the endoplasmic reticulum is of the order of 10 to 1. In the same way, cytosolic Ca^{2+} is buffered 100 to 1, meaning that for every 100 Ca^{2+} ions within the cell, only 1 ion is free to diffuse. Additionally, chemical Ca^{2+} indicators themselves also act as Ca^{2+} buffers and have also an impact in the kinetics of Ca^{2+} signaling within cells. High affinity indicators require more time to unbind Ca^{2+} and are therefore suited for slow processes at the whole–cell level and with low concentrations of calcium, as occurs during neuronal activity. Low affinity indicators provide fast responses but require high concentrations of calcium to be detectable, and are therefore suited for subcellular processes. Fluo-4 has an affinity in the mid–high range ($K_d^{Ca^{2+}} = 345$ nM at pH=7) combined with a 400 fold increase in fluorescence upon neuronal firing, making it almost perfect for monitoring neuronal activity.

Upon neuronal firing, the series of events related with calcium are as follows. The elicited action potentials (APs) trigger large and rapid calcium influx through voltage–gated channels. When an action potential reaches the presynaptic membrane, the electrical depolarization of the membrane causes the opening of channels (including calcium selective ion channels) that lead to Ca^{2+} intake. The higher concentration of Ca^{2+} enables then synaptic vesicles to fuse to the presynaptic membrane and release their contents (neurotransmitters) into the synaptic cleft, which ultimately bind the corresponding receptors in the post–synaptic membrane. Hence, in the presynaptic terminals, calcium influx triggers exocytosis of neurotransmitters containing synaptic vesicles. The amount of neurotransmitter released is correlated with the amount of Ca^{2+} influx.

In terms of imaging, calcium binding upon firing leads to a fast rise of the fluorescence level of the monitored neuron (on the order of a millisecond), followed by a much slower decay (typically of a second). The fast dynamics of the former is due to the influx of calcium through rapidly responding voltage gated ion channels, while the slow dynamics of the latter is associated to the slower pumping processes governing the outflow. This dynamics is in turn coupled with the binding–unbinding kinetics of the probe, altogether picturing a complex behavior. From a practical point of view, and with Fluo-4 in mind, the first spike in a train of activity can be easily recognized, but the subsequent ones may be harder (or directly impossible) to discern. In our measurements, we found that the bursting activity characteristic of the network typically invokes concatenated five or six spikes in each neuron, providing a fast increase in the fluorescence signal in few milliseconds, an intensity that is approximately proportional to the number of spikes. In Fig. 2.6B we show the typical fluorescence traces obtained in our recordings.

2.3.3 Advantages and drawbacks

The advantages of the fluorescence technique are the ease of application and the fast response. The actual imaging instrumentation can be tuned to balance image quality, field of view and acquisition speed. Calcium indicators can be non–invasively loaded into neurons and are very sensitive [716]. Indeed, they produce large signals (400% times increase in the case of Fluo-4), making it possible to measure the response from single neurons [690], presynaptic terminals [181] or even dendritic spines [775]. In addition, continuous advances in imaging, such as the two–photon microscopy [182], has enabled an increase in both sensitivity and penetration depth. Indeed, two–photon microscopy has allowed high–resolution image fluorescence in strong scattering tissues [686], and the monitoring of calcium dynamics in dendritic spines [775]. We note that dendritic spines are very small (with spine head volumes ranging from $0.01\mu m^3$ to $0.8\mu m^3$), and therefore their monitoring using single–unit recordings (electrodes) is very difficult. In addition, at the single–cell level, there have been an enormous development of genetically encoded calcium indicators ini the last years. A class of them, termed 'chameleons' in the literature [493], have allowed the study of localized individual organelles such as the nucleus and the endoplasmic reticulum of single cells.

For our purpose, the key advantage of calcium imaging is the ability to monitor circuit dynamics by simultaneous recording the spiking activity of an entire neuronal population confined in a 3 mm diameter mini–culture. Calcium imaging indeed offers a sufficiently high spatial resolution for single cells to be neatly monitored, and with sufficient temporal resolution. This latter aspect, however, needs clarification. The temporal resolution of this technique is indeed limited by the calcium dynamics and the indicator kinetics, and typically falls in the $5-20$ ms range, ruling out the fine detection of single spikes. As we will see in the Results chapter, we will be mostly interested in detecting the beginning of neuronal firing or the behavior of the neurons along several minutes, and therefore calcium kinetics is not critical.

The negative side of using calcium indicators is that neurons are chemically affected. After few hours of measurement (typically $4-6$ h) neurons start to gradually lose their activity until they die. To be more specific, experiments may be affected by both photo–damage, i.e. the damage of neuronal cells due to the fluorescence light itself; and photo-bleaching, i.e. the gradual alteration and degradation of the fluorescence probe to such an extend that it is unable to fluoresce. Both aspects can be minimized by running short experiments or using softer light, but the quality of the measurements can be compromised. Additionally, chemical indicators require the incubation of the culture in the presence of the solvent DMSO, which deteriorates the health of the culture at long term and, effectively, limits the use of the culture to only one measurement.

MEAs as alternative?

MEAs do not have the above limitation and are therefore suited for long recordings, but the number of cells that can be accessed is restricted by the number of electrodes and by the complex processing of the data. A standard MEAs is constituted by 64 microelectrodes 30 μm in diameter that are spatially arranged in a 8×8 grid with a typical spacing of 200 μm. Unlike calcium imaging, MEAs provide a precise measurement of electrical signal, with fast response and high temporal resolution. Indeed, this technique

offers a high temporal resolution, in the range $10 - 100$ μs, allowing accurate spike detection. However, the major drawback of standard MEAs is its poor spatial resolution, usually limited by the number of recording electrodes. This limitation implies that only a small subset of the neurons in the network is sampled. The neurons do not necessarily sit on the electrodes, they are rather dispersed randomly, and some electrodes may not register activity at all. Hence, a given electrode in general picks up the average signal of a number of neighboring neurons (population signal). Although the distance of the neurons to a particular electrode creates different electric signatures that can be analyzed to allocate the source of firing (spike sorting), such processing requires sophisticated data analysis [420].

In order to obtain high spatio–temporal measurements, dense MEAs have been investigated in recent years. In general, a good device to record neuronal activity has to meet two basic requirements: (i) high signal–to–noise ratio in the recordings of very small signals, and (ii) the ability to cope with high spatial and temporal resolution. The dilemma is that the two requirements are diametrically opposed when facing actual construction, and thus to obtain a dense micro–circuitry is not an easy task. High spatial resolution entails the use of small electrodes featuring higher thermal noise. Indeed, since noise scales inversely with size, the smaller the available space for electrodes and circuitry, the higher the noise amplification. Despite difficulties, a 512–channel multi–electrode array system in a 32×16 rectangular geometry was developed at the University of California [430] and was used to record the spiking activity of hundreds of individual neurons simultaneously [350]. The system provides 60 μm spatial resolution (60 μm electrode spacing) and 50 μs temporal resolution (20 kHz sampling rate). We note that this temporal resolution is three orders of magnitude finer than the $\simeq 5 - 20$ ms resolution typically achieved with calcium imaging. Multi–transistor arrays based on complementary semiconductor–metal–oxide (CMOS) technology, with about $10,000$ recording sites and less than 20μm inter–electrode spacing enabled also fundamental neurophysiological insights at the cellular and circuit level [317]. Nevertheless, these devices are not widely spread due to their difficult fabrication, high cost, demanding data storage and challenging analysis. At the other extreme, chemical indicators are economic and practical to manipulate, and do not require complex and extremely sensitive equipment to obtain good quality recordings.

Fluorescence calcium imaging technology is broadly used in different laboratories around the world to monitor neuronal activity at a population level. The processing of the acquired data to uncover key properties of the underlying neuronal circuit is a fascinating problem that motivated the research presented in this thesis.

Since technical devices that combine both MEAs temporal accuracy and fluorescence imaging exquisite spatial coverage are still not available, fluorescence imaging is at the moment one of the most attractive techniques to study collective phenomena in living neuronal networks.

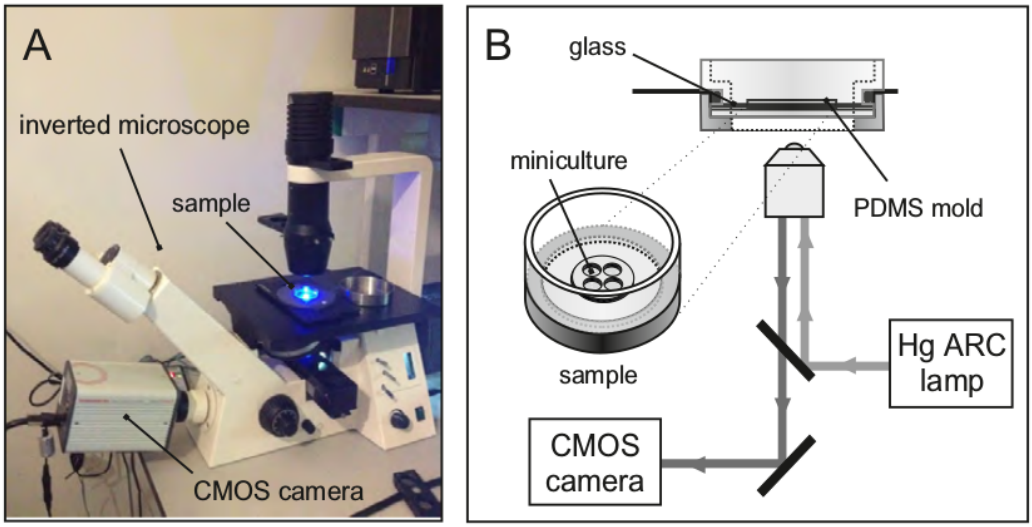

Figure 2.4: **Experimental setup.** (A) Standard configuration used in most of the experiments, showing the inverted microscope and the attached CMOS camera. The culture to be studied sits the in center of the $x - y$ stage and appears blue due to the excitation light for fluorescence. (B) Detailed sketch of the experimental system. The observation chamber contains 4 mini–cultures and is filled with EM. An arc lamp excites the fluorescence probe with a wavelength of 485 nm (blue). Fluorescence light is emitted at 506 nm (green), which is captured by the camera.

2.4 Experimental system

2.4.1 Culture preparation for experiments

Prior to imaging, cultures were incubated for 40 min in External Medium (EM, consisting of 128mM NaCl, 1mM $CaCl_2$, 1mM $MgCl_2$, 45mM sucrose, 10mM glucose, and 0.01 Hepes, treated to pH 7.4), in the presence of the cell-permeant calcium sensitive dye Fluo–4-AM [265] (Life), with 4 μl Fluo–4 per ml of EM. The culture was washed with fresh EM after incubation and placed in a recording chamber (Fig. 2.4) consisting of a petri dish with a bottom crevice that provided stabilization to the culture. The recording chamber was finally filled with 4 ml of fresh EM.

2.4.2 Imaging setup

The experimental setup used in all our experiments is detailed in Fig. 2.4. The culture sit in the recording chamber during all the measurements. The chamber was mounted on a Zeiss Axiovert C25 inverted microscope equipped with a set of objectives in the range 2.5X−20X, an optical zoom in the range $0.32 - 0.88$X, and filters for fluorescence imaging. Spontaneous neuronal activity was monitored through a Hamamatsu Orca Flash 2.8 camera attached to the microscope, in combination with a light source for fluorescence.

In more detail, the different parts of the setup are:

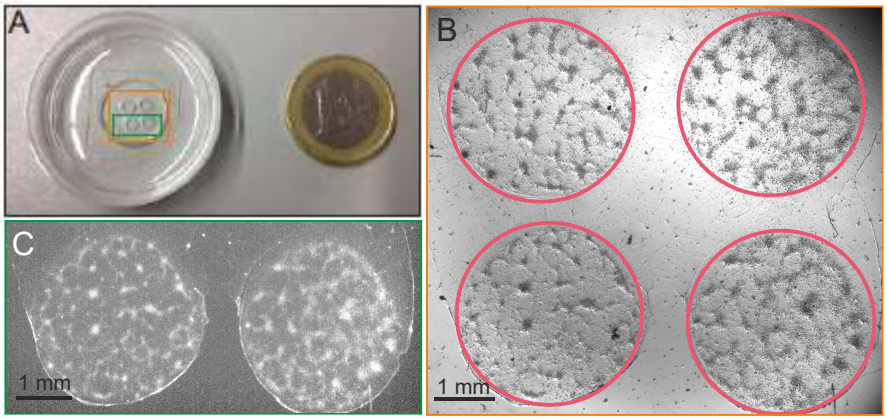

Figure 2.5: **Observation chambre and imaging configuration** (A) Picture of the observation chamber compared to 1 euro coin. On the center one can observe the glass–PDMS mold structure showing the 4 cavities, each 3 mm in diameter. (B) Fluorescence image of 2 neuronal networks in the '2 mini–cultures' configuration. (C) Bright filed image of 4 clustered networks using '4 mini–cultures' configuration.

Microscope and optical zoom. As shown in Fig. 2.4A, the inverted microscope allows for an easy allocation of the recording chamber, which can be combined with a thermostat for controlling the temperature of the culture under study. The microscope also allows easy access to the culture, which is necessary for manipulation and injection of chemicals through pipetting.

The ability to observe the structure and dynamics of the cultures depends on two main characteristics of the objectives, namely its magnification (mag) and its numerical aperture (NA). The magnification determines the size of the area covered by the objective and, together with the number of optical elements and the characteristics of the photo–detector, sets the spatial resolution of the experiment. For this reason, we attached in our setup an optical zoom to offer a higher flexibility in visualizing different culture sizes. Typically, most experiments were carried out with a 2.5X objective, a 0.33X optical zoom and the highest resolution of the camera (960×720 pixels), providing a spatial resolution of 8.51 μm/pixel and a field of view of 8.2×6.1 mm. These settings were sufficient to resolve single neurons and to simultaneously monitor four mini–cultures 3 mm in diameter, as sketched in Fig. 2.5. The numerical aperture describes the light gathering capability of the objective and determines the resolving power of the objective and the brightness of the image. In our case we used objectives optimized for fluorescence imaging with NA in the range $0.1 - 0.3$.

Fluorescence Lamp. A mercury arc plasma lamp is used in our experimental setup. This lamp has a relatively smooth emission curve in the UV to visible spectra. In combination with a filter set optimized for Fluo–4, the light emitted by the lamp goes through a bandpass filter that sharply selects wavelengths close to 485 nm (blue), exciting the fluorescence probe. The light emitted by the probe is centered around 506 nm (green) and it is acquired with the microscope and camera through a dichroic mirror in the filter set.

The mercury lamp has a lifetime of 100 h, and must be replaced immediately to pre-

vent artifacts in the acquired data. Indeed, the light intensity from the lamp fluctuates once it starts to degrade, causing the presence of artificial fluorescence peaks that can be confused as actual firing events. For this reason, and to ensure that the lamp was working perfectly in the experiments, we often recorded for few minutes the background signal of the camera, i.e. without culture, to verify the health of the lamp.

Camera and experimental constraints. We used a Hamamatsu Orca Flash 2.8, a high sensitivity, high speed camera, equipped with a CMOS sensor. The camera is specially suited for low–light fluorescence experiments, and allows full–image (960×720 pixels) acquisition and 45 frames per second (fps), i.e. 22 ms interval between images.

Higher recording speeds can be obtained by decreasing the vertical size of the images. However, higher acquisitions increase the camera noise which may mask actual firing events. Hence, an important aspect of the experiments was to find a subtle balance between image quality, acquisition speed and light intensity. The goal was to maximize the number of recordings while maintaining the culture health. For this reason, the duration of the recordings in the set of experiments described next was established so that the total monitoring of the culture did not exceed 2 h, a time over which the culture started to degrade.

We also note that a typical experiment may encompass 1h of recording at 45 fps at full image size, leading to about 100 GB of data per recording session. Processing such amount of data is complicated, and a big effort was devoted along the thesis to develop adequate software in C and Matlab to efficiently analyze the experiments.

2.5 Experiments and Pharmacology

2.5.1 Experimental Lines of research

Our study encompassed three groups of experiments, outlined below. The details of each protocol are described later.

Maturation and development of the network. Here we monitored neuronal activity along the first three weeks of network development. A batch of 24 identical cultures was prepared. Starting at *day in vitro* (DIV) 5, a culture was selected and its spontaneous activity recorded for 30 min. Another culture was then selected 24 h later and measured. This procedure was then repeated along 3 weeks.

Disintegration of the network. Here we studied the controlled weakening of the excitatory connectivity of the network, which leads to a gradual decay of neuronal interconnectivity and substantial changes in spontaneous activity. Connectivity disintegration was achieved by gradually blocking the AMPA–glutamate receptors in excitatory neurons through the antagonist CNQX. This procedure mimics the experimental protocols described in Ref. [660]. Disintegration experiments were carried out in groups of cultures prepared in a 24–well batch, but studied in a relatively mature conditions, in the range $8 - 16$ DIV, a period in which the cultures exhibit sufficiently rich spontaneous activity along the different stages of disintegration. About 6 different concentrations of CNQX

were studied for the same culture.

Degradation of the network. We here performed experiments without any drug application, and simply left a given culture in the recording system for a long period of time. The culture degrades due to photo–damage, and the experiment allows for a quantification of the changes in spontaneous activity and the degradation of network's collective dynamics as the neuronal population deteriorates and dies.

2.5.2 Specific experimental protocols

Maturation and development of the network. After selecting and incubating the culture with Fluo–4, we first recorded spontaneous activity as a long sequence of images with a total duration of 30 min, with both excitatory and inhibition connections active (*"E+I" network*). We next fully blocked inhibitory synapses with 40 μM bicuculline, a $GABA_A$ antagonist, so that activity was solely driven by excitatory neurons (*"E–only" network*). We then left the culture in darkness for 10 min for the drug to take effect, and finally measured again for 30 min with identical experimental settings.

Disintegration of the network. Following incubation, we proceed as follows. Firstly, we completely blocked inhibition with 40 μM bicuculline as well as NMDA receptors with 20 μM APV. We then waited 10 min and measured spontaneously activity for 20 min (*"E–only" activity*). Next, we started a sequence of gradual application of CNQX, and explored concentrations of 50, 100, 200, 400, 800, and 2,000 nM. After each application we waited 5 min for the drug to take effect, and measured spontaneous activity for 15 min. The total duration of the experiment was about 2 h. We verified by washing off the drug and measuring again the "E–only" network activity that the culture health was not compromised by the long duration of the experiment. Other studies that used almost identical disintegration protocols confirmed the good health of the culture throughout the experiment [660, 355].

Degradation of the network. We here left the culture to degrade at the end of a normal experiment by leaving it in the recording system for 6 h. Next we carried out 6 recordings 30 min long, leaving 30 min in between for the damage to increase. Finally, to compare the scenario of culture degradation with one of actual neuronal death, we added to the culture 10 mM of formaldehyde solution (F8775, Sigma Alderich), which causes immediate necrotic cell death [688], and recorded again. This measurement is particularly important and serves as reference to evaluate the kind of signal that one obtains when the network is totally silent.

Background signal and camera settings. In all experiments we also quantified the background signal of the recording system to assess our ability in resolving neuronal firings from noise. To do this, we removed the culture from the recording chamber and measured the noise of the camera as well as possible additional artifacts, such as fluctuations in the light of the fluorescence lamp or contamination from indirect light sources in the laboratory. We finally verified that the results obtained along the different

protocols were not influenced by any artifact from the experimental system.

Camera, microscope and light source settings were optimized to minimize photo–bleaching and photo–damage (unless otherwise stated) while providing the best signal to noise ratio throughout the measurements. All images had a size of 960×720 pixels, a spatial resolution of 4.40 μm/pixel, and 256 grey–scale levels. Images covered a a final field of view of 4.2×3.2 mm^2 that contained on the order of 2,000 neurons.

Images were acquired with a speed of 20 fps (50 ms interval between two consecutive images) for the experiments with young cultures (DIV < 7). For maturer cultures (DIV ≥ 7), we used a speed of 33 or 45 fps (respectively, 30 ms and 22 ms acquisition interval). The lower acquisition in young cultures was established to get better signal–to–noise ratio and therefore resolve better the typically weak firing events.

2.5.3 From images to data

At the end of each experiment we took bright–field images of the monitored region of the culture, which served as a good reference to establish the position of the neurons. Indeed, with some simple enhancement of these images, the neuronal cell bodies could be easily resolved by eye (see Fig. 2.6A). We next manually marked each neuron as a squared region of interest (ROI) with a typical lateral size of 10 pixels (about 40 μm). This process, though slow, provided an accurate map of the spatial location of the neurons. Typically, each culture confined in 3 mm diameter mini–cultures contained about 2,000 individual neurons. Larger, 13 mm diameter cultures (full glass coverslip) were monitored in a small region at its center, and typically contained 3,000 neurons with the camera settings specified above.

Once the cells were selected, we proceeded to obtain the fluorescence intensity of each neuron. Firstly, the original fluorescence video (in the native Hamamatsu format) was converted into a sequence of T individual images. Then, the average grey level in each ROI was evaluated along the entire image sequence, procuring the fluorescence intensity F for each neuron i as a function of time, $F_i(t) = \{f_1^i, f_2^i ...., f_T^i\}$. This analysis was carried out using the own software of the group, programmed with Borland C++ Builder 6 by Dr. Jordi Soriano.

Treatment of the fluorescence data

The raw fluorescence data was processed to remove experimental artifacts, in particular small drifts in the signal and light scattering, as described below. More importantly, the data was normalized to account for the relative increase in fluorescence.

Baseline correction and normalization. Long trains of neuronal activity may contain a small drift of the baseline signal due to photo–bleaching. Although we observed such an effect only in about 5% of the neurons, we automatically corrected this artifact by applying a moving median filter 2,000 points wide. We verified that such a correction did not modify the shape of neuronal signal during firing events. The fluorescence trace $F(t)$ was then normalized for each neuron to correct for its background brightness level

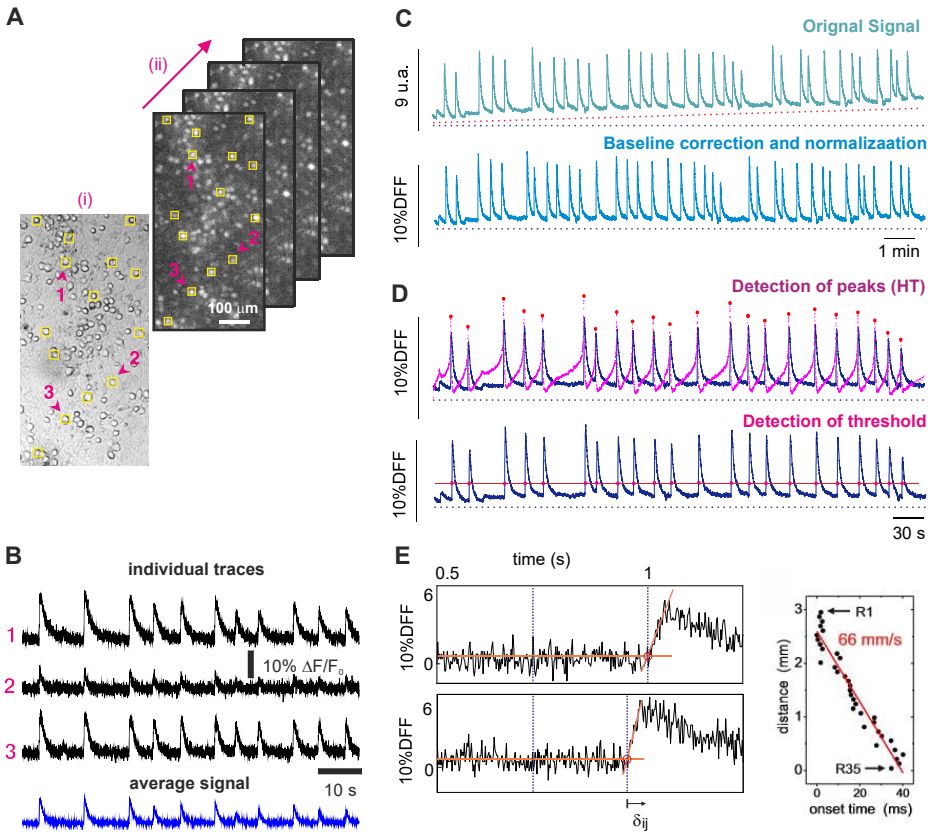

Figure 2.6: **Fluorescence signal analysis and determination of onset times in neuronal cultures**. (A) Outline illustring the conversion into individual frames using the Hokawo 2.5 software . Yellow squares depict the selection of ROIs that correspond to single neurons (ii). In front, a photo that maps he structure of each neuron. (B) Illustrative fluorescence traces of neuronal activity in three regions of interest (labeled and marked with arrowheads in the above image) along 2 min.Fluorescence traces are expressed as $\Delta F/F_0$ (background corrected fluorescence traces divided by the resting fluorescence). Both excitation and inhibition were active during the recording ("E+I" networks). Note the variability in fluorescence amplitude from neuron to neuron. The bottom trace in blue shows the fluorescence signal averaged over all the neurons in the field of view. (C) Data analysis work flows. First a raw signal is obtained $F_i(t)$ from the images (green, bottom). This signal is then detrended and normalized as $\widetilde{F}(t) = \frac{\Delta F}{F_0} \equiv \frac{F(t)-F_0}{F_0}$, with F_0 the fluorescence at rest (blue, bottom). (D) Detection of burst using the Hilbert Transform (top) and considering that the following three requirements: (i) the peaks are superiors twice the deviation standard of the mean fluorescence signal ($\tilde{g} = 2\sigma_f$) (ii) nearby wrong detections are avoided by considering a windows of 300 ms below which another firing is not accepted and (iii) the width of the burst has to be at least 50 ms to prevent camera errors to be taken as bursts. (E) The final onset time is determined as the intersection of two lines marked in the figure (right panel) and it is used to constructed the binary signals (see Chapter 6). One delay is observed between i–neuron and j–neuron (δ_{ij}). The right panel shows horizontal position of the ROIs as a unction of the their onset times, with the linear fit providing the velocity of the front.)

by computing

$$\widetilde{F}(t) = \frac{F(t) - F_0}{F_0} \equiv \frac{\Delta F}{F_0}, \tag{2.1}$$

where F_0 is the average amplitude of the background fluorescence signal at rest (without activity). The illustrative traces of Fig. 2.6C, as well as all the data shown in this work, correspond to such a corrected and normalized data.

Correction of light scattering. In some analyses we also implemented a correction for light scattering. Mathematically, the correction is carried out by considering that the total fluorescence signal of a neuron i affected by light scattering at time t, $F^{sc}_{i,t}$, is given by

$$F^{sc}_{i,t} = F_{i,t} - A_{sc} \sum_{j=1, j\neq i}^{N} F_{j,t} exp\{-(d_{ij}/\lambda_{sc})^2\}, \tag{2.2}$$

where d_{ij} is the distance between two neurons i and j and λ_{sc} is the scattering length scale (determined by the typical light deflection in the recording medium and the optical apparatus). The scaling factor A_{sc} sets the overall strength of the scattering artifact. We note that the light scattered, according to Eq. (2.2), could be completely corrected using a standard deconvolution algorithm, at least for very large fields of view and a scattering length known with sufficient accuracy. In the real setup however, the relatively small fields of view (on the order of 10 mm^2), the inaccuracies in inferring the scattering radius λ_{sc}, as well as the inhomogeneities in the medium and optical system artifacts, make perfect deconvolution impossible. The estimation of value of the scaling factor A_{sc} and the scattering radius λ_{sc} are determined by taking advantage of the possibility to select arbitrary ROIs over the images. Indeed, we selected about 10 ROIs that corresponded to empty areas (i.e. without a neuron or glial), and modified the light scattering parameters to eliminate spurious firing in these ROIs, so they ultimately showed a behavior that corresponded to a noisy background.

In general we observed that light scattering correction was small, and such a correction was therefore ignored in the analysis of the data unless otherwise stated.

2.5.4 Towards the understanding of neuronal cultures

The obtained fluorescence data for each neuron $\tilde{F}(t)$, either with light–scattering correction or not, and extended for all monitored neurons, shaped the basis for the analysis conducted in this thesis and exposed along the following chapters.

The overall goal of the analyses, and of the thesis, was to extract relevant information of the dynamics and connectivity of a neuronal culture from imaging recordings. In other words, we aim at answering a simple yet complex question: *what characteristics of a culture can we infer from just its spontaneous activity fluorescence traces?*

The answer to this question is not straightforward, but two major aspects, elaborated in the next chapters, could be delineated, namely the dynamic regimes of a neuronal network and its connectivity traits. The former was established in terms of linear and non–linear analysis, while the latter was implemented by using connectivity reconstruction concepts and information–theoretic approaches.

Chapter 3

Computational Description of Neuronal Cultures

Mathematical models and computational simulations offer useful tools to help us uncovering specific aspects of the link between individual nerve cells' dynamics and collective behavior. The latter has to be seen as either activity patterns or as functional networks derived from activity. The aim of this chapter is to bring to light computational resources, and simulate neuronal networks in the experimental context described in Chapter 2.

In the first section of this chapter we will present a brief overview of the different computational models. Next, we will introduce a *metric* model with neuronal density fields [753, 652, 691] to simulate structural connectivity. Finally, and with the structural network settled, the dynamics of individual neuron will be simulated by introducing a quadratic integrate–and–fire model with adaptation and depression (QIFAD) [36, 352, 354]. All the results of these simulations will be discussed in Chapters 4 to 6, and in the context of our experimental findings.

3.1 Modeling neuronal networks: a balance between detail and abstraction

In order to simulate neuronal networks, various possible approaches can be carried out according to the level of analysis. Realistic models of neuronal networks are usually constructed on the basis of a biophysically detailed simulation of neurons and synapses, which can be integrated into the micro–circuitry of a network previously designed. In general, efficient simulation of neuronal networks require a delicate balance between the need of sufficient details to represent the complex single–cell dynamics and the need of efficient computation while retaining essential features of neuronal behavior.

Two fundamental ingredients shape the basis for the simulation of a neuronal system. The first one is the selection of the most plausible biological model that captures the individual behavior of single neurons. The second one is the incorporation of the coupling among neurons to shape a networked population. This coupling should be sufficiently realistic when approaching neuronal cultures. In general, in the generation of a neuronal network, these two ingredients must be born in mind all the time.

The first ingredient, the selection of an adequate model, requires a good knowledge

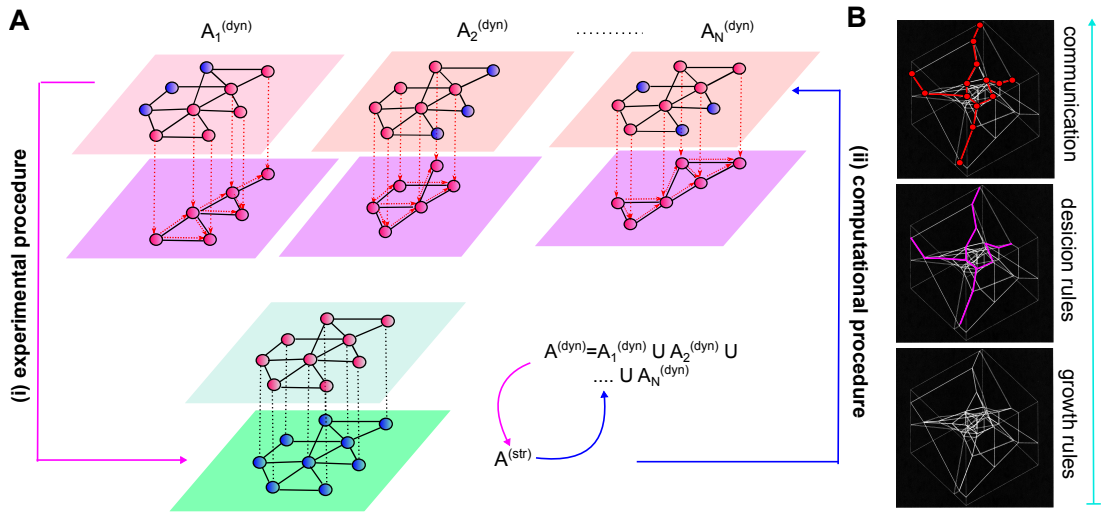

Figure 3.1: **Structure-Dynamics Interplay in Complex Network.** (A) Schematic representation of the relationship between topology and dynamics in Complex Network. (i) Experimentally, dynamical network is reconstructed proceeding as follow: two nodes are considered connected if their activity patterns present one highly degree of similarity. On basis of this criterion, the dynamical matrix is constructed. Then the union of all the dynamic matrix would have to converge to a the topological network: $A^{str} = A_1^{dyn} \cup A_2^{dyn} \cup ... A_N^{dyn}$. (ii) Computationally, this process is realized by revers order. (B) Appropriate choice of growth and decision rules determine the topology of the network and in turn its intrinsic dynamics. Crucial are them to obtain a correct simulation model.

of the detail of abstraction. For instance, when the precise molecular details of neuronal functioning are not required —as in our case— a sufficient model is the one that sees a neuron as a black box with integrate–and–fire behavior. In the next section this aspect will be treated in detail.

The second ingredient, the selection of the appropriate *physical network*, shapes the structural connectivity. For instance, metric constraints can be incorporated to take into account the fact that the probability of connectivity depends on the distance. This is a crucial aspect that is often disregarded. This physical network actually represents a *first layer of representation*, the hard–wiring of the network. A *second layer of representation* is the set of decision rules that enable the communication among neurons, i.e. the *dynamical network*. In Fig. 3.1 this two–layer concept is sketched, and illustrates the core of our research. It is noteworthy mentioning that, for simplify, we only consider one way influence from the structural (fixed topology) to the dynamical one. However, in reality, dynamical and structural networks present a symbiotic interplay grounded on an ongoing feedback, in which both networks grow and reshape continuously.

3.2 Neuronal modeling

Different levels of single-cell modeling have been proposed in the literature. A first level of analysis is the detailed compartmental models [573, 634, 393, 91, 175] which consists in dividing the neuron into a finite number of interconnected anatomical compartments and studying their electrochemical properties (Fig. 3.2A. Each compartment is assumed to be homogeneous and is modeled with equations describing an equivalent electrical circuit [572]. These models extend the cable theory of Rall [572] and, in general, are focused on understanding the impact of complex neuronal morphology on its electrical behavior [481, 461, 722, 197]. Different models can be used to reproduce realistic neuronal structures at this micro–scale level. The most prominent ones are geometric construction algorithms and biologically–inspired growth processes.

For *geometric construction algorithms*, one of the most simple but elegant model to simulate the geometric growth structures is based on L–systems. They are recursive procedure initially invented for modeling plant branching structures [429], and have been successfully applied to neural morphologies [305, 506, 44]. Other approaches that have been developed include probabilistic branching models [727, 388], Markov models [604], Monte Carlo processes [162], or diffusion limited aggregation [444].

Biologically–inspired growth processes, on the other hand, seek at mimicking the generation of neuronal morphology and its maturation [467]. In this way, different detailed biological models have been proposed in order to simulate various aspects of growth and development as well as cell proliferation [598, 638], polarization [605], cell migration [110] neurite extension [725], growth cone steering [283, 472, 401], fasciculation [316] and synapse formation [723, 675]. The need to understand these processes underlies in the fact that, throughout the evolutionary process, neurons have developed a highly specialized bodies with a clear, specific morphology (with self–similar or fractal characteristics [444, 753]) always oriented to undertake information processing [111].

At this micro–scale analysis, it is clear that the enormous computational power of neuronal circuits must be ascribed to the subtle relationship between structure and dynamics [111, 391, 22, 559, 436, 178, 299, 466, 624]. Indeed, specific branching morphologies —in particular axonal and dendritic trees— provide immense benefits not only at a geometrical and structural levels [111], but also in the reception, integration, emission, and propagation of electrical signals [111, 391]. This shape–function paradigm will be again addressed in Chapter 6. Although a detailed investigation of this shape–function problem is beyond the present thesis, it is important to keep it in mind, both to comprehend the limits of simulation models and for understanding future results.

For sake of illustration, Figs. 3.2B-E picture the electrical and morphological interplay of an individual virtual neuron at the micro–scale level. The simulations presented in the figure are implemented in the open–source software toolbox TREES, written in Matlab code [160, 1]. The growth process of dendrite arborization is simulated with a locally optimized algorithm [564, 158, 161, 159] (Fig. 3.2B) and its connectivity is represented through the respective adjacency matrix (Fig. 3.2C). The construction process takes place according to the following procedure. First, 100 points are randomly placed in a square area of lateral size 100 μm. Next, using a extended minimum spanning tree algorithm, the different nodes are connected, seeking the optimized subset of the graph that minimizes the total edge weight while preventing any loop. The optimization process

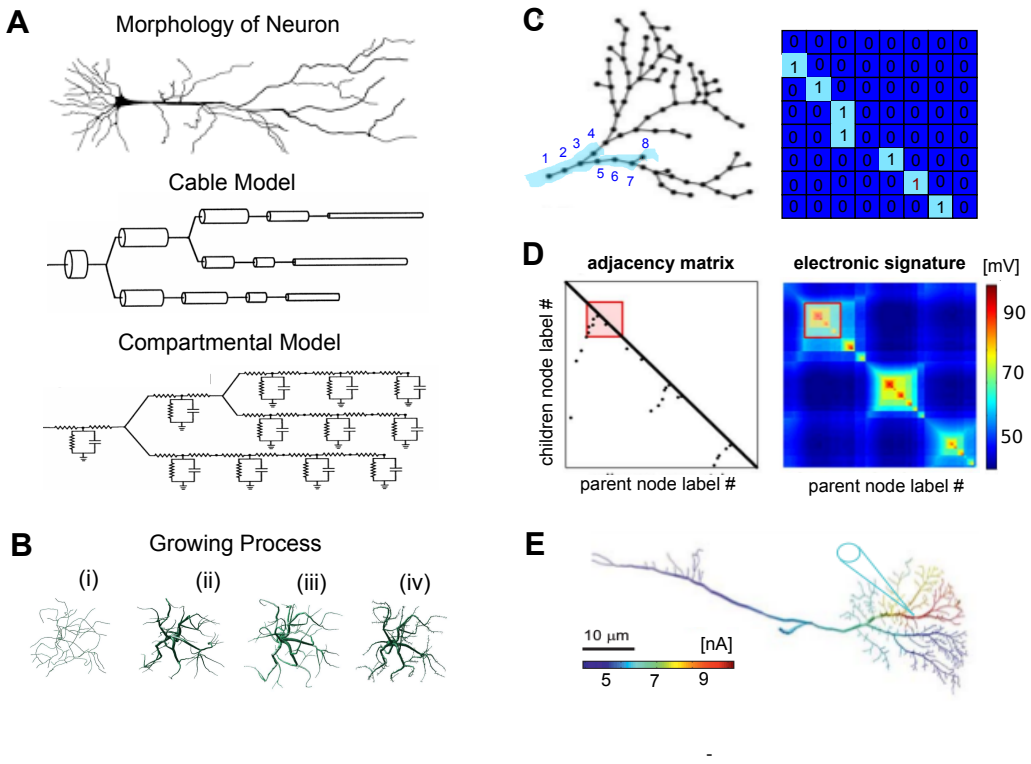

Figure 3.2: **Simulation at the micro–scale level: topological and electronic identity of a single neuron.** (A) Branching structures of neurons are discretized into respective cables that are spatially adjacent to each other and coupled through a linear resistance. In turn, each compartment is modeled by a resistive (passive leak of membrane) and one capacitive term. (B) Generating neuronal branching structures using optimized graphs: (i) 100 points are randomly placed in the range between -100μm and 100μm and connected to a root (0,0,0) using the extended minimum spanning tree algorithm, (ii) Resampling at 5μm and smoothing of the tree structure (iii) Adding realistic spatial noise in the structure (iii) A soma-like diameter protuberance is mapped onto the root and spine structures randomly are distributed along the tree. (C) The tree is represented as graph described by a adjacency matrix dA. (D) Studying the electronic properties of the neuron. Combining Kirchoff's junction law for electric circuit, the dA can be used directly to obtain a full signature of passive steady-state current propagation in the tree. Then, the electronic matrix is obtained, showing the current transfer from any node to any other. (E) The potential spread along the structure of neuron as a result of injecting current into one node. The location of of current injection is indicated by a blue pointer. All the analysis are implemented by the software package TREES toolbox [1].

is implemented in this greedy algorithm [564, 158, 161, 159] using a cost function based on biological principles for conservation of space, cytoplasm and conduction time in the neural circuitry (Cajal's laws, Chapt.V, pag. 115-125 in Ref. [111]). Impressively, more than a century ago, Ramón y Cajal already formulated fundamental anatomic principles to describe the complexity of nerve morphology that still hold. Once the branching structure is constructed, the following steps are implemented: (i) the tree is re–sampled in intervals of 5 μm, and the paths along the tree are subsequently smoothed out to produce realistic neuronal branching structures; (ii) biological spatial noise is added; (iii) a soma–like diameter protuberance is mapped onto the root of the tree structure; and (iv) spine structures are randomly distributed along the tree. Fig. 3.2C depicts the final adjacency matrix, while Figs. 3.2D-E show the electronic signature of current propagation in the trees (which uses linear algebra in combination with Kirchoff's laws of current conservation) together with the propagation pattern along the neuron.

These simulation tools, despite their relevance for describing functional processes, were not implemented in this thesis. A first reason is that the detailed propagation of electrical currents through dendrites and axons cannot be tracked with our fluorescence calcium imaging technique, and therefore a comparison between experiments and model would be unfeasible. And a second reason is that, for each single neuron, these compartmental models contain hundreds of elements, and therefore thousands of coupled differential equations must be solved at each time step. As a result, this approach is impractical to implement with our resources and computationally prohibitive.

To illustrate the complexity of the problem and the need of extreme computational resources, let us consider for instance a typical vertebrate axonal arbor. It typically makes about 10^4 synapses, with each dendrite arbor reciprocally receiving about the same number of connections. With about 10^5 neurons in a culture, one would need on the order of 10^9 parameters to give a quantitative description of an arbor's form. Totally prohibitive. Even more prohibitive when considering that 80% of neuronal synapses are shaped through spines [111]. These structures are dynamically rich, constantly moving, growing with activity and retracting during inactivity, shaping morphological plasticity both *in vivo* and *in vitro* [224, 198]. Additionally, synaptic junctions are not the only encoders of information. Neuronal morphologies exhibit an overwhelming variety and complexity of shapes that lead to different individual dynamics. Moreover, the development of neuronal tissues is an extremely complex and dynamic process very difficult to simulate. Indeed, during development, dendrites and axons undergo periods of dramatic branching addition, outgrowth, pruning, or elimination, giving rise to a highly dynamic process characterized by a great wealth of growth and remodeling [762, 309, 291].

Real neurons are therefore very complicated computational devices. However, their dynamical behavior not only depends on the morphological and electronic characteristics [79, 475, 555, 485, 720, 461, 687, 632, 745, 64, 619], but also on other agents such as chemical difference in membrane properties, in particular the type and density of ions channels [713, 712, 176, 356].

Fortunately, for large–scale network simulations, reduced compartmental models offer a good compromise between realism and computational efficiency. A first candidate is the single–compartment model of Hodgkin-Huxley (HH) [324], which reproduces electrophysiological measurements with high degree of accuracy [392, 91]. This model neglects the neuron's spatial structure and focuses entirely on how ionic currents contribute to

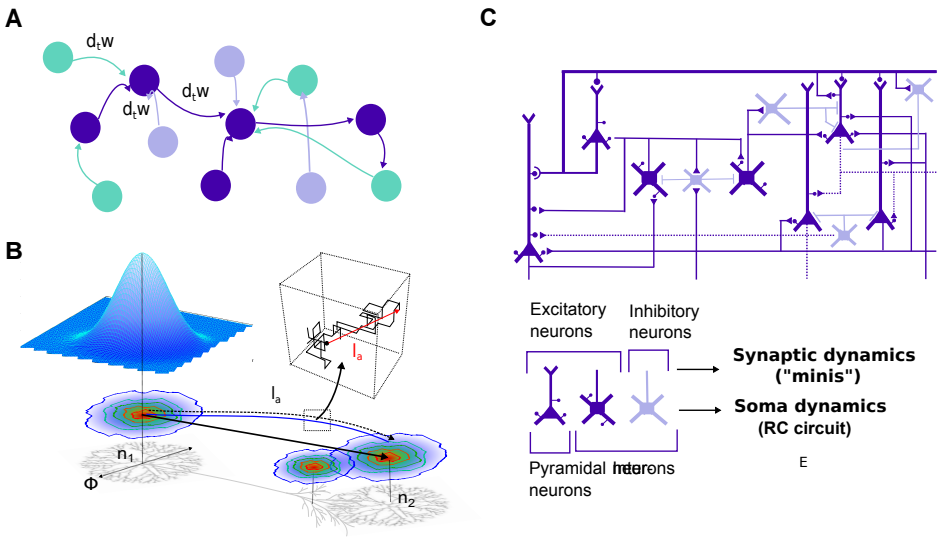

Figure 3.3: **Simulations in the meso–scale level: the topological and electronic identity of the network.** (A) Our neuronal cultures make up complex networks described by graphs where the neurons (nodes) interact by temporal dynamics of biological synapses (dynamical edge). Due to the small size of the network, the effect of propagation of the signal is neglected. (B) Simplified topological and growth model where dendrite and axon structures are simulated by statistically density "mass" functions. (C) Simplified cortical wiring diagram [636] where micro–circuitry is made up by the following electronic components: excitatory (dark blue) and inhibitory (clear blue) neurons in function of their ionic synaptic receptors or pyramidal (triangle soma) and interneurons (square soma) in function of their soma morphology. Detailed and specific patterns of connection are represented only in function of respective synapses and soma dynamics.

neuronal subthreshold behavior and spike generation. Although this model has led to a quantitative understanding of many dynamical phenomena, it still exhibits a high computational cost. Indeed, the HH system of equations consists of four coupled nonlinear ordinary differential equations, a system that is difficult to tackle both mathematically and numerically. Hence, further simplification is required.

The most interesting simplification approach reduces the set of four HH equations to a two–dimensional problem, thereby allowing an elegant analysis in terms of phase planes. The formal implementation of this reduction uses bifurcation theory [214, 332, 352], which extracts the key actors in the dynamical behavior of neurons and provides a solid ground for understanding rich phenomena such as bursting, spike–frequency adaptation, or 'resonate–and–fire' behavior, among others. Representative reduced models are the FitzHugh–Nagumo excitable neuron [227, 510], the Hindmarsh–Rose bursting neuron [321], the Izhikevich model [354], or the Leaky Integrate–and–Fire Model (LIF) [409]. The latter is of particular interest. It simulates the neuron's membrane potential in terms of an electric circuit consisting of a resistor and a capacitor in parallel, and that represent the leakage and capacitance of the membrane. Then, the membrane capacitor is charged up to a certain threshold, which suddenly discharges, produces an action potential

(spike) and resets the membrane potential to its resting value. In this model, as the name suggests, the membrane voltage operates through *integration* of the incoming currents, emitting a spike when the voltage has exceeded a predefined *threshold*. Although this model is easy to implement and has a low computational cost, it fails at describing the rich spectrum of neuronal dynamics.

In this thesis we sought for a trade off between the biological plausibility of HH dynamics and the computational efficiency of the LIF model [36, 352, 354], and considered a quadratic integrate–and–fire model with adaptation and depression (QIFAD). In this model, neuronal activity is shaped by two elements, namely the *soma dynamics* and the *synapse dynamics*. The former accounts for both the 'integration' and 'adaptation' contributions, while the latter describes the 'depression' contribution and neuron–to–neuron communication. The detailed description of all these ingredients is provided in Sec. 3.4. Fig. 3.3C cartoons a cortical network that operates with the QIFAD model. In such a simplified wiring, the cross–talking among neurons depends only on the kind of neuron. Hence, depending on the ionic synaptic receptor, we can distinguish two different electric components, namely *excitatory* (dark blue), characterized by AMPA and NMDA receptors, and *inhibitory* (clear blue), characterized by GABA receptors. For sake of completeness we also include the two major types of neuronal morphologies, pyramidal (triangular cell bodies) and interneurons (crosses).

Setting up the wiring in more realistic, larger networks with thousands of neurons is complicated. One has to decide either to mimic a given connectivity layout —for instance to replicate a specific brain region— or to establish a set of rules that *statistically* provide a sufficiently realistic layout. For the former scenario, one needs to access accurate wiring data and plug it into the simulation. This is possible when treating brain regions (such as the Human Brain Project), but not *in vitro* cultures since their connectivity is created *de novo* in each preparation. For the latter scenario, one identifies the key ingredients for connectivity formation, such as axonal and dendritic shapes, and uses them to create the structural wiring. This construction is particularly attractive for describing neuronal cultures since neurons can be treated as similar elements that connect to one another over a substrate, and following also similar rules everywhere.

Such a connectivity construction may seem an over–simplified *toy model*, but it is actually well supported. Indeed, different studies [652, 691, 560] have identified universal relationships that reveal a general neural architectural design principle. Single neurons and its dendritic and axonal trees are modeled statistically with an arbor spatial density function, and that specifies the probability of finding a branch of a particular arbor at each point in the neuronal circuit. Hence, each neuron will be characterized by the spatial distribution of its axonal and dendritic 'mass' [726, 157, 18]. In Fig. 3.3B we outline this approach. In the next section we will examine its most important considerations in greater detail and we will discuss the implications of the approaches made.

We used the code developed by J. G. Orlandi [530, 2, 3] to simulate realistic neuronal culture layouts and their corresponding dynamics. The codes simulating the models were written in C++ programming language, pre–compiled in g++ Ubuntu 4.9.2, and ran on an Intel Core i5-2450M processor with 4GB of RAM. To correctly implement them, `qt4`, `gsl` and `eigen3` dependencies were installed and configured. The work flow for the simulations was as follows. First, the network connectivity was established in Matlab using a geometrical pattern as a substrate, and different levels of neuronal aggregation

were considered. This allowed us to study the effect of heterogeneous neuronal spatial arrangement on connectivity and dynamics. Second, once the structural connectivity was fixed, global network dynamics was simulated through the QIFAD model. And third, fluorescence signal traces were obtained by incorporating calcium dynamics into the activity train of each individual neuron, and usig another simple script in Matlab.

3.3 Connectivity Modeling

As we have already seen, neurons are highly specialized cells that communicate via axons and dendrites, which can be seen as functionally and morphologically specialized tree–like processes. Trees grow up by extending their branches, and are finally stabilized upon the formation of synapses and spines [138, 523]. Neurons modulate the transmitted signals, and through the connection of a neuronal branch with another one [256]. At the micro–scale level, this branching morphologies play a crucial computational role both at the dendritic [22, 559, 436] and axonal levels [178, 299, 466, 624]. At our mesoscopic scale, however, two questions arise. Which is the impact of these structures? How can we simulate this neuronal network efficient communication to get similar biological behavior?

3.3.1 Metric construction of the network

It is important to remark that, in our construction, the connectivity is static, i.e. we do not change the wiring of the network once it is established. We start the construction procedure by setting up different spatial arrangements. They are created by using a bi–color pattern as a substrate, and where neuronal positioning and growth is allowed solely in one color (Fig. 3.4A, bottom). We used this concept to generate two distinct network topologies, namely *homogeneous* and *aggregated* (Fig. 3.4B) and that resemble the characteristic spatial arrangements of the experiments.

Homogeneous networks. We randomly distributed N pyramidal neurons over a circular area 3 mm in diameter. Each neuron was modeled as a circular cell body (soma) with fixed diameter $\phi_s = 15$ μm. We set densities of occupations in the range $\rho \simeq [100 - 3,500]$ neurons/mm^2. Neurons were labeled as either excitatory with probability $p_E = 0.8$ or inhibitory with $p_I = 0.2$.

We next generated the growth process of axons and dendrites and using the metric construction described in [530]. The growth of the axons was simulated as a random process where the final length of the axon was given by a Rayleigh distribution of the form

$$p(l) = \frac{l}{\sigma_l^2} exp\left(\frac{-l^2}{2\sigma_l^2}\right), \tag{3.1}$$

where $\sigma_l^2 = 900$ μm is the variance of the distribution and its value is chosen so that the average axonal length matches the value $\langle l \rangle \simeq 1.1$ mm. Experimental observations show that axons do not grow in a straight path but rather with a fluctuating orientation. We therefore divided the total length l into small segments $\Delta l = 10\mu$m long. The first segment was placed at the end of the neuronal cell body, and with an orientation that followed an uniform angular distribution. The ith segment was then placed at the end of

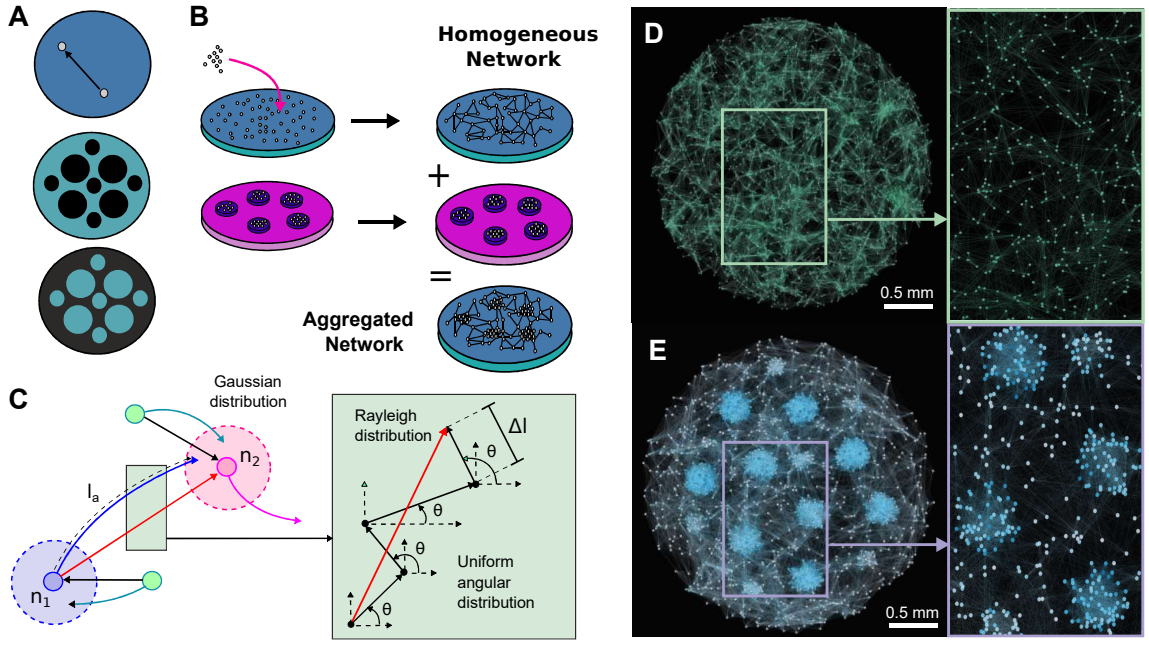

Figure 3.4: **Construction of our Structural Networks.** (A) Bi-color pattern to redirect neuronal growth and creating different topological network: homogeneous networks (i) and pattern networks size-limited size with simulated PDMS-structures (ii-iii) (B) Process of formation of one aggregated network as juxtaposition of different homogeneously networks. (C) Metric growth of the network. In the left, only four neurons are represented, indicating their soma and axons. The shaded region by the dendritic tree is depicted for two neurons (blue and pink circular areas) and described by a Gaussian distribution. A connection between two neurons (arrow) is allowed whenever the axon of a neuron crosses the dendritic tree of another one. In the right, one schematic outline of axon growth is drawn as a random process: final length (l_a) is given by a Rayleigh distribution and break down with intermediate segments (Δl) which orientation following an uniform angular distribution. (D) Final homogeneous (top) and aggregated (bottom) networks with their corresponding details obtained and used as fundamental mesh to generated the dynamics behavior. The visualization of this network was drawn using the open–source Gephi software [4]

the previous one, and oriented with an angle θ following a Gaussian distribution around the previous segment given by

$$p(\theta_i) = \frac{1}{\sqrt{2\pi\sigma_\theta^2}} exp\left(-\frac{(\theta_i - \theta_{i-1})^2}{2\sigma_\theta^2}\right), \tag{3.2}$$

where σ_{i-1} is the angle between the segment $i-1$ and the $x-y$ plane. $\sigma_\theta \simeq 15^o$ is chosen to obtain a long persistence length and small curvatures. The growing process is then repeated until all segments are laid down. On the other hand, dendritic trees are modeled as disks of diameter ϕ_d which were drawn from a Gaussian distribution with mean $\mu = 300$ μm [753]. In Tab. 3.1 we provide the set of parameters that were used to simulate the formation of the networks.

To set the boundary conditions at the edge of the circular substrate, we considered that it consisted of a *reflective wall* in which the reflected axonal section had the same

Table 3.1: **Network Parameters for simulations.** Set simulations parameters used for modeling the growth up and construction of network topology. This input arguments are specified in the configuration file at the beginning of the run the program.

Network Parameters	Value
System-wide Parameters	
System size LxL	L = 5-20 mm
Density	$\rho = 10^2$-10^3 neu/mm^2
Morphological Parameters	
Soma size (fixed)	r_a = 7.5 μm
Dendritic tree (Gaussian pdf)	μ = 150 μm, σ = 20 μm
Axonal length (Rayleigh pdf)	σ = 800 μm
Axonal segment length (fixed)	l_s = 10 μm
Axonal segment angle (G.pdf)	μ = 0, σ = 0.1 rad

angle respect to the wall as the incident section.

Once the growth process was set, the network connectivity was established on the basis of geometrical constrains: a connection $i \to j$ was constituted with probability α when the axon of a neuron i intersected the dendrite tree of a neuron j (Fig. 3.4C). In the simulations we used values of α in the range of $[0.3 - 1]$.

Our network construction provided directed networks with inherited metric correlations. For simplicity, neurons connected to one another with the same weight. The final *structural* connectivity values of all pairs of neurons (i, j) were stored in the directed adjacency matrix A^{str} which defines the underlying physical structure. A schematic outline of this metric growth is shown in Fig. 3.4C, with a typical example of a homogeneously network in Fig. 3.4D

Aggregated networks. They were created by first diving the total number of neurons N into two subsets. The first one was distributed homogeneously over the 3 mm diameter substrate with a total number of neurons N_H; the second one comprised N_A neurons that were split into 15 islands of approximately 0.2 mm in diameter randomly distributed over the substrate. Connectivity in each subset was then established following the above rules, and then the subsets physically merged. Those neurons in the homogeneous subset that fell within the area of an island were eliminated and their connections assigned to the physically closest neurons in the island. This construction ensured that both subsets were interconnected within them and between them. Different neuronal densities were explored in the simulations, and maintaining constant the ratio $N_A/N_H \simeq 0.1$. A sketch of the creation of an aggregated network through the overlap procedure is shown in Fig. 3.4B. An example of a final aggregated network is depicted in Fig. 3.4E.

3.3.2 Justification and implications of the approaches made

In the brain, dendritic trees are responsible of local connectivity while axons shape directional communication. Also, experimental studies [694] showed that axons extend over long distances, along specific pathways, and with a highly stereotyped manner to find their correct targets (e.g. through genetic codification or fine tuned biochemical signaling). Indeed, each axonal arbor in the brain is responsible for carrying and distributing the information across specific regions of the neuronal circuit. Each of these areas represents the 'territory' of the axon, and each dendritic tree picks up the information available in this territory. Consequently, the structure of the axons is the asset that

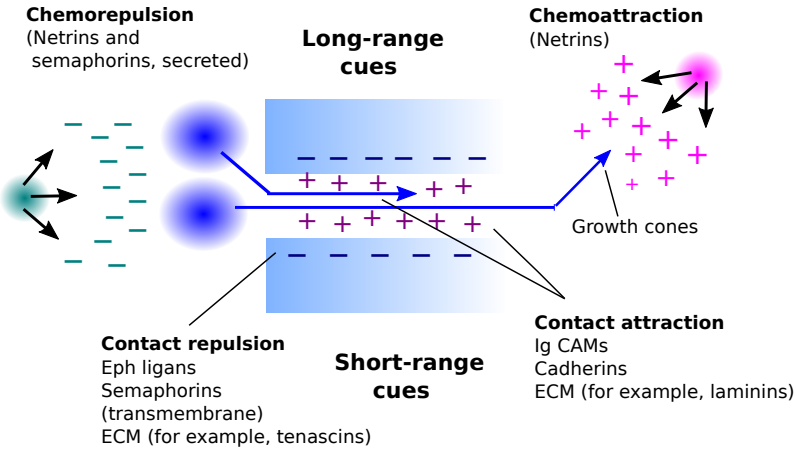

Figure 3.5: **Accurate guidance decision forces in the axonal growth.** Four mechanism contribute to guidance in growth axons: contact attraction, chemeotraction, contact repuslion, and chemoerepulsion.

impacts connectivity the most and, in the last instance, determines the network topology and dynamics at the meso–scale level.

This scenario contrast with neuronal cultures and our model, where connectivity can be view as local, with rare long–range connections, and without any guidance of axons. In this sense, a connection may occur when the axon of a given neuron intersects the dendrite region of any other neuron (Fig. 3.4C). For those neurons that fulfill this geometric condition, a connection is established with probability α. We set this probability to be independent of the overlapping length between the axon and the intersecting dendritic tree, and with values of α between 0.3 and 1. In denser neuronal structures, where neurons could be almost touching one another, one could set a lower α, for instance in the range $0.1 - 0.2$.

The established rules for the formation of the axons need some discussion. In our model, we simply set a quasi–straight segment–by–segment growth. A better model could incorporate at the end of each segment a specialized 'sensor' that would set the next segment according to some guidance rule. Hence, in this context, a natural question comes rapidly into mind: would this growth process be mediated by a short or a long–range mechanism? It is fascinating the fact that this question has a twofold answer. Indeed, the Ramón y Cajal's studies [574] already pointed out that axon guidance might be mediated by long–range chemoattraction mechanisms. In the same way, recent studies have suggested that target cells secrete diffusive chemoattractants [447, 203, 301, 313, 145] or chemorepellents [554, 226, 639, 145], substances that help guiding axons to long distances. In addition, axons can also be guided at short–range by contact–mediated mechanisms at the cell surface, particularly extracellular matrix molecules [183]. It is curious to note that those molecules functioning as long–range attractants and repellents (netrins and other semaphorins) are structurally related to molecules that function as short–range attractants or repellents (laminins and other semaphorins). This suggests that long–range guidance molecules may have evolved from their short–range counterparts. Despite its molecular origin, the important point is that axons appear to be guided through short and long–range mechanisms of balanced attraction and repulsion forces (Fig. 3.5). Consequently, the outcome of a particular guidance decision seems to reflect this detailed balance that operates at the target point.

Despite the attractiveness of guidance mechanisms for modeling, we observe that axons in neuronal cultures do not have the guidance mechanisms as in naturally formed

tissues. Furthermore, growth factors (and other possible molecules that could operate as guiding agents) are incorporated in the culturing media in a homogeneous manner. Thus, in this regard, we believe that axons in neuronal cultures grow isotropically and therefore our modeling scenario should be sufficient to represent the connectivity of a neuronal culture.

Concerning the dendritic growth model, some aspects can be also discussed. First, we note that the growth of dendritic trees can be described as a self–avoiding random walk. However, the resulting structure has a much higher density than the axons and therefore our statistical approach is valid. Moreover, some studies have shown that the particular biological growth rules of dendrites lead to arbor density functions that are Gaussian [753, 652, 213]. Indeed, the spatial morphology of dendritic tree of pyramidal neurons are built through a universal statistically self–similar process and governed by simple general principles grounded on a Gaussian density function.

The issue of why evolution selected this density function can be analyzed in different ways and presents strong implications in the communication process. The Gaussian arbor density function indeed provides a number of advantages for the system. First, this distribution is the function of a given size (measured as the standard deviation) that has the maximum entropy. This means that information is gathered and distributed in the most random way across the territory. Consequently, the synaptic partners will have the best change of finding its corresponding target, and arbor 'traffic jams' would be minimized. Second, this distribution is intrinsically separable. Such a quality means that arbor's density in different directions are independent, and thus the density function can be written as a product of independent terms. This property implies that such a distribution is extremely tractable from an analytical viewpoint.

Finally, it is worth commenting that a crucial step for the formation of neural circuits is the selection of synaptic partners, i.e. the establishment of an actual connectivity. A first hypothesis is that each synaptic connection is uniquely specified. This idea contrasts with a second hypothesis in which connections are randomly established. The first alternative involves the use of a vast quantity of information, whereas the second ones provides a much easier implementation. The latter is actually backed–up by evidences [652]. Consequently, the existence of the simple Gaussian density function discussed above — which is present in all arbors— naturally fits with the second hypothesis, and suggests that evolution selected this simple design principle [652]. In addition, in a network where connections are made at random, a scalable architecture enables the growth of the system without affecting the number of connections between pairs of neurons [691]. Indeed, a Gaussian structure preserves the average number of connections between pairs of arbors of different size. We note that recursive structures are ideal candidates to use in reconfigurable systems. This property is highly interesting for an adaptive system swamped in a changing environment.

3.4 Dynamic Model

Within a mathematical point view, neurons are excitable, non–linear dynamical systems. Their analysis show that they operate close to a bifurcation point that separates a resting or *quiescent* state from an excited one that corresponds to a long excursion in the phase

state. In general, neuronal excitability can be studied in a deterministic way through a separation of time–scales, and with a fast voltage variable (the membrane potential) and a slow recovery variable. The resting state of a neuron corresponds to a stable equilibrium. Sufficiently strong inputs can push the system into a stable periodic orbit, corresponding to periodic spiking activity. The mathematical description of neuronal dynamics, in the context of the QIFAD model used, is described next.

3.4.1 Soma dynamics

The simulation of the soma dynamics and the generation of action potentials was grounded in a quadratic integrate–and–fire model with adaptation [36, 352, 354]. This description leads to a system of two coupled non–linear ordinary differential equations, of the form

$$C\frac{dv}{dt} = R_q(v - v_r)(v - v_t) - R_U U + R_S I_S + R_\eta \eta, \tag{3.3}$$

$$\tau_a \frac{dU}{dt} = k_b(v - v_r) - U, \tag{3.4}$$

with the auxiliary after–spike resetting

$$\text{if} \quad v \geq v_p \quad \text{then} \quad v \leftarrow v_c,\, U \leftarrow U + \Delta U. \tag{3.5}$$

Eq. (3.3) specifies the dynamics of the soma membrane potential $v(t)$ with a quadratic growth, where C is the membrane time constant, also called leaky capacitance. Three effective currents get into the soma: U is an inhibitory current that accounts for the internal slow currents generated by the activation of K^+ ion channels and the inactivation of Na^+ channels; I_S is the synaptic inputs from other neurons; and η is a noise term understood as a random bombardment of small currents. The parameters R_U, R_S and R_η are the resistances associated with their respective currents. The quadratic term $(v - v_r)(v - v_t)$ has two fixed points, one stable ($v = v_r$) and one unstable ($v = v_t$), and that characterize the dynamics of the neuron.

Eq. (3.4) describes the dynamics of the inhibitory current U, with τ_a the main time–scale of the inhibitory current and k_b its sensitivity to sub–threshold fluctuations of the membrane potential,. ΔU describes the after–spike reset of U caused by slow high–threshold Na^+ and K^+ conductances, a behavior that accounts for *adaptation* in the system.

This set of equations is good enough to describe neuronal activity. For $v < v_t$, the inputs are not sufficient to trigger instability and the membrane potential relaxes towards its resting potential v_r. For $v > v_t$, inputs suffice to make the potential grow fast, up to a preset peak value $v \geq v_p$ that is associated to the generation of a spike. The potential is then reset to the value v_c.

From a computational perspective, in the numerical simulations we used a reduced form of the above equations, given by

$$\tau_c \dot{v} = k(v - v_r)(v - v_t) - u + I + \eta, \tag{3.6}$$

$$\tau_a \dot{u} = b(v - v_r) - u, \tag{3.7}$$

$$\text{if} \quad v \geq v_p \quad \text{then} \quad v \leftarrow v_c, u \leftarrow u + d. \tag{3.8}$$

We note that the equations are identical except for a redefinition of the constants. The fast variable v follows the same quadratic integrate–and–fire model as in the original formulation, and is coupled to the slow variable u. The parameters used in the dynamical simulation are provided in Tab. 3.2.

The reduced model reproduces well the vast repertoire of soma dynamics of cortical neurons. Indeed, by modifying the four parameters $\{k, \tau_a, b, d\}$ different individual behaviors can be obtained, including regular spiking, intrinsically bursting, chattering, fast spiking, low–threshold spiking and resonator, among others [354].

In this Thesis we were interested in analyzing the effect of network topology on the dynamics of the network. We therefore chose a set of parameters that provided the most typical *modus operandi* of neurons, and considered the regular spiking behavior (RS type) as our standard single neuron dynamical unit. Hence, the concept of *bursting* along this Thesis has to be understood as a network collective event (*network bursts*), and not as a single neuron phenomenon of repeated activation.

3.4.2 Synaptic dynamics

In several neuronal network models, neurons are viewed as the only computational entities, with the synapses simulated as passive scalar parameter ('weights'). However, biological synapses exhibit rich temporal dynamics, are able to perform computational tasks, and show rich plasticity over a wide range of time scales. Indeed, modeling work based on experimental measurements has demonstrated that the computational power of the network is increased through the use of dynamic synapses [455]. Below, we elaborate on the model that we used to take synaptic action into account.

We first consider that each connection between two neurons is associated to a chemical synapse with its own dynamics. For simplicity we consider that when a neuron generates an action potential, all its presynaptic terminals release neurotransmitters at the same time.

Let us consider the dynamics of a synapse that connects neuron i with neuron j ($i \rightarrow j$). When the neuron i generates a spike at time t_m, it triggers the release of neurotransmitters at the synapse and induces a post–synaptic current at neuron j. This current travels from the synapse to the soma and depolarizes the membrane, facilitating the generation of an action potential at neuron j. Hence, the total input currents on neuron j is given by

$$I_j(t) = \sum_{i=1}^{k_j^{in}} \sum_{t_m < t} E_i(t, t_m), \tag{3.9}$$

where $E_i(t, t_m)$ is the current induced by neuron i at time t as a result of the action potential generated at time t_m. The first sum comprises all input connections k_j^{in} on neuron j, and the second one all spikes previously generated. Note that the subset t_m

Dynamics Parameters	Value
Soma Parameters	
Resting membrane potential	v_r= -60 mV
Threshold membrane potential	v_t= -45 mV
Peak membrane potential	v_p= 35 mV
Reset membrane potential	v_c= -50 mV
Normalized membrane capacitance	C= 50 ms
	k = 0.5 mV^{-1}
	τ_a = 50 ms
	b = 0.5
	d= 50 mV
Synapse Parameters	
Depression recovery time	$\tau_D = 5 \cdot 10^2 - 2 \cdot 10^4$ ms
Depression decay	β = 0.8
AMPA current-strength	g_A = 10-50 mV
AMPA current decay time	τ_A = 10 ms
NMDA current strength	g_N = 0.4-1.5 mV
NMDA current decay time	τ_N = 150 ms
$GABA_A$ current strength	g_G = 20-100 mV
$GABA_A$ current decay time	τ_G = 20 ms
Noise Parameters	
White noise strength	$g_s = 3 \cdot 10^2$ mV^2ms
White noise auto-correlation	$<\eta(t)\ \eta(t')>=2g_s\delta(t-t')$
Shot noise frquency	λ =0.01 - 0.05 ms^{-1}
Shot noise strength (minis)	g_m = 10-50 mV
Shot noise decay time	$\tau_m = \tau_A$
Simulation Parameters	
Algorithm	Forward Euler
Time step	Δt = 0.01-0.1 ms
Typical run time	10^4 s

Table 3.2: **Dynamical Parameters for simulations.** Set of simulation parameters used for modeling network dynamics. The input arguments are specified in the configuration file within the software code.

is in general different from neuron to neuron, and can be viewed as the spike history of neuron i.

Each of the post–synaptic currents is modeled as a sudden increase in intensity at the time of action potential t_m, followed by an exponential decay. Axonal propagation delays are neglected because the propagation velocity of action potentials in axons (on the order of 1 m/s) is considerably faster than the velocity of neurotransmitters' release and subsequent stimulation ($\simeq 0.15$ m/s). The post–synaptic currents due to the firing of neuron i can be expressed as

$$E_i(t, t_m) = g_r D_i(t_m) exp\left(-\frac{t - t_m}{\tau_r}\right) \Theta(t - t_m), \tag{3.10}$$

where g_r is the strength of the synapse (associated to the receptor density at the post–synaptic terminal) and τ_r the characteristic decay time of the post–synaptic current. The subindex r specifies the associated ionics membrane receptors involved. For our excitatory

currents we considered the AMPA and NMDA receptors since they are the main source of activity in network bursts. For our inhibitory currents, we only considered the GABA receptors. In Tab. 3.2 we provide the values used for each of the synapses' strengths.

The last important element is synaptic depression and that accounts for the loss of firing efficiency upon repeated spiking. Synaptic depression in Eq. (3.10) is modeled as an internal variable $D(t)$ that describes the depletion process of glutamate presynaptic vesicles [282]. Hence, this kinetic parameter determines the dynamic behavior of synaptic transmission. The rate of depression is modeled as [719, 718, 36]

$$\dot{D} = \frac{1}{\tau_D}(1 - D) - (1 - \beta)D\delta(t - t_m), \tag{3.11}$$

where τ_D is the characteristic recovery time associated to the recycling of synaptic vesicles [261, 139]. This recovery time is important and actually controls the interval between consecutive network activations (*inter–burst interval*). Although this parameter may differ from network to network and along development, it typically takes values in the range of $0.5 - 20$ s in cultured neurons similar to ours. In Eq. (3.11), the depression variable D is initially set as 1 (no depression) and decreases by $D \to \beta D$ ($\beta < 1$) after each current injection. The parameter β fixes the strength of depression in the synapses' conductivity.

We note that, unlike inhibitory and adaptive mechanisms (which reduce responsiveness to all inputs), short–term depression is input–specific and provides a dynamic gain–control mechanism, increasing the efficiency of transmission. Indeed, the depression mechanism leads to a dramatic increase in the sensitivity of a neuron to subtle changes in the firing patterns of its afferents [15]. Like other forms of short–term plasticity, synaptic depression causes the response of a cortical neuron to depend on the previous history of afferent firing. Consequently, neuronal response of a single cell has to be understood in the context of previous activity.

3.4.3 Model for Calcium Dynamics

The above model is the basis for obtaining a train of spikes in each neuron. The next and final step in our simulations consists in generating the corresponding calcium fluorescence signal to mimic the data obtained in our experiments. We implemented such a conversion by using the model proposed by Vogelstein *et al.* [736]. Firstly, we resampled the spiking signal by a sweep speed of 50 frames per second in accordance to the experimental acquisition rate. Secondly, we proceeded to simulate the calcium dynamics considering that each action potential elicited by a neuron at time t resulted in a change in the calcium concentration of

$$[Ca^{2+}]_t - [Ca^{2+}]_{t-1} = -\frac{\delta t}{\tau_{Ca}}[Ca^{2+}]_{t-1} + A_{Ca}n_t, \tag{3.12}$$

with $A_{Ca} = 50\ \mu M$ and $\tau_{Ca} = 1$ s. The quantity n_t is the total number of action potentials. The resulting dynamics leads to a fast increase of calcium intra–cellular concentration that binds the fluorescence probe, resulting in a fast increase of fluorescence upon activation, followed by a slow decay.

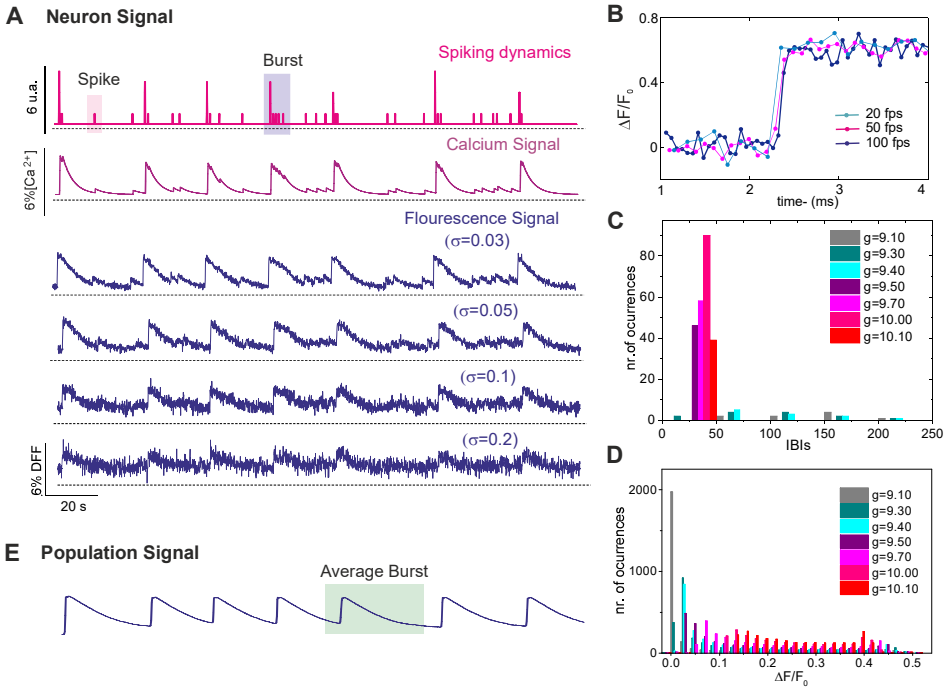

Figure 3.6: **Dynamics resulting from synthetic networks.** Panel (A) illustrates the simulated spiking activity of a single regular RS neuron with its corresponding calcium and fluorescence signals with different signal-to-noise ratio. (B) Sampling of the signal with different windows. Histogram of IBIs (C) and amplitude of fluorescence (D) of different networks where the strength $g = g_{AMPA}$ is modified from 9.10 to 10.10. (E) Flourescence signal of neuron's population.

Finally, the net fluorescence level F associated to the activity of a neuron i is given by the following saturating static nonlinear function,

$$F_{i,t} = \frac{[Ca^{2+}]_t}{[Ca^{2+}]_t + K_d} + \eta_t, \tag{3.13}$$

where $K_d = 300$ μM is the saturation concentration and η_t is a Gaussian distributed noise with zero mean. This noise represents the fluctuations in fluorescence inherent in imaging systems. In order to simulate the different experimental conditions —for instance acquisition speed, which lowers exposure time and increases noise— we adjusted the standard deviation of noise in the range $[0.01 - 0.1]$. Fig. 3.6A illustrates the simulated spiking activity of a single regular RS neuron with its corresponding calcium and fluorescence signals. One sampling of 50 frames per second is used for simulating the experimental context worked by us. In B the signal is sampled with different frames rates. In C and D are pictured the histogram of IBIs and $\Delta F/F_0$ for different networks wehere we have tuned G_{AMPA}, leaving fixed $g_{GABA} = -42$ and $g_{NMDA} = 0.4$. Finally, the fluorescence signal of neuron's population is also attached.

Chapter 4

ANALYSIS AND RESULTS I: Linear Dynamics

Neuronal cultures are prominent systems to study the development of connections in living neuronal networks and the interplay between connectivity, activity and function. In this chapter, we use spectral analysis to characterize global dynamical and structural traits of neuronal cultures. Firstly, we observe that the power spectrum can be used as a signature of the state of the network, for instance when inhibition is active or silent, as well as a measure of the network's connectivity strength. Secondly, the power spectrum identifies prominent developmental changes in the network such as the $GABA_A$ switch. Thirdly, the analysis of the spatial distribution of the spectral density, in experiments with a controlled weakening of connectivity through CNQX, an AMPA–glutamate receptor antagonist in excitatory neurons, reveals the existence of communities of strongly connected, highly active neurons that display synchronous oscillations.

4.1 Time Series Models

Given the importance of experiments in this thesis, the starting point of our research consisted in analyzing the structure of fluorescence traces, either from single neurons or from the averaged population. The fluorescence data $f(t) \equiv F_t$, measured in fixed discrete intervals along time, was then modeled as time series, i.e. $\{F_t; t \in Z\}$ ($Z = \{1, 2...T\}$), where T is the total duration of an image sequence sampled with a time interval τ, e.g. $\tau = 20$ ms for a camera acquisition speed of 50 fps.

A time series is often modeled as a sum of two terms,

$$f(t) = x(t) + \epsilon(t), \tag{4.1}$$

where $x(t)$ is a systematic component and $\epsilon(t)$ a random component. The desired signal component is $x(t)$, which may be represented by a low order polynomial. In such a situation, the objective of the time series analysis is to estimate the coefficients of polynomial. However, when $x(t)$ is a highly complex waveform that requires very high order polynomial representations, the approach of fitting a polynomial becomes impractical. In this case, a stochastic approach is more appropriate. Consequently, $x(t)$ is modeled as a stochastic function but different from $\epsilon(t)$.

Generally, a time series $f(t), t = 0, 1, 2, ..$ is assumed to follow a certain probability model that describes the joint distribution of the random variables $\{F_t\}$. The mathematical expression describing the probability structure of a time series is termed *stochastic process*. Thus, the sequence of observation of the series is actually a sample realization of the stochastic process that produced it.

4.1.1 Markov processes

We here briefly review the concept of Markov process. Let us consider a stochastic process $\{F_t\}$, and where each F_t assumes a value in the space Φ. The process $\{F_t\}$ is a Markov process when, given the value F_t, then the values F_h $(h > t)$ do not depend on the values F_s, $s < t$. In other words, $\{F_t\}$ is a Markov process if it is a conditional distribution function satisfying,

$$P(F_h|F_s, s \leq t) = P(F_h|F_t), \quad h > t. \tag{4.2}$$

The importance of the Markov processes is that the evolution of a system only depends on its present state, and not of the previous ones.

4.1.2 Linear Stochastic Processes

A time series model is said to be linear or nonlinear depending on whether the current value of the series is a linear or nonlinear function of past values. In brief, linear methods means that the intrinsic dynamics of the system is governed by the *linear paradigm*, i.e. that small causes lead to small effects. Linear methods interpret all regular structure in a data set, such as a dominant frequency through linear correlations.

There are two widely used linear time series models in the literature: (i) the Autoregressive (AR) [92] and (ii) the Moving Average (MA) models. Combining these two, the Autoregressive Moving Average (ARMA) model has been also proposed in the literature [92, 156]. And, in general, there are important works treating linear stochastic models, and with long history, including Yule [773, 774], Walker [](1931), Slutsky (1937), Wold (1938), Kendall (1945), Bartlett (1946), Quenouille (1952,1957), Doob (1953),Grenander and Rosenblatt (1957), Hannan (1960), Robinson (1967), among others. Below, we treat in more detail the AR, MA, and ARMA.

Autoregressive (AR) Model

In this model one considers a time series of equally–spaced quantities F_t, $(t = 1, 2, ...)$, that obey,

$$F_t = \mu + \sum_{j=1}^{p} \phi_j F_{t-j} + \epsilon_t, \tag{4.3}$$

where $\epsilon_t \sim N(0, \sigma^2)$ is a white noise of zero mean and σ^2 variance, μ the average of the time series $\{F_t\}$, $\vec{\phi} = (\phi_1, \phi_2, ..., \phi_p)$ the vector of model coefficients, and p a positive integer. The AR model establishes that a realization at time t is a linear combination of the p previous realization plus some noise term, producing linear autocorrelations between past and future observations. This is a standard autoregressive model framework, commonly abbreviated as $AR(p)$ where p is the order of the auto–regression. When the

data is related over time, AR is a group of linear prediction formulas which offer the simplest class models for exploring dependences.

Moving Average (MA) Model

Here, instead of using the past values, one considers the past *errors* in a regression–like model. The moving average process MA(q) is then defined as

$$F_t = \mu + \sum_{j=1}^{q} \psi_j \epsilon_{t-j} + \epsilon_t, \tag{4.4}$$

where μ is the average of the time series $\{F_t\}$, $\vec{\psi} = (\psi_1, \psi_2, ..., \psi_p)$ the parameters of the model to determine, and $\epsilon_{t-j} \simeq N(0, \sigma^2)$ (with $j \in [0, ..., q]$) white terms. The value of q is called the *order* of the MA model. We note that each value of F_t from Eq. (4.4) can be viewed as a weighted moving average of the past few forecast errors. Conceptually, MA models are a linear regression of the current value of the series against the white noise or random shocks of one or more prior values of the series.

Autoregressive Moving Average Models (ARMA)

The autoregressive moving average process of orders p and q [ARMA(p,q)] combines both AR and MA models into a unique representation. Then, the ARMA process of order p and q is defined as

$$F_t = \mu + \sum_{j=1}^{p} \phi_j F_{t-j} + \sum_{j=1}^{q} \psi_j \epsilon_{t-j} + \epsilon_t, \tag{4.5}$$

where μ is the average of the time series $\{F_t\}$, $\vec{\phi} = (\phi_1, \phi_2, ..., \phi_p)$ and $\vec{\psi} = (\psi_1, \psi_2, ..., \psi_p)$ the vectors of model coefficients to determine, and $\epsilon_{t-j} \simeq N(0, \sigma^2)$ (with $j \in [0, ..., q]$) the white noise terms.

We note that the AR model depends on the lagged values of the data to model, while the MA model is based on the errors (residuals) of the previous forecasts made. Then, the mixed ARMA model takes into account both factors when making predictions.

4.2 Linear Time Series Analysis

The objective of time series analysis is to understand and identify the stochastic process underneath an observed series and then forecast future values of a series from solely its past values [25]. Indeed, the challenge of linear time series analysis is to extract the autocorrelation elements of the data, either to understand the trend itself or to model the underlying mechanisms.

4.2.1 Time–Domain Analysis

Temporal representation is usually the first (and most natural) way to describe an evolving system, since almost all signals are obtained from devices that record the temporal variations of a magnitude under study [45].

In a time domain analysis, the variable is always measured and analyzed against time. As we have seen, the most remarkable feature of time series is that successive values are not independent; they are correlated with one another, i.e. they are serially correlated or autocorrelated. Some of the most useful tools for describing this serial (or temporal) dependent structures of a univariate time series are the auto–covariance and the autocorrelation functions.

1.2.1.1. Auto-covariance and autocorrelation Functions

If $\{F_t; t \in Z\}$ is a time series, then for any $t_i, t_j \in Z$, we define the autocovariance function, denoted by $\gamma(t_i, t_j)$, as

$$\gamma(t_i, t_j) = \langle [F_i - \mu_{F_i}][F_j - \mu_{F_j}] \rangle = \langle F_i F_j \rangle - \langle \mu_{F_i} \mu_{F_j} \rangle. \tag{4.6}$$

The rescaled (standarized) version of the autocovariance provides the autocorrelation, given by

$$\rho(F_i, F_j) = \frac{\gamma(t_i, t_j)}{\sqrt{\sigma^2_{F_i}}\sqrt{\sigma^2_{F_j}}}, \tag{4.7}$$

where $\sigma^2_{F_i} = \mathrm{Var}(F_i)$ and $\sigma^2_{F_j} = \mathrm{Var}(F_j)$ represent the variance of F_i and F_j, and σ_{F_i} and σ_{F_j} the standard deviations, respectively.

If one considers that our time series $\{F_t; t \in Z\}$ are *weakly stationary* [1], then both the autocovariance and the autocorrelation functions depend only on the difference between t_i and t_j, termed *delay time* or *lag*, i.e. $\delta = t_j - t_i = |j - i|\tau$. Therefore, Eqs. (4.6) and (4.7) can be rewrite as

$$\gamma_F(\delta) = \sum_{t=1}^{T-\delta} (f_t - \mu)(f_{t+\delta} - \mu), \tag{4.8}$$

and

$$\rho_F(\delta) = \frac{\sum_{t=1}^{T-\delta} (f_t - \mu)(f_{t+\delta} - \mu)}{\sum_{t=1}^{T} (f_t - \mu)^2}. \tag{4.9}$$

Intuitively, the covariance between F_t and $F_{t+\delta}$ indicates the relative shift between F_t and $F_{t+\delta}$. If the series are uncorrelated the covariance is then zero, and

$$\gamma_{F_t F_{t+\delta}} = \langle F_t F_{t+\delta} \rangle - \mu_{F_t} \mu_{F_{t+\delta}} = \langle F_t \rangle \langle F_{t+\delta} \rangle - \mu_{F_t} \mu_{F_{t+\delta}} = 0. \tag{4.10}$$

However if the series are correlated in some way, then their covariance will be nonzero. Indeed, for $\gamma_{F_t F_{t+\delta}} > 0$, then $F_{t+\delta}$ tends to increase as F_t increases, and for $\gamma_{F_t F_{t+\delta}} < 0$, then $F_{t+\delta}$ tends to decreases as F_t increases. In the first case, the covariance is positive and one says F_t and $F_{t+\delta}$ are positively correlated. On the other hand, when F_t is small compared to $F_{t+\delta}$, the covariance is negative and one says that F_t and $F_{t+\delta}$ are negatively correlated. We note that while statistically independent variables are always uncorrelated, the oposite is not necessary true.

[1] Other terminologies are *covariance stationarity*, *stationarity in the wide sense*, or *second-order stationarity*. The time series $\{F_t; t \in Z\}$ is said to be *covariance stationary* if: (i) $\langle F_t \rangle = \mu$ (constant for all t), (ii) $Var(F_t) = \sigma^2 < \infty$ (i.e., a finite constant for all t) and (iii) $\gamma(t_i, t_j)$ depend only on $t_i - t_j = \delta$.

4.2.2 Frequency-Domain Analysis

The analysis of a time series in the frequency domain is carried out through the spectral density, which identifies the cyclic nature or periodicity in the time series. The spectral [2] analysis of a process is a suitable tool for bringing to light periodic components. This representation allows us to focus on the study of the frequency distribution of signals and its corresponding distribution of energy.

4.2.2.1. Fourier Transform

The Discrete Fourier Transform (DFT) of a time series $\{F_t; t \in Z\}$ is defined as

$$\mathcal{F}\{F_t\} = \frac{1}{\sqrt{T}} \sum_{n=0}^{T-1} f(t_n) e^{-i2\pi kn/T}, \quad n \in Z, \tag{4.11}$$

and its inverse as

$$\mathcal{F}^{-1}\{F_t\} = \frac{1}{\sqrt{T}} \sum_{k=0}^{T-1} F(f_k) e^{-i2\pi kn/T}, \quad n \in Z. \tag{4.12}$$

where the frequency component is given by $f = \frac{k}{Tf_s}$, with f_s the sampling frequency.

Regarding implementation, two consideration must be taken into account.

Frequency resolution. If the sampling frequency f_s is fixed, from the Nyquist theorem it follows that the maximal useful frequency is $f_{T_s} = f_s/2$. Then, the only degree of freedom that we have left in the data processing is the length T on the DFT. The width of a frequency bin (also called *frequency resolution*) is given by $f_r = \frac{f_s}{T}$. Then, the DFT will produce only $T/2 + 1$ distinct complex numbers. They correspond to the frequencies $f_i = if_s$, $m = 0, ..., T/2$. The first element, f_0, corresponds to the 'DC' component, i.e. the average of the signal. The last element, $T/2$, corresponds to the Nyquist frequency $f_{Ny} = (T/2)f_{res} = f_s/2$ and has no imaginary part because of the complex–conjugate symmetry of the output array. Hence, from a practical perspective, one obtains $T/2$ frequency bins of width f_s/T as output. The apparent loss of information is explained by the fact that the output consists of complex numbers while the input is real.

Implementation. Usually the DFT is computed through a very efficient algorithm known as the Fast Fourier Transform (FFT) [315, 682]. When the length of the time series T is a power of 2, computational complexity drops from $O(T^2)$ for a DFT to $O(T \log_2(T))$ for the FFT (see Annex I). This results in a substantial reduction of computational effort for large T. When the length of the time series is not a power of 2, then the length can be artificially increased by adding zeros up to the next power of 2. This is called *zero–padding*.

[2] We note that the word 'spectrum' was introduce for the first time at the scientific literature by Newton in relation to the decomposition of white light into a band of colors when the light crossed a glass prim. This term is derived from the Latin root 'specter' which means 'ghostly apparition'.

4.2.2.2. Power Spectrum Density

Power spectrum density (PSD) is a type of frequency–domain analyses that provides the frequency distribution of the power of a signal. Provided a deterministic signal $x(t)$ for which

$$E = \int_{t=-\infty}^{\infty} |x(t)|^2 dt \tag{4.13}$$

exists, then one can associate E as the *energy* of signal, and its Fourier transform exists. This integral is sometimes cannot be defined for some signals. For instance, all random signals as well as many periodic signals provide an infinite energy through this definition. Hence, it is customary to use the average power $\bar{P}$ of a given finite sample of the signal, or the energy delivered in a fixed amount of time, i.e.

$$\bar{P} \propto \lim_{T\to\infty} \frac{1}{2T} \int_{-T}^{T} |x(t)|^2 dt. \tag{4.14}$$

In discrete time series, if f_k is the kth value of a time series of T points with sampling period $\tau = \Delta t$, its energy E is defined as

$$E = \sum_{k=0}^{T-1} |f_k|^2 \Delta t. \tag{4.15}$$

When the series is produced by a stationary stochastic process of infinite duration rather than by a deterministic waveform of finite duration, the energy is usually infinite and the quantity of interest is the spectral density function (*power*) ξ defined as the energy per unit time,

$$\xi = \frac{E}{T\Delta t} = \frac{1}{T} \sum_{k=0}^{T-1} |f_k|^2. \tag{4.16}$$

Important aspects to be considered when treating with the power spectrum density are:

Characterization of the dynamics. Spectral analysis is a traditional approach to characterization the dynamics of the system. For periodic signals, peaks at the fundamental frequency, and its corresponding harmonics, should be identified in the spectrum. Quasi–periodic signals, on the other hand, provide peaks that are linear combinations of two or more irrationally related frequencies (often giving the appearance of a main sequence and sidebands). At the extreme of chaotic dynamics, the PSD presents broad band components, with an exponentially decay at high frequencies. Stochastic behavior has a power spectrum that decreases as $1/f^{\alpha}$, with α termed the *fractal exponent* (or power–law exponent or spectral decay) and varies between 0 and 1. Depending on the α values, different stochastic processes can be classified. For $\alpha = 0$ the PSD is constant and there is equal power in all frequencies. This is called *white noise* and it is produced by a random processes where each point in time is an independent and identically distributed random variable with zero mean and finite variance. For $\alpha = 1$ one identifies *Brownian noise*, i.e. just integrated white noise. The random processes here are called random walk

or Brownian motion. For $\alpha = 1/2$ one observes *pink noise*, a behavior that has identified in very different systems, from various physical and biological systems to financial systems. Intermediate colored noises can be obtained by tunning the spectral exponent α, producing a PSD characterized by a decrease in power with increasing frequency. Unfortunately, as we will shortly see, when working with experimental signals, the similarity of the PSD between chaotic and colored noises makes difficult a neat distinction. Consequently, other methodologies are required in order to complete the analysis.

Correlation and PSD. From Eq. (4.24) one can observe that the Fourier Transform of the auto–correlation function is directly the PSD. Consequently, the analysis of the temporal correlations of the system can be performed simply through the PSD. When the correlation function presents an exponential decay, then the series is said to have short–range dependences (SRD) or correlations. When the decay is lower than an exponential one, then it is said to present long–range dependences (LRD). This property may be due to the existence of a divergent correlation length (theoretically divergent) or to the absence of a characteristic correlation length. In the latter case, the correlation is associated with a decay that follows a power law.

A typical LRD system is one where the autocorrelation function decays asymptotically, i.e.

$$\rho_F(\delta) \sim \delta^{-\gamma} \quad 0 < \gamma < 1, \tag{4.17}$$

and implies that the value of the signal at i influences all values at $j > i$, with the influence decaying very slowly.

The direct estimation of the autocorrelation function ρ of a time series is limited by the effect of the noise. This raises a serious problem when the signal presents long–term correlations, since the dynamics is characterized by the asymptotic behavior of $\rho(\delta)$ when $\delta \to \infty$.

If the series is stationary, spectral analysis techniques can be applied and the PSD of the series $f(t)$ can be calculated as a function of the frequency f. Since the PSD is only the Fourier transform of the autocorrelation function, when the series has long–range correlations, then

$$PSD(f) \sim f^{-\beta}, \tag{4.18}$$

where β is related to the γ exponent of the correlations as

$$\beta = 1 - \gamma. \tag{4.19}$$

In summary, the direct estimation of the autocorrelation function is limited to the fulfillment of signal stationarity. That is, the invariability of the mean value, standard deviation and moments of higher order, as well as the invariability of the autocorrelation function totemporal translations.

Implementation. The estimation of the power spectrum density via FFT is computationally efficient and generally yields reasonable results. However, there are certain inherent performance limitations of the FFT approach. A first problem in computing periodogram estimates is that the variance is large, of the order of $(\text{PSD})^2$. A second problem is that the variance does not decrease for $T \to \infty$. There are two ways to decrease the variance of the periodogram estimates, either through averaging in the time domain or through averaging in the frequency domain.

In our case, to analyze the spectral content of fluorescence signals, we computed the PSD of the normalized traces $\tilde{F}(t) = \Delta F/F_0$ by using the Welch periodogram method [751, 304] implemented in Matlab 7.12.0. The signal is divided into Hamming windows of 256 points (approximately 10 s), and 50% overlap. To estimate the FFT, 1,024 points were used, with zero–padding when required. Because we used a sample frequency of 20 Hz for young cultures and 33 Hz for mature ones, the frequency resolution ranged between 0.019 Hz and 0.032 Hz, respectively. The corresponding frequency ranges varied in the interval $(0.078 - 10)$ Hz and $(0.128 - 16.5)$ Hz. Finally, the averaged spectrum for the whole neuronal population was computed when required, for instance to compare global network characteristics during the maturation of the cultures.

Limitations of the Analysis. Although the above analyses are valid under extremely general conditions, the present some very important restrictions. On the one hand, the Fourier Analysis requires that the system operates close to the linear region. On the other, the generated data must be strictly stationary and periodic. We note that physiological signals usually have finite durations, are of a non–stationary nature, and typically come from non–linear systems. Hence, spectral analyzes based on the Fourier transform have a rather small field of applicability.

Therefore, it is evident that the Fourier Transform and its derived representations are not sufficient to fully capture the characteristics of many of the non–stationary signals. It is necessary to go a step further towards the joint representation of the temporal and frequency characteristics, i.e. towards a two–dimensional representation that combines both approaches.

4.2.3 Time–Frequency Analysis

Location and principle of Heisenberg–Gabor

From Eq. (4.11), and after analyzing the spectrum of F_k in more detail, one can observe that they are only a set of coefficients obtained by expanding the signal $f(t)$ to a family of signals of infinite duration $e^{-i2\pi kn/T}$, completely delocalized in time.

To simultaneously locate a signal in time and frequency, one can consider the expected value and its dispersion from each of the two representations provided in Eqs. (4.11) and (4.12). Hence, one can consider $|f(t)|^2$ and $|F(k)|^2$ as distributions of probability and analyze their mean and standard deviation [45], i.e.

$$\mu_t = \frac{1}{E}\sum_{n=0}^{T-1} t|f_n|^2\Delta t, \tag{4.20}$$

$$\mu_f = \frac{1}{E}\sum_{n=0}^{T-1} f|\mathcal{F}(f_n)|^2\Delta f, \tag{4.21}$$

$$\sigma_t^2 = \frac{4\pi}{E}\sum_{n=0}^{T-1}(t-\mu_t)^2|f_n|^2\Delta t, \tag{4.22}$$

$$\sigma_f^2 = \frac{4\pi}{E}\sum_{n=0}^{T-1}(f-\mu_f)^2|\mathcal{F}(f_n)|^2\Delta f. \tag{4.23}$$

In these equations E is the energy of the system, which is assumed to be finite and given by

$$E = \sum_{k=0}^{T-1} |f_k|^2 \Delta t < \infty. \tag{4.24}$$

The signal can be then located in the time–frequency plane around the position (μ_t, μ_f) and comprising a domain whose area is proportional to the time–bandwidth $A = \sigma_t \cdot \sigma_f$. From the definition of the Fourier Transform, the product $\sigma_t \cdot \sigma_f$ obeys

$$\sigma_t \cdot \sigma_f \geq 1. \tag{4.25}$$

This restriction, termed the *Heisenberg–Gabor inequality*, reflects the fact that a signal can not simultaneously present an extension arbitrarily small in time and frequency [141]. The lower limit of this inequality is reached for Gaussian functions.

Hilbert Transform: Instantaneous frequency and group delay

Another way of analyzing a signal simultaneously in time and frequency deals with the concept of instantaneous frequency. This concept uses the Hilbert transform (H), which associates any real signal $f(t)$ a complex signal $f_a(t)$, termed *analytic signal*, defined as

$$f_a(t) = f(t) + iH(f(t)), \tag{4.26}$$

where

$$H(f(t)) = \frac{1}{\pi} \oint_{\infty}^{\infty} \frac{1}{t - t'} f(t')dt'. \tag{4.27}$$

Here $\oint$ represents the Chauchy integral. This definition has a very simple interpretation in the frequency domain, since $H(t) \equiv H(f(t))$ has the same Fourier Transform as $f(t)$ but the coefficients corresponding to negative frequencies are zero, while the strictly positive ones double their amplitude and the DC component is maintained [141]. Mathematically,

$$\mathcal{F}(h(t)) = 0 \quad f < 0, \tag{4.28}$$

$$\mathcal{F}(h(t)) = \mathcal{F}(0) \quad f = 0, \tag{4.29}$$

$$\mathcal{F}(h(t)) = 2\mathcal{F}(f) \quad f > 0. \tag{4.30}$$

Therefore, the analytic signal $f_a(t)$ can be easily obtained from the real signal by canceling the spectrum of $f(t)$ in the negative frequencies, since the information is not altered for real signals, $\mathcal{F}(-f) = \mathcal{F}^*(f)$. Such a procedure finally provides $H(t)$, which allows to define in a unique way the concept of *instantaneous amplitude* and *instantaneous frequency*, of the form

$$a^{ins}(t) = |H(t)|, \tag{4.31}$$

$$f^{ins}(t) = \frac{1}{2\pi} \frac{d(Arg(H(t)))}{dt}. \tag{4.32}$$

Although the instantaneous frequency characterizes (locally) the frequency behavior as a function of time, it is useful to characterize the *delay group*, which determines the time behavior as a function of the frequency, as

$$t_g = -\frac{1}{2\pi}\frac{d(Arg(\mathcal{F}(f_a(t))))}{dt}. \tag{4.33}$$

This quantity measures the mean time of arrival for each frequency f. In general, the instantaneous frequency and the group delay result in two different curves in the time–frequency plane. The are approximately identical when the product $\sigma_t \cdot \sigma_f$ is large.

We note that the concept of instantaneous frequency implicitly assumes that, for each time instant, there is only one single frequency component. Likewise, the delay group has to concentrated around a single time instant at a given frequency. Unfortunately, most of the physiological signals, as ours, are multicomponent, in the sense that different simultaneous actors shape the signal, and therefore these signals do not comply with the above requirements.

Short–Time Fourier Transform or Gabor Transform

In many instances, physiological signals present temporal variations of frequency that cannot be detected through the Fourier transform. This issue can be addressed with the Gabor Transform, also called Short–Time Fourier Transform (STFT). The method consists in applying the Fourier Transform on fractions of the signal properly windowed [141]. This strategy allows to study the evolution of the frequencies in time, but assuming that the signal fulfills the stationarity condition within each window. Formally, the Gabor transform of a signal $f(t)$ is defined as

$$G_D(F_t) = \frac{1}{\sqrt{T}}\sum_{n=0}^{T-1} f(t_n)g_D^*(t_n - t)e^{-i2\pi kn/T}, \tag{4.34}$$

where g_D^* is the window of width D centered at t, and $*$ denotes the conjugate complex. In essence, $G_D\{F_t\}$ is similar to the Fourier Transform of Eq. (4.11), but with the introduction of the window g_D^*. The Gabor Transform can also be seen as the scalar product between the signal and the family of complex exponentials modulated by the windows g_D^*, i.e.

$$G_D(F_t) = \langle f(t_n), g_D^*(t_n - t)e^{-i2\pi kn/T}\rangle, \tag{4.35}$$

where the window g_D^* is inserted to locate the Fourier transform of the signal at time t. Hence, for the Gabor Transform to be computable, the chosen window must be of large amplitude at the vicinity of t and should decay rapidly. Amongst the different possibilities for a window, Gabor proposed the Gaussian one, given by

$$g_\alpha(t) = \left(\frac{\alpha}{\pi}\right)^{1/4} e^{\frac{-\alpha}{2}t^2}. \tag{4.36}$$

Since the Fourier transform of a Gaussian function is also a Gaussian, this windows allows for a simultaneous localization in time and frequency. As a reminder, the Gaussian functions do not have compact support, that is, they have values different from zero in the whole range $-\infty$ to $+\infty$. The parameter α measures the speed at which the function

approaches to zero asymptotically. Thus, it becomes necessary to truncate the function to a length D assuming that, at the edges, the values are almost zero.

The Gabor transform is redundant in the sense that it maps every instant of the original signal to a value in the time–frequency domain. To reduce this redundancy, the Gabor Sampling Transform is usually used, which is achieved by taking the values of the transform at certain points in the time–frequency space, of the form

$$G_D(f,t) \to G_D(mF, nT), \tag{4.37}$$

where T and F represent the sampling intervals in time and frequency. Depending on the resolution required, the selection of T and F decreases redundancy and saves computational load, but it may occur that the reconstruction of the signal can not be directly carried out.

Finally, the spectrum can be calculated as

$$I(f,t) = |G_D(f,t)|^2 = G_D^*(f,t) \cdot G_D(f,t), \tag{4.38}$$

giving rise to a representation of the signal in the time-frequency domain. This representation, called the *spectrogram*, offers an elegant description of the evolution of the different frequencies that shape the signal.

The Gabor transform offers a good time–frequency representation of the signal, but suffers from the limitation imposed by the Heisenberg–Gabor principle. If the window used is too narrow (in time), the resolution frequency will be very poor, whereas if the window is very wide, the location will not be sufficiently accurate. Signals that represent slow processes will require long time windows, whereas signals with fast transients (with high frequency components) will be parameterized better with shorter windows. Hence, in our analysis of experimental data, we used an intermediate window. Other alternatives, and that provided similar results, would be based on the Wavelet Transform [300].

4.3 Case Study: Embryonic Cortical Cultures

In the following, we use the linear analysis tools outlined above to uncover distinct traits during the development and controlled connectivity disintegration of neurons in culture.

4.3.1 Network development

To investigate distinct features of spontaneous activity due to varying neuronal connectivity, we first treated the scenario in which the network grows and matures along several days *in vitro* (DIV).

Neurons in our preparations lacked any initial connectivity. However, development occurred rapidly. We already observed connections as early as 24 h after plating and, consistently with other studies [660], neurons were electrically excitable by DIV $2-3$. Spontaneous activity appeared by DIV $5-6$, subsequently changing in strength and structure as the culture matured and evolved further. Fig. 4.1 illustrates this behavior for a given culture batch, and with both excitation and inhibition active ('E+I' network). Representative fluorescence traces of average network activity along 15 days of development are provided in Fig. 4.1A. For this batch, we observed the first occurrence of

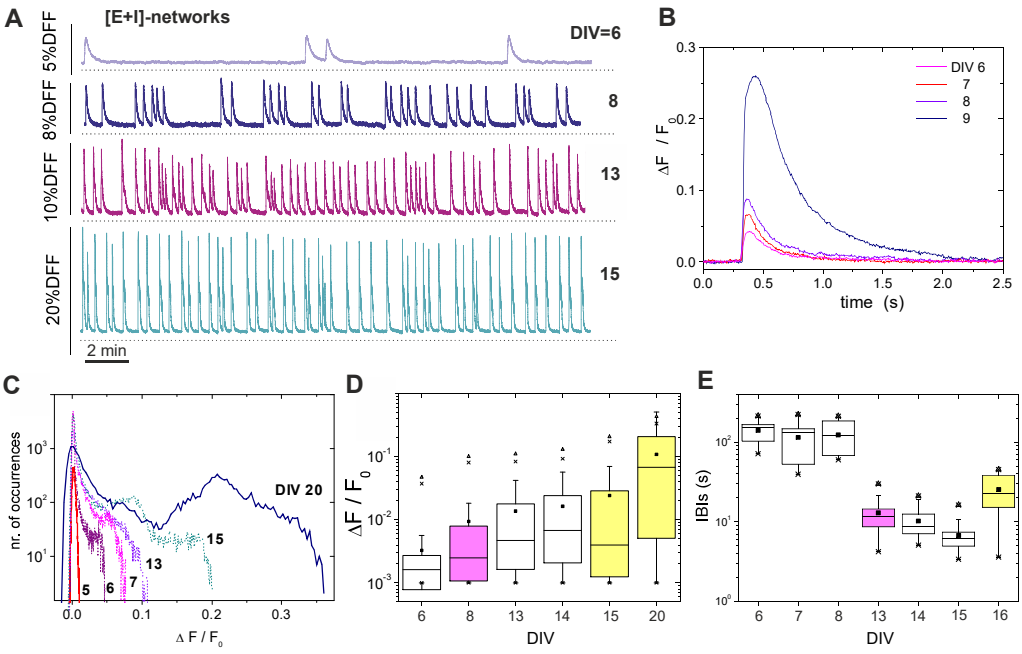

Figure 4.1: **Network development.** (A) Examples of fluorescence traces of spontaneous activity along 15 days of development. All measurements correspond to cultures from the same batch. Traces are the average over the monitored network population ($\simeq$ 2000 neurons). The peaks of fluorescence signal identify bursting episodes. The time elapsed between two consecutive bursts define the interburst interval (IBI). The measurement at day in vitro (DIV) 6 corresponds to the first observation of spontaneous bursting activity in the batch. (B) Detail of a bursting event (averaged over the monitored network population) during the early stages of development to illustrate the substantial increase in fluorescence amplitude after DIV 8. (C) Histogram of the network-averaged fluorescence signal for representative stages of development. Bursting activity is absent at DIV 5, giving rise to a fluorescence histogram that is close to a Gaussian distribution. The distributions broaden as bursts emerge and increase in amplitude. (D) Box plots of the statistical analysis of the fluorescence distributions. Note the logarithmic scale in the vertical axis. The mean of the distribution (■) and its maximum value (▲) substantially increase by DIV $\gtrsim$ 8 (pink) and after DIV 15 (yellow), suggesting major evolutionary switches of the network. In the figure, whiskers represent 25 and 75% confidence intervals, and crosses (x) 1 and 99 %, respectively. (E) IBIs box plot analyses. The broad IBI distribution observed for young cultures significantly changes to a narrow distribution with stable IBI timing after DIV 8, to change again toward a higher variability by DIV $\gtrsim$ 15.

bursting at DIV 6. At earlier days, the bursting dynamics was either absent or too sparse to be detected. Although the presence of bursts is clear at DIV 6, their interburst timing is irregular and the firing amplitudes low. By DIV 8 the fluorescence amplitude substantially increased and bursting became more regular, reaching a stage of high periodicity by 2 weeks after plating. At later stages of development we observed different trends from batch to batch, with firing amplitudes and interburst intervals (IBIs) stabilizing or decreasing.

Fig. 4.1B depicts the shape and strength of a burst among different evolutionary stages. Bursts are time–shifted for the onset of network activation to coincide. The plot reveals the gradual increase in bursting amplitude during the early stages of development, and the sudden jump at DIV 9, which hints at strong changes in both neuronal excitability and network connectivity. The example of Fig. 4.1B highlights the dominance of the burst shape (amplitude and width) on the structure of the recorded signal. This is further evidenced in Fig. 4.1C, which shows the distribution of fluorescence amplitudes for the population–averaged signal along maturation. The distribution at DIV 5 is close to a Gaussian distribution, indicating the absence of firing events sufficiently strong to be detected by the camera. As development continued, the histogram of amplitudes became distinctly right–skewed, with progressively higher values of fluorescence. A detailed statistical analysis of the changes in fluorescence is provided in Fig. 4.1D, and illustrates the strong asymmetry of the fluorescence distributions. Interestingly, the major changes in firing amplitude occurred by the end of the first and second weeks *in vitro*. The average firing amplitudes (denoted by a black square) as well as the maximum measured amplitudes (up triangles) abruptly increased at these stages.

These changes in network dynamic behavior were also captured by the distribution of IBIs, which showed a tendency to become well timed as the cultures matured (Fig. 4.1D). The average IBI reduced from high, broadly distributed values in the range $100 - 200$ s at DIV $5 - 8$ to narrowly distributed values around $10 - 20$ s after DIV 8. By DIV 16 the network dynamics changed again toward a more erratic behavior and larger IBIs.

4.3.2 Emergence of inhibition during development

The evolution of inhibitory action during development is depicted in Fig. 4.2. A first interesting feature is the observation that the blockade of inhibition at early stages of development silenced the culture or strongly disrupted its activity. This is clearly shown in the network–averaged traces at DIV 5 and 8 in Fig. 4.2A. Such a disruption is a consequence of the depolarizing action of GABA at early developmental stages and that confers it an excitatory role [70]. Therefore, the blockade of $GABA_A$ effectively reduced excitation and, in turn, the mechanisms for the network to spontaneously fire. GABA changed to its normal inhibitory action by DIV 7, an event known as *GABA switch* [254, 660]. The blockade of inhibition at this and subsequent stages resulted in strong bursting due to the excess in excitation, which is revealed by the high fluorescence amplitudes at DIV 15 (Fig. 4.2A).

The distribution of fluorescence amplitudes in Fig. 4.2B also illustrates the changing role of inhibition during development. 'E+I' networks showed bursting activity already at DIV 5, with broad fluorescence distributions that gradually increased in width as bursts strengthened in maturer stages. 'E–only' networks, however, showed at DIV 5

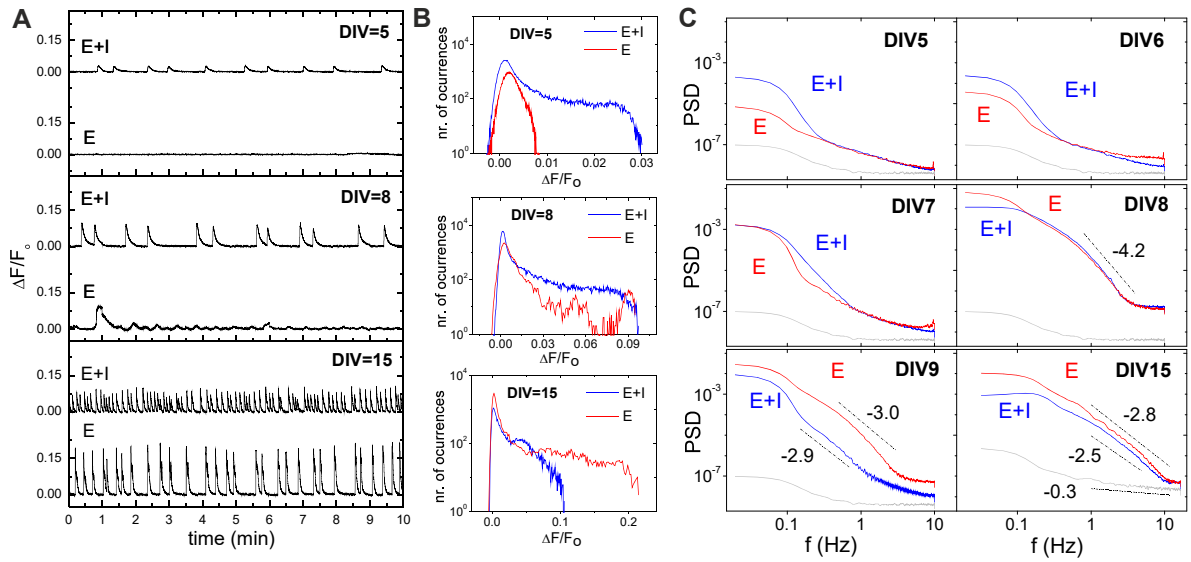

Figure 4.2: **Influence of inhibitory action during development and GABA switch** (A) Illustrative population-averaged traces of spontaneous activity during development, and comparing "E+I" (top traces) and "E-only" signals (bottom ones) on the same culture. GABA has an excitatory role at early developmental stages and therefore its blockade effectively reduces excitation and silences the network. GABA switches to its normal inhibitory role by DIV $\simeq 6-7$. In maturer cultures, the blockade of inhibition increases excitation and the strength of the bursting episodes. (B) Corresponding fluorescence amplitude distributions, depicting the gradual increase in values as maturation progresses. At DIV 8 the blockade of inhibition neither silences the network nor strengthens firing, signaling the GABA switch event. (C) Power spectrum densities (PSD) of the spontaneous activity signals, averaged over the monitored population, and along representative stages of development. The gray curve shows the PSD associated to the noise of the camera. The PSD for "E+I" (blue) and "E-only" recordings (red) are markedly different except during GABA switch, at DIV $\simeq 7-8$, signaling its occurrence. The lines and their slopes are a guide to illustrate the markedly different behavior of the PSD between noise and actual measurements.

a distribution of fluorescences close to Gaussian ones, although the slight deviation at high fluorescences hinted at some sporadic, individual neuronal activity. Bursting was observed by DIV $7-8$, though very erratic due to GABA switch. At the other extreme of development (DIV 15) network behavior completely changed, and the bursting amplitudes in the 'E-only' condition were much higher than in the 'E+I' one.

In general, the blockade of inhibition in cultures older than 1 week resulted in a substantial increase of the fluorescence amplitudes, larger IBIs and a higher regularity of bursting episodes. These distinct traits of 'E-only' networks are a consequence of the absent firing–regulatory role of inhibition, inducing the neurons to fire until the excitatory neurotransmitter's pool is exhausted [139].

4.3.3 Power spectrum density during development

We observed that GABA switch could be well identified by analyzing the network average fluorescence signal in terms of the power spectrum density (PSD), and comparing the two network conditions along development. As shown in Fig. 4.2C, at DIV 5 and 6 the 'E-only' signal is below the 'E+I' one. The spectra for the 'E-only' case also scales with lower slopes, indicating a much different behavior of the network, which is either silent or very weak in activity. By DIV $7-8$ the spectral curves cross one another. Most likely inhibition has here a mixed role across the culture during the GABA switch event, leading to a similar spectral trend in the two network conditions. GABA is completely inhibitory at DIV 9 and maturer cultures, and the 'E-only' curves are now the ones with the highest energy compared to the 'E+I' case.

We also show in Fig. 4.3 the evolution of the PSD for three different batches and covering different ranges of the maturation process. We show only the 'E+I' data to emphasize developmental traits. The plots depict the general trend that the PSD moves upwards and with progressively higher slopes as the cultures matured and the bursts strengthened. At DIV 5, which conforms to the first occurrence of bursting activity for this batch, the corresponding PSD curve is distinctly above the noise level.

Overall, the shape of the PSD curves and their relative shift substantially changed during evolution, signaling the progressive increase in bursting amplitudes and frequency. After the second week *in vitro*, however, the cultures seemed to reach a stable phase, with all spectra showing similar amplitudes and effectively collapsing into one another. The PSD here fits well a power law behavior $P \sim f^{-\alpha}$, with $2.3 \lesssim \alpha \lesssim 2.8$. We note that we could not ascribe these values to particular traits of the cultures, and that further investigations are required. It may occur that, simply, these values reflect fluorescence dynamics at the PSD level, and therefore they may not convey any biophysical meaning.

4.3.4 Network disintegration

Here we investigated the deterioration in spontaneous activity when the excitatory connectivity of the network is progressively weakened by CNQX, an AMPA–glutamate receptor antagonist in excitatory neurons. In these experiments we fully blocked NMDA and $GABA_A$ receptors to restrict ourselves to the simplest scenario. Fig. 4.4A illustrates, for a mature culture at DIV 16, the evolution of the average 'E-only' spontaneous activity for increasing concentrations of CNQX. We also provide the activity data for the un-

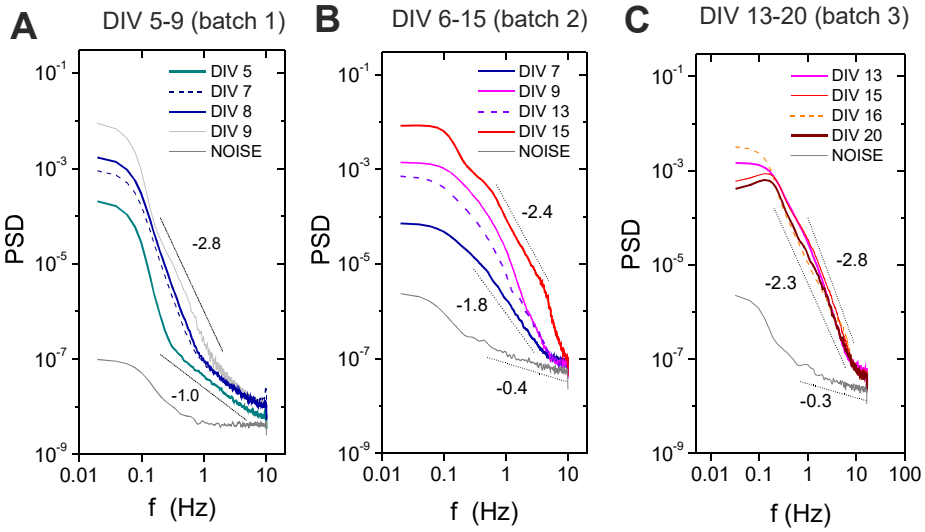

Figure 4.3: **Power spectrum density (PSD) during development for "E+I" networks.** The plots show the PSD evolution for three different culture batches (AC), covering in total about 3 weeks of development. The PSD gradually shifts upwards as the network matures, a feature that is accompanied by a tendency of the PSD to scale as a power law $P \sim f^{-\alpha}$. Mature cultures at DIV $\gtrsim$ 13 appear close to one another, suggesting that approximately after 2 weeks in in vitro cultures have reached a stable stage. The dotted black lines are a guide to the eye to illustrate the increasing values of along maturation.

perturbed, 'E+I' network for comparison. For [CNQX]= 0 (full connectivity strength), the network spontaneous activity showed the usual high–amplitude bursting behavior together with the large IBI characteristic of the dynamics solely driven by excitation. Small additions of CNQX mainly disrupted the average interburst interval, which increased remarkably as compared to the initial case. As the disintegration progressed, concentrations of [CNQX] $\gtrsim$ 200 nM modified both the fluorescence amplitude and the IBI. At extreme values of weakening, [CNQX] $\gtrsim$ 2000 nM, global network activity was rare or stopped completely.

While high concentrations of CNQX completely disrupted bursting, i.e., population–spanning coherent activity, we should note that uncorrelated, neuron–to–neuron activity was still present. Although these events were scarce, we systematically detected their presence in the studied cultures.

To investigate variability in culture age, we carried out the same disintegration protocol for cultures at different stages of maturation. As depicted in Fig. 4.4B, the bursting amplitudes in all these cases showed a similar trend. Initially, the blockade of inhibition in the transition from 'E+I' to 'E-only' connectivity ramped up the bursting amplitude to a maximum, but the subsequent gradual network disintegration leaded to a progressive decay in amplitudes until bursts disappeared altogether.

This general trend in the decay of bursting amplitudes did not hold for the bursting activity of the network, which was quantified as $1/\langle \text{IBI} \rangle$. As shown in Fig. 4.4C, although most of the cultures at DIV $\lesssim$ 13 exhibited a gradual decay in activity upon CNQX application, those cultures at DIV $\lesssim$ 14 displayed an increase in activity at specific

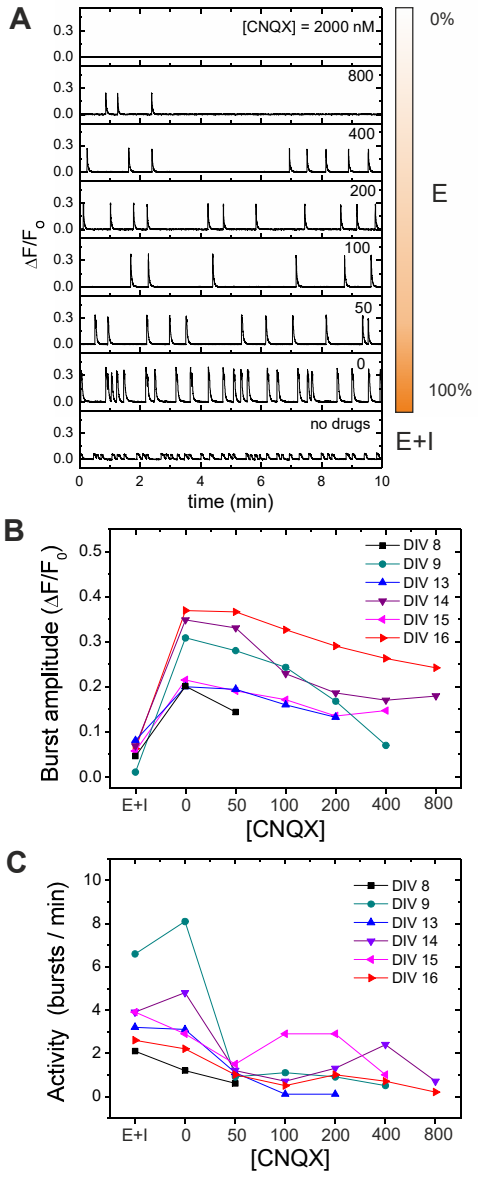

Figure 4.4: **Network disintegration through CNQX in an "E-only" network.** (A) Examples of spontaneous activity traces for 7 concentrations of the AMPA-excitatory antagonist CNQX, in a mature culture at DIV 16. During the disintegration protocol inhibitory synapses are silenced through application of 40 μM bicuculine. NMDA synapses are also blocked by 20 M APV. Fluorescence traces are compared with the unperturbed, "E+I" case. For [CNQX] = 0, activity is characterized by high amplitudes and large interbust intervals (IBIs) compared to the "E+I" case. As CNQX is applied, both the bursting amplitude and timing change, until all bursting activity disappears for large [CNQX]. The bar at the right side of the traces illustrates the relative strength of the excitatory connectivity. (B) Population–averaged bursting amplitudes during the disintegration process and for different culture ages, showing the steady decay in bursting amplitudes as CNQX increases. (C) Average network activity, quantified as $1/\langle IBI \rangle$, during disintegration. Young cultures decrease in activity and become silent at lower CNQX concentrations than maturer cultures. Maturer cultures show a mixed behavior in which activity initially decreases, to abruptly increase for some CNQX concentrations. The data for DIV 16 shown in panels (B) and (C) correspond to the exemplary traces of panel (A).

concentrations of CNQX. This erratic behavior seems indeed a distinct feature of mature cultures, and hints at the existence of network mechanisms in these cultures that promote activity, possibly to compensate the weakening in connectivity. Moreover, the fact that the increase in activity upon CNQX application occurs at different concentrations from one culture to another may indicate that development drives each culture to slightly different circuit architectures and connectivity strengths.

4.3.5 Power spectrum density during disintegration

The study of the disintegration process in terms of the PSD is shown in Fig. 4.5A for a culture at DIV 13. This figure portrays the general trend observed in most of the experiments. The PSD initially increased from the 'E+I' condition to the 'E-only' one due to the large amplitude of the bursts in the absence of inhibition. Next, the gradual

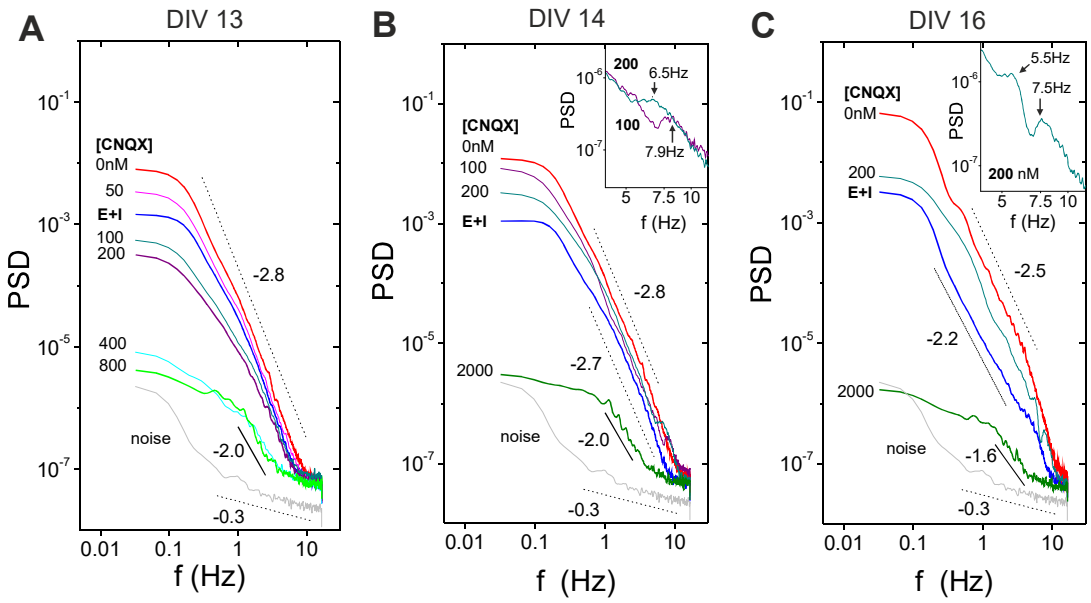

Figure 4.5: **Power spectrum density (PSD) in mature cultures during network disintegration through CNQX.** (A) General trend of the PSD for a culture at DIV 13. For [CNQX]= 0 the PSD exhibits its highest energy, which is associated to the high amplitude of the bursting episodes. The PSD energy gradually decreases with CNQX, and for [CNQX] $\gtrsim$ 800 nM bursting is absent and the PSD reveals temporal correlations arising from individual neuronal activity. PSD structure at this extreme concentrations is clearly different from the background noise. (B) A culture at DIV 14 showing peaks in the PSD at 7 and 8 Hz, which correspond, respectively, to [CNQX]= 200 and 400 nM. The inset provides a detail of the peaks. (C) A culture at DIV 16 showing the presence of two peaks, at 5.5 and 7.5 Hz, for [CNQX]= 200 nM. The inset shows a detail of the peaks.

addition of CNQX decreased the overall power as well as the PSD slope, concurrently with the progressive decay in bursts amplitudes. However, for large concentrations of CNQX –and rare or inexistent bursting– the PSD exhibited a scaling trend that is distinctly different from both the bursting behavior and the background noise. This scaling suggests that the PSD is capturing temporal correlations between neurons individual firing events. We note that these neuron–to–neuron interactions could not be detected in measurements with strongest connectivity strengths ([CNQX] $\lesssim$ 400 nM) due to the dominance of bursting behavior in network activity.

This general trend actually showed some interesting variations, illustrated in Figs. 4.5B-C. For the example at DIV 14 (Fig. 4.5B) we observed evidences of peaks in the PSD at frequencies $f \simeq$7-8 Hz. These peaks were particularly strong at CNQX concentrations of 100 and 200 nM. Remarkably, these concentrations also corresponded to the ones in which network activity increased upon disintegration. Indeed, we systematically observed a correlation between those experiments in which activity increased at specific values of CNQX and the presence of peaks in the PSD. Another example is provided for a culture at DIV 16 (Fig. 4.5C). In this case we observed two peaks (at around 5 and 7 Hz) for [CNQX]= 200 nM, the concentration at which network activity increased for this culture.

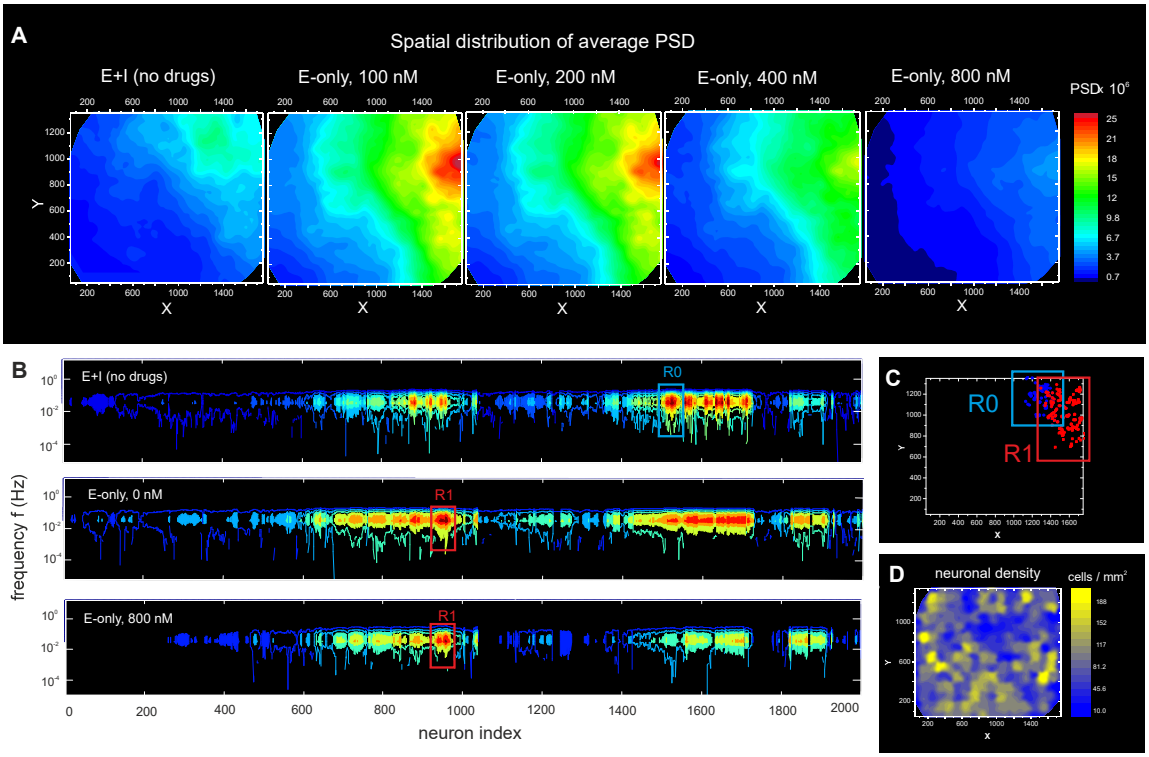

Figure 4.6: **Distribution of spectral energy across a culture during disintegration through CNQX.** Data corresponds to the experiment at DIV 16 shown in Fig. 4.5C. (A) For a given neuron, its PSD (averaged over frequencies) is displayed in the (x, y) space according to the spatial location of the neuron. The analysis is then extended to cover all the $\simeq$ 2000 monitored neurons in the field of view, finally providing a color map of the PSD distribution across the network. For the unperturbed, "E+I" network, the neurons with the highest PSD form a compact spot in the top-right corner of the field of view. The blockade of inhibition both shifts and increases the size of this "highly energetic" group of neurons. This region progressively reduces in size as CNQX is applied, but maintains a spatial cohesion up to the complete disintegration of the network. (B) Color coded PSD values as a function of the frequency f and the neuron index. Neurons are ordered by spatial proximity to highlight two groups of "highly energetic" neurons, termed R0 and R1, that maintain their strong energy and spatial cohesion during disintegration. (C) Spatial location of the R0 and R1 neuronal ensembles in the field of view. (D) Neuronal density map, calculated by counting the number of neurons in a square unit area 100 m wide. The high energetic groups R0 and R1 do not correlate with an area of the network particularly populated.

4.3.6 PSD and network spatial traits

To further explore the PSD potential in characterizing neuronal network features, we analyzed the spatial distribution of spectral energy across the culture. We first considered the average energy, i.e., the mean value of the PSD distribution. Fig. 4.6A shows the map of spectral energy for the PSD data of the culture at DIV 16 depicted in Fig. 4.6C. Spectral energy is shown for the 'E-only' condition along different stages of disintegration. The 'E+I' data is also provided for reference.

We note that, by considering the entire spectral energy, the PSD values are dominated by the low frequency contributions, i.e., those associated with the amplitude of the bursts. Hence, the map of spectral energy in these conditions effectively shows the distribution of bursting amplitudes across the network.

An interesting feature of the map shown in Fig. 4.6A is that the distribution of energy is inhomogeneous. Neurons with high bursting amplitudes are concentrated in the top–right corner of the field of view, and constitute by themselves a group of spatially close neurons that fire together with similar amplitudes, a quality that is maintained even at high levels of disintegration. We also note that, in the transition from 'E+I' to 'E-only' connectivity, the spatial location of the 'highly energetic' neurons substantially changes, evidencing that the balance between excitation and inhibition plays an important role in shaping network's local dynamical features.

The physical closeness of these 'highly energetic' neurons is emphasized in Fig. 4.6B, which shows the spectral energy as a function of the neuron index, with neurons ordered by spatial proximity. The plot marks two particularly relevant communities, labeled R0 and R1, whose containing neurons maintain a high spectral energy up to complete disintegration of the network. The location of these two groups in the monitored region of the culture is shown in Fig. 4.6C. We remark that we monitor only a small region of the culture. Therefore, these groups of neurons may also share some traits with (or their dynamics influenced by) other neurons outside the field of view. For sake of discussion, we also provide in Fig. 4.6D the neuronal density map, which highlights those regions in the field of view that are more densely populated. A direct comparison with Fig. 4.6C shows that the two communities R0 and R1 of energetic neurons do not correlate with particularly dense areas, revealing the importance of non–local phenomena (both in circuitry and dynamics) in shaping specific neuronal activity traits.

We carried out this spatial analysis with all the monitored cultures, and covering from very young (DIV $5-6$) to mature (DIV $\lesssim 20$) cultures. In general we observed that young cultures up to DIV $\lesssim 10$ displayed a rather homogeneous spatial disintegration, with no identifiable 'highly energetic' communities. However, for cultures at DIV 14 and older we systematically observed an inhomogeneous disintegration combined with the existence of communities. The location of these communities varied from culture to culture, and evinces that mature cultures break the initial network isotropy and develop slightly different connectivity layouts.

4.3.7 PSD and coherent neuronal oscillations

Figs. 4.7B-C introduced the observation that some cultures exhibited a PSD characterized by the presence of peaks at frequencies f in the range $5-10$ Hz. These peaks were stronger at specific concentrations of CNQX, suggesting the emergence —or reinforcement— of

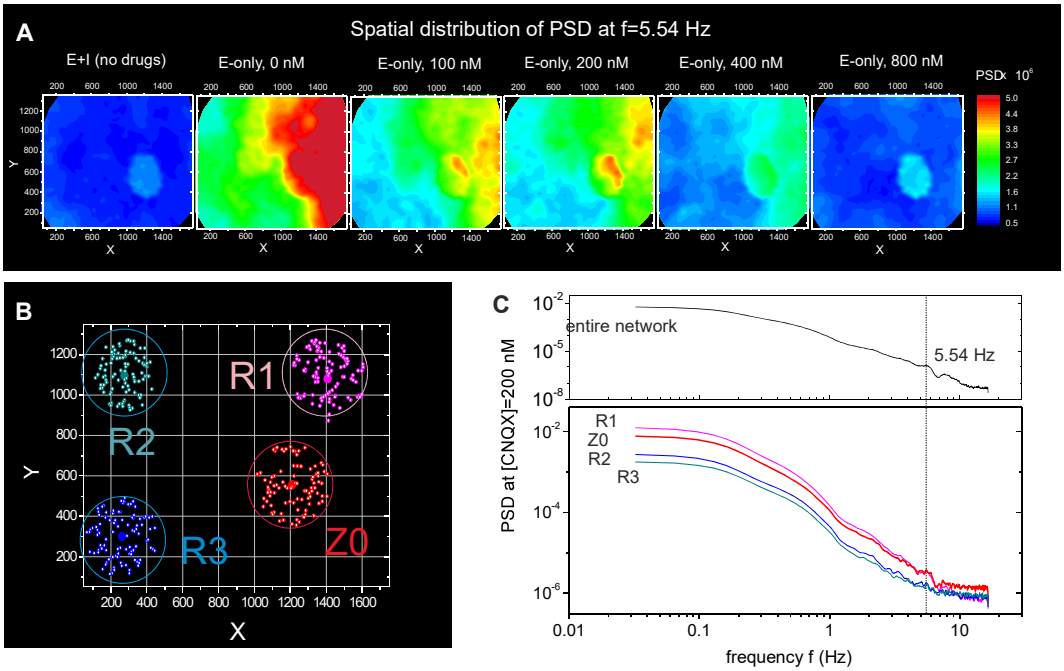

Figure 4.7: **Emergence of synchronous oscillations during network disintegration through CNQX.** Data corresponds to the experiment at DIV 16 shown in Fig. 4.5C. (A) Spatial distribution of the PSD at a frequency of 5.54 Hz and for different connectivity conditions, "E+I" and "E-only" with gradual weakening. The presence of a compact spot at the center–right of the PSD map highlights a neuronal community (termed Z0) that synchronously oscillates at this frequency. Oscillations with strong amplitude also appear along the right edge. For [CNQX] = 200 nM the Z0 community displays the highest difference in energy compared to the neighboring regions. (B) Location of 4 different communities. For each community, the central dot marks the position of a selected neuron whose power spectrum is averaged over all the 100 closest neurons (white dots within a circle). (C) PSD of the four communities for the "E-only" connectivity at 200 nM. The community Z0 and R1 show a clear peak in the PSD at f = 5.54 Hz. The PSD at this frequency is also higher in these two communities compared to the others.

collective oscillatory modes in the network for a precise coupling strength between neurons.

To further investigate these oscillatory modes, we considered again the experiment at DIV 16 (whose PSD is shown in Fig. 4.5C and Fig. 4.6) and took special attention to the PSD properties at the frequency $f = 5.54$ Hz. At this value, a peak is well identifiable at [CNQX]= 200 nM. Fig. 4.7A shows the spatial distribution of energy at this frequency for the two network conditions, 'E+I' and 'E-only', as well as along gradual disintegration through CNQX.

We first note the remarkable contrast in the spatial distribution of energy at $f = 5.54$ Hz between the 'E+I' and 'E-only' conditions. The former shows a compact spot of energetically similar neurons, while the latter displays an almost symmetric coverage, with a low energy region on the left that contrasts with a high energy one on the right. Again, these distinct maps reveal the importance of inhibition in shaping network dynamics.

Second, the study also reveals the evolution of this highly energetic spot throughout weakening. Indeed, for the 'E+I' condition, the difference in energies between this spot and the neighboring areas is relatively small, by 10%. This small difference actually made difficult the detection of this spot in the PSD of Fig. 4.7C. As the connectivity of the network shifts to the 'E-only' condition and CNQX is applied, we observe that the difference between the energy in this spot and its neighborhood ramps up to about 45% at [CNQX]= 200 nM, a difference that progressively decreases as the disintegration accentuates, although the compactness of the spot is well maintained.

We additionally investigated in more detail the differences in the PSD between the observed compact spot and the neighboring areas. For simplicity, we restricted the analysis to the 'E-only' connectivity condition at [CNQX]= 200 nM weakening. Fig. 4.7B depicts four investigated communities. In each community we selected a central neuron and averaged its PSD with the 100 closest neighbors (white dots within a circle in Fig. 4.7B). We label as Z0 the community that corresponds to the 'spot' mentioned above, and by R1–R3 the rest of communities.

The corresponding PSD distributions are shown in Fig. 4.7C together with the average over the entire network for clarity. We first note that the Z0 and R1 communities have a much higher energy than the others, and that both are markedly characterized by a peak in the PSD at 5.54 Hz. This peak is difficult to observe in the other communities. By comparing these results with the network–averaged PSD, we conclude that both Z0 and R1 are the main contributors to the observed peak at 5.54 Hz, and that Z0 is the community that remains highly coupled throughout disintegration.

To gain insight into the origin of these synchronous oscillations, we also carried out an analysis in which we investigated the link between the oscillations and the bursts themselves. As shown in Fig. 4.8A, we first separated the original fluorescence signal into two contributions, one containing the low–frequency modulation associated to the shape of the bursts, and another one containing the rest of the signal. The corresponding PSD analysis (Fig. 4.8B) revealed that the shape of the bursts dominates the behavior of the spectral curves and therefore masks the dynamics of the network. On the contrary, the PSD of the filtered data retains both the dynamical traits of the network and completely captures the oscillatory behavior. We also investigated the properties of the signal in between bursting episodes, and excluded any contribution of the background signal to the presence of the oscillations. We therefore confirmed that the oscillations occurred

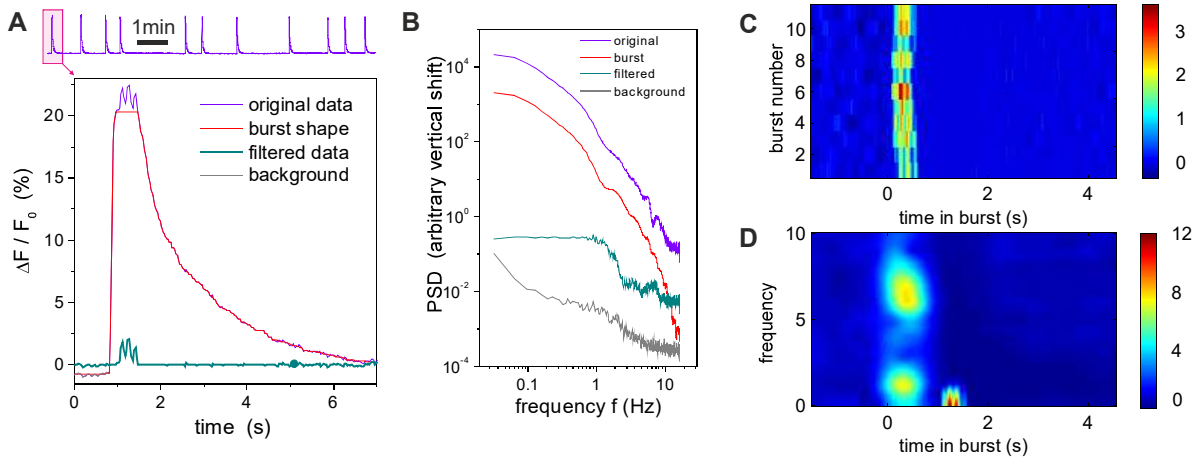

Figure 4.8: **Oscillations originate in the bursts.** Data corresponds to the experiment at DIV 16 for [CNQX] = 200 nM. (A) The top trace depicts the average fluorescence time series of a group of 100 bursting neurons that constitute the Z 0 community. The first burst of this series and its manipulation is shown in detail in the bottom panel. The blue trace corresponds to the original fluorescence signal, and reveals a well pronounced oscillatory behavior at the peak of bursting. The original signal is separated into two contributions: the burst shape (red) and the oscillatory signal (green). Burst shape is estimated by applying a median filter with length L = 33 frames (1 sec); the resulting trace follows the slow dynamics of the burst while the oscillatory signal keeps the higher frequency components. Activity out of the busting episodes (background signal, gray trace) is computed by connecting the periods in between bursting events. (B) The spectral analysis of the resulting signals reveals that the burst trace dominates the shape of the power spectrum, and actually keeps the greatest fraction of energy from the original signal. The oscillatory component has a much lower energy but retains network activity correlations (in the range 1 – 5 Hz approximately) as well as the oscillations at 5.5 and 7.5 Hz. The signal out from the bursting episodes does not exhibit any oscillatory components. Curves are vertically shifted a factor 50 from one another (and using the background signal as reference) to better highlight the different shapes of the power spectrum. (C) Fluorescence trace of the oscillatory signal for all the 11 bursting episodes of the recording, locked to the initiation of each episode (dashed white line), showing that oscillations originate within the bursts themselves. (D) Their corresponding averaged Gabor transform, picturing the presence of an oscillation in the 5 –7 Hz range that only appears once the bursts have reached their maximum amplitude and start the decaying phase.

concurrently with the bursts themselves. This is highlighted in Fig. 4.8C, which compares the traces of the filtered signal along the different bursts. In all cases, the onset of the oscillatory behavior practically coincides with the beginning of bursting ($t = 0$ s in the plots). The frequency analysis of these traces (averaged over all the bursting episodes) is shown in Fig. 4.8D, revealing a peak at $5 - 7$ Hz, i.e., the range of the initially described characteristic frequencies.

We extended all the above analyses to other cultures characterized by peaks in the PSD. We observed qualitatively similar traits, i.e., the existence of communities with markedly strong synchronous oscillations, the presence of specific CNQX concentrations at which the strength of the oscillatory mode was maximum, and the link between oscillations and bursts. The frequencies of the oscillatory modes as well as their spatial distribution significantly varied among cultures and developmental ages, emphasizing again the formation of specific network features during maturation.

4.3.8 Unhealthy cultures

Fig. 4.5 showed that the PSD could capture, in a regime of suppressed bursting, temporal correlations among the firing patterns of individual neurons. Such a burst elimination was achieved by significantly reducing neuronal coupling through CNQX. Based on this observation, we hypothesized that such a network–spanning affectation could also occur in conditions where the health of the culture was compromised. To test such a possibility, we carried out a simple test in which we left the cultures to degrade, at the end of a normal experiment, by leaving them in the recording system for several hours. Cultures did not contain any connectivity blockers, so the loss of activity was ascribed to the deterioration of the network.

Photo–damage in such an experiment induced neuronal death and severe disruption in the normal neuronal network behavior, which was evidenced by the extinction of bursting episodes. However, close inspection of the recordings showed that local activity, in the form of individual firing or groups of persistently active neurons, was still identifiable. Fig. 4.9A shows traces of network–averaged fluorescence to compare the healthy and unhealthy states. We also show the fluorescence signal corresponding to the noise of the camera.

The corresponding PSDs of these measurements are shown in Fig. 4.9B. Remarkably, the PSD for the deteriorated, unhealthy culture displays a neat scaling that is not masked by the bursts structure. Also, the PSD is qualitatively similar in shape as the one for healthy cultures and [CNQX]= 800 nM. Interestingly, we measured clearly different exponents. For the healthy and CNQX–drugged networks we consistently measured exponents of $\alpha \simeq 2.0$, while for the unhealthy experiments we obtained $\alpha \simeq 3.0$. Such a different values reveal different temporal correlations or dynamical modes in the network, and hints at the potential of PSD analysis to quantify the health of neuronal networks.

4.4 Discussion

In these studies we used two major approaches to access different neuronal circuitries, namely the monitoring of network development along 3 weeks and its controlled disintegration through application of CNQX. In both cases we observed distinct features in

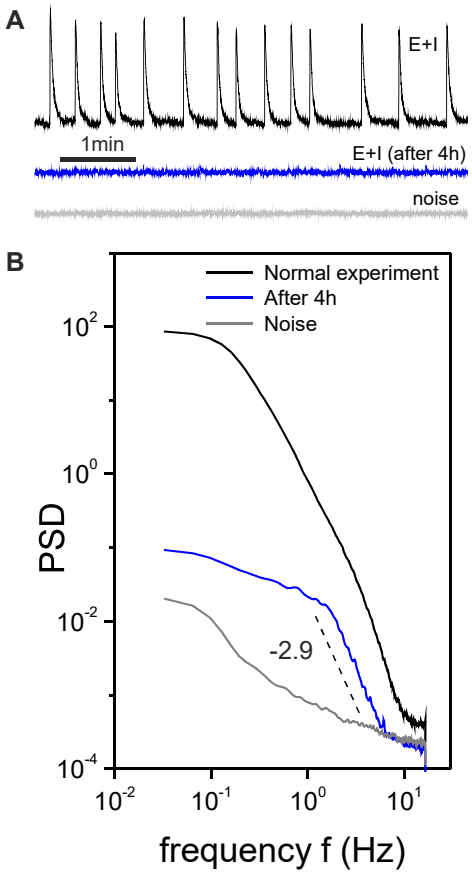

Figure 4.9: **Unhealthy cultures.** (A) Traces of fluorescence spontaneous activity in a "E+I" culture recoded in healthy (top) and unhealthy (center) conditions. The unhealthy state was induced by maintaining the culture under continuous light exposure for 4 h, which resulted in the death of several neurons. The unhealthy network showed individual neuronal firing but was deprived of bursting activity. The bottom trace shows the noise of the recording system. (B) Corresponding PSD curves. The unhealthy state shows a trend very different from both the healthy state and the noise, with a scaling at high frequencies that may arise from temporal correlations between individual neuronal firings.

the shape of the fluorescence signal and its associated PSD. The PSD could capture relevant events during development, revealed locality features in the neuronal network, and highlighted the presence of synchronous oscillatory modes within neuronal communities.

Flourescence signal and PSD

The recorded fluorescence signal displayed different traits depending on both the age of the neuronal culture and its connectivity strength. First, young cultures under DIV $\lesssim 5$ did not display bursts, and the network dynamics was characterized by sparse individual neuronal firings of very low amplitude. We detected the presence of these events in the histograms of fluorescence amplitude (Fig. 4.2B), which deviate from Gaussian distributions at high fluorescence values. However, the PSD curves corresponding to these 'young' traces were similar to the ones obtained by measuring the noise of the camera.

Hence, in young cultures and the context of fluorescence imaging, one cannot use the power spectrum to quantify temporal correlations between neurons or other dynamical features.

Second, cultures at DIV $\gtrsim 6$ did show bursts, with a structure (amplitude, width and interburst timing) that depended on maturation. The corresponding PSDs reflected such variations, and we could detect GABA switch as well as the relative strength between excitation and inhibition by comparing the PSD curves of the 'E+I' and 'E-only' conditions (Fig. 4.2). Also, the rise in bursting amplitudes during development was reflected in the PSD by a gradual increase in the average power (Fig. 4.3). The PSD curves for mature cultures showed a rather good collapse with a slope $\alpha \gtrsim 2.5$, indicating the advent of a more stable network state. Despite the variations from culture to culture, such a trend was systematic. Hence, in principle we could 'guess' the developmental stage of a culture, and even some coarse properties, based in the average energy and slope of the PSD.

We must note, however, that the shape of the PSD arises from a complex combination of factors, including the fast jump in fluorescence at the beginning of bursting, the width of the bursts, the slow decay of fluorescence back to the resting state, and the timing between burst. One would therefore need a detailed exploration of these different parameters to fully understand the information that the PSD can provide. Given the variety of bursting regimes that a neuronal culture can convey [728, 742, 741], such a exploration is a considerable endeavor.

And, third, we observed distinct features in the PSD between the development of the network and its disintegration through CNQX. The former includes the growth and strengthening of connections, both locally and globally, and thus the overall network dynamics constantly evolve. The latter weakens homogeneously the excitatory connectivity in the network, leading to essentially a similar network dynamics with progressively reduced bursting. Hence, young cultures are not equivalent to fully disintegrated mature ones. The two experimental approaches are therefore complementary and reveal distinct features. Indeed, a remarkable observation in the experiments with CNQX is that, for concentrations that led to almost no bursting at [CNQX] between 800 and 2000 nM, we observed significant individual neuronal firing across the culture. Given the maturation of the network, these firings were of sufficient strength to exceed the noise of the system. Only in these conditions the PSD followed a scaling that we believe was capturing correlations between neurons (Fig. 4.5).

The investigation of temporal correlations from PSD analyses is indeed a powerful concept since it may unveil dynamical traits of the network, e.g., in the form of synaptic inputs or intrinsic neuronal interactions[704, 188, 210]. The significance of the scaling by itself in our data, as well as the information that these correlations provide about the interplay activity–connectivity in the network, needs detailed investigation. Notably, the observation that healthy and unhealthy cultures exhibit different scaling exponents suggest that such studies could provide a basis to describe pathological or deteriorated cultures from the analysis of the PSD. In this context, an additional experimental tool that would provide valuable insight is the incorporation of connectivity guidance in the culture substrate, for instance in the form of biochemical fixation or physical trapping [204, 754]. Dynamics in such 'patterned cultures' substantially differ from standard ones due to the dictated connectivity [349, 705], and would possibly give rise to different temporal correlations.

Development and network traits

Several works in the literature have investigated the emergence of network–spanning bursting episodes during development. Consistently with our work, bursts were reported to appear by DIV $5-6$ [371, 528, 742], showing a low amplitude and irregular timing. These studies used micro–electrode arrays (MEAs) as activity–measuring technique, and also revealed that the activity contained both individual firing events and bursts. As said before, this individual spiking was also present in maturer networks (DIV $\simeq 10$ and older), and we actually used the valuable information that they provide to reconstruct neuronal connectivity in the context of Transfer Entropy [676], as discussed in Chapter 6.

Mature cultures exhibited stronger and more bursting as a consequence of the progressive maturation of synapses and the increase in their number [508, 371, 528]. Interestingly, we observed a stabilization in bursting amplitudes as well as a decrease in bursting firing frequency by DIV $18-20$ (Figs. 4.1D and E). These results are consistent with the studies of Van Pelt *et al.* [724, 728] who reported that, in cortical cultures similar to ours, burst duration and firing amplitudes reached maximum values by DIV 18, to later stabilize or decrease as network evolved further.

The different spatial analyses of the PSD (Figs. 4.6 and 4.7) for mature cultures during network disintegration revealed strong inhomogeneities in the distribution of spectral energies, with compact spots of high energy. Spectral energy is directly linked to the amplitude of the bursts which, in turn, is related to the number of the elicited action potentials [609]. If we assume that neurons firing with large bursting amplitudes have a higher input connectivity, then the combination of strong firing and spatial closeness identifies neuronal communities that are highly interconnected. The cohesion within a community is maintained up to complete disintegration of the network. Chiappalone *et al.* [134] showed that spatially close neurons are progressively more functionally connected as the network matures; and Soriano *et al.* [660] showed that, in CNQX disintegration experiments similar to ours, groups of neurons spatially close maintained their interconnectivity and collective firing when stimulated electrically.

Hence, we ascribe this spatial inhomogeneities in the PSD to the formation of highly conserved topological communities that maintain unique local features despite changes in global network dynamics. We indeed hypothesize that the communities observed by Chiappalone *et al.* [134] are the same as our groups of 'highly energetic neurons'.

High frequency synchronous oscillations

The PSD curves upon CNQX disintegration revealed the existence of high–frequency oscillations in the range $5-10$ Hz, which were remarkably strong and spatially localized at particular concentrations of CNQX. These oscillations were observed solely in mature cultures and, in general, we detected them both in the 'E+I' and 'E-only' conditions. A detailed study of the fluorescence traces revealed that the oscillatory modes originated from activity within the bursts themselves. Interestingly, Shein Idelson *et al.* [349] reported oscillations in small neuronal circuits formed by compact cell aggregates. They observed collective oscillatory modes within network bursts in the range $25-100$ Hz, and the authors associated them to synchronous oscillations during the decaying phase of the network burst.

Our observed oscillations are markedly strong in localized communities, suggesting that the oscillations emerge as a result of recurrent activity within these communities. We found puzzling, however, the observation that the CNQX concentrations at which the oscillations displayed the highest amplitude coincided with sudden increases in global network dynamics. We suggest that the network may activate correction mechanisms at a critical connectivity weakening to revert the deterioration of activity. These mechanisms may arise from local reinforcements in synaptic strength or connectivity, as well as from changes in the excitability of the neurons themselves.

It may also occur that these communities of oscillatory activity play a role in the network, for instance as centers for the initiation of activity, as suggested by Orlandi *et al.* [530] through the framework of 'noise focusing'. In this framework, neuronal architecture is responsible for amplifying background activity, which propagates towards specific foci or basins of attraction that ultimately initiate the bursts. Although along this thesis we made efforts to relate these foci of burst initiation with our oscillatory communities, experiments proved difficult and not sufficiently conclusive.

Finally, we remark that these oscillations seem to be inexistent in young cultures (or too weak to be detected), which strengthens the argument that strong coupling within the cell community is required for their generation. An aspect that requires investigation, however, and that could be completed along the thesis, is the set of parameters that tune the frequency of the oscillations. A possibility that we explored was to change the relative weight between AMPA, NMDA and GABA receptors. Again, our results were not sufficiently strong to support any conclusions. However, Shein Idelson *et al.* [349] showed that the oscillations disappeared altogether when GABA was fully blocked, which was not observed in our case.

Chapter 5

ANALYSIS AND RESULTS II: Nonlinear Dynamics

In this Chapter we introduce a brief overview of nonlinear time series analysis via symbolic dynamics in physiological systems. The phase–space formalism with embedding techniques is used to study the problem of the reconstruction of the underlying dynamics of our experimental neuronal data. We first treat the method of derivatives, the method of delays and the global principal components decomposition. Next, recurrence analysis techniques will be proposed with the aim of characterizing the different dynamical patterns that emerge in the state space and their topological regularities. Finally, a nonlinearity test using Monte Carlo techniques will be developed. All these analyses will be carried out in the experimental framework described in Chapter 2. The obtained results will be contrasted with the numerical simulation of different synthetic networks referenced in Chapter 3.

5.1 Statement of the problem

Neuronal networks exhibit such a rich wiring architecture and inherent nonlinear dynamics that shape one of the most prominent examples of complex systems. Surprisingly, when neuronal tissues are dissociated and left to grow on a glass cover slip, their neurons self–organize to form a new network characterized by rich spontaneous activity and a non–trivial connectivity. How single neurons self–organize to form a complex functional network is a problem that is still not fully understood. And the problem is very rich indeed. The understanding of causal interactions at the population level requires the comprehension of the coupling and intrinsic dynamics of the constituting neurons. Such a *dissection* effort can reveal information about the complexity of the system, its governing parameters, its sensitivity to disturbances, and its closeness to a bifurcation point [673]. The aim of this Chapter is to elucidate some of these aspects using techniques from nonlinear time series analysis.

We framed our study in data embedding techniques [755]. However, since the dynamic behavior of a single neuron is already well characterized [324], we focused on the description of the dynamic behavior of neuronal populations at a mesoscale level. We note that our approach is *top down*, i.e. we aim at extracting details of the system from its overall behavior. Thus, in our approach we used the global signal of the network

—and that reflects the average activity of a large population of neurons— to pinpoint the behavior of individual neurons. We used as global signal the average fluorescence signal of the network.

Along this Chapter, we will proceed as follows. First, we will treat the quest of using solely *one* time series —the experimental fluorescence trace— to reconstruct the underlying dynamics of the neuronal population. For this purpose, state space reconstruction (SSR) methods will be exposed [537, 689, 611, 610, 101] and, taking into account our experimental context, the most appropriate method will be chosen [689, 611, 610]. Second, we will focus on characterizing the objects that emerged from the state space and their internal recurrences, and using recurrence plots (RPs) and recurrence quantification analysis (RQA) as main tools. Third, we will show different test to validate the results obtained for SSR, RPs and RQA. And, fourth, we will integrate the above methodologies and analyses s explained to compare experimental data with synthetic, simulated networks.

The first endeavor, the reconstruction problem from only one time series is simply reduced, consists in practical terms in the determination of two characteristic parameters, namely the *embedding dimension* m and the *time delay* δ. The former is the dimension of the system and renders the number of independent variables needed to described the population dynamics. The latter parameter entails the existence of a rule–based behavior in which the new state of the system is a function of one or more previous states. Hence, the functional dependence of a new state with one or more previous states, leads to the prominent problem of determining the number of previous states that must be considered. Conceptually, these previous states can be viewed as a time distance (or temporal windows), and is precisely the information that δ provides. To be more precise, δ captures the maximal temporal window that includes all events causally connected. It is worth noticing that the hallmark of nonlinear structure involves a short–term predictability time distance in the data set which is often not obvious to extract from a simple representation in the temporal or spectral domain. Additionally, $\delta \to 0$ for linear dynamics since any time window is causally connected, whereas in systems with uncorrelated dynamics $\delta \to 0$, i.e. its distance is of length one. We recall as well as that, for a phenomenon emerging from linear stochastic —or Gaussian— mechanisms, its power spectrum is the only information required to understand the system. However, for a phenomenon emerging from a nonlinear deterministic dynamical system, it is necessary to understand the system in greater detail in order to predict and control it [100]. Indeed, nonlinearity is often the root of complex behavior. Moreover, some processes can often be perceived as erratic or random in a one–dimensional time series representation, whilst hidden rhythms can be detected in a m–dimensional representation. Indeed, these specific patterns can be visible by plotting each data point as a function of its predecessor, giving rise to the SSR concept and therefore allowing for a better study of the underling population dynamic. As we will see, this representation, usually termed phase portrait, is a particularly simple application of time delay embedding and will be the starting point of our analysis. Finally, for completeness, once the SSR is carried out, the next step will be to assess the goodness of the reconstruction. This will entail analyzing under which conditions this 'new' reconstruction of the dynamics preserves the topological properties respect to the 'real' one. We note that the verification of correct SSR is of utmost importance to deliver acceptable future outcomes. However, this will be not an easy

task, especially when working with short and noisy experimental time series.

The second endeavor, the objects and their recurrences emerging from the space state, is not going to be a piece of cake, either. Indeed, as we have previously seen, physiological systems are presented to us as an open dissipative system that is constantly challenged and modulated by noise, where recurrent dynamical patterns are interposed with periods of stochasticity (pauses). Indeed, physiological signals rarely present pure dynamical patterns. Quite the contrary, they are irregular signals, composed of hidden patterns and deterministic structure, with different overlapping dynamics. Hence, along this part of the Chapter, we will use recurrence plots (RPs) [204] and recurrence quantification analysis (RQA) [779, 750, 471] to characterize the different dynamics, breaking them down into distinct behaviors. The selection of these nonlinear tools was decided for different reasons. Firstly, we aimed to complete the results obtained in the Chapter 4, and RPs and RQA offer us means to characterize the dynamical structure of time series both qualitatively and quantitatively [204]. Secondly, RPs and RQA are very useful tools to detect dynamical changes, offering us the ability to locate bifurcation behaviors and transients in the dynamical system without the need of *a priori* assumptions regarding the underling equations of motion [714, 471]. Thirdly, and more importantly in our experimental context, their usage is further advised when one works with short and noisy experimental signals [776].

Conceptually, RPs and RQA are based on the following guiding principles and procedures. Once the SSR in inferred, with a view of the study of internal recurrence, we will calculate the distance matrix between all the states of SSR (*target* states) and their respective *neighbors*. As we shall see, the definition of the term neighbor will be of outmost importance. Next, we will analyze the different recurrent pattern that emerged in this matrix, and both in a qualitative and quantitative ways. In particular, three different patterns will be studied: (i) single points, which characterize stochastic dynamics; (ii) diagonal lines, which represent segments of parallel orbits; and (iii) vertical and horizontal lines, which typically reflect sporadic and abrupt dynamics. The quantitative analysis of the distributions of these patterns will allow us to define different statistics and, in turn, the underling dynamics by specifying the degree of determinism (%DET), the degree of randomness (%RAND), the degree of laminarity (%LAM) and the trapping time (%TT) of our dynamical system, among others. We note that our goal is to determine what kind of dynamics presents our population, for instance is the system is periodic, quasi–periodic or chaotic. Although this issue seems straightforward to answer, in practical terms we cannot exactly quantify it in a precise and detailed manner. Indeed, by using experimental constituted by short and noisy signals, this task was not easy.

The third endeavor, validation tests for SSR, RPs and RQA, will make emphasis on the validity and range of applicability of the analyses. In particular, we will keep a careful eye on determining the degree of nonlinearity that these signals present and the underling dynamics, and to put the analyses carried out in Chapter 4 in the context of the present ones.

The fourth and final endeavor, comparison between experiments and simulations, will integrate all the described methodologies and analyses to explore and constrast the experimental and simulated networks.

Finally, it bears noting that the first three conceptual and methodological endeavors are presented next in a summarized form in order to make them clearer for a broad

audience. For an extensive analysis, the interested reader can consult the referential books in nonlinear time series analysis of H.Tong [707], C.Diks[192], H.Kantz and T.Schreiber [374], M.Small [650] and C Hafner [303], inter alia.

From a computational perspective, to perform nonlinear time series analysis we used the TISEAN software package [314, 5] combined with the TSTOOL software package developed at Göttingen University [6] and implemented in Matlab 2013b. C++ MEX–files were pre–complied with g++-4.9.2-10 compiler. The visualization of Recurrence Plots was carried out with an own Matlab 2013b script. To compute Recurrence Quantification Analysis, a commandline of Unix by Nobert Marwan was used [7]. In Annex I we attach an illustrative small script to perform the analyses.

5.2 State Space Reconstruction

We are interested in studying the dynamics and evolution of a phenomenon where n–variables interact determining a specific state $\vec{x}(t_i) = (x_1(t_i), x_2(t_i), ..., x_n(t_i))$ in the phase space. This phenomenon will be described by a set of differential equations whose solution is the evolution function that determines the behavior of the system along time. However, *a priori*, these equations and all the n-variables are unknown.

From an experimental context, one can only perform partial observations of the phenomenon, with access to few physical observables that are not necessarily characteristic variables of the system. Generally, these observables can be written as scalar time series, $\{s(t_i), i = 1, 2, ..., P\}$, with P the recording time. Data is equally spaced according to a sampling interval Δt. In our particular case, this time series corresponds to fluorescence traces, either from an individual j–neuron ($\{f_j(t_i), i = 1, 2, ..., P\}$) or from a population ($\{F(t_i), i = 1, 2, ..., P\}$). With the aim of simplifying the notation, hereinafter we will simply use the notation $\{f(t_i), i = 1, 2, ..., T\}$. Our goal consists in the reconstruction of the underlying dynamics of the system in a new state space with the sole information of the experimental time series, and keeping the topological properties of the system.

According to the Taken's theorem [689], based on the embedding theorem of Whitney [755], a correct reconstruction of the underlying dynamic is possible using only this scalar time series. Indeed, this physical observable, even if is not characteristic of the system, could be related to coordinates of the original state space and, therefore, to characteristic n-variables of the system, as follows:

$$\vec{x}(t_i) = \mathbf{h}(f(t_i)), \tag{5.1}$$

where $\mathbf{h}$ is an unknown nonlinear generic function, termed *measurement function* in the literature [121]. Then, the SSR problem consists in recreating states in this new space, termed *pseudo–state space* or *embedding space*, and where the only information available is contained in this time series. In essence, this methodology is based in considering the observed time series as a projection (an output) of the real underlying dynamics of the system. The basic idea lies in assessing whether the past and the future values of a temporal series contain sufficient information of non–observable variables. The fact that all deterministic structures lead to the predictability in the data set can be harnessed to reconstruct the dynamics by plotting each data point as a function of its predecessor.

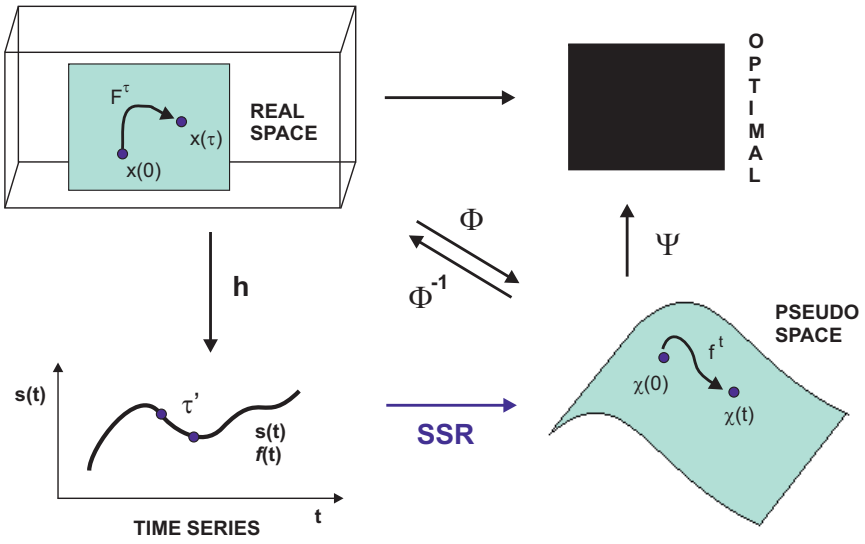

Figure 5.1: **The reconstruction problem.** The true dynamical system F, its states $\vec{x}(t) = (x_1(t), x_2(t), ..., x_n(t))$ and the measurement function **h** are inaccessible, and are locked in a black box. The only accessible information is the time series $f(t) = \{f(t_1), f(t_2), ..., f(t_P)\}$ corresponding to a fluorescence recording containing P points, separated by a sampling interval Δt. The reconstructed map Φ is an *embedding* when it is possible to build a smooth, one–to–one coordinate transformation Φ:$\{\mathbb{X} \to \mathbb{Y}\}$ with its corresponding smooth inverse Φ^{-1}.

In this sense, the information of past and future contained in the time series can be encapsulated in a m-dimensional state vector. As we will see below, all the methods for state space reconstruction are based on this fundamental concept. A schematic outline of this problem is shown in Fig. 5.1.

Once the underlying dynamics is reconstructed, a second crucial aspect to be considered is whether the reconstructed objects in this new pseudo–space preserves the topological properties of to the original ones. According to Takens' theorem [689, 611], a faithful reconstruction is guaranteed as long as the embedding dimension is greater than twice the topological dimension d, i.e. $m \geq 2d + 1$, where m is the dimension of embedding. Then, it has been argued [464, 689] that for a sufficiently large embedding dimension, the attractor of the underlying original system has a smooth, one–to–one correspondence with the reconstructed one. Therefore, in this theoretical condition, important topological properties such as the Liapunov exponent, KS entropy, eigenvalues of fixed points, the fractal dimension of an attractor and correlation dimension are kept invariants.

Unfortunately, Takens' theorem assumes the availability of an infinite amount of noise–free data. In signal processing language, this means that the data has infinite precision, is not affected by noise and is not band–limited. In real experiments, with noisy and finite precision datasets, such reconstruction is not straightforward, and one needs to proceed carefully in its implementation.

Three standard methods have been developed for SSR, namely the Method of Derivatives (MD) [537], the Method of Delays (MOD) [689, 611, 610], and the Method of Singular Value Descomposition (SVD), also known as Karhunen–Loève Decomposition

or Principal Component Analysis (PCA) [101]. A relationship between these three standard methods is given by Gibson *et al.* [271] and, actually, these three methods are related through a linear transformation. In addition, and directly related to our experimental context, Gibson *et al.* provide a theoretical guideline for choosing the optimal conditions for a correct reconstruction when the methods are affect by noise. In order to render the analysis in a more comprehensible way, in the following sections we explain first all the general aspects shared by the different methods, to next describe each method in detail and, finally, treat the analysis of our experimental signals. We note that the strengths and drawbacks of each method must be put in context of our experimental conditions, in particular the poor signal–to–noise ratio (SNR) and the limited sampling rate of the acquired data.

We can illustrate the difficulty of the problem at hand by describing first a useful and widely used alternative for a two–dimensional reconstruction, the Hilbert Transform [336]. In Fig. 5.2 we provide examples of a two–dimensional phase portrait corresponding to spontaneous activity data of typical mature neuronal culture (DIV=16) that contains 2000 neurons. SSR was constructed by pivoting the respective field signals $f(t)$ of 10 min recordings with a frame rate of 50 fps ($T \sim 3 \times 10^4$ samples). The left plot shows the evolution of the [E+I] network, i.e. without the application of any drugs. The right plot depicts the [E] network (inhibition blocked) and along different stages of connectivity weakening through CNQX. Both plots show that an unfolding of the dynamics can be easily and quickly pictured by representing the Hilbert Transform $|H(f)|$ as a function of the orginal series $f(t)$. It is remarkable to point out that recurrences can be regarded as rotations in the physical space. Then, in this sense, the instantaneous frequency [337] of the rotations (phase shift of $\pi/2$) given by the Hilbert Transform, contains much more informations that the Fourier or wavelet frequency components. Indeed, the Hilbert Transform provides a decomposition into a finite and often small number of 'intrinsic mode functions' which yield this instantaneous frequencies. This local analysis for characteristic time scales in the data gives sharp identifications of embedded structures, and is particularly suitable for the study of non–stationary time series. Hence, this methodology provides an efficient and adaptive computational method that is very useful to detect abrupt changes in dynamics, in particular, in the case of nonlinear structures. Unfortunately, there is no a higher–dimensional extension, i.e. this method only provides two–dimensional phase diagrams. Since in general we lack knowledge of the dimensionality of our system, we have to advance towards more general alternatives.

In the following the describe in detail the three standard methods for SSR analysis.

5.2.1 Method of Derivatives (MD)

This method was investigated by Packard *et al.* [537] and uses the derivatives of the time series.

For illustrative purposes, and in order to understand the relationship between the original and the new pseudo–state space, let us consider the following three–dimensional dynamical system:

$$\frac{d\vec{x}}{dt} = \mathbf{F}(\vec{x}), \qquad \vec{x} = (x_1, x_2, x_3). \tag{5.2}$$

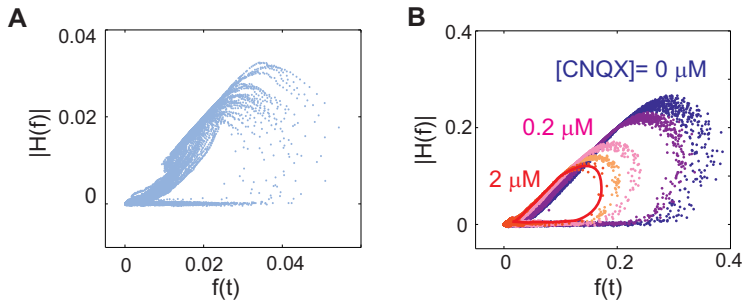

Figure 5.2: **SSR with Hilbert Transform.** Two–dimensional phase portrait with Hilbert Transform method: (A) [E+I]-network, DIV=16 and (B) [E]-network, DIV=16, [CNQX]=0nM (blue), [CNQX]=100nM (violet), [CNQX]=200nM (violet clear), [CNQX]=400nM (orange) and [CNQX]=800nM (red). Direct methodology without prior knowledge of any input embedding parameters.

Then, for locally smooth changes, we can always define the change of variable $\vec{y} = (y_1, y_2, y_3)$ as $\vec{y} = (x_1, dx_1/dt, d^2x_1/dt^2)$. Eq. (5.2) then becomes

$$\frac{dy_1}{dt} = y_2, \tag{5.3}$$

$$\frac{dy_2}{dt} = y_3, \tag{5.4}$$

$$\frac{dy_3}{dt} = \mathbf{G}(y_1, y_2, y_3), \tag{5.5}$$

with $\mathbf{G}(y_1, y_2, y_3)$ a nonlinear function. Although the function $\mathbf{G}(y_1, y_2, y_3)$ is *a priori* unknown, one can proceed to reconstruct each new state with this derivative field to, later, fit the obtained object to a theoretical model and determine $\mathbf{G}(y_1, y_2, y_3)$. Therefore, the dynamics in this new space will be related to the dynamics of the original real space through only this nonlinear transformation $\mathbf{G}(y_1, y_2, y_3)$, termed the *reconstruction map*. In this way we may proceed from the real state space (x_1, x_2, x_3) to the new *pseudo–space of derivatives* $(x_1, dx_1/dt, d^2x_1/dt^2)$.

In our particular case, the underlying dynamics and each corresponding state $\vec{\chi} = \chi_i$, will be characterized as

$$\chi_i{}^{(MD)}(m) = \{f(t_i), f'(t_i), f''(t_i)\}, \tag{5.6}$$

where the new coordinates $\{f(t_i), f'(t_i), f''(t_i)\}$ can be written as a linear combination of derivative field $\{y(t_i), y'(t_i), y''(t_i)\}$. We note that, with this methodology, the dimension of the system m is unknown. The extension of this approach to higher–dimensional dynamical systems is straightforward by considering higher derivatives. In this case, the coordinates are derivatives of successively higher order, i.e.

$$\chi_i{}^{(MD)}(m) = \{f(t_i), f'(t_i), ..., f^{m-1}(t_i)\}, \tag{5.7}$$

where $f^{m-1}(t)$ is a numerical approximation to the $(m-1)$–th derivative of $f(t)$. With this methodology, one can picture the necessary condition for a successful reconstruction.

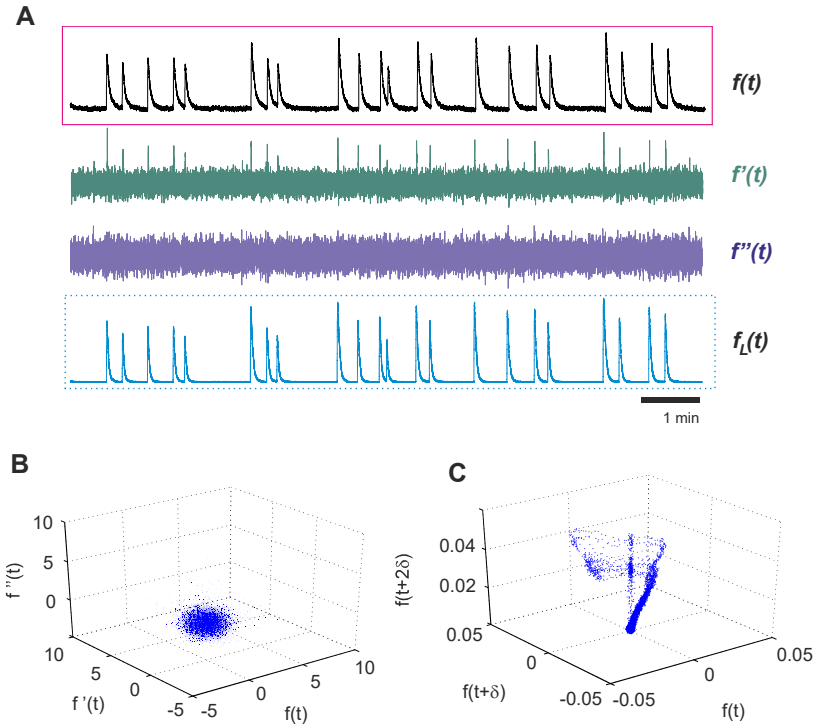

Figure 5.3: **The increasing noise with the method of derivatives (MD).** (A) Fluorescence trace $f(t)$ with their corresponding first $f'(t)$ and second $f''(t)$ time–derivative. Noise reduction can be turned on describing the fluorescence trace with Legendre polynomials $f_L(t)$ (bottom). (B) SSR with the method of derivatives (MD) (C) SSR with the method of delays (MOD).

Indeed, in order to guarantee that the topological quantities computed for the reconstructed attractor are identical to those in the original state space, we require that the structure of the tangent space (the linearization of the dynamics at any point in the state space) is preserved by the reconstruction process. Hence, in general, we will always have to remain close to linearity to ensure the validity of reconstruction.

Theoretically, the natural way for the SSR is through the derivatives field. Indeed, the derivative phase–portrait has the advantage of a direct interpretation in terms of process dynamics, and can be extended using estimates of higher order derivatives. However, as differentiation increases noise, this method is usually used to describe low dimensional systems, and thus is not suitable for noisy and short experimental signals. Estimates of higher order derivatives can be very variable when noise is present, and therefore the first derivative is typically the only focus of attention. As shown in Fig. 5.3, the evident disadvantage of this method is that a noisy component of the initial realization is enhanced with each subsequent step of differentiation. For experimental signals (noisy and short time series) and for high–dimensional systems the MD method is clearly not suitable. an additional negative aspect deals with the inhomogeneity, understood as permuting 'fast' and 'slow' dynamics, a feature also present in our experiments and illustrated in Fig. 5.3.

5.2.2 Method of Delays (MOD)

Let $f(t)$ be a set of measures of one variable of the system. Takens [689] suggested that instead of derivatives one can use delay coordinates $\{f(t), f(t+\Delta t), f(t+2\Delta t), ...\}$, where $\Delta t = \delta$ is a time delay appropriately chosen. Using Taylor series expansions, the respective derivatives of the set of measures can be approximated as:

$$\frac{df(t)}{dt} \approx \frac{f(t+\Delta t) - f(t)}{\Delta t}, \tag{5.8}$$

$$\frac{d^2 f(t)}{dt^2} \approx \frac{f(t+2\Delta t) - 2f(t+\Delta t) + f(t)}{2\Delta t^2}. \tag{5.9}$$

Then, for a value of Δt carefully chosen, the new information contained from every new derivative is also held in the series of the delay coordinates. Following this approximation, the time series can be embedded into a new state space where the m–dimensional time–delay vector ${\chi_i}^{(MOD)}$ is given by:

$${\chi_i}^{(MOD)}(m, \delta) = \{f(t_i), f(t_i - \delta), ..., f(t_i - (m-1)\delta)\}, \tag{5.10}$$

with $i = 1, 2, ..., N + (m-1)\delta$, m the *embedding dimension* and δ the *delay time*. Mathematically, one can evenly take forward delays or backward ones, but conceptually, this notation obey causality. Formerly, the m–dimensional time–delay vector represents each state ${\chi_i}^{(MOD)}(m, \delta)$ of a dynamical system at a snapshot in time in this new space. Then, the total number of states T becomes $T = P - (m-1)\delta$. For sake of simplicity, and since this method was the one chosen for SSR of our data, we will hereinafter omit the superscript of Eq. (5.10), so that ${\chi_i}^{(MOD)}(m, \delta) \equiv \chi_i(m, \delta)$. The set of all these states is represented by the so–called *delay matrix* (also termed *trajectory matrix*), $\mathbb{X}(m, \delta) = \chi_{ij}(m, \delta)$ ($\mathbb{X} \in \mathbb{R}^{Txm}$), which describes the sequence of all delay vectors or states in the embedding space over time. For further analysis, we used its normalized form

$$\mathbb{X} = \frac{1}{\sqrt{T}} \begin{pmatrix} \chi(t_0) \\ \chi(t_0 + \tau) \\ . \\ . \\ . \\ \chi(t_0 + i\tau) \\ . \\ . \\ . \\ \chi(t_0 + (T-1)\tau) \end{pmatrix}. \tag{5.11}$$

or, otherwise,

$$\mathbb{X} = \frac{1}{\sqrt{T}} \begin{pmatrix} f(t_0) & f(t_0-\delta) & ... & f(t_0-(m-1)\delta) \\ f(t_1) & f(t_1-\delta) & ... & f(t_1-(m-1)\delta) \\ . & & & \\ . & & & \\ . & & & \\ f(t_i) & f(t_i-\delta) & ... & f(t_i-(m-1)\delta) \\ . & & & \\ . & & & \\ . & & & \\ f(t_T) & f(t_T-\delta) & ... & f(t_T-(m-1)\delta) \end{pmatrix}, \tag{5.12}$$

where $t_i = t_0 + i\tau$, with $\tau \equiv \Delta t$ the sampling interval. Then, every state χ_i has its corresponding *target* $f(t_i) = f_i$, upon which this state is pivoted. Clearly, $\tau \ll \delta$. We note that the delay coordinates have the interesting property that the signal to noise ratio one each component is the same.

The main drawback of this method is that the values of the embedding parameters $\{\delta, m\}$ are *a priori* unknown. Before explaining the various methodologies used to pinpoint the appropriate values of $\{\delta, m\}$ for a good reconstruction, let us recall their physical meaning. The delay time δ is the minimal time windows that separates two events causally disconnected. Hence, this time window length is of particular importance because determines, in a certain sense, the amount of information passed from the time series to the embedding vectors. On the other hand, the minimal embedding dimension m gives the upper number of degrees of freedom. It therefore represents the minimal number of differential equations required for modeling the system under study. Conceptually, the embedding dimension m can be expressed as $m = 1 + m_p + m_s$, where m_p is the number of samples taken from the past and m_f the number of samples taken from the future. Then, Eq. (5.10) can be rewritten as

$$\chi_i(m, \delta) = \{f(t_i + m_f\delta), ..., f(t_i), ..., f(t_i - m_p\delta)\}. \tag{5.13}$$

We note that for $m_f = 0$ the reconstruction is *predictive*; Otherwise it is is *mixed*.

The fundamental embedding theorem was first introduced by Takens [689], and later extended by Sauer [611]. Theoretically, their studies revealed that a correct reconstruction of the dynamics is always possible for $m \geq 2d + 1$, being d is the real topological dimension of the reconstructed object. Hence, such a condition gives us a first constraint for m. As we will see soon, beyond a minimum value $m = m^*$, the reconstructed object in state space remains invariant, independently of the embedding dimension, so $\chi_i(m^*, \delta) \approx \chi_i(m > m^*, \delta)$. Concerning the value of δ, *a priori* we do not have any constrains. But, as we have seen above, small windows of δ are preferable to ensure the linear approximation of the trajectory in each point of the state space and the correct reconstruction of the underling dynamics. Our data, however, is noisy and short, and hence one would prefer intermediate rather than small δ values. In conclusion, and within our experimental framework, the choice of embedding parameters $\{\delta, m\}$ is not immediate and their selection has a significant effect on the quality of the SSR. The estimation of the good values for $\{\delta, m\}$ is one of the first difficulties of delay–coordinate embedding.

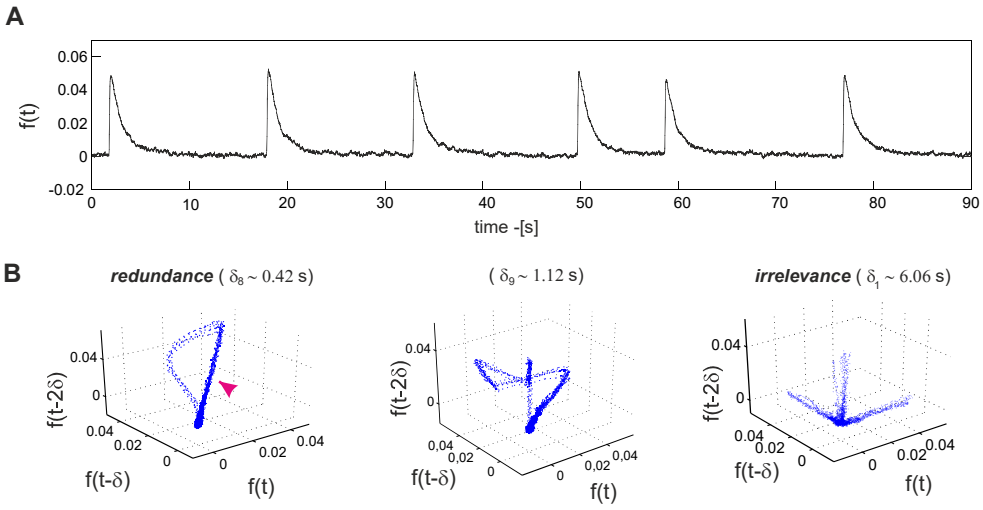

Figure 5.4: **SSR with MOD.** Reconstruction of the dynamics from a fluorescence trace of a [E+I]–network at DIV=12. (A) Analyzed fluorescence trace. (B) SSR orbits using different values of delay time: $\delta_8 = 0.42$ s (left), $\delta_9 = 1.12$ s (center) and $\delta_1 = 6.06$ s (right). The geometrical concept of *redundance* (small δ) and *irrelevance* (large δ) [121] are also shown. At the center, correct reconstruction is obtained with $\delta_9 = 1.12$ s, which has been estimated using the method of Gibson [271]. We have used $m = 3$ in all cases, although *a priori* the embedding value of dimension m is unknown.

Determination of the time delay δ

The choice of the correct delay δ requires a delicate balance between two opposed effects present in the physiological signals, namely noise and complexity. The importance of δ is pictured in Fig. 5.4. The figure shows a representative fluorescence trace in Fig. 5.4A and SSR plots for gradually higher δ in Fig. 5.4B. For small delays, the m coordinates of each state $\chi_i(m, \delta)$ become strongly correlated and therefore the embedded dynamics is lock along the identity line and squeezed in the direction perpendicular to it (red arrow in Fig. 5.4B, left plot). This pathological dynamics is termed *redundance* and is highly affected by noise [121]. At the other extreme, large delays cause overly unphysical reconstructions since the dynamics at a time point become effectively causally disconnected from the dynamics at a later time. Hence, even simple time series look extremely aberrant, shaping what is known as *irrelevance* [121]. We note that, for chaotic dynamics, large delays lead to increasing complex SSR. In our case, however, the dynamics is quasi–periodic and the effect of large δ cause all states $\chi_i(m, \delta)$ to be projected on the orthogonal direction, degenerating the resulting orbit (Fig. 5.4B, right panel). Hence, intermediate values of δ are the desirable. Fig. 5.4B, central panel, shows an example of a good reconstruction, and with $\delta = 1.12$ s. In terms of the fluorescence data, for an average width of the bursts of $\tilde{w} \sim 3.52$ s, the selected δ value is about a third of it.

The three illustrative phase actually shape three distinct geometries of the reconstructed attractor. In our experimental traces, we always observed them. At the approximate range of $\delta \in [0.46 - 2.2]$ s the structure of the attractor remains essentially invariant. In general, our working regime for a correct SSR falls within this range. The

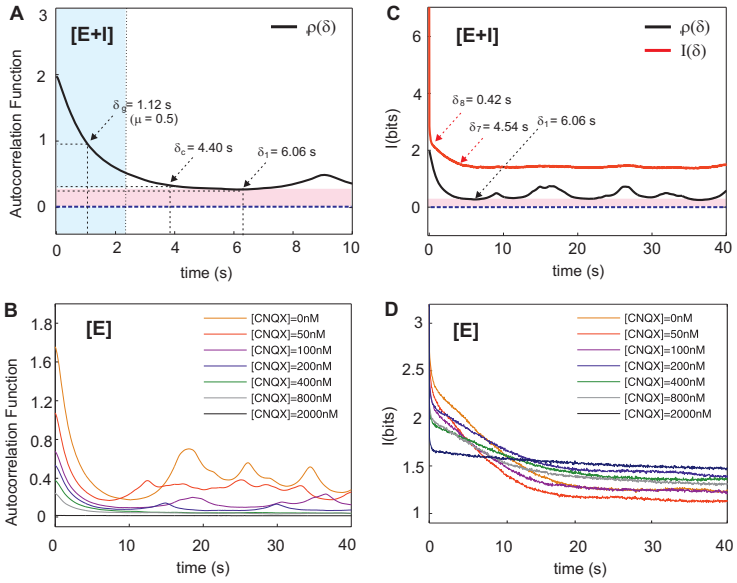

Figure 5.5: **Determination of Delay with Autocorrelation Function and Mutual Information.** Autocorrelation function $\rho(\delta)$ for a time series of 30.000 data (10 min recording, 50 fps) measured from the 'E+I' network experiment (A) and its disintegration process, 'E' only network (B) (DIV=12). Due to the effect of noise, this function doesn't vanish (shaded pink region). The first minimum of $\rho(\delta_1)$ is $\delta_1 \simeq 6.06$ s. $\delta_c \simeq 4.40$ s is the correlation time defined as the delay where the autocorrelation function is 1/e. $\delta^* \simeq 2.24$ s (red dashed line) is computed through the Gibson method [271] $\delta^{*2} = 12\langle f_L^2\rangle / \langle (f_L')^2\rangle$, with $f_L(t)$ the fluorescence trace described with discrete Legendre polynomials and f_L' its time–derivative, respectively [271]. δ_9 was computed as $\delta_9 = \mu\delta^* \sim 1.12$ s, with $\mu = 1/2$ [271]. In (C) and (D) is represented the mutual information $I(\delta)$ from the same time series for the 'E+I' network and its disintegration process, respectively. $\delta_7 \simeq 4.54$ s makes the $I(\delta_7)$ function "small" and $I(\delta_8)$ has an inflection point at $\delta_8 \sim 0.42$ s.

'arms' of the orbit gradually fall as δ grows and reach the 'irrelevance' case. In our studies, the quality of the reconstruction of the attractor can be visually assessed using these geometrical concepts of 'redundance' and 'irrelavance'. However, in order to compute all the experiments we need an automated processing.

In the literature, different methodologies have been proposed to automatically estimate δ. A first criterion commonly used is based on linear decorrelation, which δ is selected according to the vanishing point of the autocorrelation function $\rho(\delta) = \langle f(t)f(t-\delta)\rangle$. We denote as δ_1 the value obtained with this method, which would correspond to $\rho(\delta_1) = 0$. Unfortunately, in our traces, it is difficult to assess the vanishing point of the autocorrelation function since it does not reach zero, as illustrated in Fig. 5.5A. Indeed, due to noise, this function presents spurious residual values in the initial $5-25\%$ range of the function. Hence, other criteria have been proposed.

A second criterion sets δ_2 as the first minimum of the autocorrelation function. This first minimum is related to the 'period' of the system, in our case the average value of the inter–burst–interval, $\langle IBI\rangle$. Clear minimums can be detected for fluorescence traces from both 'E+I' networks and 'E' only networks, and in stages of CNQX disintegration in the range [CNQX]$\in [0-200]$ nM approximately, as shown in Fig. 5.5B. However, the obtained

δ_2 values are typically too high, in the range $[6-10]$ s, giving rise to degenerated orbits, i.e. of the 'irrelevance' kind (right panel of Fig. 5.4B). In addition, as shown in Fig. 5.5B, δ_2 is less clear as the network is gradually silenced and, for the last disintegrations, the autocorrelation function presents a sharp decrease due to the absence of bursting.

A third criterion seeks for a lower and upper bounds for δ by taking advantage of the relation between the autocorrelation function and the covariance matrix [27]. Using this idea, an appropriate δ_3 value is the one in the range $\delta_c \geq \delta_3 \geq 4\delta_c$, with δ_c the value in which the autocorrelation function is $1/e$, as shown in Fig. 5.5A. By using this method, our data also procures a too broad range of δ_3, in the band $4.40 \geq \delta_3 \geq 17.6$s.

A fourth criterion was suggested by King et al.[383], in which δ is given by the time in which the second derivative of the autocorrelation function changes sign for the first time. In other words, δ_4 is chosen as the first inflection point of the autocorrelation function. Nonetheless, an overestimation was also achieved, leading to degenerated structures in the SSRs.

A fifth criterion takes advantage of infinite time series in non–periodic systems, and uses the Fourier Transform [101]. The authors suggested to consider a $\delta^\dagger$ given by the inverse of the band–limiting frequency obtained from power spectrum, i.e, $\delta^\dagger = 2\pi/w^\dagger$, where $w^\dagger$ is the band limiting frequency. Next, the good choice of δ, that we call δ_5, is the one that satisfies $\delta_5 \geq \delta^\dagger$. Although, autocorrelation–based methods have the advantage of a shorter computational time as compared to the fast Fourier Transform (FFT), it was shown that both strategies procured inconsistent results [27, 468, 230]. We therefore discarded the FFT strategy.

While the autocorrelation function measures a linear dependence and temporal correlations, mutual information [631, 230] provides the key to quantifying *spatial coherence* [446, 764], giving a better general decorrelation. This idea provided additional criteria for determining δ. Indeed, Fraser and Swinney [230] proposed that the value of δ corresponding to the first minimum of the mutual information, $I(\delta_6) = 0$, should be a good choice for delay coordinates. They justified this procedure on the grounds that small values of I implies that $f(0)$ and $f(\delta)$ are statistically independent, minimizing the redundance of coordinates. Several years later, Liebert and Schuster [427] proved that the minimum of $I(\delta_6)$ coincides with those of the correlation integral C_m. Unfortunately, as illustrated in Fig. 5.5C, mutual information curves of our data are all monotonically decreasing functions. Again, proceeding similarly as correlation, we also obtained large δ_7 corresponding small values of $I(\delta_7)$. Another criterion proposed, it was taken δ_8 values corresponding its first inflection point. Nevertheless, small values were obtained, $\delta_8 \sim 0.42$ s (Fig. 5.5C), producing orbits of the 'irrelevance' kind (left panel of Fig. 5.4B).

We stress that the main drawback of all these methods is that they are computed from the original signal (an scalar time series) and not from the full reconstructed state space. Indeed, the preceding methods guarantee decorrelation (linear or general) between two successive coordinates $f(t_j)$ and $f(t_j - \delta)$ of the reconstructed state χ_j. But, obviously, the observation that $f(t_j)$ and $f(t_j - \delta)$ uncorrelated, and that $f(t_j - \delta)$ and $f(t_j - 2\delta)$ are also uncorrelated, does not imply that $f(t_j)$ and $f(t_j - 2\delta)$ are in turn uncorrelated. Hence, although the computational cost of all this methods is low, the obtained δ values are clearly not adequate for our experimental signals.

The method that we finally found as optimum is the one proposed by Gibson *et al.* [271] and that is adequate for noisy signals. This method provides an upper limit for δ

given by

$$\delta^* = 2\sqrt{\frac{3\langle f_L^2\rangle}{\langle (d_t f_L)^2\rangle}}, \tag{5.14}$$

where $f_L(t)$ is the fluorescence trace described as discrete Legendre polynomials and $d_t f_L$ its time–derivative, respectively. The authors showed the appropriateness of describing the fluorescence trace as discrete Legendre polynomials due to its potential to average out noise (see Fig. 5.3A, bottom). They argued that this transformation reduces noise as far as it is structured as isotropic Gaussian noise since the change of coordinates makes the variance maximum and, consequently, maximizes the signal–to–noise ratio. As we will see, similar effects are achieved when conducting SSR through PCA.

The upper bond that Eq. (5.14) provides is obtained by analyzing the regime of work where the SSRs, derived through MD, MOD and PCA methods, can be approximated by a coordinate changes. Indeed, it is possible to demonstrate that alternative methods of reconstruction, such as derivatives and PCA, are actually coordinate transformations on delay vectors [271]. In particular, the rotation from delay coordinates to Legendre coordinates diagonalizes the covariance matrix, although it is a non–linear transformation in contrast with PCA. Therefore, a further rotation is need to approximate it to PCA. The threshold where this approximation breaks down is determined by the upper limit δ^* in Eq. (5.14). Consequently, a successful embedding is obtained for $\delta \ll \delta^*$. We note that this has strong implications since all the analysis that we are going to carry out will be close to a linear regime. In line with this argument, one can observe that the transformation from delay coordinates to the original coordinates is typically nonlinear. This is one of the reasons to use this method when treating experimental data. For practical application, the authors gave an optimal value of $\delta_9 = \mu\delta^*$ where μ is a fixed constant. Although, unfortunately, the parameter μ is undetermined, one typically takes $\mu \lesssim 1$. Indeed, based on empirical results, Gibson *et al.* suggested $\mu \approx 1/2$ to get correct SSRs [271]. In our particular case, there is not a simple rule for determining μ automatically, and it could depend on the experiment. In general, in our measurements we could use $\mu \in [0.3 - 0.5]$. However, although μ is *a priori* undetermined, correct reconstructions and fair values of δ_9 are obtained. An example was actually provided before, in Fig. 5.4B, central panel. We finally note that this method provides a very efficient computational implementation, about 10 times shorter than the autocorrelation algorithm.

Determination of the embedding dimension

Provided δ, we proceeded to determine the embedding dimension $m = m(\delta)$. In our case, the input values of δ are calculated with the Gibson method [271], so $\delta = \delta_9$. In general, the standard way to obtain m consists in determining the value m^* in which the structure of the reconstructed object remains invariant, so $\chi_i(m^*, \delta_9) \approx \chi_i(m^* < m, \delta_9) \approx \chi_i(\delta_9)$, where $i = 1, ...T$ and $m = m^* + 1, ..., \infty$.

Just as in δ, the adequate selection of m is complicated. Dimensions below m^* lead to dynamical systems that are compacted in an unnatural way, with a pathological geometry termed *folded*. At the other extreme, values of m too large lead to redundancy and an artificial symmetry is introduced. Next, we elaborate on the strategies to calculate the embedding dimension.

One of the most widely used methods for determining m is the False Nearest Neighbors (FNN) developed by Kennel *et al.* [381, 373, 380]. The pivotal idea of this method consists in assessing the number of neighbors of a state along the trajectory that change as m grows. Let us suppose that the minimal embedding dimension for a given time series $f(t)$ is m^*. In a m^*–dimensional delay space, the reconstructed attractor would have a correspondence one–to–one with the original signal in the real space and its topological properties would be preserved. Then, due to the assumed smoothness of the dynamics, the neighbors of the real space are mapped onto neighbors in the delay space. By contrast, in an embedding with $m < m^*$, the states would be projected onto neighborhoods of other states to which they do not belong. These points are called *false neighbors*. Hence, a pair of points would be *true neighbors* when, as m grows, they remain close together, so their respective distances are invariants. Therefore, by gradually increasing the dimension, the number of false neighbors drops to zero and an appropriate embedding can be determined, being m^* is the minimal embedding dimension.

The implementation of the FNN algorithm follows Ref. [5]. Given an input value of δ_9 calculated through the Gibson method [271], we start by exploring a range of m values between 1 and 50. For each state χ_i we look for its kth–nearest neighbor χ_k in $\mathbb{R}^m$ and calculate their corresponding Euclidean distance as

$$d^2({\chi_i}^m, {\chi_k}^m) = \sum_{j=0}^{m-1} [f(t_i - j\delta) - f(t_k - j\delta)]^2. \tag{5.15}$$

We next iterate the procedure for successively higher embedding dimensions $\mathbb{R}^{m+1}$, and calculate the distance between ${\chi_i}^{m+1}$ and the same kth–nearest neighbor ${\chi_k}^{m+1}$. We note that, when evolving from dimension m to $m+1$, we only add the $m+1$ coordinate to each of the corresponding states, and Eq. (5.15) reads

$$d^2({\chi_i}^{m+1}, {\chi_k}^{m+1}) = d^2({\chi_i}^m, {\chi_k}^m) + [f(t_i - m\delta) - f(t_k - m\delta)]^2. \tag{5.16}$$

Additionally, for capturing embedding errors, the increase in distance can be simply computed as the following ratio,

$$\xi(i,m) = \left[\frac{d^2({\chi_i}^{m+1}, {\chi_k}^{m+1}) - d^2({\chi_i}^m, {\chi_k}^m)}{d^2({\chi_i}^m, {\chi_k}^m)} \right]^{1/2} = \\ = \frac{|f(t_i - m\delta) - f(t_k - m\delta)|}{d({\chi_i}^m, {\chi_k}^m))}. \tag{5.17}$$

This ratio has to obey $\xi(i,m) > \xi_{\text{thr}}$, with ξ_{thr} a given threshold. Indeed, a value of ξ higher than this heuristic threshold ξ_{thr} would mark this state as 'false nearest neighbor'. The criterion of having an embedding dimension m^* sufficiently high ensures that the fraction of states obeying $\xi > \xi_{\text{thr}}$ is maximum. A perfect reconstruction would mean that no false neighbors exist.

The fact that the distances between neighboring points do no change when measured in $\mathbb{R}^m$ and in $\mathbb{R}^{m+1}$, does not necessary mean that these points are also true neighbors on the original attractor. Noisy states fall outside these classes, but, usually, they are incorrectly included as true neighbors, producing an overestimation of m. This is illustrated in

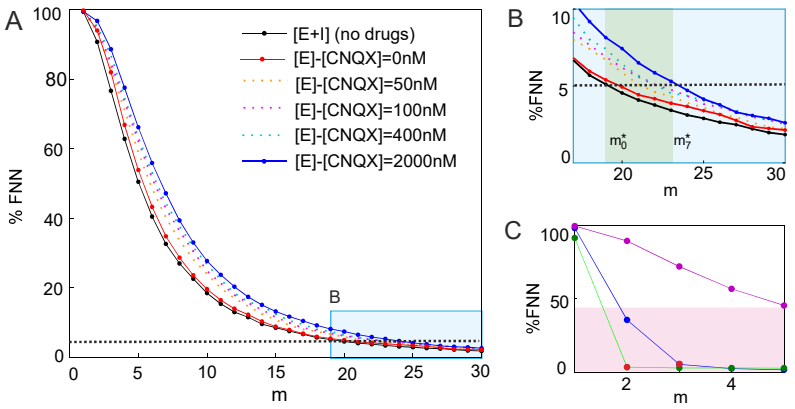

Figure 5.6: **Determination of embedding dimension with the False Nearest Neighbors (FNN) algorithm**. (A) The percentage of false nearest neighbors as a function of the embedding dimension for 30.000 data points from an [E+I]-network at DIV=12, 50 fps acquisition, studied at different levels of disintegration through CNQX. Horizontal dashed line refers the 5% level of false neighbors used as discriminative threshold value ξ_{thr}. (B) The final (δ_9, m_1) values obtained for each disintegration were the following: (0.53 s, 19) for the [E+I] condition with no drugs (continuous black line); (0.86 s, 20) for [E]- network with [CNQX]= 0 nM (continuous red line); (0.76 s, 22) for 50 nM (dot dashed red line); (0.43 s, 23 for 100 nM (dotted dashed violet line); (0.77 s, 22) for 200nM (dotted dashed green line); and (5.12 s, 24) for 2000 nM (continuous blue line). Green shaded area marks the obtained regime for m^*. (C) Curves from noise free Lorenz (blue, $\delta_9 = 0.55$ s and $m = 3$) and Hénon (green, $\delta_9 = 0.55$ s and $m = 2$) time series. We also show a Hénon time series (violet, $\delta_9 = 0.55$ s and $m = 10$) corrupted by noise (pink shaded area). The delay time value δ_9 was calculated using the Gibson method and FNN implementation was carried out through the TISEAN package [5].

Fig. 5.6A, which pictures the percentage of false nearest neighbors as a function of the embedding dimension m for a typical experiment of CNQX disintegration. For practical purposes, a 5% level of false neighbors was used to discriminative threshold value ξ_{thr} Due to the effect of noise, high values of m^* were obtained, in the range of $m \in [19 - 24]$ (Fig. 5.6B) This observation was present in all analyzed experiments. The effect of noise in the estimation of m^* is clear when comparing with artificial signals where the noise can be tuned, as shown in Fig. 5.6B. Here, the percentage of false nearest neighbors is plotted as a function of the embedding dimension for noise free, Lorenz and Hénon time series, as well as a for Hénon time series affected by 10% of noise. One clearly observes that, as expected, $m = 2$ is sufficient for the Hénon and $m = 3$ for the Lorenz system, whereas the value of m is more difficult to ascertain in the noisy case.

In order to minimize the effect of noise, Cao [116] provided another robust algorithm to estimate the minimum embedding dimension. Similar to the idea of FNN, the author defined the ratio $\alpha(i, m)$ as

$$\alpha(i, m) = \frac{d({\chi_i}^{m+1}, {\chi_k}^{m+1})}{d({\chi_i}^{m}, {\chi_k}^{m})}, \tag{5.18}$$

where the Euclidean distance is given by the maximum norm, i.e.,

$$d({\chi_i}^{m}, {\chi_k}^{m}) = \max_{0 \leq r \leq m-1} |f(t_i - r\delta) - f(t_k - r\delta)|. \tag{5.19}$$

Then, with the aim to reduce the effect of noise, the mean value of all $\alpha(i,m)$ is calculated as

$$E(m,\delta) = \frac{1}{T}\sum_{i=1}^{T}\alpha(i,m). \tag{5.20}$$

This quantity depends only on m and δ. To investigate its sensitive when evolving from m to $m+1$, the following quantity is defined,

$$E1(m) = \frac{E(m+1)}{E(m)}. \tag{5.21}$$

Usually, for deterministic data $E1(m)$ attains a saturation value m^* as m increases. This m^* is the minimum embedding dimension that we are actually interested to obtain. However, since available observed data samples are limited and affected by some degree of stochasticity, it is necessary to define another quantity which is useful to distinguish deterministic signals from stochastic ones, as follows

$$E^*(m) = \frac{1}{T}\sum_{i=1}^{T}|f(t_i-\delta m) - f(t_k-\delta m)|, \tag{5.22}$$

and

$$E2(m) = \frac{E^*(m+1)}{E^*(m)}. \tag{5.23}$$

For random data, the future values in a time series are independent of the past values, and therefore the quantity $E2(m)$ will be equal to 1 for any embedding dimension. However, for deterministic data, $E2(m)$ is certainly related to m and, as a result, it cannot be a constant for all m.

The importance and actual differences between $E1$ and $E2$ are illustrated in Fig. 5.2.2, which plots these functions for the same CNQX data shown before. Although the experimental recordings contained 30.000 points, we observed that the results do not strongly depend on the number of data points were used, contrary to the FNN method. For the analysis shown in the figure, we used fixed delay time δ_9 previously calculated with the Gibson method. The minimum embedding dimensions were determined for each stage of disintegration, and are shown as vertical lines. Like the FNN method, the obtained trend suggests that m increases as disintegration advances (panels A to D in the figure). However, a comparison with the FNN method shows that smaller values of m are achieved, in the range $m \in [10, 20]$. In addition, $E1$ and $E2$ methods allow to distinguish deterministic data from random one. Indeed, for the strongest disintegation (Fig. 5.2.2D), the quantity $E2(m)$ stabilizes to 1 for all m, and evinces the noise–affected nature of the fluorescence traces, particularly at high disintegrations. By contrast, weak disintegrations —panels A to C— exhibit a clear degree of determinism since $E2(m)$ changes according to m.

These two methods still present drawbacks. Firstly, in both methods, the threshold used to select the minimum embedding dimension is not grounded on any objective criterion. Secondly, for the FNN method, the false nearest neighbor definition implicitly brings up a cutoff distance ξ_{thr} characterization that *a priori* is also unknown. Thirdly, despite the correction applied by Cao [116], both methods still remain sensitive to the presence of noise, leading to an overestimation of the embedding dimension. Fourthly

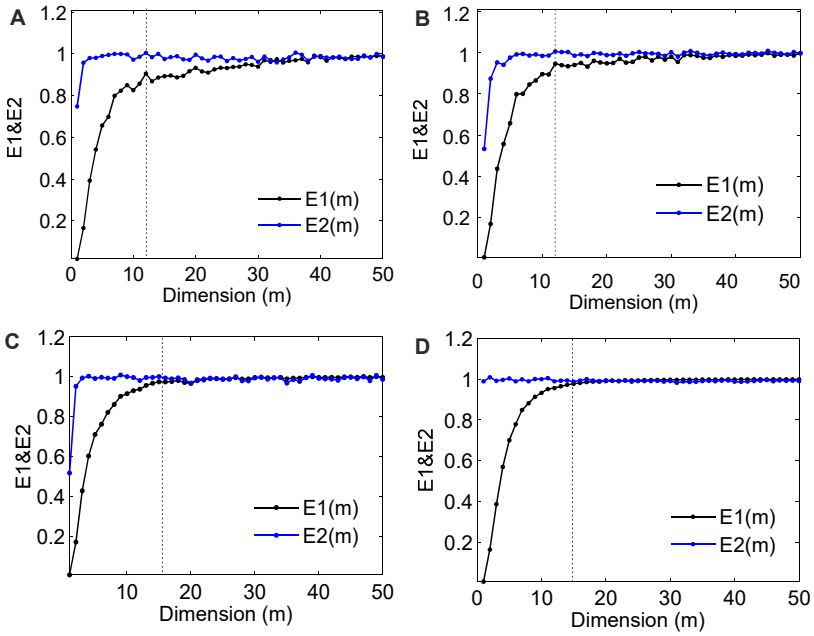

Figure 5.7: **Determination of the embedding dimension through the Cao's method.** The panels show the values of $E1(m)$ and $E2(m)$ for gradually higher disintegration through CNQX. Experiment was carried out at DIV=12, and fluorescence data consisted of time series with 30.000 points (10 min of recording at 50 fps). The delay time δ_9 was calculated with the Gibson method using $\mu = 0.5$. (A) [E+I] data (no drugs), with $\delta_9 = 0.53$ s and $m_2 = 12$, (B) [E] netwok, with [CNQX]= 0 nM, providing $\delta_9 = 0.86$ s and $m_2 = 12$, (C) [E]-[CNQX]= 400 nM with $\delta_9 = 1.51$ s and $m_2 = 14$ and (D) [E]-[CNQX]= 2000 nM with $\delta_9 = 5.12$ s and $m_2 = 16$. The vertical continuous lines correspond to the minimum embedding dimension m_2. Cao's method was carried out with the TSTOOL software package [6] implemented in Matlab 2013b.

and finally, although in principle the embedding dimension is independent of δ, for short and noisy time series different results can actually be obtained. Indeed, different values of m are derived when changing δ.

To solve all these problems, in the next section we describe an algorithm —derived from information theory— to simultaneously calculate the embedding parameters $\{\delta, m\}$.

Simultaneous determination of δ and m

Along the above analyses we assumed that m and δ were not correlated, and thus that they could be determined independently. In reality, however, they can be intimately related for data series of short duration and noisy, as in our experiments. Indeed, the estimation of m depends on δ, and vice versa. For example, the fraction of false nearest neighbors does not fall to zero for a given m as δ increases, but rather the estimated m increases slowly with δ.

The optimal embedding parameters $\{\delta_0, m_0\}$ can be concurrently obtained by using a differential–entropy based method proposed in Refs. [262, 8] The idea is to start by setting a range of δ values from 1 to 500, and m values from 1 to 50. Then, for each (δ, m) pair, the corresponding delay matrix $\mathbb{X}(\delta, m)$ is computed and, finally, the differential

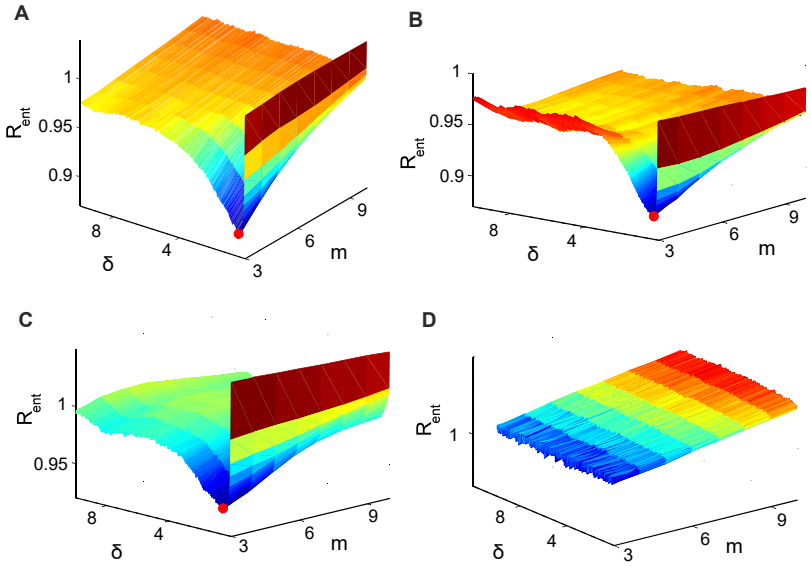

Figure 5.8: **Determination of embedding parameters with the ER method.** Estimation of embedding parameters $\{\delta_0, m_0\}$ for experiment of DIV=12 in different stage of disintegration. Each fluorescence trace is a time series of 30.000 points with sampling time $\tau = 20ms$ and camera speed of $v = 50$ fps. (a) [E+I]-(no drugs) with $\{\delta_0, m_0\} = \{0.40, 3\}$, (b) [E]-[CNQX]=0nM with $\{\delta_0, m_0\} = \{0.70, 3\}$, (c) [E]-[CNQX]=400nM with $\{\delta_0, m_0\} = \{0.82, 3\}$, and (d) [E]-[CNQX]=2000nM with $\{\delta_0, m_0\} = \{7.93, 4\}$ where $[\delta] = s$ and $[m]$ is dimensionless. The minimum of ER–function gives the embedding parameters $\{\delta_0, m_0\}$ which they are indicated by red open circles. Calculations were made using the software package [8], described by [262] and implemented in Matlab 2013b.

entropy $H(f(t), \delta, m)$ calculated using the Kozachenko–Leonenko (K-L) estimator, as follows

$$H(f(t), \delta, m) = \sum_{j=1}^{T} ln(Td_{ik}) + ln(2) + C_E, \tag{5.24}$$

where T is the number of states χ_i, $d_{ik} = d({\chi_i}^m, {\chi_k}^m)$ is the Euclidean distance of the i–th delay vector to its kth–nearest neighbor and $C_E \approx 0.5772$ is the Euler constant. Because K–L entropy is not robust with respect to dimensionality, the authors argued that it can be compensated by normalizing $H(f(t), m, \delta)$ with respect to an ensemble of surrogates $f_s(t)$ of the signal $f(t)$,

$$I(\delta, m) = \frac{H(f(t), \delta, m)}{< H(f_{s,j}(t), \delta, m) >_j}. \tag{5.25}$$

Here, the index j refers to the $j-$th surrogate. In our case, a set of 99 surrogates were generated using the iterative Amplitude Adjusted Fourier Transform (iAAFT) method [618] which retains within the surrogates both the distribution of fluorescence amplitudes and the autocorrelation structure of the original signal. Additionally, to correct for excessively high embedding dimensions inherent in noisy signals, the minimum

description length method was next implemented, giving rise to the Entropy Ratio (ER) function, R_{ent},

$$R_{ent}(m,\delta) = I(m,\delta) + \frac{mln(M)}{M}, \tag{5.26}$$

where M is the number of delay vectors, which is kept constant for all values of m and δ. Finally, R_{ent} was optimized and its minimum determined, yielding to the optimal set of embedding parameters $\{\delta_0, m_0\}$.

The implementation of this methodology to our experimental data is shown in Fig. 5.2.2. We again use the same CNQX disintegration data as in previous figures. In panels A–C of the figure, and that correspond to experiments without drugs or weak disintegration, a clear minimum is observed. Indeed, the existence of a minimum is directly related to the presence of structure in the signal, i.e. sudden increases in the fluorescence. In contrast, for time series with no clear structure such as network with [CNQX]= 2000 nM (panel D) the method does not yield to a clear minimum.

In general, the ER methodology procured consistent embedding parameters across different experiments, a result that emphasizes the potential of ER for treating our data. By comparing this method with the previous ones, we observed that δ_0 values were in general smaller than $\delta_1 - \delta_9$. Furthermore, δ_0 values also fell within the confidence interval predicted by Gibson [271]. In regard to the m values, m_0 values were also smaller than $m_1 - m_2$.

The ER method provided consistent SSR that were far from the pathological extremes of 'redundance' and 'irrelevance', and therefore ER was chosen as the best method to characterize our SSRs. However, it must be said that in some cases we observed some artificial symmetries, suggesting that m was still too low. This particularly occurred in experiments from young cultures (DIV$\lesssim$12), with computed embedding dimensions m in the range $2-3$.

5.2.3 Method of Principal Components Analysis

Principal component analysis (PCA[1]) is a linear tool to decompose multidimensional data into linearly independent coordinates. The central idea of PCA is to reduce the dimensionality of a data set in which there are a large number of interrelated variables, while retaining the largest possible variation present [101]. In our particular case, we proceeded to use PCA as a coordinate transformation on delay reconstructions in order to eliminate linearly dependent coordinates and artificial symmetries.

Mathematically, PCA consists in diagonalizing the trajectory matrix $\mathbb{X}$ in order to obtain its singular vectors and its singular values. Following our notation, we consider that the data has T points, with embedding parameters $\{m, \delta\}$. Hence, the key idea behind the method is based on the singular value decomposition (SVD) of the embedding matrix $\mathbb{X}$ (containing the set of states χ_{ij}),

$$\mathbb{X} = V\Sigma U^{\dagger}, \qquad \mathbb{X} \in \mathbb{R}^{Txm}, \tag{5.27}$$

[1]PCA is also called *Karhunen-Loève decomposition*, *principal value decomposition* and *singular systems analysis*. One can often find the use of the term PCA for the sole use of mutivariate data, while the term *singular spectrum analysis (SSA)* is used for time–delay reconstruction of univariate data.

where V is a $T \times T$ orthogonal matrix of the *left–eigenvectors* $\vec{v}$ of $\mathbb{X}$, Σ is the diagonal $T \times m$ of the *singular values* σ of $\mathbb{X}$, and U is an $m \times m$ orthogonal matrix of the *right–eigenvectors* $\vec{u}$ of $\mathbb{X}$.

We note that $\vec{v}$, $\vec{u}$ and σ form the left–eigenvectors, right–eigenvectors and singular values of matrix $\mathbb{X}$ if they satisfy the following equations,

$$\mathbb{X}\vec{u} = \sigma\vec{v}, \quad \mathbb{X}^\dagger\vec{v} = \sigma\vec{u}. \tag{5.28}$$

Since the trajectory matrix $\mathbb{X}$ is not symmetric, the above decomposition is not immediate. The simple way to proceed is as follows. From $\mathbb{X}$ we construct two positive–defined symmetric matrices $\mathbb{X}\mathbb{X}^\dagger$ and $\mathbb{X}^\dagger\mathbb{X}$. Each one can be then decomposed as

$$\mathbb{X}\mathbb{X}^\dagger = V\Sigma U^\dagger U\Sigma V^\dagger = V, \Sigma^2 V^\dagger, \tag{5.29}$$

$$\mathbb{X}^\dagger\mathbb{X} = U\Sigma V^\dagger V\Sigma U^\dagger = U.\Sigma^2 U^\dagger. \tag{5.30}$$

It is important to keep in mind that $T \geq m$. We can now show that $\mathbb{X}\mathbb{X}^\dagger$ (of size $T \times T$) and $\mathbb{X}^\dagger\mathbb{X}$ (of size $m \times m$) will share m eigenvalues, while the remaining $T - m$ eigenvalues of $\mathbb{X}\mathbb{X}^\dagger$ will be zero.

From Eq. (5.30) we can now identify the eigenvectors and eigenvalues for $\mathbb{X}^\dagger\mathbb{X}$ as the columns of U and the diagonal elements of Σ^2. Then we can write the following expression,

$$\mathbb{X}^\dagger\mathbb{X}\vec{u} = \sigma^2\vec{u}. \tag{5.31}$$

Next, we can multiply on both sided by $\mathbb{X}$ to get

$$\mathbb{X}\mathbb{X}^\dagger\mathbb{X}\vec{u} = \sigma^2\mathbb{X}\vec{u}. \tag{5.32}$$

This expression indicates that we have an eigenvector $\vec{v} = \mathbb{X}\vec{u}$ and an eigenvalue σ^2 for $\mathbb{X}\mathbb{X}^\dagger$ as well, since

$$\mathbb{X}\mathbb{X}^\dagger\vec{v} = \sigma^2\vec{v}. \tag{5.33}$$

So far we have shown that $\mathbb{X}\mathbb{X}^\dagger$ and $\mathbb{X}^\dagger\mathbb{X}$ share m eigenvalues. We still need to prove that the remaining $T - m$ eigenvalues of $\mathbb{X}\mathbb{X}^\dagger$ are zero. To do that, let us consider an eigenvector $\vec{v}_\perp$ for $\mathbb{X}\mathbb{X}^\dagger$, so that $\mathbb{X}\mathbb{X}^\dagger\vec{v}_\perp = \beta_\perp\vec{v}_\perp$, with $\beta_\perp$ the eigenvalues. This eigenvector is orthogonal to the m eigenvectors $\vec{v}$ already determined. Using the decomposition $\mathbb{X}\mathbb{X}^\dagger = V\Sigma^2 V$, we immediately see that the eigenvalues $\beta_\perp$ must all be zero,

$$\mathbb{X}\mathbb{X}^\dagger\vec{v}_\perp = V\Sigma^2 V\vec{v}_\perp = 0\vec{v}_\perp. \tag{5.34}$$

Hence, the rank $\Re$ of $\mathbb{X}\mathbb{X}^\dagger$ is determined by the smallest dimension of $\mathbb{X}$, i.e. $\Re(\mathbb{X}\mathbb{X}^\dagger) = \Re(\mathbb{X}^\dagger\mathbb{X}) = \Re(\mathbb{X})$ $(\Re \leq m)$.

For delay vectors, we define the corresponding $T \times T$ covariance matrix $\Xi_\mathbb{X} \in \mathbb{R}^{TxT}$ as

$$\Xi_\mathbb{X} \equiv \frac{1}{T}\mathbb{X}\mathbb{X}^\dagger, \tag{5.35}$$

where we have removed the mean of the data, i.e. $\chi_{ij} := \chi_{ij} - \langle\chi_i\rangle$. Throughout this section, we use Ξ to indicate a covariance matrix and a subscript to indicate the coordinate system. Note that in the limit of large time series $(T \to \infty)$ and small δ

($\delta \to 0$), $\Xi_{\mathbb{X}}$ approximates the autocorrelation function of the time series. In this sense, PCA decomposes a time series into a set of orthogonal bases of decreasing energy. Hence, according to Eq. (5.29), we proceed to the decomposition of $\Xi_{\mathbb{X}}$ in order to characterize its eigenvectors and its set of eigenvalues, $\{\sigma_i^2\}$. Then, the eigenvectors corresponding to the largest eigenvalues of $\Xi_{\mathbb{X}}$ project the data onto these directions, and that are indeed the directions where the data exhibits most variation. These projections of the data on the principal axes are called *principal components*, also known as *PC scores*. Then, by setting $\tilde{U}$ as the matrix of eigenvectors sorted according to the eigenvalues, we can picture the new coordinate transformation of the data,

$$\mathbb{Y} \equiv \tilde{U}^{\dagger}\mathbb{X}, \tag{5.36}$$

which represents a rotation of the delay coordinates [271]. The covariance matrix of these new transformed variables reads

$$\Xi_{\mathbb{Y}} \equiv \mathbb{Y}\mathbb{Y}^{\dagger}, \tag{5.37}$$

or, otherwise,

$$(\Xi_{\mathbb{Y}})_{ij} = \langle y_i y_j \rangle. \tag{5.38}$$

By using the definitions of $\mathbb{Y}$, $\Xi_{\mathbb{Y}}$ and $\Xi_{\mathbb{Y}}$ and considering the orthonormality of $\tilde{U}$, we can obtain

$$\Xi_{\mathbb{Y}} = U^{\dagger}\Xi_{\mathbb{X}}U = \Sigma^2, \tag{5.39}$$

which indicates that the covariance matrix of PC is diagonal and its components are linearly independent. We note that Eqs. (5.38) and (5.39) also show that the eigenvalues measure the variance of PC, i.e.

$$\sigma_j^2 = \langle y_j^2 \rangle. \tag{5.40}$$

The set of T eigenvalues, $\{\sigma_i^2\}$, $i \in [0, T-1]$, is called the *singular spectrum* and, by convention, it is given in descending order:

$$\sigma_1^2 \geq ... \geq \sigma_m^2 > \sigma_{m+1}^2 = ... = \sigma_T^2 = 0, \tag{5.41}$$

where $\sigma_m^2 > 0$, $\sigma_{m+1}^2 = 0$, and $\Re(\Xi_{\mathbb{Y}}) = \Re(\Xi_{\mathbb{X}}) = \Re(\mathbb{X}) = m$. The covariance matrix defined in Eq. (5.35) is large and difficult to treat from a practical point of view. However, from the relations provided by Eqs. (5.31) and (5.33), we find that it is sufficient to decompose the smaller $m \times m$ matrix as

$$\mathbb{D} \equiv \frac{1}{m}\mathbb{X}^{\dagger}\mathbb{X}. \tag{5.42}$$

Given a decomposition of $\mathbb{D}$ we can find the interesting non–zero principal directions and components for $\Xi_{\mathbb{X}}$, $V = \mathbb{X}U(\Sigma^2)^{-1}$.

The importance of PCA analysis is that provides an upper limit for the embedding dimension m through a simple recursive algorithm, described in detail in Ref. [101]. Essentially, the idea is to apply PCA on the delay matrix $\mathbb{X}$, and using a fixed δ value and

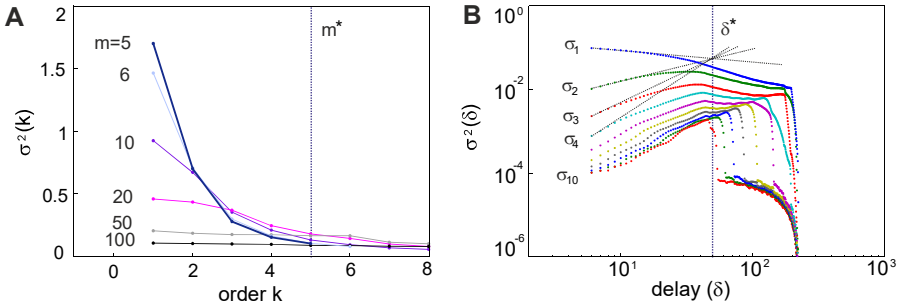

Figure 5.9: **Singular Spectrum in function of embedding dimension (m) and delay (δ).** (A) Singular Spectrum $\{\sigma_i^2\}$ obtained in function of different mxm-covariance matrices. Delay time is fixed and estimated with ER-method ($\delta = 42$ ms). An upper threshold of statistical dimension $S^* \sim 5$ (dashed vertical blue line) is estimate when singular spectrum vanished, $\sigma(k \sim S^*) \sim 0$ (B) Singular Spectrum $\{\sigma_i^2\}$ as a function of delay time in the range $[2-500]$ ms. Embedding dimension is calculated with ER-method ($m = 3$). Critical windows is estimated dashed vertical blue line, $\delta^* = \delta_w \sim 52$ ms) fitted the scaling region of the four first singular values.

a progressive increase of m. Such a procedure is exemplified in Fig. 5.2.3A, which shows the decrease of the singular spectrum $\{\sigma_i^2\}$ and the determination of an upper threshold for the statistical dimension S^* ($S^* \simeq 5$) when $\sigma(k > S^*) \simeq 0$. The upper threshold of the embedding dimension is then established as $m < S^*$. We remark, however that S^* depends crucially on the quality of the data, as well as on the sampling time scale [731]. In the example shown in the figure, the delay time was fixed and calculated through the ER–method [262] and m varied between 1 and 100.

Fig. 5.2.3B shows the singular spectrum $\{\sigma_i^2\}$ plotted as a function of the delay time for a fixed embedding dimension $m = 3$. A threshold is observed (vertical line, $\delta^* = \delta_w \simeq 52$ ms) that a non–scaling region from a scaling one. Above this threshold, the scaling regime breaks down and higher–order effects emerge in both the eigenvalues and eigenvectors. Additionally, for $\delta \geq \delta^* = \delta_w$, PCA is outside the domain of validity of the small–window solution [271], where $\delta_w = (1 - m)\delta$.

The sensitivity of the statistical dimension S^* on the quality of the data and sampling time can be mathematically expressed as [27]

$$S^* = \frac{2m}{\pi}\sqrt{a\tau\left(\frac{\sigma_f^2}{\sigma_n^2} - a\tau\right)}, \tag{5.43}$$

where σ_f^2 and σ_n^2 are the variances of the fluorescence trace and its associated noise, respectively. Hence, S^* depends on the sampling time τ of the recording, the variance of the amplitude of fluorescence σ_f, the noise level of the data σ_n and m. The constant a is a parameter that has to be tuned depending on the data under study. Albano *et al.* [27] presented computational evidences that for a given time series, the singular–value spectrum depends principally on δ_w, in accordance with the results obtained by Caputo *et al.* [117], in connection with correlation dimension. Indeed, the windows length δ_w determines the *form* of the singular spectrum, with a rise in δ_w producing an increase

in the number of significant singular values. Therefore, before applying this method, a proper characterization of δ_w or $\{\delta, m\}$ is crucial for ensuring consistent outcomes. Moreover, the study of Kugiumtzis [402] provided a physical meaning to this time window length δ_w. The author suggested that, geometrically, δ_w complies $\delta_w \geq \delta_p$, where δ_p is the mean orbit period i.e. the mean time between two consecutive visits to a local neighborhood. We note thayt in our particular case, δ_p correspond to the mean width of the burst, so $\delta_p \approx \tilde{w}$, because it is the time required by the system to travel around an orbit. For low dimensional chaotic systems showing pseudo–periodicity, the mean orbital period can be naturally associated to the mean time between visits to a Poincaré section. The author argued that it may be reasonable to set δ_w equal to the "memory" of the system.

We also note that the singular values σ_j of $\mathbb{X}$ correspond the the square roots of the set of m non–zero eigenvalues $\{\sigma_i^2\}$, $i \in [0, m-1]$. Then, the dynamics of the cloud of points in an embedded attractor can be statistically described in a linear way by its principal axes. The decomposition of the embedding matrix can be then written as a lineal combination of its vector bases. Since PCA is the minimal representation of information that is coded in the system, it can be used to determine a suitable subspace to distinguish between patterns that belong to different classes. This idea has been nicely applied, in neuronal cultures similar to ours, to classify neuronal populations with distinct dynamics [609].

Finally, and practically speaking, PCA provides also a good tool to estimate noise–dominated coordinates. As already seen, PCA is an optimal coordinate transformation in the sense that it minimizes noise amplification [121, 271]. Indeed, PCA reduces noise by the switch to a new coordinate system that maximizes variance, and consequently, maximum signal-to-noise ratio. Strictly speaking, however, PCA can filter out only isotropic Gaussian noise. Broomhead and King [101] noted that often the singular spectrum decreases until it hits a plateau, after which the eigenvalues are roughly equal. One possible (but no necessary) explanation for a plateau is the presence of the Gaussian noise on the time series. Hence, in this case, the advantage of PCA over delays is that it brings to light this problem, and the delay reconstruction can be characterized roughly by PCA. For instance, the experimental data obtained from a deterministic dynamical system should have a spectrum of singular values that should split into a deterministic–dominated set and a noise–dominated one. The former would exhibit a rapid roll–off in magnitude down to the "noise floor", while the latter would exhibit a relatively small and nearly constant magnitude.

5.3 Recurrence Plots

Recurrence plots (RPs) were first introduced in the physics literature by Eckmann in 1987 [205] and it is a technique of nonlinear data analysis to characterize complex systems, detect hidden recurrent dynamical patterns and reveal non–stationarity [534, 41]. This method is used in this work with the aim to visualize and analyze the different recurrent structures emerging in the state space of experimental fluorescence data.

The recurrence plot shapes a two–dimensional graph that reveals all the instants in which the state space of a dynamical system *recur*. That is, the RP unfolds all the times

when the trajectory of the dynamical system visits roughly the same area in the phase space (*recurrence of the state*). In essence, RP consists in characterizing the distance matrix of all the recurrent states where only the nearest neighbors are plotted.

In this section we consider the analysis of the delay matrix $\mathbb{X}$ with embedding parameters $\{\delta, m\}$ calculated through the ER–method [262]. With this information at hand, the distance matrix R_{ik} of each state χ_i respect to their nearest neighbors χ_k is given by

$$R_{ik} = \varepsilon_i - d(\chi_i, \chi_k), \tag{5.44}$$

where ε_i is the cutoff distance that defines the *nearest neighbor* and $d(\chi_i, \chi_k)$ is the Euclidean distance between the states χ_i and χ_k. Here, the *nearest neighbors* are defined as the set of all the states χ_k lying inside the ball $B_{\varepsilon_i}(\chi_i)$ of radius ε_i centered at χ_i, i.e. $B_{\varepsilon_i}(\chi_i) = \{\chi_i : ||\chi_i - \chi_k|| \leq \varepsilon_i\}$. Our analysis is focused to analyze the distribution of these recurrent states. However, only two type of neighbors are of interest. Excluding noisy states, we were interested in the *sojourn points* (or *consecutive state*) and *true recurrence points* (or *Poincaré recurrence*) [258, 257].

The rationale of this classification lies on the two different mechanisms for the formation of recurrent neighbors. The first mechanism is simply that two points on the same orbit keep close together for sufficient time. This is the case of sojourn points defined as the sequence of $\chi_{i+1}, \chi_{i+2}, ..., \chi_{i+k}$ (excluding χ_i) that shape an orbit. Such closeness is called autocorrelation by Theiler [696], and tangential motion by Gao and Zheng [258, 257]. However, one needs to realize that spatial closeness does not necessary mean temporal closeness. The second mechanism is that pairs of states in different orbits keep close together for sufficient time. These are the Poincaré recurrence states, denoted as the sequence of states such that $\{||\chi_i - \chi_{i+\delta_p}|| \leq \varepsilon_i\}$, with δ_p the period of the orbit.

In Fig. 5.10A–left we show a 2D schematic outline of Poincaré recurrence points (violet dots) and sojourn points (pink dots) in $B_{\varepsilon_i}(\chi_i)$. A 3D schematic representation is shown on the right. We notice that the combination of two Poincaré points and the respective sojourn points generate diagonal lines in the RPs that are separated by the period the orbits (δ_p), as illustrated in Fig. 5.10B–left. For a pure periodic system, these lines are spread with infinite length (Fig. 5.10B–right). The analysis of these diagonal lines in the RPs was one of the main focus of interest in our research. However, before analyzing this different patterns, we must specify the determination of the cutoff radius ε_i and the norm used in our particular case, referred in Eq. (5.44).

Characterization of the cutoff radius. A crucial aspect of the analysis is the determination of the optimal radius ε_i. Indeed, a careful choice of the parameter ε_i is essential to ensure the consistency of the analysis. A ε_i too small would lead to lead to no recurrence points at all. Conversely, a ε_i too large would place every point close to any other point. Hence, a ε_i too large includes points in the neighborhood that are, simply, consecutive points on the trajectory. This effect is called *tangential motions* and causes thicker and longer diagonal structures in the RP. Indeed, the apparent patterns of the final plot depends on the values of such threshold. In this way, ε_i should not be chosen neither too large nor too small, and a compromise for its value has to be found.

The cutoff distance ε_i can be considered either variable or fixed. In the original definition of RPs, the neighborhood is a ball and its radius ε_i is chosen in such a way that it contains a fixed amount of nearest neighbors N_n of states χ_i [205], procuring an asymmetric matrix, i.e. $r_{ij} \neq r_{ji}$. Using this neighborhood criterion, ε_i can be adjusted

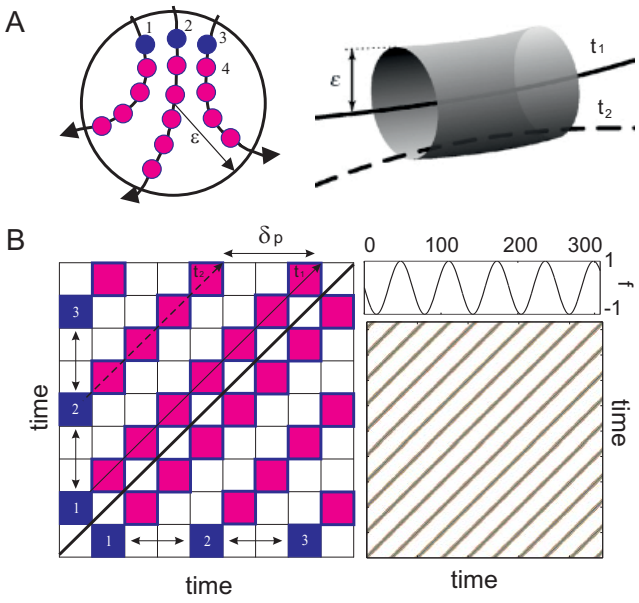

Figure 5.10: **Poincaré recurrence states and sojourn points: formation of diagonal lines**. (A) On the left, a schematic representation of recurrence points for Poincaré states (violet dots) and sojourn points (pink dots) in $B_{\varepsilon_i}(\chi_i)$. On the right, 3D representation of two parallel trajectories (orbits) enclosed in a tube of radius ε_i. A diagonal line in the RP would correspond to a section of a trajectory (dashed curve) that stays within an ε distance from another section (solid curve). A fixed radius is considered in this study for all states χ_i, and thus $\varepsilon_i = \varepsilon$. (B) Outline of the formation of diagonal lines in the RP for a periodic system (sinusoidal), which appear as a result of parallels orbits. On the left, detail of the lines. On the right, broader picture of the RPs. In the process of generating the diagonal lines, Poincaré and sojourn states are the only ones involved.

in such a way that the recurrence point density *Rec* has a fixed predetermined value, i.e. $Rec = N_n/N$. However, in the literature, the most widely extended criterion uses ε_i as a constant, so $\varepsilon_i = \varepsilon$, $\forall i$ [777]. Then, the interpretation of RPs is simplified and they become symmetric matrices, $r_{ij} = r_{ji}$. This point of view is the one applied to our work.

In order to characterized ε, different criterion (or "*rules of thumb*") has been proposed in the literature, and include: (i) ε should be a few per cent of the maximum phase space diameter [489], i.e. it should not exceed 10% of the mean or the maximum phase space diameter [780, 394]; (ii) ε should take a value such that the recurrence point density in RP is approximately 1% [778]; (iii) ε has to be chosen such that it is five time larger than the standard deviation of the observational noise, i.e. $\varepsilon \geq 5\sigma_n$ for noisy data [702]; and (iv) $\varepsilon \approx \frac{1}{10}\sigma_f$ [469], with σ_f the standard deviation of the fluorescence, and $\sigma_n < \frac{1}{50}\sigma_f$ [702].

For our studies, the criteria (ii) and (iv) were discarded since they provided too low values, making the analysis of the RPs structure unfeasible. Generally, rules (i) and (iii) gave similar patterns in RPs and they were good candidates for our fluorescence traces. However, we finally chose criterion (iii), where $\varepsilon \approx 5\sigma_n$, for two practical reasons. Firstly, because this approach is recommended for noisy data. And, secondly, in the context of CNQX disintegration experiments, we wanted to avoid a mobile threshold for each

disintegration stage. This choice is also appropriate in the context of noise. Indeed, during the disintegration experiments, the distribution of background noise shows almost no change. We note however, that the background noise slightly differed from a neuronal culture to another, and therefore we had the artifact that the threshold fluctuated across cultures.

We note that this threshold radius ε represents the error associated to the determination of the neighbor's distance. So, ideal recurrence states are all those that concur on the state space, and therefore their respective distances vanish ($d_{ik} = d_{ki} \to 0$, $\varepsilon \approx 0$). In this sense, one can choose the cutoff radius as $\varepsilon \approx \alpha\sigma_d$ where the σ_d is the standard deviation of delay matrix $\mathbb{X}$ and α is a parameter to determine, typically in the range $1 - 10$. It is worth observing that the matrix $\mathbb{X}$ is constructed using the same fluorescence data as the one for the delayed time interval, so σ_d takes values similar to σ_f, the standard deviation of fluoresce trace. However, taking $\varepsilon \approx \sigma_f$ would lead to a high density of recurrence states, making again difficult the detailed analysis of the structures in the RPs.

Finally, we stress that the criterion (ii) is adequate when treating non–stationary data since a non–scaling region in the recurrence point density will be detected [778]. Indeed, this concept introduces another possible criterion, consisting in the study of the variation of recurrence states density as a function of the cutoff radius. For stationary data, the threshold could be obtained by looking at a scaling region in the recurrence point density. This methodology procures similar values as criterion (iii), but the computational cost is higher. In Sec. 5.4.1 (Correlation Dimension) we will review this issue again, where we will test the validity of the results and pinpoint the relationship between the correlation integral of Grassberger and Procaccia [289, 288] and the density of recurrence states.

Characterization of norm. The norm function geometrically defines the size (and shape) of the neighborhood surrounding each reference point. The most common norms are referred in the literature as L_1–norm and L_2–norm (or Euclidean norm) and the L_∞-norm (Maximum or Supremum norm) [218, 702]. The recurrence area is the largest for the L_∞-norm, the fewest for the L_1–norm and intermediate for the Euclidean, L_2–norm. L_∞–norm allows to study RPs theoretically because the analytical expressions can be solved in a much simpler way than the others [218, 702]. It is also easier to compute than any other norm. L_∞-norm is broadly used since it serves to emphasize the broad characteristics of the reconstruction. At the other extreme, L_1–norm reveals more local details of the reconstruction. In this work we used the Euclidian norm as an intermediate compromise that distorts the least the emerging structures.

5.3.1 Structure of recurrence plots

At a first glance, the visual inspection of RPs allows for a qualitative analysis of low and high dimensional phase space trajectories, offering a global impression of the underlying dynamics of the system. Following Eckman *et al.* [205] and Marwan *et al.* [470], and according to different granularity levels, we can interpret RPs via large scale (*typology*) and small scale patterns (*texture*).

The *typology*, on the one hand, provide an overview of the involved dynamics of the system, and that can be classified as homogeneous, periodic, drifting and disrupted. Homogeneity in recurrence plots usually implies that the studied system is characterized

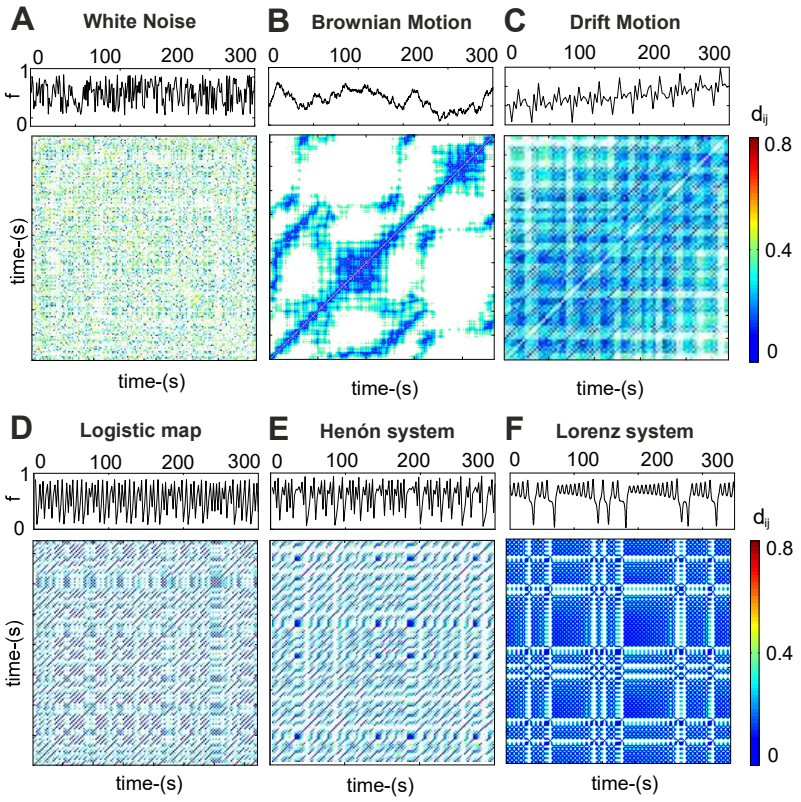

Figure 5.11: **RPs of noisy and chaotic signals.** Characteristic typology of RPs: (A) Homogeneous (uniform distributed White noise) (B) Disrupted (fractional Brownian motion, H=0.75) and (C) Drift (periodic structured with a linearly increasing term). (D) Logistic map (E) Henonón system and (F) Lorenz system.

by stationary and autonomous dynamics. On the other, the *texture* reveal small–scale structures in the RPs. Three different patterns can be usually distinguished, namely *single dots*, *diagonal lines* and *vertical* (or *horizontal*) lines. We note that $r_{ik} = r_{ki}$, and therefore the density, length and distribution of vertical lines are equal to horizontal ones.

Next we will provide some examples of RPs in different dinamycal systems to later discuss the information that the *texture* can reveal about the system.

In Fig. 5.11A a typical homogeneous recurrence plot for a white noise process is pictured, which is characterized by the absence of regular patterns. However, when the global dynamics is the result of an inference logic function or a well–defined one, then different structures in the RPs begin to emerge. In Fig. 5.11B one can observe the typical crumbly patterns arising during a fractional Brownian motion. In this case, disrupted patterns are shaped due to abrupt changes in the dynamics as well as extreme events, leading to white areas or colored bands in the RPs. Another interesting scenario correspond to a *drift typology* (Fig. 5.11C) in which there is a change in the density of recurrence points around the main diagonal. This pattern is typical for signals with drift. The top–left (or bottom–right) corner of the RP plot has a lower density of points, reflecting the slowly varying dynamics. To illustrate the structure of RPs in chaotic systems, Figs. 5.11D-F shows three typical cases of chaotic dynamics, namely Logistic

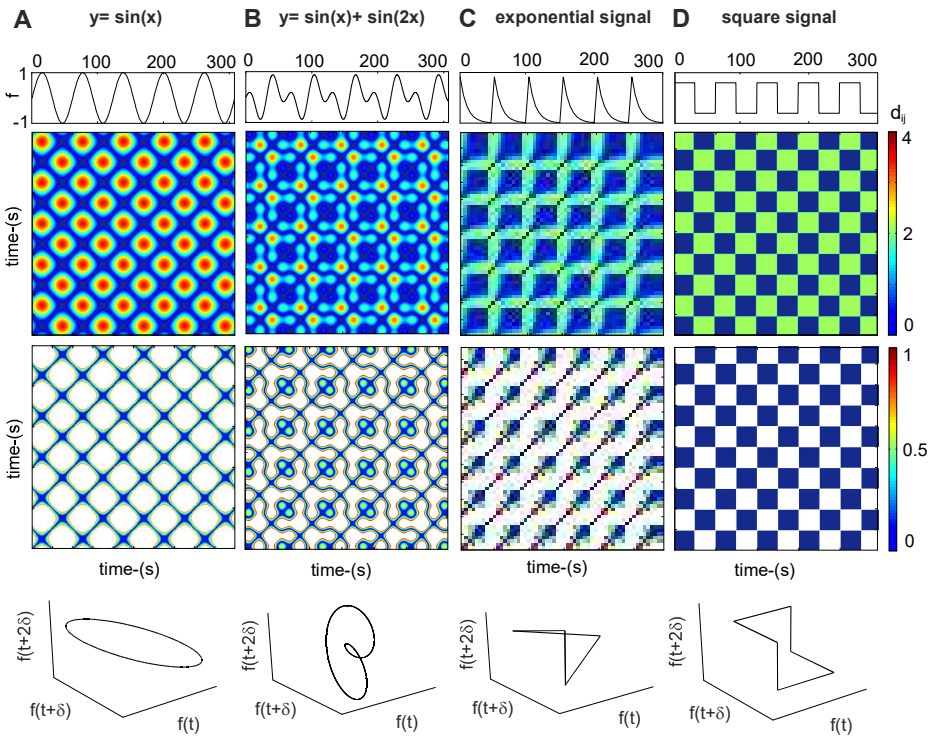

Figure 5.12: **RPs of periodic signals.** Characteristic *typology* of recurrence plot of periodic systems. (A) Sine wave, $y = sin(x)$. (B) Overlap of two sine waves with a $1:2$ relation of frequencies, $y = (sin(x) + sin(2x))$. (C) Periodic exponential function, $y = e^{-\tau x}$, with $\tau = 1/2$ (D) Square wave, $y = sign(sin(x))$. From top to bottom: traces, untresholded RPs (URPs), partially thresholded RPs with a lower cutoff ε, and SSRs. For the latter, and for clarity, only one orbit is represented.

Map (D), Henón system (E), and Lorenz system (F).

In general, systems in between periodic and chaotic behavior show clear repetitive structures such as diagonal lines or patterns of vertical and horizontal lines (*checkerboard* structures). This is clear in Fig. 5.12, which shows different periodic structures. In the figure, and for each signal, we show four levels of representation. From top to bottom, the first one is an example of the signal under analysis; the second one is the computed distance matrix, which can be viewed as *untresholded* RP (URP); the third one is the *thresholded* matrix, obtained after applying a cutoff ε; and the fourth one is a reconstruction of the orbits. Special emphasis should be placed on Figs. 5.12C-D since those structures are very similar to our fluorescence traces.

As introduced before, the local analysis of the RPs reveals small–scale structures, i.e. the *texture*.

The first structure of interest are *single dots*. They are characteristic of rare states that fluctuate over time. If single, isolated points are observed, then the dynamics can be viewed as uncorrelated or random (e.g., Fig. 5.11A).

The second structure are *diagonal lines*. They reflect segments of the trajectory that run parallel to another segment, i.e. the trajectory visits the same region of the state space at different times. Hence, diagonal lines are representative of correlated states

and reveal the internal recurrences of the system (e.g., Fig. 5.12). In our particular case, they would identify periodic bursting episodes. The length of diagonal lines is determined by the duration of such similar local evolution of the trajectory segments. We note that periodic dynamical systems present long diagonal lines that tend to infinity, whereas chaotic movements show shorter diagonal lines (e.g., Figs. 5.11D-F). One could also include *bowed* lines, i.e. lines with a non–constant slope. They would indicate that the evolution of states is similar at different epochs but with different velocity.

The third structure are *vertical (horizontal)* lines. They mark time intervals in which a state does not change, or change very slowly. In this case, one says that the system is trapped for some time. This 'trapping' is a typical behavior of laminar states and is termed *intermittency*. As shown in Fig. 5.12D, a bi–stable signal shows these trapped states, leading to a typical checkerboard structures in their typology. For completeness, we also include here the 'Laminar states'. They represent the vertical or horizontal lines that emerge after applying a threshold to the lower values of the RP, i.e. those areas in white. For chaotic systems (e.g. the Lorenz system in Fig. 5.11F), these lines would reflect drastic changes in the dynamics. In our case, the emergence of these white lines mark the beginning of a bursting episode.

5.3.2 Recurrence Quantification Analysis (RQA)

Recurrence Quantification Analysis was developed by Zbilut and Webber [779, 750] and extended with new measures of complexity by Marwan *et al.* [471]. The recurrence of states is a fundamental property of deterministic dynamical systems [42, 120, 373], and a quantification offers objective ways to investigate the underlying dynamics of a system. Indeed, the *measures* that are introduced in this Section quantify the three main texture structures of RPs outlined above, i.e. singular states, diagonal lines and vertical (or horizontal) lines.

For simplicity in the analysis of the data, we will consider thresholded RPs only. They are obtained by thresholding the distance matrix r_{ik} as

$$r_{ik} = \Theta(R_{ik}) = \Theta(\varepsilon_i - d(\chi_i, \chi_k)), \tag{5.45}$$

with Θ the Heaviside function. Through this operation, RPs emerge as *bi–color* maps.

Below we describe the considered measures. Their values in illustrative RPs are provided in Fig. 5.13.

1. **Density of Recurrence States (RR).** This is the most basic measure, and includes both single dots and lines. It is given by

$$RR(\varepsilon) = \frac{1}{T^2} \sum_{\substack{i,k=1 \\ i \neq k}}^{T} r_{ik}(\varepsilon), \tag{5.46}$$

   where T is the number of considered states χ_i.

2. **Density of Recurrence Singular States (RRS).** It is defined in the same way, but includes single dots only. Due to resolution effects, the recurrence singular states are defined as structures with a maximum thickness of 4 pixels, and that

corresponds to $\delta_{sp} < 100$ ms for $\tau = 20$ ms. In Fig. 5.13E one can observe that the density of recurrent states in the case of white noise is higher than for periodic (Figs. 5.13A-B) or chaotic dynamics (Fig. 5.13C-D).

3. **Measures based on Diagonal Lines.** Determinism or predictability inherent of the system in the RPs is reflected in segments of diagonal lines. Depending on their number, length and distribution, different statistics can be defined. The following statistics are the most important ones, and they are the core to later analyze the data of our experiments:

   - **Determinism** DET**.** It is the fraction of recurrence points that form diagonal structures longer than l_{min}, i.e.

   $$DET = \frac{\sum_{l=l_{min}}^{N} lP(l)}{\sum_{i,k}^{N} r_{ik}}, \tag{5.47}$$

   where *P(l)* is the histogram of the lengths l of the diagonal lines. In our analyses we consider a minimum length of 5 pixels ($\delta_{min} = 100$ ms for $\tau = 20$ ms). We note that, by definition, the RP always contains a diagonal line as bisector, termed the *line of identity (LOI)*. Hence, to study properties based on diagonal lines without artifacts, it is important to exclude the LOI together with other diagonal lines in a small corridor around the LOI. This small corridor sets the thickness of a diagonal line and represents the *tangential motion* of the phase space trajectory that results from the finite value of the threshold value ε. In our case we used $\delta_{Th} \sim 100ms$ (~ 5 pixels) for $\tau = 20$ ms to establish the thickness of the diagonal lines. As shown in Figs. 5.13A-B, DET is higher in periodic dynamical systems than in stochastic ones (Fig. 5.13E-F). Intermediate values are obtained in the case of chaotic behavior (Fig. 5.13C-D).

   - **Longest diagonal line** L_{max}**.** This measure quantifies the longest diagonal line found in the RP. L_{max} is simply the length of the longest diagonal line segment in the plot, excluding the main diagonal line of identity. Ideally, $L_{max} \to \infty$ for periodic dynamics, $L_{max} \to 0$ for stochastic movements, and exhibits intermediate positive values for chaotic behaviors (Fig. 5.13C-D).

   - **Divergence** Div**.** This measure is the inverse of L_{max}, i.e. $Div = \frac{1}{L_{max}}$. Div becomes a very important measure since it inversely scales with the most positive Lyapunov exponent [205, 714]. Indeed, positive Lyapunov exponents reflect the rate at which trajectories diverge. The higher Div, the more chaotic (less stable) the signal is. Thus, Div is related to the exponential divergence of the phase space trajectory and with the KS entropy of the system, i.e. with the sum of the positive Lyapunov exponents. The faster the trajectory segments diverge, the higher Div is (and the shorter the diagonal lines are).

4. **Measures Based on Vertical (or Horizontal) Lines.**

   We can find vertical (or horizontal) lines in the presence of laminar states in intermittent regimes. The measures based on vertical (or horizontal) lines are calculated according to their number, their length and their distribution. They are:

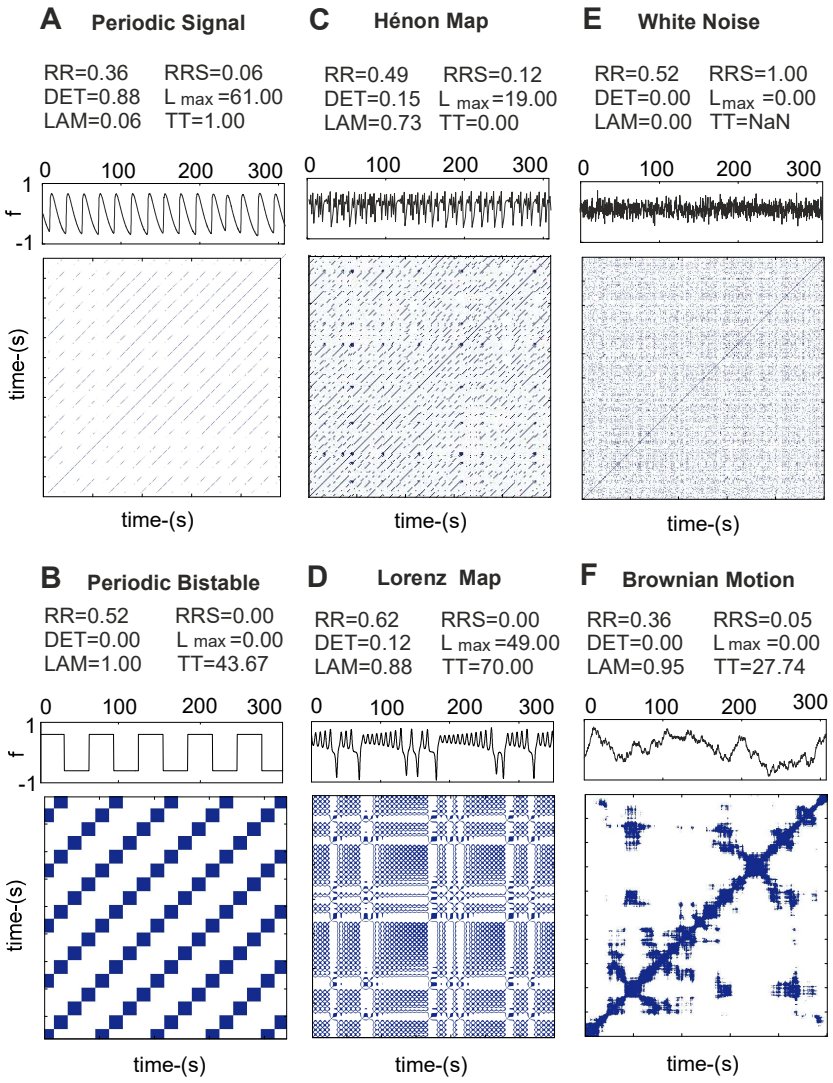

Figure 5.13: **RQA** Characteristic texture of RPs and RQA from: (A) Periodic signal ($y = sin(x)$), (B) Periodic bi-stable signal ($y = sign(sin(x))$), (C) Henonón system, (D) Lorenz system, (E) Homogeneous (uniform distributed White noise) (B) Disrupted (fractional Brownian motion).

- **Laminarity LAM.** It is analogous to DET except that it measures the percentage of recurrent points comprising vertical lines. Let the total number of vertical lines of length v in the RP be given by the histogram $P(v)$, then the ratio between the recurrence point forming the vertical structures and the entire set of recurrence points is computed as

$$LAM = \frac{\sum_{v=v_{min}}^{N} vP(v)}{\sum_{v=1}^{N} vP(v)}. \tag{5.48}$$

  The LAM is computed for those vertical lines of length v that exceed a minimal length $v_{min} = 5$ pixels. This parameter represents the occurrence of laminar states (intermittency) in the system, i.e. time intervals in which the system does not change, without describing the duration of the laminar phases. As observed in Fig. 5.13, LAM is very small for periodic dynamics (panel A), inexistent for stochastic processes (panel E) and prominent for chaotic behaviors (e.g panel D). Indeed, these structures are very characteristic in chaotic dynamics due to the natural tendency of these systems to shrink in some points and then extend across the state space. Contractions and expansions in the space state, thus, is the origin of high Laminarity. The extreme condition would be a bistable system such as the one in Fig. 5.13B and that produces a checkerboard pattern in the RPs, with $LAM = 1$. In bistable systems, dynamics switches between very different states or remains trapped in a given one for a considerable amount of time. We note that, when the transition regime from one state to the other is periodic, then the global dynamics will be also periodic (Fig. 5.13B), and not chaotic.

- **Trapping time TT.** This quantity provides the average length of vertical structures, and is given by

$$TT = \frac{\sum_{v=v_{min}}^{N} vP(v)}{\sum_{v=v_{min}}^{N} P(v)}. \tag{5.49}$$

  TT estimates the mean time that the system is trapped at a specific state. In our experiments, TT would be strongly linked to the average inter–burst interval, $\langle IBI \rangle$.

5.3.3 RQA stability

RQA is independent of data set size, of data stationarity, and of assumptions on the statistical distribution of data. RQA gives a local view of the series behavior, because it analyses distances of pairs of points, not a distribution of the distances. In consequence, unlike autocorrelation, RQA is able to analyze fast transients and to localize in time the features of dynamical variations. Thus, an important aspect that offers RQA is that it allows to detect dynamical transitions. We note that DET and L_{max}, which are based on the diagonal lines, show clear maxima at the periodic–to–chaos (or vice versa) transitions [714]. The measure of L_{max} finds all of such transitions, but DET does not detect all of them.

Interestingly, the ratio DET/Lam can be useful to discriminate between periodic–to–chaotic (or vice versa) transitions. On the other hand, since for periodic dynamics the measures quantifying vertical structures are zero, different chaotic regimes can be identified by using measures based on vertical (or horizontal) lines [471] such as LAM. As we will see later in our cultures, their low–dimensionality made very difficult to detect chaotic transitions and, therefore, such a study was not carried out.

Finally, it is also important to highlight that the main drawback of RQA is that the set of statistical estimators are subject to wide fluctuations depending on the cutoff radius ε. This difficulty largely hinders the analysis and its posterior interpretation, and we will see in the next section.

5.4 RQA Testing

5.4.1 SSR, RPs and RQA Test: Correlation Integral

The correlation integral of Grassberger and Procaccia [289, 288] is a measure of the frequency with which patterns in a data series are repeated. From the embedded data, the correlation integral is calculated as

$$C_T^{(m)}(\varepsilon) = \frac{1}{T(T-1)} \sum_{i \neq j} \Theta(\varepsilon - d(\chi_i, \chi_j)), \tag{5.50}$$

where $\Theta(x)$ is the Heavyside function ($\Theta(x) = 0$ for $x \leq 0$ and $\Theta(x) = 1$ for $x > 0$), $d = d_{ij}$ is the Euclidian distance between two states χ_i and χ_j, and T is the number of states. The correlation integral $C_P^{(m)}(\varepsilon)$ provides the probability of measuring a distance smaller than ε between two randomly chosen points χ_i and χ_j. We note that Eq. (5.50) is similar to Eq. (5.46) for the density of recurrent states except for the proportionality factor, and depends on T^{-1}. Like in RQA, in order to avoid spurious effects we carried out the 'Theiler correction' in the correlation integrals [696, 697]. Theiler suggested to exclude from the calculation of Eq. (5.50) all vectors whose corresponding coordinates are correlated. This can be done by using a window $w > 1$. For a sampling frequency f, the length of the window is, in time domain, equal to $T = w/f$. Theiler suggested taking T equal to the 'autocorrelation time' of the signal. In our studies, we used a fixed value of $\delta_T \sim 100$ ms.

Then, as the number of points tends to infinity, and as the distance between them tends to zero, the correlation integral for small values of ε takes the following scaling form, and independently of the embedding dimension m

$$C(\varepsilon) \sim \varepsilon^{D_2}, \tag{5.51}$$

with the exponent providing the correlation dimension D_2 of the attractor corresponding to the measured signal. Hence, D_2 can be obtained from the local slope of $log(C(\varepsilon))$ as a function of $log(\varepsilon)$, where the range of ε–values of this linear region is called the 'scaling region'. This estimate is called the 'coarse grained estimate' of D_2. Formally,

$$D_2 = \lim_{\varepsilon \to 0} \frac{log(C(\varepsilon))}{log(\varepsilon)}. \tag{5.52}$$

We were interested in applying these analysis to our experimental data. In Fig. 5.14A the correlation integral is plotted in a double logarithmic manner, with the x–axis corresponding to $\log(\varepsilon)$ and the y–axis corresponding to $\log(C(\varepsilon))$ for a mature culture ($DIV = 16 \pm 2$)). The different lines in the plot correspond to the correlation integral for increasing embedding dimensions, starting with $m = 2$ and ending with $m = 30$. The slope of the correlation integral in the linear scaling region (II) corresponds to the value of the estimated correlation dimension D_2 of the attractor in the state space. This can be seen in a different way in Fig. 5.14B. Here the first derivative of the correlation integral —which corresponds to the local slope of the plot in (A)— is plotted as a function of $\log(\varepsilon)$. In case that a plateau is present in this D_2–plot, a numerical estimation of D_2 of the system can be simply obtained by reading its value on the y–axis. This is actually what we observed along region II (green shaded area), and obtained $D_2 \simeq 2.4 \pm 0.3$ ($m \simeq 8 \pm 1$) for [E+I]-network, $D_2 \simeq 1.1 \pm 0.3$ ($m \simeq 3 \pm 1$) and $D_2 \simeq 1.3 \pm 0.3$ ($m \simeq 4 \pm 1$) for [E]-network with [CNQX]=0 nM and 800 nM, respectively.

We note that the precision of the method is not sufficient to determine whether the dimension takes null, integer or fractional values. However, since $m > 2D_2 + 1 \simeq 2d + 1$, this alternative method provides us a lower limit of the embedding dimension m and hence bounds the real dimension of the attractor d. In conclusion, this method is an alternative way to test the validity of state space reconstruction. An other important consideration is that, the emergence a plateau through the collapse of all the curves for any m, ensures that the structure of the reconstructed attractor (and the morphology of RPs) is similar independently of m in this range of ε.

Along region II, the estimation of RQA fluctuates to a lesser extent in comparison with the other two regions, whereas in regions I and III the fluctuations and variability are too high to draw conclusions on the underlying dynamics of the system. We note that region I appears due to the short duration of the experimental signals and their noisy nature. Additionally, since all recordings have the same duration T and the same background noise, it is natural to observe in region I the same fluctuating behavior and structure for the three experimental conditions.

Fig. 5.14B also shows that regions II and III decrease in the course of disintegration. These regions actually disappear when the network is silenced (at about [CNQX]$\simeq=$ 2000 nM). This behavior indicates that regions II and III heavily depend on the bursting dynamics, either from the number or shape of the bursting of episodes. Then, the minimum ε_0 (dash black vertical line), and that marks the border between regions I and II, gives the optimum neighbor cutoff radius ε. We note that this value can also be estimated by calculating the density of recurrence states as a function of ε and by determining the ε of the crossover between regions I and II. Such an alternative approach is provided in Fig. 5.15A). It is worth noting that, in our specific experimental case, the procured values of ε_0 through Fig. 5.15A are very similar to the ones obtained through the approximation of $\varepsilon = 5\sigma_s$ along Region II. Hence, in our fluorescence traces, these two criterion are suitable to choose an appropriate threshold radius, although the first choice is computationally more efficient. Additionally, as shown in Fig. 5.15B-C, it is important to highlight the strong dependence of DET, LAM and L_{max} on ε, which makies the overall analysis very difficult.

It is important to remark that having a finite correlation dimension D_2 does not

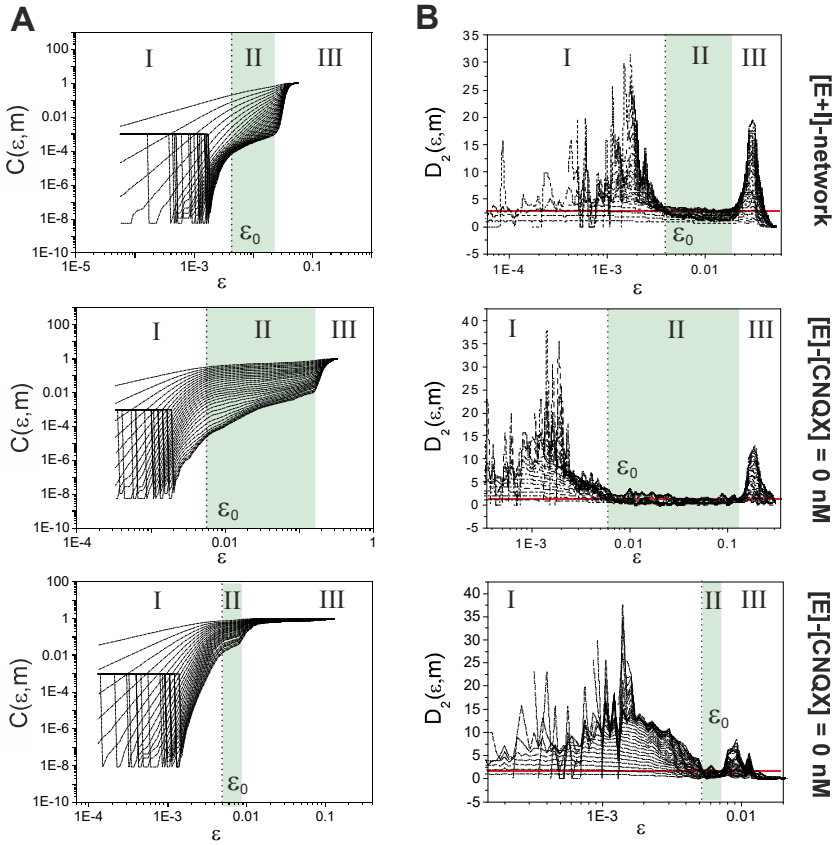

Figure 5.14: **Determination of Correlation Dimension.** Computation of correlation integral $C(\varepsilon)$ (A) and correlation dimension (B) for a mature culture ($DIV = 16 \pm 2$) in the disintegration process. In (B) the numerical estimation of D_2 (horizontal red continuous line) obtained are the following: $D_2 \sim 2.4 \pm 0.3$ ($m \sim 8 \pm 1, \varepsilon_0 \sim 4{\cdot}10^{-3}$, $\varepsilon \in [4{\cdot}10^{-3}, 2{\cdot}10^{-2}]$) for [E+I]-network, $D_2 \sim 1.1 \pm 0.3$ ($m \sim 3 \pm 1, \varepsilon_0 \sim 6{\cdot}10^{-3}$, $\varepsilon \in [6{\cdot}10^{-3}, 1{\cdot}10^{-1}]$) and $D_2 \sim 1.3 \pm 0.3$ ($m \sim 4 \pm 1, \varepsilon_0 \sim 5{\cdot}10^{-3}$, $\varepsilon \in [5{\cdot}10^{-3}, 7{\cdot}10^{-3}]$) for [E]-network with [CNQX]=0 nM and 800 nM respectively. The minimum ε_0 (dash black vertical line), border of region I-II, give the optimum neighbor cutoff radius ε. The existence of one plateau (region II, shaded area) indicates the emergence of well defined attractor. In this region the morphology of RP is qualitatively similar and RQA fluctuate to a lesser extent.

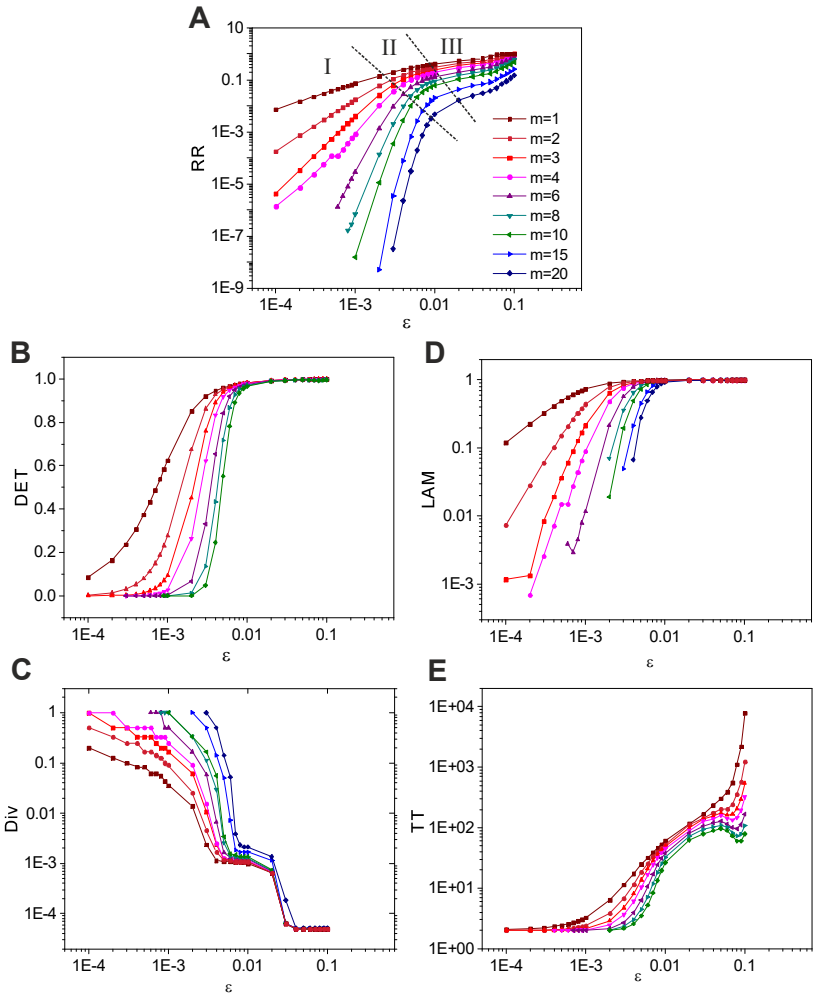

Figure 5.15: **Density of recurrence states and RQA measures in function on cutoff radius and embedding dimension.** (A) Density of recurrence states in function on ε and m for a 'E+I' netwrok for the experiment of Fig. 5.14. The existence of one plateau (region II) indicates the emergence of well defined attractor. (B-D) Testing RQA measures in function on ε and m: (B) Determinism (DET), (C) maximum diagonal line length (L_{max}) (D) Laminarity (LAM) and (E) mean vertical (or horizontal) line length (TT).

necessary imply the existence of chaotic dynamics in the neuronal cultures, since colored noise may also give rise to it [533]. In order to distinguish chaos from noise, one usually builds a control signal that has the same power spectrum as the measured one, but with randomized phases. Then, one compares the measured and control signals via the correlation integral slope. Only when the two look different one can conclude that the measured signal is of chaotic nature and not noise. This analysis is called *surrogate data testing* and is an important validation approach in nonlinear statistical physics to confirm the existence of inherent nonlinear behavior. This analysis is treated in the next section.

5.4.2 Tests for nonlinearity

Traditional nonlinearity tests

The degree of nonlinearity can be measured in several ways. All quantifiers of nonlinearity show fluctuations, and therefore it is necessary use Monte Carlo techniques to assess the significance of the results. The method of *surrogate data* [699] has become very useful to address such a question, and provides a general and flexible statistical approach for identifying nonlinearity in time series [616].

There are four main aspects concerning surrogate data that need to be considered [700, 618]: (i) the exact definition of null hypothesis H_0, (ii) the generation of a surrogate data set, (ii) the choice of nonlinear statistical discriminators q, and (iv) the statistical test. Additionally, as standard procedure, one first makes a hypothesis about the data and then tries to falsify such a hypothesis.

In essence, a null hypothesis H_0 is first formulated, for example that the data has been created through a stationary Gaussian linear stochastic process (ARMA process). Then, several random surrogate data sets are generated according to H_0 using Monte Carlo techniques. Finally a statistic discriminator —in general, the value of a nonlinear parameter— is calculated for both the original time series and the surrogate set. If the value of the computed statistic discriminator for the original series is significantly different than the value for the surrogate set, the null hypothesis is rejected. One concludes that the data were not generated through a linear process and nonlinearity is assumed.

Null hypothesis. In our studies, the null hypothesis that we formulated was that the underlying dynamics was generated as a stationary Gaussian linear process. According to this null hypothesis, $f(t_i) = h(s(t_i))$, where $s(t_i)$, $i = 1, ..., T$, is a realization of a Gaussian linear stochastic process, and h is a static measurement function, possibly nonlinear. Then, the null hypothesis of an underlying Gaussian linear stochastic process can also be formulated by stating that all structures to be found in a time series are exhausted by computing first and second order quantities: the mean and the variance of amplitude distribution and the auto–covariance function (or power spectrum, PS) of the time series. By implication, the generation of a surrogate data set $\{f_s\}$ (of the same length T) to represent this null hypothesis, must fulfill the following two conditions: (i) $PS_{f_s} = PS_f$ (or $\rho_{f_s} = \rho_f$) , (ii) $A_{f_s} = A_f$, where PS is the power spectrum, ρ is the autocorrelation function and A is the empirical amplitude distribution. To determine these quantities we proceed as follows.

Surrogate Data For univariate time series, two approaches have been suggested for generating surrogate data that is consistent with the null hypothesis of linearly Gaussian processes. A first approach consists in fitting an explicit linear model to the data (e.g., an autoregressive moving average, or ARMA, model) and then to iterate the model to generate the data [287, 99, 405, 255]. A second approach considers the Fourier Trasnform (FT) of the data set, randomizes the phases and then inverts the transform [532, 701, 376].

Although these two approaches are essentially equivalent, in practice they present substantial differences. Additionally, the ARMA one has a major drawback, and is that the goodness of the fit is not always possible. Indeed, when the observed time series is nearly periodic or a highly sampled continuous data, then the values of the ARMA coefficients are underestimated and the algorithm diverges to infinity. Interestingly, algorithms based on FT are numerically more stable and computationally more efficient. And the strategies for a randomization of the phases (or a shuffling of the time–order of the data) are robust when compared to a smooth fit. For FT, any discretization that was present in the original data will be also reflected in the surrogate data. Hence, in this thesis, the FT approach was used.

The FT algorithm is described in more detail in Ref. [699]. Given a time series $f(t)$, we first apply $\mathcal{F}$, the discrete Fourier transform operator, to obtain $\widehat{\mathrm{F}}(k) = \mathcal{F}\{f(t)\} = A(k)e^{i\phi(k)}$ where $A(k)$ is the complex amplitude and $\phi(k)$ is the phase. Then a 'phase–randomized' Fourier transform $\widehat{\mathrm{F}}(k)$ is carried out by rotating the phase ϕ at each frequency through an independent random variable φ which is chosen uniformly in the range $[0, 2\pi)$. In order for the inverse FT to be real one must symmetrize the phases, so that $\phi(k) = -\phi(-k)$. Finally, the application of the inverse FT provides the surrogate data $f_s(t)$.

A major limitation of the FT algorithm is that it does not reproduce 'pure' frequencies sufficiently well. Nearby frequencies in Fourier spaces 'contaminate ' one another, and hence when their phases are randomized, they end up 'overlapping' each other and spurious low–frequency effects are introduced. As we observed int the previous Chapter, a second limitation is that spurious high frequencies can be also introduced as an artifact of 'pure' FT use. Indeed, when assuming that a time series is periodic with period N, a jump–discontinuity arises between the last and first points of the time series, introducing artificial high frequencies in the spectrum. Although for highly sampled continuous data this effect is strong, it should not be important when the time series is stationary and is sufficiently long, much longer that the period associated to the dominant frequency of the signal.Our fluorescence traces can be viewed as stationary (in the sense that network intrinsic dynamics and connectivity do not chage) but they are in general short. Hence, in order to reduce this artifact, it is important to *tailor* the length T of the data set so that $f(t_0) \approx f(t_T)$. Additionally, this problem can also be addressed by windowing the data before computing the FT, as carried out in the Chapter 4. Then, the time series is multiplied with a window function which vanished at the ends. Since windowed Fourier Transform (wFT) also introduces a spurious low–frequency at the PS, one needs to introduce further corrections.

Overall, to correct these biases in the PS and equalize the amplitude distribution of both sets (the original data and surrogates), two different approaches have been proposed in the literature, namely the Amplitude Adjusted Fourier Transform (AAFT) and the Iterative Amplitude Adjusted Fourier Transform (iAAFT). These are popular algorithms

to generate an ensemble of surrogate realizations consistent with the null hypothesis of linearly Gaussian process. Both conserve the amplitude distribution in the real space and accurately reproduce the PS of the original data sets.

The AAFT method was first discussed in Ref. [699]. The first step consists in creating a Gaussian time series $f_g(t)$, where each element is generated independently from a Gaussian pseudo–random number generator. Next, the time sequence $f_g(t)$ is reordered so that the ranks of both original and surrogated time series agree. This means that if $f(t_n)$ is the nth–smallest of all the $f(t_i)$, $\forall\ i \in [1, T]$, then $f_g(t_n)$ will be the nth–smallest of all the $f_g(t_i)$,$\forall\ i \in [1, T]$. Then, the built $f_g(t)$ is a time series which 'follows' the original time series $f(t)$ and has a Gaussian distribution of amplitudes. The surrogate of $f_g(t)$, so–called $f_{g,s}(t)$, is created using the FT or wFT algorithm. Finally, if the original time series $f(t)$ is time reordered so that it follows $f_{g,s}(t)$ in the sense that the ranks agree, then the time–reordered time series provides a surrogate $f_s(t)$ of the original time series $f(t)$ which matches its amplitude distribution. The 'underlying' time series $(f_g(t), f_{g,s}(t))$ are Gaussian and they are generated through a linear stochastic mechanism.

The AAFT algorithm should be correct asymptotically in the limit of $T \to \infty$. For finite T however, $f(t)$ and $\{f_s(t)\}$, have the same distribution of amplitudes by construction, but they do not usually have the same PS. The reason for this effect lays in the performed phase randomization procedure, which preserves the Gaussian distribution only on average, but not the fluctuations. Hence, spurious nonlinearities are introduced in the two–amplitude adjustment procedure, which will result in a bias on the empirical power spectrum. Effectively, a white component to the spectrum is added, which introduces a bias towards a slightly flatter spectrum. Hence, an altered spectrum may emerge due to such systematic errors, leading to a false rejection of the null hypothesis.

The iAAFT, precisely comes here into play with the aim of correcting this deviation. It was proposed in Ref. [616] as an improved algorithm of AAFT, and its goal is to iteratively approach the original PS or stop when no changes in the amplitudes are observed. The algorithm starts with an AAFT surrogate or with a random shuffle of the data points. In each iteration the PS is adjusted first and then the amplitudes. To obtain the desired PS, at each iteration the FT of iterated time series is calculated and its squared coefficients are replaced by those of the original time series. The phases are kept unaltered. After this step, the amplitudes of the iterated time series are altered. Hence, in the second iteration, the amplitudes are adjusted by ranking their values and replacing them by the values of the original time series, leading to the same ranking. Both iterative steps are repeated until a convergence threshold is reached. In Fig. 5.16A one can observe different surrogates generated with the iAAFT, and compared with the original data.

Nonlinear statistical discriminant. Different measures of nonlinearity have been traditionally implemented:

1. *Higher order cumulants* of the auto–covariant function or the PS are the traditional measures of nonlinearity [617, 374, 577]. Hence, linear (two point) auto–covariances can be generalized by introducing more than one lag. In the spectral domain, this generalization leads to the bi–spectrum and poly–spectra [577]. We used the third–

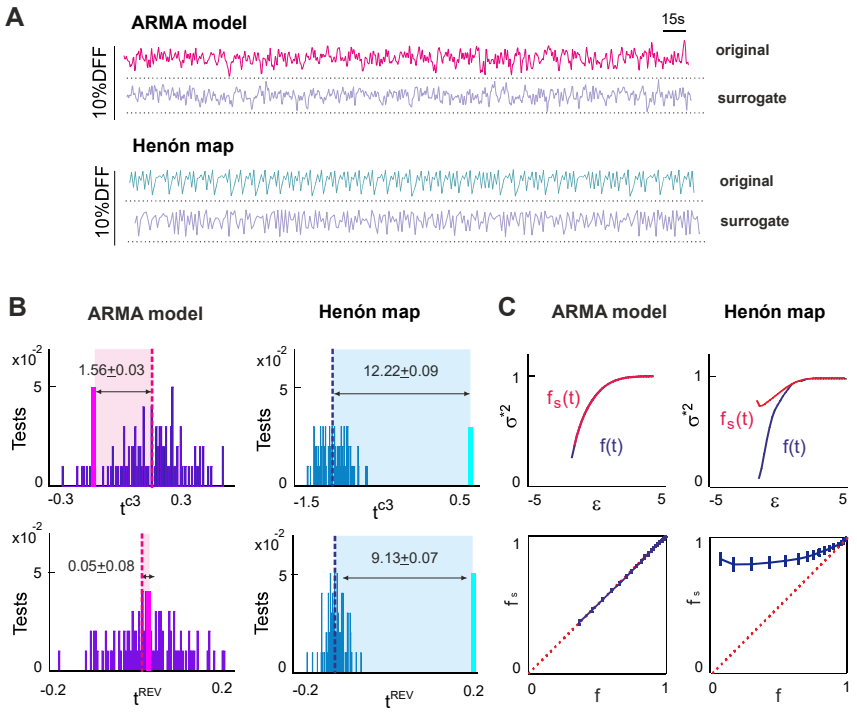

Figure 5.16: **Test for nonlinearity**. (A) Generation of Surrogates using iAAFT algorithm for an ARMA model and Henón Map. (B) Statistical test for nonlinearity discriminating on ARMA model and Hénon map. The traditional measures used are the followings: third–order covariance (t^{C3}, top) and (ii) time–reversibility quantity (t^{REV}, bottom). In each subplot the measure of $\mathscr{S}$ is annexed. (C) Detection of Nonlinearity using Delay Vector Variance (DVV). DVV plots (top) and DVV scatter diagrams (bottom) are annexed by the respective models.

order auto–covariance, defined as

$$t^{C3}(\delta) = \frac{\langle f(t_k) f(t_k - \delta) f(t_k - 2\delta) \rangle}{|\langle f(t_k) f(t_k - \delta) \rangle|^{\frac{3}{2}}}. \tag{5.53}$$

2. *Time reversibility*. It is a simple quantity which is frequently used to detect deviations from time–reversibility, and is given by

$$t^{REV}(\delta) = \frac{\langle (f(t_k) - f(t_k - \delta)^3) \rangle}{\langle (f(t_k) - f(t_k - \delta)^2) \rangle^{\frac{3}{2}}}, \tag{5.54}$$

where δ is the time delay. Since the statistics of a linear stochastic process is always symmetric under time reversal, t^{REV} can be a strong signature of nonlinearity. Hence, this quantity is one of the most attractive discriminants, as is discussed in detail in Ref. [193]. In particular, it has been widely used for testing for nonlinearity with surrogate data [699, 706].

Statistical Test. To compare the differences between the original and surrogated distributions, we use a Student–t test. We define our measure of 'significance' as the

difference between the original, q, and the mean surrogate value, μ_{q_s}, divided by the standard deviation of the distribution of q_s surrogates, i.e.

$$\mathscr{S} \equiv \frac{|q - \mu_{q_s}|}{\sigma_{q_s}}. \tag{5.55}$$

Although *significance* is properly a dimensionless quantity, it is usual to provide values of $\mathscr{S}$ in terms of 'sigmas'. The p–value is given by $p = \mathrm{erfc}(\mathscr{S}/\sqrt{2})$ and corresponds to a Gaussian–distributed statistics of surrogates. Numerical experiments showed that this is a reasonable approximation and computational efforts are very small [699]. A value equal to or exceeding 2σ supports the rejection of the null hypothesis at 95% confidence level.

Through standard propagation of errors, we write the error bar on $\mathscr{S}$ as $\Delta\mathscr{S}$, i.e.

$$\begin{aligned}\left(\frac{\Delta\mathscr{S}}{\mathscr{S}}\right)^2 &= \left(\frac{\Delta|\mu_q - \mu_{q_s}|}{|\mu_q - \mu_{q_s}|}\right)^2 + \left(\frac{\Delta\sigma_{q_s}}{\sigma_{q_s}}\right)^2 \\ &= \frac{(\Delta\mu_q)^2 + (\Delta\mu_{q_s})^2}{(\mu_q - \mu_{q_s})^2} + \left(\frac{\Delta\sigma_{q_s}}{\sigma_{q_s}}\right)^2.\end{aligned} \tag{5.56}$$

Assuming that the error of the sample mean based on T observations is given by $(\Delta\mu)^2 = \sigma^2/T$, and the error of the sample standard deviation is $(\Delta\sigma)^2 = \sigma^2/T$, we can write

$$\left(\frac{\Delta\mathscr{S}}{\mathscr{S}}\right)^2 = \frac{\sigma_q^2/T + \sigma_{q_s}^2/T}{(\mu_q - \mu_{q_s})^2} + \frac{1}{2T}. \tag{5.57}$$

The absolute error bar is then given by

$$\Delta\mathscr{S} = \sqrt{(1 + 1/2\mathscr{S}^2)/T + (\sigma_q/\sigma_{q_s}^2)/T}. \tag{5.58}$$

When only a single realization of the time series is available, then $\sigma_q = 0$ and the second term of the above Eq. (5.58) is ignored.

As an example, we carried out a statistical test for nonlinearity on the ARMA linear model and on the Hénon map. As shown in Fig. 5.16, the null–hypothesis is rejected in the Hénon map, and using either t^{C3} ($\mathscr{S} = 12.22 \pm 0.09$) or t^{REV} ($\mathscr{S} = 9.13 \pm 0.07$). However, the ARMA is not statistically different from its surrogates.

Delay Vector Variance Method

The 'delay vector variance' (DVV) method proposed by Gautama *et al.* [263] is a phase–space based method for detecting the presence of determinism and nonlinearity in a time series. This approach is somehow related to the false nearest neighbors method [381, 373, 380] and the one proposed by Kaplan [58, 375].

The implemented algorithm is summarized below. For an optimal embedding parameters $\{\delta_0, m_0\}$, we generated the matrix of delays and computed the mean, μ_d, and standard deviation, σ_d, over all pairwise distance between states, $d_{ij} = d(\chi_i - \chi_j)$, with $i \neq j$. Next, we generated the neighbor set Ω_i of state χ_i such that $\Omega_i = \{\chi_i \mid d_{ik} \leq \varepsilon\}$. This set comprised all the states (or DVs) that were closer to χ_i state than a certain

distance ε, taken from the interval $[min\{0, \mu_d - n_d\sigma_d\};\ \mu_d + n_d\sigma_d]$, i.e. uniformly spaced, where n_d is a parameter controlling the span over which to perform the DVV analysis. Next, for every set Ω_i, the variance of the corresponding targets, σ_i^2, was computed. The average over all sets Ω_i, normalized by the variance of the time series σ_f^2, yielded the measure of unpredictability σ^{*2}

$$\sigma^{*2} = \frac{(1/T)\sum_{k=1}^{2}\sigma_k^2}{\sigma_f^2}, \tag{5.59}$$

where T is the number of sets $\Omega_i(\varepsilon)$.

A graphical representation of the DVV analysis is obtained by plotting σ^{*2} as a function of the standardized distance ε. The *minimum target variance*, σ_{min}^{*2} which corresponds to the lowest point of the curve, is a measure of the amount of noise present in the time series. Indeed, σ_{min}^{*2} is inversely proportional to the prevalence of a deterministic component over a stochastic one. Hence, low σ_{min}^{*2} values indicate a strong deterministic component.

On the other hand, the analysis addressing the linear or nonlinear nature of the original time series is examined by performing DVV analysis on both the original and the set of surrogate time series. Due to the standardization of the distance axis, these plots can be conveniently combined within a scatter diagram, where the horizontal axis corresponds to the DVV plot of the original time series, and the vertical to the surrogated time series. If the original time series yields to DVV plots that are similar to the surrogates, then the DVV scatter diagram falls in the diagonal line, and the original time series is judged to be linear. Otherwise, the DVV scatter diagram deviates from the bisector line and the original time series is judget to be nonlinear. An example is provided in Fig. 5.16C, for the ARMA model and the Henón map. The deviation from the bisector line is clear for the latter and, thus, the system is ascribed to be nonlinear. The degree of nonliearity can be qunatified through the root mean square error (RMSE) between the σ^{*2}'s of original time series and the σ^{*2} of the average over the DVV plots of the surrogate time series. In this way, a single statistical test t^{DVV} is obtained as

$$t^{DVV} = \sqrt{\langle(\sigma^{*2}(\varepsilon) - \frac{\sum_{i=1}^{N_s}\sigma^{*2}(\varepsilon)}{N_s})^2\rangle}, \tag{5.60}$$

where $\sigma^{*2}(\varepsilon)$ is the target variance at distance ε from the ith surrogate, and the average is taken over all the distances ε that are valid in both the surrogates and original DVV plots.

5.5 Case Study - Cortical Cultures

5.5.1 Fluorescence traces and orbits

We investigated the structure of the fluorescence traces in cortical cultures using different interventions, either along maturation of the networks or by weakening the excitatory connectivity (see Chapter 2). Figure 5.17A shows two typical experiments, one corresponding to the maturation of the network along development (days *in vitro*, DIV), and

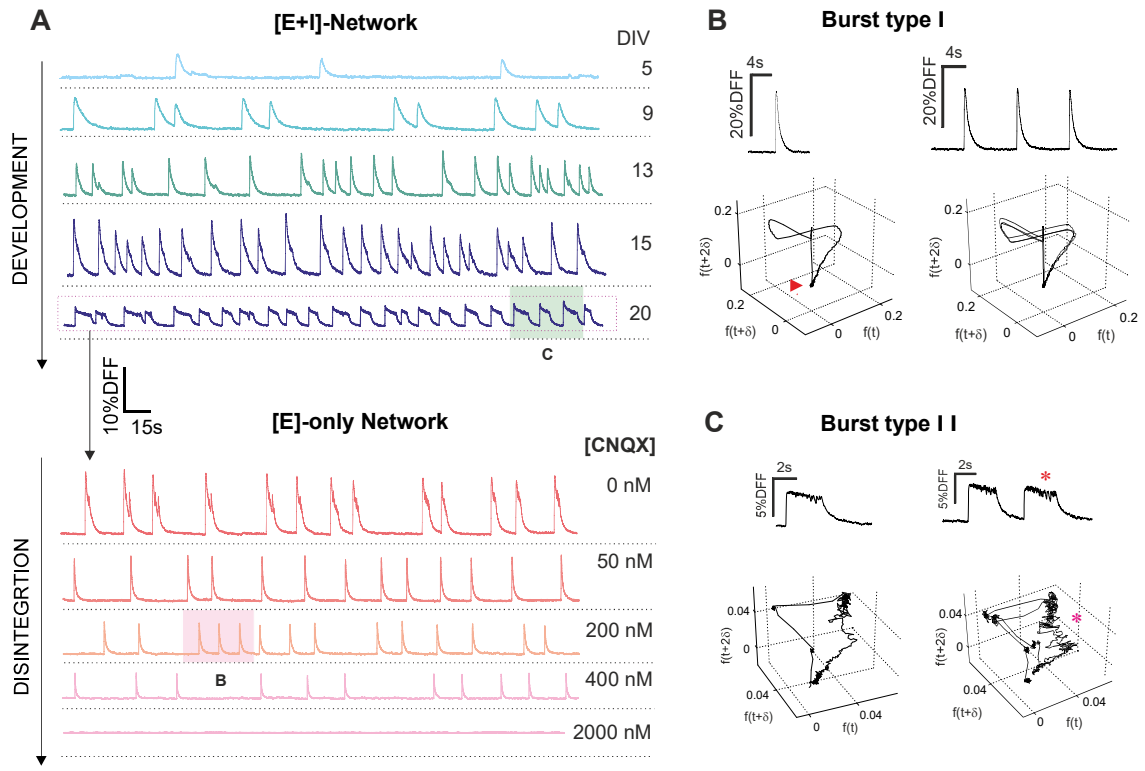

Figure 5.17: **Characteristic fluorescence traces and state space reconstruction (SSR)**. (A) Typical fluorescence traces for representative experiments, and illustrating the average fluorescence of the neuronal network along CNQX disintegration experiments and maturation. (B) The plots show the phase portraits constructed using the time delay method for two fluorescence traces corresponding to burst type I (left) and a type II (right). The fluoresce traces corresponding to the phase portrait are shown in the inset.

another corresponding to the disintegration through CNQX at a particular DIV. For the maturation experiments, the first signs of activity are observed at DIV 5, and it is characterized by the existence of bursts with small amplitude A and long inter–burst interval IBI. Typically, as maturation progresses, A gradually grows and IBI decreases, both reflecting a gradual increase in activity. For the disintegration experiments, we consider a mature network at DIV 16. The fluorescence trace when both excitation and inhibition are active ('E+I' network) shows relatively low A and low IBI. When inhibition is blocked, A and IBI substantially increase, reflecting an increase in average connectivity for the former and the entire depletion of neurotransmitters for the latter. As CNQX is applied, A gradually diminishes and the spontaneous activity events become rare, i.e. IBI also increases. These collection of traces show that the shape of the burst, and their inter–timing, convey the most significant information of the dynamics of the system.

Our goal is to unveil dynamical properties of the network from these traces. We apply the *time–delay method* to these temporal series to obtain the corresponding underlying dynamics. Two different structures of bursts (Type I and II) are typically found in our

fluorescence traces, as one can observe in Fig. 5.17B. An illustrative example of Type I bursts is shown in Fig. 5.17B (top), which depicts the space state reconstruction for a single burst (left) and a short series of them (right). The reconstruction was carried using a particular value of the delay time δ, whose computation is described later. Conceptually, the noisy contributions of the fluorescence signal are concentrated in a small region in the space state plot (indicated with a red arrowhead). The fast increase in fluorescence upon firing corresponds to a sharp jump in the space state, and the subsequent decay of fluorescence in the burst is reflected as a long excursion in the space state. The more complex the structure of the burst, the longer the excursion. As an example, we provide in Fig. 5.17B (bottom) another burst that significantly differs in structure from the above one. We note that bursts initiate and finish in the noisy areas of the fluorescence signal and therefore they can be viewed as closed *orbits* in the space state. Hence, the variability between orbits along the entire recording, as shown in the right panels of Fig. 5.17B, effectively reflects the dynamic richness of the neuronal network.

5.5.2 Determination of the optimal embedding parameters

In order to reconstruct the underlying dynamics of the experimental data, we computed the embedding parameters $\{\delta, m\}$ in a simultaneously manner through the E–R method. However, *a priori*, the different methods previously explained in the foregoing sections were also tested. The obtained results are summarized in Tab. 5.1.

Regarding the determination of δ, different considerations have to be mentioned. An overestimation of δ is obtained with autocorrelation and mutual information criteria, due to noise and short length of fluorescence traces. In general, the Gibson criterion leads to correct reconstruction and fair values of δ using $\mu \in [0.3 - 0.5]$. Likewise, appropriate values of δ are also estimated with the E–R method, and fall within the same range as Gibson. The general trends observed throughout the experiments is the following. Overall, δ decreases with DIV, reflecting the gradually higher number of bursting episodes; whereas δ increases with CNQX, reflecting the loss of activity and the gradual dominance of noise in the signal. Similar effects are observed in the degradation process upon photo–damage. Values between the range $[0.7 - 1]$ s were obtained.

Concerning the determination of the embedding dimension m several aspects should be pointed up. Given a fixed value of δ calculated with the Gibson method, we proceed to estimate the embedding dimension m with the FNN and Cao's methods in the different experimental context. As before, an overestimation of m was obtained due to the noisy nature of our short signals. In contrast, m values decreased when applying the E–R method, giving a minimum such that $m > 2D_2 + 1$. In general, the values of S^* obtained with the PCA method are slightly higher than m_0.

The final results obtained are detailed as follows.

Young cultures ($DIV \lesssim 7 \pm 2$) presented high values of m ($m \gtrsim 5 \pm 2$) showing the asynchronous dynamical regime of the network. Similar results were obtained in the last stage of disintegration ([CNQX]= 2000 nM, $m \gtrsim 5 \pm 2$) or degradation ($m > 5 \pm 2$) of the network. In this context, the network presented a high–dimensional dynamics, where each single neuron fired erratically. A tangled and messed knot is obtained as SSR, either for network behavior or single individual neuron. Consequently, no plateau is observed in the D_2–plot and no results can be extracted. Indeed, in these conditions, we cannot

say anything specific about the dynamics of the network and the individual behavior of single neurons.

From the second week onwards ($DIV \gtrsim 7 \pm 2$), low values of m are obtained due to the emergence of highly coherent bursting behavior in the network. Hence, we observed $m \simeq 3$ both along maturating and disintegration, indicating that once activity is present in the network, its coherence is preserved. For mature cultures ($DIV \gtrsim 15 \pm 2$) high values of m ($m \gtrsim 5 \pm 2$), S^* ($S^* \gtrsim 7 \pm 2$) and D_2 ($D_2 \gtrsim 1.8 \pm 0,3$) are again obtained. However, in this context, the scenario is completely distinct. Here, the neuronal networks present a rich and complex bursting dynamics and a clear plateau (region II) appears in the D_2–plot. Additionally, in the state space, a structured object emerged. It is worth noting that m reflected the shape of the bursts: $m \in [3-4]$ by burst type I and $m \gtrsim 5$ by burst type II. In Fig. 5.18 one can see the evolution of the correlation dimension $D_2(\varepsilon, m)$ obtained during the maturation and disintegration of different cultures. The evolution of optimum radius ε_0 and the radius used ε for the RPs and RQA analysis are also included.

5.5.3 Simulated fluorescence traces

Before deepening into the analysis of experimental data, it is worth looking first at the result from simulations. As described in Chapter 3, we considered two kinds of networks, homogeneous and aggregated.

Simulated homogeneous cultures

To examine the dynamics in homogeneous networks, we considered different neuronal densities and strengths of the excitatory connections g_{AMPA}. Our goal was to determine which conditions led to the existence of network bursts that encompassed the entire population. We first considered the case with excitation and inhibition active ('E+I' networks). As shown in the heat map of Fig. 5.19A, left panel, both a high density of neurons ($\rho \gtrsim 2000$ neurons / mm^2) and sufficient strength of connections ($g_{\text{AMPA}} \gtrsim 9.5$) were required to observe high activity in the network, understood as more than 1 burst/min. We note that the green shaded region in the top–right corner provides an activity of $2-5$ bursts/min, comparable to our experiments. In the blue region, the neurons fire asynchronously and the population does not achieve a coherent regime. The black region indicates a saturation zone. We obtained similar results for networks with only excitation ('E' only networks). As expected, the lack of inhibition effectively increased g_{AMPA}, leading to a decrease in activity as a result of the complete depletion of neurotransmitters, as observed in the experiments.

The points in the heat maps marked as '1' and '2' correspond to regions from which typical fluorescence traces were extracted for analysis.

We next proceeded to analyze the recurrence plots associated to the fluorescence traces of the simulations. Figure 5.19B depicts the two characteristic fluorescence traces and their corresponding recurrence plots. For the 'E+I' network, the high activity leads to a purely periodic signal without inter–burst regions, and therefore the recurrence plot exhibits long diagonal signals that reflect this periodicity. For the 'E' network, activity is high but inter–burst intervals are visible. The recurrence plot is characterized by a well–repeated, chess–like pattern that captures the shape of the bursts. The fact that

			δ (s)				m (dimensionless)		(δ,m) (s, dimensionless)	
			Autocorrelation Function	Mutual Information	Gibson Method δ^*	Gibson Method $\delta_9=\mu\,\delta^*$ (μ=0.5)	False Nearest Neigbors	Cao's Method	Entropy Ratio Method	Optimal Parameters (δ_0, m_0)
Development [E+I]-Network	DIV	Nº Exp.	δ_1	δ_7	δ^*	δ_9	m_1	m_2	δ_0	m_0
	5*	4	11±3	8±3	5.0±0.4	2.5±0.2	34±4	21±6	1.8±0.5	8±2
	6	5	12±5	7±3	4.6±0.3	2.3±0.5	26±5	11±4	1.3±0.3	5±2
	7	8	9±4	7±4	3.2±0.5	1.6±0.6	23±3	13±3	1.2±0.4	4±1
	8	8	8±2	7±4	2.6±0.4	1.3±0.4	15±6	9±4	1.0±0.2	3±1
	9	6	8±5	8±4	2.8±0.3	1.4±0.5	16±4	10±3	0.7±0.3	3±1
	10	4	6±4	7±3	2.0±0.4	1.0±0.6	21±4	15±4	0.9±0.4	3±1
	13	6	5±3	7±5	2.4±0.4	1.2±0.4	23±2	9±7	1.0±0.5	3±1
	15	6	6±3	9±4	2.8±0.6	1.4±0.3	19±4	12±4	0.8±0.4	3±1
	16	4	6±3	9±5	2.2±0.5	1.1±0.2	23±7	7±5	0.9±0.6	4±2
	20	4	4±3	6±4	2.4±0.4	1.2±0.5	28±9	11±4	1.1±0.6	6±3
Disintegration (DIV=12, n=6)	Network		δ_1	δ_7	δ^*	δ_9	m_1	m_2	δ_0	m_0
	[E+I] (no drugs)		5±3	6±3	2.2±0.6	1.1±0.5	25±7	11±6	0.8±0.4	3±1
	[E]-[CNQX]=0nM		9±4	9±2	3.2±0.4	1.6±0.3	22±8	15±4	1.6±0.5	3±1
	[E]-[CNQX]=50nM		7±3	8±3	2.6±0.5	1.3±0.4	23±6	13±5	1.4±0.6	3±1
	[E]-[CNQX]=100nM		6±3	7±2	1.8±0.4	0.9±0.6	24±6	12±6	1.5±0.4	3±1
	[E]-[CNQX]=200nM		7±4	7±3	2.2±0.6	1.1±0.5	21±7	14±7	1.8±0.5	3±1
	[E]-[CNQX]=400nM		6±3	7±2	2.2±0.6	1.1±0.4	28±8	18±8	3.3±0.4	3±1
	[E]-[CNQX]=800nM		9±5	8±3	5.0±0.5	2.5±0.5	31±5	21±7	4.8±0.6	4±1
	[E]-[CNQX]=2k nM		11±4	7±4	5.8±0.6	2.9±0.6	35±6	23±8	$\geq$ 5.2	4±1
Degradation [E+I]-network (DIV=12,n=4)	Time(t)-(min)		δ_1	δ_7	δ^*	δ_9	m_1	m_2	δ_0	m_0
	t=0		5±3	6±4	1.2±0.3	0.6±0.3	20±4	9±4	0.9±0.6	3±1
	t=60		5±2	4±3	1.0±0.4	0.5±0.4	20±5	8±4	0.6±0.5	3±1
	t=120		4±3	5±3	1.4±0.3	0.7±0.3	22±4	12±4	0.7±0.6	3±1
	t=180		7±4	5±4	3.9±0.4	1.9±0.4	23±5	11±6	0.6±0.4	3±1
	t=240		9±5	6±4	4.4±0.4	2.2±0.4	23±5	20±5	1.1±0.5	3±1
	t=960*		11±5	9±5	7.2±0.5	3.6±0.3	28±5	25±6	$\geq$ 4.5	5±1
	Noise		10±5	11±5	7.5±05.	3.7±0.5	32±7	23±6	$\geq$ 4.7	6±1

Table 5.1: **Embedding parameters of the experimental data calculated using different methods**. Data is organized according to the kind of experiments, development of the culture (top), and disintegration through CNQX (medium) and degradation of the culture (bottom). For each experimental conditions, the results of either the delay time δ or the embedding dimension m were averaged among n realizations. δ_1 was obtained as the point at which the autocorrelation function $C(\delta)^2 = \langle [f(t)f(t+\delta)]^2 \rangle$ vanished, with $f(t)$ the observed fluorescence trace. δ_7 corresponded to the first minimum of the mutual information analysis as described in Refs. [631, 230]. δ^* is computed through the Gibson method [271] as $\delta^* = 12\langle f_L^2 \rangle / \langle (d_t f_L)^2 \rangle$, with $f_L(t)$ the fluorescence trace described with discrete Legendre polynomials and $d_t f_L$ its time-derivative, respectively [271]. δ_9 was computed as $\delta_9 = \mu\delta^*$, with $\mu = 1/2$ [271]. Given δ_9, m_1 was calculated using the False Nearest Neighbors Method [381, 373], while m_2 was obtained through the Cao's method [116]. The embedding parameters used in the analysis of our data were simultaneously computed through the E-R method [262], and are denoted as δ_0 and m_0.

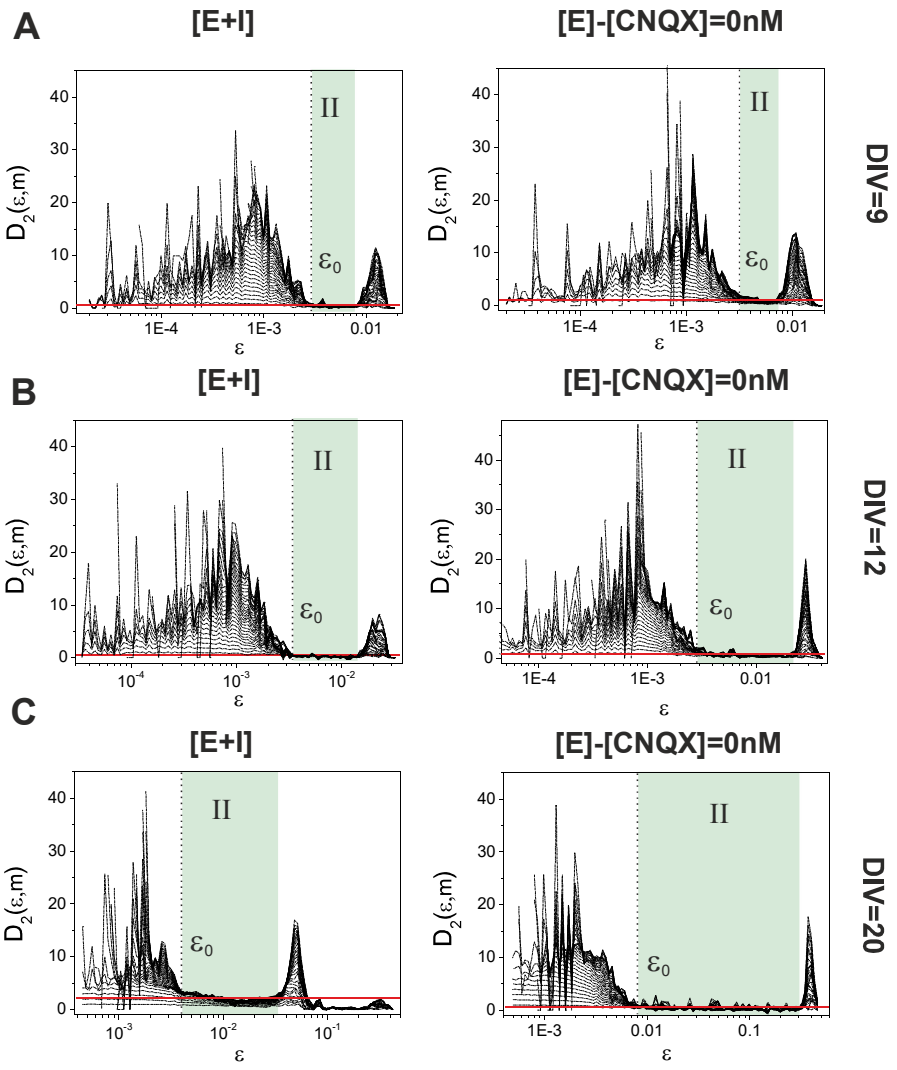

Figure 5.18: **Correlation dimension during development and disintegration**. Testing the embedding parameters $\{\delta, m\}$ and the cutoff radius ε using the compute of D_2 and ε_0 during the maturation and disintegration of different cultures: (A) DIV=9 [E+I], $D_2 = 0.3 \pm 0.4$, $\varepsilon_0 = 3{\cdot}10^{-3}$, $\varepsilon \in [3{\cdot}10^{-3}, 7{\cdot}10^{-3}]$ ($\{\delta, m\} = \{0.6, 3\}, \varepsilon = 5{\cdot}10^{-3}$), [E]-[CNQX]=0nM, $D_2 = 0.3 \pm 0.3$, $\varepsilon_0 = 2{\cdot}10^{-3}$, $\varepsilon \in [2{\cdot}10^{-3}, 6{\cdot}10^{-3}]$ ($\{\delta, m\} = \{0.7, 3\}, \varepsilon = 5{\cdot}10^{-3}$), (B) DIV=12: [E+I], $D_2 = 0.4 \pm 0.2$, $\varepsilon_0 = 2{\cdot}10^{-3}$, $\varepsilon \in [2{\cdot}10^{-3}, 1{\cdot}10^{-2}]$ ($\{\delta, m\} = \{0.7, 3\}, \varepsilon = 5{\cdot}10^{-3}$), [E]-[CNQX]=0nM, $D_2 = 0.6 \pm 0.3$, $\varepsilon_0 = 3{\cdot}10^{-3}$, $\varepsilon \in [3{\cdot}10^{-3}, 2{\cdot}10^{-2}]$ ($\{\delta, m\} = \{1.2, 3\}, \varepsilon = 5{\cdot}10^{-3}$), (C) DIV=16: [E+I], $D_2 = 2.1 \pm 0.6$, $\varepsilon_0 = 5{\cdot}10^{-3}$, $\varepsilon \in [5{\cdot}10^{-3}, 2{\cdot}10^{-2}]$ ($\{\delta, m\} = \{0.8, 6\}, \varepsilon = 5{\cdot}10^{-3}$), [E]-[CNQX]=0nM, $D_2 = 0.8 \pm 0.4$, $\varepsilon_0 = 7{\cdot}10^{-3}$, $\varepsilon \in [7{\cdot}10^{-3}, 0.3]$ ($\{\delta, m\} = \{0.7, 3\}$, $\varepsilon_0 = 5{\cdot}10^{-3}$). The embedding parameters $\{\delta, m\}$ are calculated with the E–R method and ε is five time larger than the standard deviation of the observational noise.

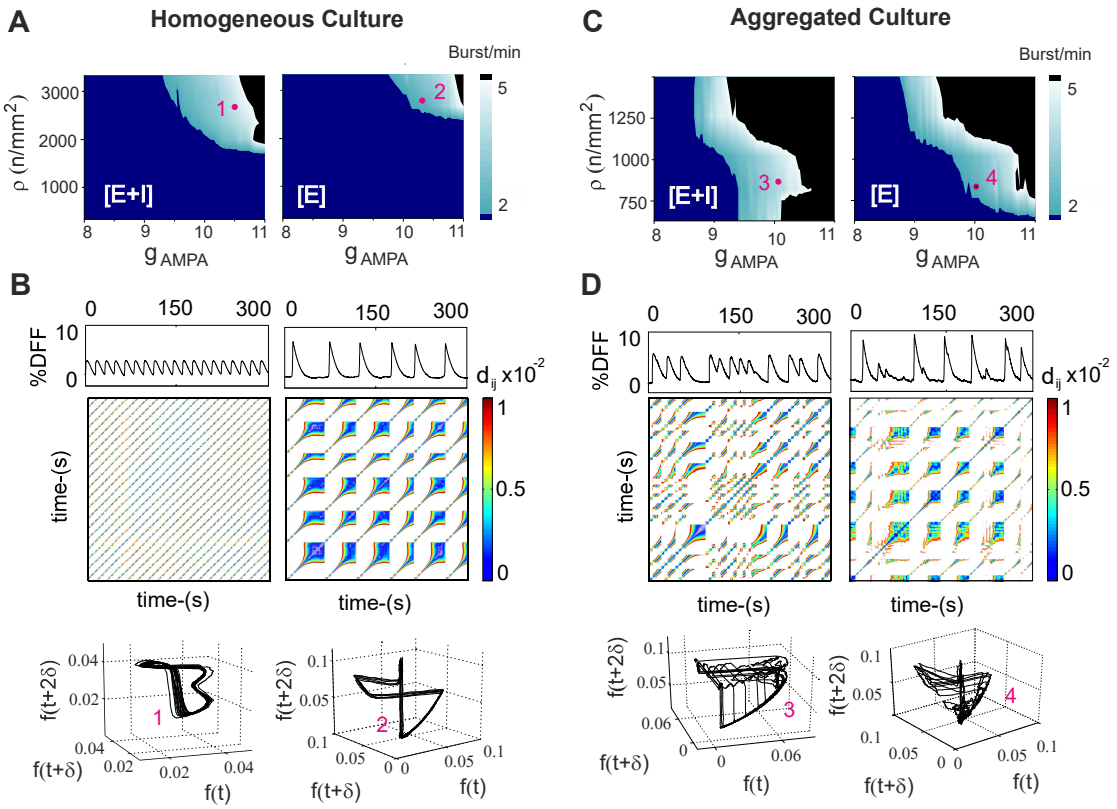

Figure 5.19: **Dynamical regime for homogeneous an aggregated neural networks**. Dynamical regime considering different densities and strength of the excitatory connections g_{AMPA} for homogeneous (A) and aggregated (C) 'E+I' and 'E'–only networks. Characteristic fluorescence traces with their corresponding RPs and orbits are annexed in (B) and (D) for the respective networks.

the entire recurrence plot exhibits a similar, reproducible pattern, reflects the fact that the shape and timing of the bursts are very similar. Indeed, the spatial regularity of the recurrence plot reveals the regularity of the dynamics. The horizontal and vertical lines reflect abrupt changes in the traces, which actually correspond to the relaxation of the system after a bursting episode.

The length of the diagonal lines is associated to the ability of the system to exhibit a repetitive dynamics, which would correspond to periodic, identical bursts. In this sense, the longer the length of the diagonal lines, the higher the predictability of the system. The orbits showed at the bottom of the plots reflect this feature. The orbits are very similar in shape and their distance is small, indicating a highly repetitive dynamics.

Simulated aggregated cultures

To consider the effect of aggregation, we generated additional networks that included regions of a high density of neurons (see Chapter 3). The physical aggregation has important consequences in the dynamics of the network, since now a strong bursting

regime appears already at low densities and weak connectivity (Fig. 5.19C). Points '3' and '4' highlight two representative regions whose fluorescence traces have been analyzed. These traces and the corresponding recurrence plots are shown in Fig. 5.19D. These plots exhibit now a much richer spatial structure that emerges from the variability in the shape and timing of the bursts, also reflected by the dissimilar orbits. This more complex dynamics is due to the spatial aggregation of the neurons. While homogeneous cultures exhibit a coherent, all or none, activations, the aggregated ones show a loss in coherence, with neurons or groups of neurons firing at different times. Hence, the spatial richness of the recurrence plots is an indicator of the repertoire of activity patterns that the network conveys. The origin of this repertoire is complex, and can be ascribed to network underpinned circuitry, neuronal dynamics or both.

Simulations provide a background to understand the experimental results. We can now deepen in the analysis of the data previously introduced, namely the development of an 'E+I' network along 3 weeks, and the disintegration of a mature culture through CNQX.

5.5.4 Development experiments

Representative experiments are shown in Fig. 5.20. Young cultures at DIV 9, sufficiently mature to show sustained activity, display a very simple shape of the burst, which leads to orbits that almost collapse to one another and recurrence plots with a simple pattern. For clarity, in the recurrence plots we show on the top the *typology*, i.e. the structure at large temporal scale, while on at bottom we show the *texture*, i.e. the details at short temporal scales. The traces and the recurrence plots are indeed very similar to the ones observed in the simulations for homogeneous networks.

Along development, there is a range between DIV 9 and 11 where the system is very stable, with quasi–periodic, low activity bursts with large amplitudes and similar shapes. As maturation progresses, however, the structure of the bursts change, which is reflected in a much richer recurrence plots and more complex orbits by DIV 12. At longer times, e.g. DIV 16 and DIV 20, the dynamics change with the emergence of bursts with lower amplitude and a shape of the bursts that is characterized by the existence of a short plateau at the peak of the bursts, i.e. a region of persistent high fluorescence levels. This plateau is associated to oscillations in sub–population of neurons, probability reflecting recurrent activity (as discussed in Chapter 4).

These examples show that the recurrence plot reflects the dynamic richness of the system and that help quantifying the evolution of the network along time.

To characterize in detail the data provided by the RPs, we analyzed in detail a number of descriptors, two based on the structure of the diagonal lines (determinism DET and L_{max}), and two based on the structure of horizontal or vertical lines (laminarity LAM and the trapping time TT).

Between DIV 4 and 6, cultures do not show activity, and therefore the fluorescence data actually reflects the noise of the system, which is included as reference. Low values of DET, L_{max}, LAM and TT were obtained. Homogeneous RPs characterize this early stages, where all the recurrent states form isolated single points. At DIV 7, after GABA switch, the activity starts to appear, though weak, and ramps up quickly at longer DIV. The DET increases abruptly with activity, and reflects the presence of bursts with a

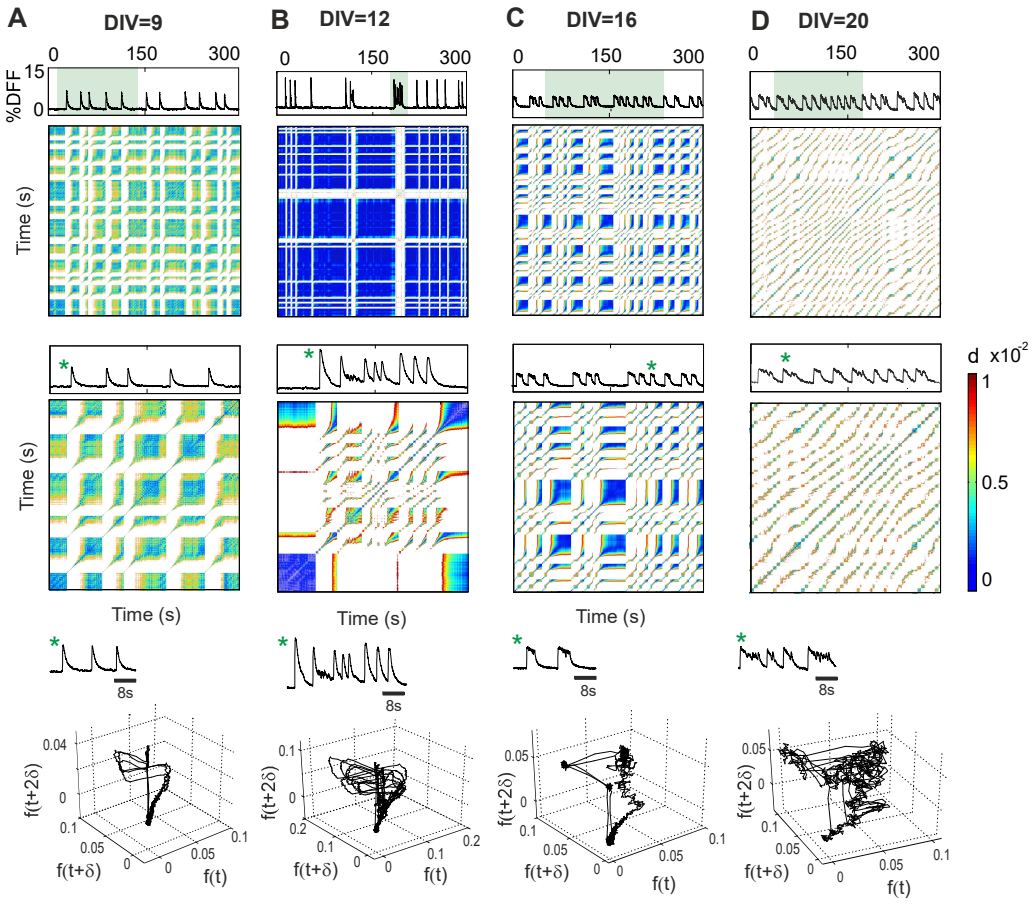

Figure 5.20: **Recurrence plots along network development.** Structure of recurrence plots for fluorescence time series in cultures of developing ages between (A) DIV=9, (B) DIV=12, (C) DIV=16 and (D) DIV=20. The left plots show the traces together with their large scale (*typology*) and fine details (*texture*). The right plots show a detail of the shape of the bursts and the corresponding orbits.

persistent shape, identical along the recording, i.e. neatly overlapping orbits. DET reaches a maximum and later decays, indicating an increase in the variability in the shape of the bursts and therefore the orbits. This is clearly supported by the numerical simulations. We conclude that the aggregation fosters a richer dynamics that cause variability among bursts. Interestingly, homogeneous cultures exhibit bursts more regular in shape than the aggregated ones, and therefore the homogeneous ones have a higher DET.

L_{max} accounts for the longest diagonal lines, and reflects the similarity among orbits. Large L_{max} would indicate large segments of two parallel orbits, while small L_{max} would reflect strong variability among orbits. Hence, L_{max} reflects the fluctuations in the shape of the bursts. In the experiments, we first observe that L_{max} increases at short DIV due to the emergence of bursts, and later fluctuates. Although a slight upward trend appears, it is very weak. Experimentally, fluctuations are strong along DIV, and may indicate strong variation in the dynamic state of the network along maturation. Interestingly, aggregated

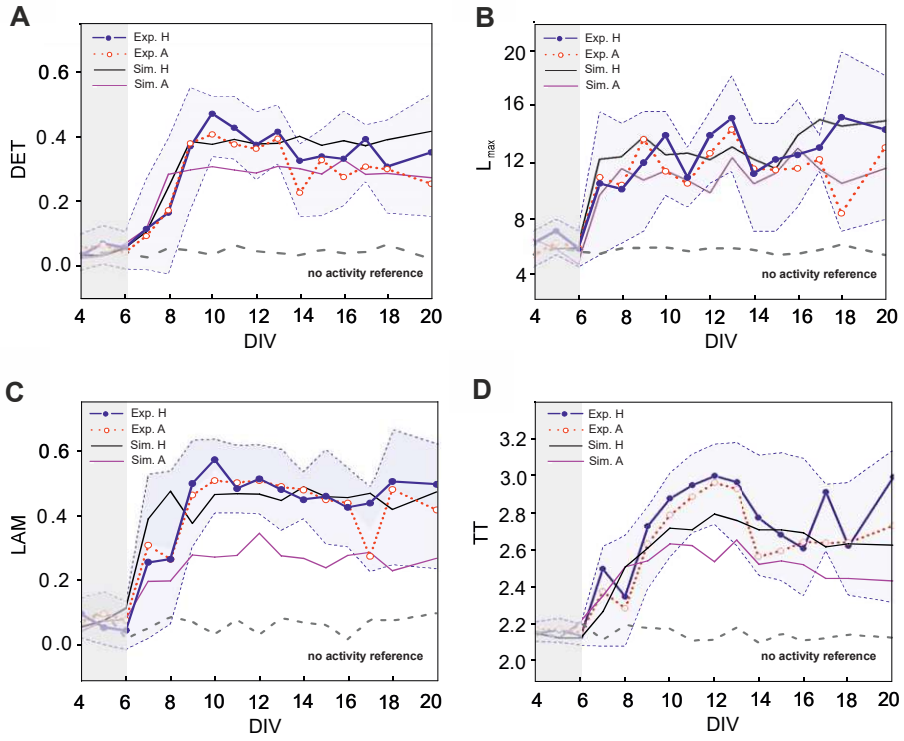

Figure 5.21: **RQA analysis along network development.** RQA analysis throughout the first three weeks of maturation of different cultures computed within a $3x10^3$–points: (A) Determinism (DET), (B) maximum diagonal line length (L_{max}) (C) Laminarity (LAM) and (D) mean vertical (or horizontal) line length (TT).

cultures typically show smaller L_{max} as compared to homogeneous ones, and reflects again their richer bursting shapes and dynamics. Simulations qualitatively exhibit the same trend.

The laminarity LAM reflects the density of recurrence points in horizontal or vertical lines, while the trapping time TT represents its average length which correspond with the $\langle$IBI$\rangle$. Low LAM and TT values were obtained for young cultures (DIV $\lesssim 7 \pm 2$), characteristic of homogeneous RPs made up of single uncorrelated states. When the bursting dynamics appeared, checkerboard structures emerged in the RPs. Then, due to these bi–stable signals, two states were clearly differentiated. Clusters of noisy point in the state space gave rise to horizontal and vertical lines. These lines presented long length due to the low firing rate and the high $\langle$IBI$\rangle$. As maturation progressed, the firing rate increased and the $\langle$IBI$\rangle$ decreased, causing a decline of LAM and TT. Since aggregated cultures present a higher firing rate than homogeneous ones, the LAM and TT obtained in aggregated networks was lower than in its counterparts.

We must highlight here that we could observe two clear changes in the dynamics during the first twenty days of maturation of the cultures. The first change was detected around DIV 7 ± 2, with the activation of inhibition (GABA–switch), as we already pointed out in the Chapter 4. The second change is observed around DIV 14 ± 2 in some cultures. In these cultures, the firing rate increased considerably, $\langle$IBI$\rangle$ decreased,

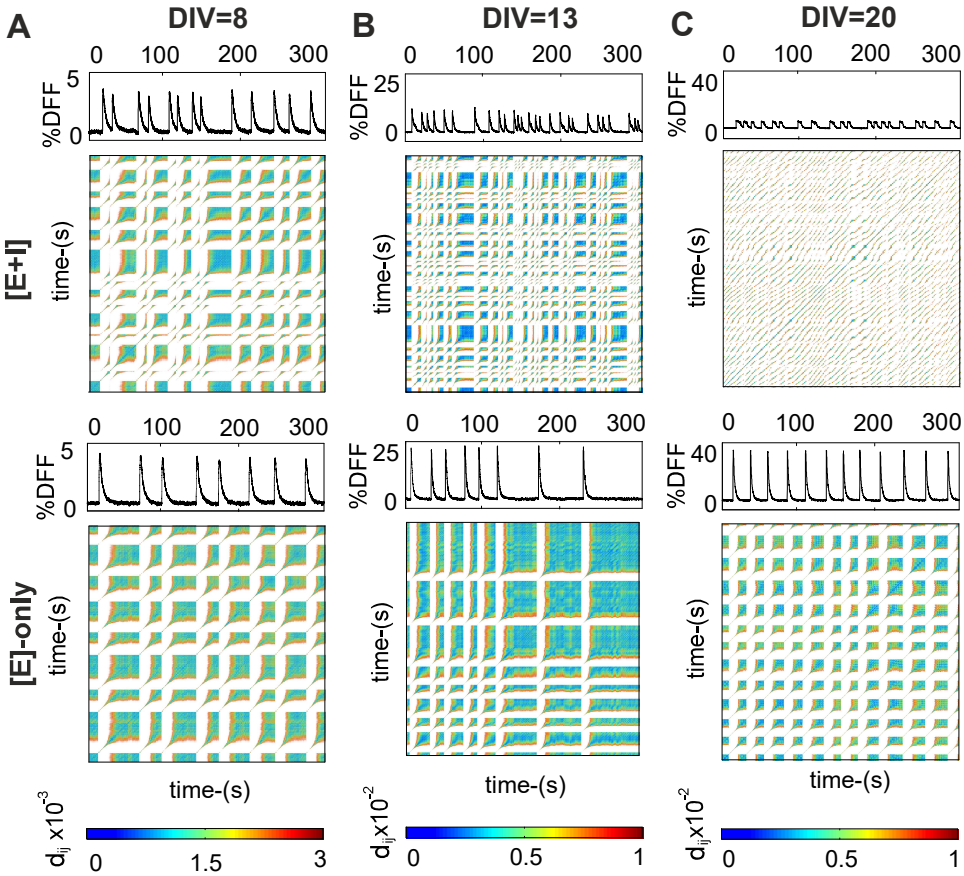

Figure 5.22: **Recurrence plots along network disintegration.** Structure of RPs throughout the disintegration process of different cultures computed within a 3x10^3–points: (A) DIV=8: 'E+I'–network (top) and 'E'–[CNQX]= 0 nM (bottom), (B) DIV=12: 'E+I'–network (top) and 'E'–[CNQX]= 0 nM (bottom), (C) DIV=20: 'E+I'–network (top) and 'E'–[CNQX]= 200 nM (bottom).

and inter–bursts oscillations were detected. Indeed, in these cultures orbits of type II emerged, and exhibited embedding dimensions $m > 5$.

5.5.5 Disintegration experiments

Experiments manipulating the connectivity of the network by GABA and AMPA blockade are shown in Fig. 5.22. For young cultures (DIV $\simeq 8\pm2$), which show characteristic bursts of type I, the blockades of GABA preserved the structure of the patterns but reduces their density, indicating that the dynamics of the system simply reduced the amount of bursting events. These young cultures showed poor and erratic activity, which is reflected in the RPs by the absence of diagonal lines. Low values of DET, L_{max}, LAM and TT were obtained (Fig. 5.23A-D). Due to the weakening of the network, its breakdown rapidly occurred around [CNQX]= 200 nM. No substantial change in dynamics was observed

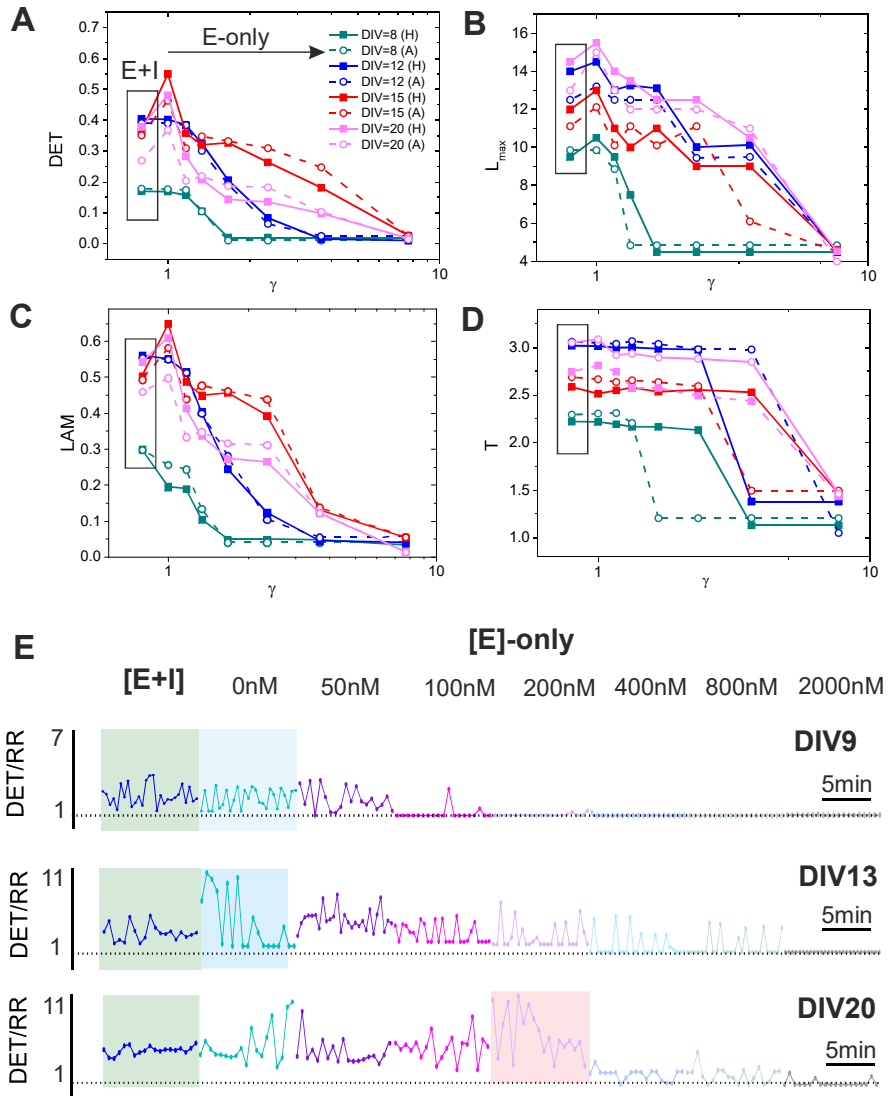

Figure 5.23: **RQA analysis along network disintegration.** RQA analysis throughout the disintegration process of different cultures computed within a 3x10^3–points: (A) Determinism (DET), (B) maximum diagonal line length (L_{max}) (C) Laminarity (LAM) and (D) mean vertical (or horizontal) line length (TT).

when GABA was blocked in the transition from 'E+I' and 'E' networks. This fact was also observed when the DET/RR ratio was calculated along disintegration. For this calculation we considered a moving windows of 1024 points (Fig. 5.23E, top, shaded green–blue zone). Not differences were observed in homogeneous and aggregated young cultures.

'E+I' and 'E' networks at DIV 12 ± 2 also showed very characteristic bursts of type I throughout the disintegration process (Fig. 5.22B). However, upon blocking of the inhibitory currents, the amplitude of fluorescence substantially grew and produced longer orbits, causing an increase in the L_{max} (Fig. 5.23B). Moreover, the subsequent disintegration of 'E' only networks presented signals in which the shape of the bursts were very similar, which also produced an increase in the DET and predictability. However, the $\langle$IBI$\rangle$ substantially increased and the number of bursts, decreased producing an increase of LAM and TT (Fig. 5.23C-D). We remark that the most important change that we detected weas the transition from 'E+I' networks to 'E' ones, as observed in Fig. 5.23E (shaded green–blue zone). In contrast, during the disintegration of 'E' network no changes were noticeable.

Finally, 'E+I' networks from DIV 20 ± 2 displayed a characteristic burst type II while the corresponding 'E' networks exhibited bursts of type I. The blockades of GABA altered the shape of the bursts and produced a clear change in the dynamics. The structure of RPs was clearly modified, as shown in Fig. 5.22. For 'E' networks and [CNQX]= 0 nM, the different bursts along a recording were very similar, while the 'E+I' ones showed more variability. Thus, DET and L_{max} increased in the transition from 'E+I' to 'E'. As happened with the other disintegrations, the $\langle$IBI$\rangle$ increased upon CNQX application, and the number of bursts decreased producing a increase of LAM and TT (Fig. 5.23C-D). However, as shown in Fig. 5.23E (middle, shaded green–blue zone), an interesting change occurred during the disintegration of the 'E' networks at [CNQX]= 200 nM, with an increase in the DET/RR ratio that suggests a higher periodicity and predictability of the signal. This change is very weak, however, and since the RQA substantially fluctuates, it is difficult to confirm that a dynamical change took place.

5.5.6 Test for nonlinearity

The results obtained from the nonlinearity testing are included in Tab. 5.2. Figure. 5.24 shows three characteristic fluorescence traces from young and old cultures, and with the corresponding surrogates. The top traces correspond to a time series without collective dynamics (DIV $= 5 \pm 2$), the central ones to type I bursting (DIV $= 9 \pm 2$) and the bottom ones to type II bursting type II (DIV $= 20 \pm 2$). The length of each time series analyzed in every computation is approximately of 30,000 samples.

Illustrative examples of the outcomes are shown in Figs. 5.25 and 5.26. During development, and only for mature homogeneous and aggregated cultures (DIV $\gtrsim 14 \pm 2$) small traces of nonlinearity were detected ($\mathscr{S} \geq 2$) (Figs. 5.25C-D). Indeed, null hypothesis ca not be rejected in the young cultures, since both nonlinearity measures, $t^{C3}(\delta)$ and $t^{REV}(\delta)$, of the original fluorescence traces fall within the surrogate distribution (Figs. 5.25A-B), with $\mathscr{S} < 2$ (see also Tab. 5.2). Similar results were obtained along disintegration, as exemplified in Fig. 5.25D for the 'E' networks at [CNQX]= 800 nM. In general, null hypothesis could not be rejected along disintegration, and suggests that lin-

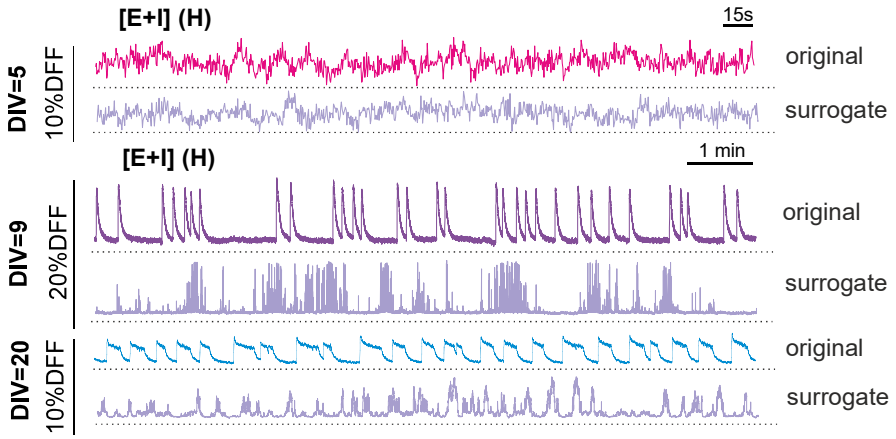

Figure 5.24: **Generation of surrogates using iAAFT algoithm from ours experimental traces.** Characteristic fluorescence traces from young and old cultures with one corresponding surrogate.

ear behavior seems to represent this experiments. We must, however, that these analyses strongly depend on the value of time delay δ.

In order to perform DVV analysis on the original $f(t)$ signal and a number of surrogate time series $f_s(t)$, different considerations were previously taken into account. Firstly, it was necessary to select the maximal span parameter, n_d, which determined the range of standardized distances to consider. This parameter controls the span over which to perform the DVV–analyses. Visual inspection of the convergence of DVV plot to unity should be used for setting it, i.e. by typically starting at a value $n_d = 2$ and gradually increasing it through unit steps until DVV plots converge to unity. We adopted $n_d = 3$ in all the analyses. The number of standardized distances for which target variances were computed, N_{tv}, were set to 50. The number of reference DVs considered, N_{sub}, was 200 for all the analyses. For each time series, we performed a set of DVV–based nonlinearity analyses for a range of parameter values using a set of $N_s = 99$ surrogates. Studies of Gautama *et al.* [264] analyzed the sensitivity of this method to parameters, and exploring four different time series, three of them nonlinear. The authors indicated that the only parameters with a notable effect with respect to nonlinearity detection were the embedding dimension, m and the maximal span, n_d. However, the authors also concluded that the effect was minor for reasonable parameter values, i.e. $m \in [3, 10]$ and $n_d \geq 1$, corresponding to our range of operation.

The result of analysis for 'E+I' networks show that RMSE decreased during the development of cultures. Lower values of RMSE were obtained for mature cultures (DIV $\gtrsim 14 \pm 2$, see Tab. 5.2) indicating the deviation from the bisector line of the original versus surrogated data in the DVV–scatter plot (Fig. 5.26), and similarly for homogeneous mature cultures (DIV=20) and aggregated ones (DIV=9). For young cultures upon disintegration ('E' only networks) small values of RMSE were obtained.

In addition, a graphical representation of DVV–analyses by plotting σ^{*2} as a function

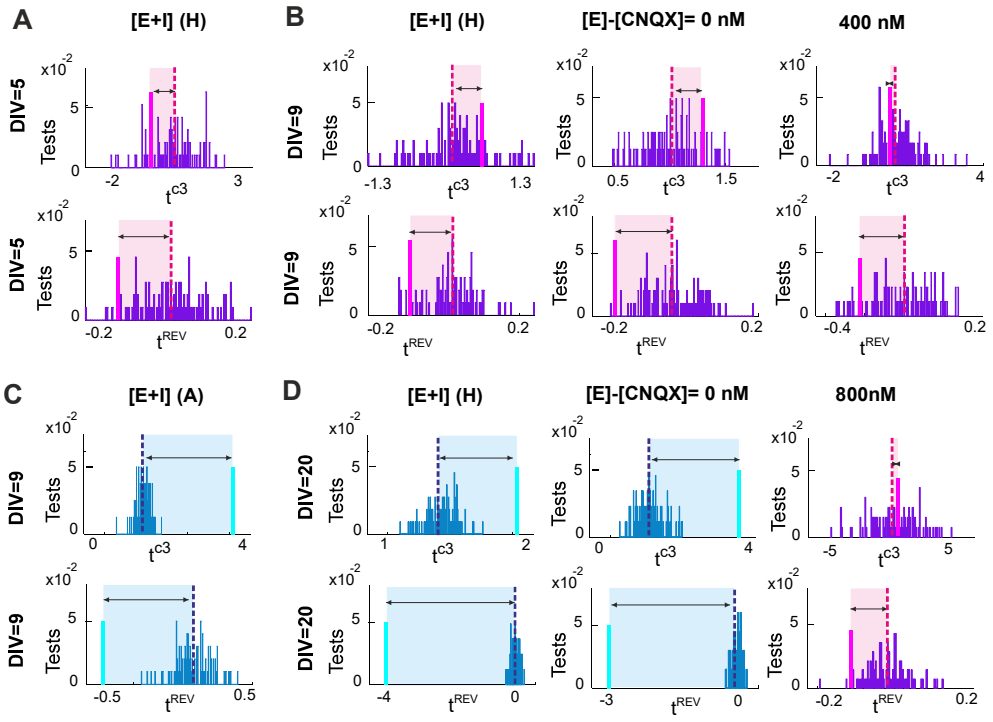

Figure 5.25: **Test for nonlinearity.** Statistical test for nonlinearity from different cultures: (A) DIV=5: "E+I"–homogeneous networks, (B) DIV=9: "E+I"–homogeneous networks and its corresponding two disintegration ([CNQX]=0 and 400 nM), (C) DIV=9: "E+I"–aggregated network and (D) DIV=: "E+I"–homogeneous networks and its corresponding two disintegration ([CNQX]=0 and 400 nM). Third–order coavariance (t^{C3}, top) and time–revesibility qunatity (t^{REV},bottom) were used as discriminants.

of the standardized distance, ε gives information regarding one of the fundamental properties of the signals, i.e. its predictability. Two extreme cases correspond to a white noise (entirely unpredictable) and a deterministic signal (entirely predictable). The *minimum target variance*, σ^{*2}_{min}, which corresponds to the lowest point of the curve, is a measure for the amount of noise which is present in the signals. Lowest σ^{*2}_{min} were obtained for mature cultures (DIV $\gtrsim 14 \pm 2$) in contrast with the obtained for a young cultures and disintegrated statges (Fig. 5.26).

5.6 Discussion

Emergence coherent dynamics

We observed than the networks display different dynamical states, such as 'synchronous regular' (SR) and 'asynchronous irregular' (AI). In the SR states, the global variables display coherent low–dimensional behavior. Before GABA switch the population presents AI states with exponentially distributed individual neuronal discharges. Analysis with

			Third-order auto-covariance		Time-Reversibility		DVV Method
	DIV	**Nº Exp.**	**S^{tc3}**	**RT**	**S^{trev}**	**RT**	**RMSE**
Development [E+I]-Network	5*	4	2.1±0.8	35	0.98	0.98	0.98
	6	5	1.2±0.7	58	0.97	0.97	0.97
	7	8	1.5±0.6	26	0.81	0.81	0.81
	8	8	2.0±0.5	54	0.95	0.95	0.95
	9	6	2.5±0.8	65	0.96	0.96	0.96
	10	4	4.2±0.9	69	0.78	0.78	0.78
	13	6	5.5±0.7	75	0.89	0.89	0.89
	15	6	8.6±0.5	82	0.76	0.76	0.76
	16	4	7.6±0.4	*99*	0.67	0.67	0.67
	20	4	7.9±0.8	85	0.65	0.65	0.65
Disintegration (DIV=12, n=4)	**Network**		**S^{tc3}**	**RT**	**S^{trev}**	**RT**	**RMSE**
	[E+I] (no drugs)		3.2±0.5	52	0.87	65	2.2±0.6
	[E]-[CNQX]=0nM		11.3±0.8	*99*	0.82	*100*	3.2±0.4
	[E]-[CNQX]=50nM		8.5±0.7	*100*	0.86	*100*	2.6±0.5
	[E]-[CNQX]=100nM		7.6±0.6	65	0.83	*99*	1.8±0.4
	[E]-[CNQX]=200nM		4.1±0.6	36	0.85	*84*	2.2±0.6
	[E]-[CNQX]=400nM		5.3±0.5	75	0.91	*74*	2.2±0.6
	[E]-[CNQX]=800nM		1.6±0.7	59	0.90	54	5.0±0.5
	[E]-[CNQX]=2k nM		0.2±0.9	19	0.98	63	5.8±0.6
Disintegration (DIV=16, n=4)	**Network**		**S^{tc3}**	**RT**	**S^{trev}**	**RT**	**RMSE**
	[E+I] (no drugs)		7.6±0.4	*99*	0.64	*100*	2.2±0.6
	[E]-[CNQX]=0nM		5.5±0.6	*99*	0.75	*99*	3.2±0.4
	[E]-[CNQX]=50nM		4.2±0.5	54	0.77	*100*	2.6±0.5
	[E]-[CNQX]=100nM		3.2±0.7	41	0.84	*100*	1.8±0.4
	[E]-[CNQX]=200nM		2.3±0.7	32	0.85	35	2.2±0.6
	[E]-[CNQX]=400nM		3.3±0.6	58	0.93	45	2.2±0.6
	[E]-[CNQX]=800nM		2.6±0.9	47	0.95	40	5.0±0.5
	[E]-[CNQX]=2k nM		0.6±0.5	24	0.98	38	5.8±0.6
Degradation [E+I]-network (DIV=12,n=4)	**Time(t)-(min)**		**S^{tc3}**	**RT**	**S^{trev}**	**RT**	**RMSE**
	t=0		2.8±0.6	35	3.1±0.4	0.73	1.2±0.3
	t=60		4.3±0.8	23	5.4±0.5	0.87	1.0±0.4
	t=120		2.5±0.7	45	2.1±0.7	0.83	1.4±0.3
	t=180		2.6±0.7	35	3.4±0.5	0.91	3.9±0.4
	t=240		1.1±0.6	25	1.7±0.7	0.92	4.4±0.4
	t=960*		0.5±0.3	21	0.7±0.7	0.98	7.2±0.5
	Noise		0.3±0.8	45	0.8±0.4	57	0.97

Table 5.2: **Test for nonlinearity for ours experimental cultures**. Results of test for nonlineartity using as discriminating measures the third order auto–covariance (t^{C3}) and the time–reversibility (t^{REV}) for our neuronal cultures during development, disintegration and degradation process. To compare the difference between the original value and surrogated distribution is attached the values of 'sigmas' deviation in the first column and the results of the rank test in the second one. Signicant rejections of the null hypothesis at the level of 0.1 are given in italics letters. In the DVV–analysis, the degree of nonlinearity is quantify through the root mean square error (RMSE) between the σ^{*2}'s of original time series and the σ^{*2} of the average over the DVV plots of the surrogate time series.

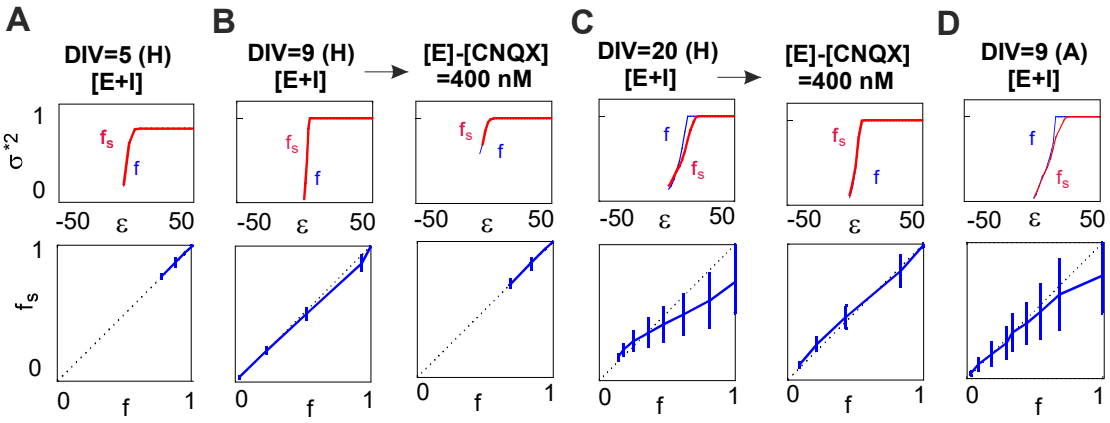

Figure 5.26: **Detection of nonlinearity using Delay Vector Variance (DVV-analysis) for our neuronal cultures.** The delay vector variance method for detecting determinism and nonlinearity is used in the our neuronal cultures: (A) DIV=5 "E+I"–homogeneous network (B) DIV=9 "E+I"–homogeneous network and ts corresponding disintegration "E"–only network ([CNQX]=400 nM) (C) DIV=16 "E+I"–homogeneous network and ts corresponding disintegration "E"–only network ([CNQX]=400 nM) (D) DIV=9 "E+I"–aggregated network. The degree of nonlinearity and determinism increases from young cultures to matures ones, as well as in aggregated cultures, while decreasing during disintegration. The error bars indicate one standard deviation from the mean of σ^{*2}.

the Caoś method reveled that the global system presented strong randomness. The usage of the ER method allowed us to determine the embedding dimension in the range $m \simeq [3-8]$. No attractors emerged in the state space, and only a mixed of states was observed. Homogeneous RPs were formed, and high values of RRS ($\simeq 1$) and TT ($\simeq 99$) were obtained. In addition, DET, LAM and L_{max} reached values close to zero. DVV–analyses evidenced that nonlinearities were detected in the first week of maturation.

After GABA switch, dynamics with bursting type I emerged, characterized by a low embedding dimension $m \simeq 3$, with dimensions of correlation $D_2 \lesssim 1.5$. Periodic or quasi–periodic dynamics characterized this second stage of development. Regulars orbits emerged in the state space giving rise to typical RPs with checkerboard structures in their typolgy. The appearance of similar orbits created the diagonal lines in the RPs, increasing the values of DET and L_{max}. In addition, being a bi–stable system, the value of LAM also shot up. Intermediate values of TT were obtained in this stage of development. Finally, DVV–analyses also evidenced the absence of nonlinearities.

The local analyses suggest that a stochastic nature at small scales (neurons) can coexist with a more coherent behavior at large scales (average). Indeed, the existence of coherent behavior in systems with large degree of freedom is surprising, but in Nature it is more common than exceptional. Studies of simple models in the limit of large network size with a high connectivity degree [14, 269, 286, 308, 729, 760] revealed that, in the absence of external source of strong stochastic noise, they tend to settle into temporally ordered states producing a linear response and periodic dynamics.

Besides, our simulations revealed that quasi–periodic regimes were obtained for networks with weakened synaptic strengths, in both aggregated and homogeneous topologies.

Pure oscillatory dynamics were obtained only in homogeneous networks with a critical size over $N \gtrsim 10^4$. Such dynamics we never observed in the Laboratory, possibly due to our investigation with small networks.

Ripening and changes in the dynamics

During the development of cultures, one line of experiment presented a change in the dynamics. Mature cultures (DIV $\geq 14\pm2$), both aggregated and homogeneous, portrayed a type II bursting dynamic. We observed an increase in the embedding dimension ($m \geq 4$) and in the dimension of correlation ($D_2 \geq 1.5$). Cao's method determined the presence of a deterministic component. The existence of a plateau in the representation of D_2 as a function of the cutoff radius ε indicated the emergence of a well defined attractor. Its 3D–representation evidenced unfolded orbits with low amplitudes and long excursions across the state space. Colorful RPs were obtained with varied geometrical patterns with shorter diagonal and curved lines. Lower values of DET and L_{max} were obtained. Intermediate values of LAM and TT came up. Using the test for nonlinearity, null hypothesis was rejected and the presence of nonlinearities was ensured.

Simulations revealed that such dynamical patterns were obtained in aggregated cultures with strong synaptic strengths. In the homogeneous case, this dynamics was also detected. However, nonlinear regimes in extended coupled systems of finite sized networks models of spiking neurons (I&F neurons) were well characterized [123, 124]. Indeed, Cessac *et al.* [123] exhibited theoretical and numerically a sharp transition between a neural death regime where all neurons are asymptotically silent, and a phase with long transient, having the appearance of a chaotic dynamics. Interesting is the fact that such transition occurs only when the variance of the synaptic weights increases, being the individual dynamics chaotic in (non generic) regions of the synaptic weights space, whereas a further increase leads to a periodic dynamics with small periods. It should be noted that in our case, when inhibition is blocked, the synaptic weights increase (see Chapter 6) and periodic dynamics emerge.

Loss of complexity and 'dynamical disease'

Low–dimensionality chaos dynamics was detected only for mature cultures (DIV $\gtrsim 14\pm2$), while when these 'E+I' networks were disintegrated and inhibition was blocked, different periodicity regimes were obtained. Indeed, when inhibition was blocked, the embedding dimension dropped to $m \simeq 3$, concurrently with the dimension of correlation $D_2 < 1$. As evidenced by the Cao's method, deterministic component are gradually reduced during the disintegration until theu disappear. Finally, in the last stage, when the 'E' only network was silenced, the embedding dimension increased up to 4.

In the first stage of disintegration 'E' only networks presented type I bursting with regular orbits. Periodic or quasi–periodic dynamics characterized the RPs with the typical checkerboard structures in their typopolgy. RPs experienced a loss of complexity. Higher values of DET and L_{max} were obtained. Intermediate values of LAM and TT were gathered. In mature cultures, DVV–analysis revealed nonlinearity in the first stages of disintegration. However, as the connectivity was gradually weakened, the null hypothesis could not be rejected. DVV–analysis reflected the increase of noise and a decline of RMSE. In addition, the DET/RR analysis during the disintegration process of mature

cultures suggested an increase of DET and the predictability of the system. However, since the DET and LAM measures highly fluctuate with small changes in ε (Fig. 5.15B and D), it is difficult to ascertain whether a change in dynamics truly occurred or not.

One of the most debated issues is whether chaotic behavior constitutes an evidence for healthy or pathological brain states [277, 276, 275, 552, 648]. Glass and Mackey [274] introduced the term 'dynamical disease', which captures the notion of abnormal rhythms, and that could be either more irregular or more regular than normal, denoting pathological situations where the control had been lost. Studies of Goldberger and West [277, 276] suggested the hypothesis that the dynamics of a healthy physiological system would produce apparently highly irregular and highly complex types of variability and fluctuations [592, 164, 565, 540, 659, 671, 362], whereas disease and even aging is associated with less complexity and more regularity. The authors argued that chaos should be healthy because it provides the organism with an 'information–rich (broadband) state' and 'spectral reserve' while that periodic behavior can foreshadow disease [276]. Several studies had calculated correlation dimensions from different states of human EEG and provided evidences for low–dimensional chaos for slow–wave sleep [50, 478], as well as for pathological states such as epilepsy [47, 348, 347, 600, 229, 550, 345, 698, 418, 642, 346, 599, 551, 602, 39, 499, 501, 500], Alzheimer [357, 358], Parkinson's disease [710, 507, 549], schizophrenia[211, 385], depression [512, 710] or the terminal state of Creutzfeldt-Jakob disease [189, 49, 674].

These observations, in the context of our results, interesting reflect the fact that basic patterns of brain dynamics can be associated with different 'functional networks' or 'functional sources'. It seems that dynamics is characterized by a highly dimensional complexity, and that a relatively low and fluctuating level of synchronization of the neuronal networks are associated tp normal, ongoing dynamics during a no–task, resting state in healthy subjects. Hence, the highly periodic, repeated bursting episodes of our cultures could be ascribed to a pathological state. Indeed, hyper–synchronous states are linked to degenerative illnesses and impaired information processing. Only intermediate levels of rapidly fluctuating synchronization, possibly due to critical dynamics near a phase transition, are associated with normal information processing [673].

Chapter 6

ANALYSIS AND RESULTS III: Reconstruction of connectivity

Mapping the brain's wiring diagram at different scales is a fundamental aspect in the quest for understanding how a living neuronal network processes information at both local and global scales. Such a mapping is difficult and can be carried out using different strategies, from direct dissection to the *reconstruction* of connectivity from activity data. The latter is an important field of research in neurophysics and was one of the pillars of this thesis.

Hence, in this Chapter we describe our efforts to extract the *mesoscale connectome* of our neuronal cultures derived from embryonic rat brains. As we shall see, on the sole basis of the information provided by the activity of individual neurons, we *reconstructed* the underlying connectivity of the network. We proceeded as follows. Firstly, we developed different approaches that were tested using the synthetic traces of simulated networks described in Chapter 3. From this testing, the most appropriate method for the reconstruction of connectivity was then chosen and applied to the experimental data outlined in Chapter 2. All the results were contrasted with the simulations and their corresponding null models.

6.1 The reconstruction paradigm

In order to reconstruct the topological connectivity of our neuronal cultures, we considered a bottom–up perspective. Neurons' fluorescence traces were used as our starting point for analysis. We focused on studying the mutual influence between any two neuronal time series. We took special attention in analyzing how the prediction of a time series could be improved by the incorporation of the knowledge of a second times series. In the case that an improvement existed, then we could say that the second series had a causal influence on the first one [758].

Throughout our work, neuronal networks are mainly described by three different types of connectivity, and that reflect three parallel *layers* of investigation, namely anatomical, functional and effective. Anatomical or topological connectivity simply refers to the set of physical or structural connections that link neuronal units at a given time. Functional connections indicate a statistical dependence between the activity of neuronal units, whereas effective connectivity shows a causal relationship between them. The

physical architecture or anatomical connectivity is the trait that, experimentally, is the most difficult to uncover, and it is totally unknown to us. However, some degree of inference is possible from the knowledge of the functional or effective connectivity maps. Although the different layers change in time and influence one another (e.g. plasticity or development), for simplicity we just considered them as static maps. Consequently, in our analysis we considered that only the structural layout determined the functional repertoire of dynamics of the network.

Our most important (and debatable) assumption for reconstruction is that the spontaneous activity of the neuronal culture produces intrinsic correlation patterns that largely reflect its internal connectivity.

6.1.1 Network description and adjacency matrices

In general, the study of network connectivity is carried out using graph theory and information–theoretical techniques. Thus, each neuronal population is modeled as a graph, $G = (N, E)$ comprising a set N of *vertices* or *nodes* together with a set E of *edges* or *arcs*. Each node represents a single neurons and its respective interactions are depicted through their edges.

We consider that a given network topology is entirely described by the *adjacency matrix* of the network $A^{(str)}$ where the elements $a_{ij}^{(str)}$ represent the structural edges linking nodes i and j. Our goal is to rebuild this architecture with the only knowledge of measured activity in the respective neurons.

We therefore consider that, by measuring the degree of similarity between the activity profiles of each pair of neurons, it is possible to generate the dynamical matrix $A^{(dyn)}$ whose elements depict statistical relationships among neuronal traces. Then, any pair of neurons will be considered as *connected* when the strength of the statistical relationship is above a given threshold. In this sense, this *thresholded* dynamical adjacency matrix $A^{(dyn)}$ might be seen as an approximation to the structural adjacency matrix $A^{(str)}$, and in a way that $\lim_{t\to\infty} A^{(dyn)} \approx A^{(str)}$. We note that, in principle, large time series would provide better results since the number of observed neuron–to–neuron interactions would be also larger. However, this could compromise our *static* consideration, i.e. that the structural connectivity does not evolve in time. Additionally, and not less important, large time series would make the analysis intractable due to the size of data, and compromise the health of the living network upon measurements. Hence, our aim here is to assess the validity of reconstruction strategies with short and noisy time series ($\mathrm{T} \simeq 10 - 20$ min) and extract information on tne connectivity of the cultures.

In this thesis we considered different strategies to infer statistical relationships among firing neurons. The use of simulated networks proved invaluable to pinpoint the best method. Thus, we detail below the explored techniques and the applied procedures to assess their validity. Once all these analysis were carried out, we proceeded to characterize the topological properties of our living networks referenced in Chapter 2. To perform network analysis, we used the BGLMatlab library [9] combined with a Matlab package written by J.G.Orlandi [10, 11] oriented specifically to calcium imaging signals. Networks were displayed using Gephi [**?**], an open source software distributed under GPL3.

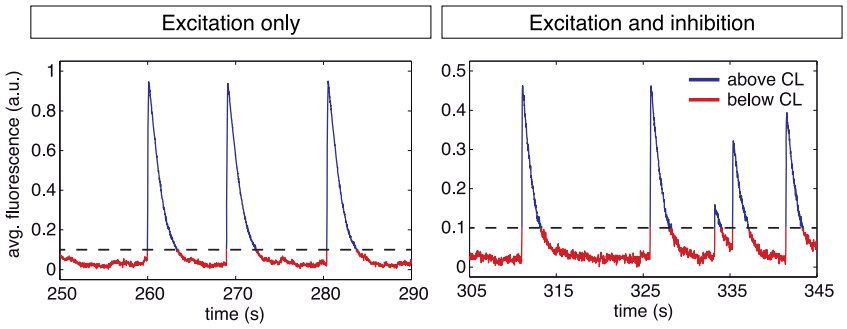

Figure 6.1: **Signal conditioning.** The graphs show the separation of the signal in two regimes according to the conditioning level (dotted line). A first regime encompasses the low activity events (red curves), and a second regime includes the bursting regimes only (blue). The same conditioning procedure is applied in both 'Eonly' networks (left) and in 'E+I' ones (right).

6.2 Tools for connectivity reconstruction

6.2.1 Fluorescence data and raster plots

Due to the poor signal–to–noise ratio of the fluorescence traces of single neurons, in this section we proceed to transform the recorded time series into *binary* firing sequences. Hence, firstly, in a preprocessing step, we apply a basic discrete differentiation operator to calcium fluorescence time series $f_{i,t}$, with i the index of the neuron and t the time step, in order to enhance the detection of potential spike events [676].

Therefore, secondly, given a network node i, we define $\delta f_{i,n} = f_{i,n+1} - f_{i,n}$ with the goal to improve the signal–to–noise ratio and consequently, to allow for a better sampling of probability distributions with a limited number of data points. The rationale behind this idea is that a firing neuron exhibits a sharp increase in fluorescence in just a single time step. This does not occur in the noisy regions of the fluorescence traces, which correspond to the neuron at rest. Thirdly, in order to detect single dynamical states, and not unphysical fluorescence transients, we proceed to filter δf_n with respect to the average behavior of the whole population. For that, we compute

$$g_t = \frac{1}{N} \sum_{i=1}^{N} \delta f_{i,t}, \tag{6.1}$$

where N is the number of neurons. We then consider as activations only the data points at time instants in which this average fluorescence difference g_t is below a predefined threshold parameter $\tilde{g}$. So, we consider only the time points that fulfill $\{t : g_t < \tilde{g}\}$. Practically, this conditioning eliminates the large–amplitude network bursts, and retains as firings those fluorescence values in between the noise level and the threshold. Hence, it is important to properly set $\tilde{g}$ to be sure that neuron–to–neuron firings, and not coherent behavior, are the interactions shaping the time series. In general, we observed that optimal reconstructions were obtained in a narrow range surrounding the conditioning value close to twice the standard deviation of the signal.

Finally, to build the actual time series for analysis, the continuous range of fluorescence values is quantized into a finite number B of discrete levels. We took for simplicity $B = 2$,

i.e. existence of activity (1) or none (0). Therefore, our point of departure is a *temporal raster plot* corresponding to a binary matrix that contains the firing pattern of each single neuron.

6.2.2 Dynamical Matrix: Similarity measures

A crucial and delicate stage of the reconstruction of network connectivity is the selection of similarity measures, which capture the degree of concordance between the traces of activity of each pair of neurons. Following he above conditioning, each neurons is given as a *binary firing sequence*. Considering the whole set of neurons, we proceed to calculate the elements of the dynamical matrix $A^{(dyn)}$, determined as similarity coefficients between pairs of neurons. Below we detail the different approaches that we considered to obtain $A^{(dyn)}$.

Cross–correlation Coefficient

Cross–correlation (XC) is a measure of similarity between two series that takes into account the relative temporal shift among any two series. XC is a dimensionless index, and it is generally used to measure a bivariate association between two variables, i.e.

$$\rho_{X,Y} = \frac{\sum_{n=1}^{T}(x_n - \mu_X)(y_n - \mu_Y)}{(T-1)\sigma_X\sigma_Y} = \frac{\sum_{n=1}^{T}(x_n - \bar{x})(y_n - \bar{y})}{\left[\sum_{n=1}^{T}(x_n - \bar{x})^2 \sum_{n=1}^{T}(y_n - \bar{y})^2\right]^{1/2}}. \tag{6.2}$$

This measure is invariant to linear transformation of either variables. In order to simplify the notion, we rewrite $\rho_{X,Y} = \rho_{ij}$ where $X = \{x_n\}$ and $Y = \{y_n\}$ are the binary signals of activity of two different neurons i and j. Then, the score assigned to each potential link is given by the largest cross-correlogram peak for delay times in the range between $t = 0$ and $t_{max} = 200$ ms, as follows

$$XC_{Y\to X} = \max_{\Delta t\in[0,t_{max}]}\{\rho_{X,Y}|g_n < \tilde{g}\} = max_\delta\{\rho_{ij}|g_{n+1} < \tilde{g}\}. \tag{6.3}$$

Consequently, the obtained connectivity matrix is weighted and undirected because the symmetry of the cross–correlation function.

Partial Correlation Coefficient

Partial correlation coefficient (PCC) is a linear multivariate symmetric measure quantifying the strength of the direct connection between X and Y but modulated by the effect of a set of controlling random variables removed. Formally, the partial correlation between X and Y given a set of controlling variables Z, written as $\rho_{XY|Z} \equiv \rho_{ij}^k$, is the correlation between the residuals R_X and R_Y resulting from the linear regression of X with Z and of Y with Z, respectively. Using the recursive formula, the partial correlation coefficient can be written in terms of simple correlation coefficients

$$\rho_{ij}^k = \frac{\rho_{ij} - \rho_{ik}\rho_{jk}}{\sqrt{(1-\rho_{ik}^2)(1-\rho_{jk}^2)}}. \tag{6.4}$$

Thus, the partial correlation between X and Y given Z represents the correlation between X and Y after removal of the dependence on Z.

Regarding the implementation of this measure, although the implementation of the recursive algorithm given by Eq. (6.4) presents an exponential complexity, the use of functional programming using recursive calls reduced the complexity to $O(T^3)$. However, an easier implementation with the same complexity $O(T^3)$ can be carried out by considering that partial correlations between random variables can be determined by inverting the covariance matrix $\Xi = (Cov(X, Y))$ [460]. This point of view was used in the present work and the partial correlation matrix was obtained through the following steps. First we proceeded to invert the covariance matrix, $g = \Xi^{-1}$. Second, we normalized the resultant matrix g as $\tilde{\pi} = \tilde{h} \cdot g \cdot \tilde{h}$, with $\tilde{h}$ the diagonal matrix and $\tilde{h}_{ij} = g_{ij}^{-1/2}$, $i = 1, ..., N$. And third and finally, to arrive to the partial correlation matrix π, the off–diagonal elements of π have to be multiplied by -1, [756] $\pi_{ij} = -\tilde{\pi}_{ij}$ for $i \neq j$. The small script implemented with Matlab is attached in Annex I.

Mutual Information Coefficient

Mutual information (MI) between two stochastic variables X and Y provides an estimation of the amount of information gained about X when Y is known. In others words, MI measures the statistically shared information between the two variables [615]. This linear measure [323] is a particular case of the of the Kullback–Leibler divergence [404], an information–theoretic measure of the distance between two probability distributions. Then, in this sense, it can be used as a similarity measure [230], as is given by

$$MI(X, Y, \delta) = -\sum_{x \in X, y \in Y} P(x_n, y_{n-\delta}) log \frac{P(x_n, y_{n-\delta})}{P(x_n) p(y_{n-\delta})}, \tag{6.5}$$

where $P(x_n, y_{n-\delta})$ denotes the joint probability of X and Y at certain temporal delay δ, and $P(x_n)$ and $P(y_n)$ would be the marginal probabilities of X and Y, respectively. In order to gain the highest amount of information about the dynamics between neuron i and j, the score for Mutual Information (MI) reconstructions was evaluated as

$$MI_{Y \to X} = \max_{\Delta t \in [0, t_{max}]} \{MI(X, Y, \delta) | g_{n+1} < \tilde{g}\} = max_{\delta} \{MI(X, Y, \delta) | g_n < \tilde{g}\}. \tag{6.6}$$

Although MI is a nonlinear generalization of familiar correlation functions [424], it contains no inherent directionality. Hence, the obtained connectivity matrix represents a weighted and undirected graph.

Generalized Transfer Entropy Coefficient

Transfer Entropy (TE) is an statistical measure that quantifies the amount of directed transfer of information between two random processes [323, 615]. In this sense, TE defines the amount of uncertainty reduced in future values of Y when past values of X and Y are known. Indeed, TE which is related to concept of Granger causality [285] has been proposed to distinguish effective driving detecting asymmetries in the interaction of

subsystems. Given two discrete time series X and Y, TE can be defined by computing the corresponding Kullback entropy [403]

$$TE_{Y\to X}(k,l) = -\sum_{x\in X, y\in Y} P(x_{n+1}, x_n^{(k)}, y_n^{(l)}) \log_2 \frac{P(x_{n+1}|x_n^{(k)}, y_n^{(l)})}{P(x_{n+1}|x_n^{(k)})}, \tag{6.7}$$

where p denotes the transition probability conditioned to the past k and l observations of the temporal series X and Y. TE assume that X and Y are two discrete Markov process, and can interpreted as the distance in probability space (known as the Kullback–Leibler divergence) between the 'single node' transition matrix $P(x_{n+1}|x_n^{(k)})$ and the 'two nodes' transition matrix $P(x_{n+1}|x_n^{(k)}, y_n^{(k)})$. It is worth noting that Eq. (6.7) can be seen as the difference between two entropy rates

$$TE_{Y\to X}(k,l) = h_X - h_{X,Y}, \tag{6.8}$$

where h_X is the entropy rate

$$h_X = -\sum_{x\in X} p(x_{n+1}, x_n^{(k)}) \log_2 p(x_{n+1}|x_n^{(k)}), \tag{6.9}$$

and $h_{X,Y}$ is a generalized entropy rate conditioning on the source state as well

$$h_X = -\sum_{x\in X, y\in Y} p(x_{n+1}, x_n^{(k)}, y_n^{(l)}) \log_2 p(x_{n+1}|x_n^{(k)}, y_n^{(l)}). \tag{6.10}$$

The entropy rate h_X accounts for the average number of bits needed to encode an additional state of the system if all previous states are known [615], while the entropy rate $h_{X,Y}$ is the entropy rate capturing the average number of bits required to represent the value of the next destination's state if source states are included in addition. On this basis, one can write

$$h_X = -\sum_{x\in X, y\in Y} p(x_{n+1}, x_n^{(k)}, y_n^{(l)}) \log_2 p(x_{n+1}|x_n^{(k)}). \tag{6.11}$$

Then, if the next state of destination is independent of the source, the entropy rate h_X is equivalent to the rate $h_{X,Y}$, i.e.

$$p(x_{n+1}, x_n^{(k)}, y_n^{(l)}) = p(x_{n+1}, x_n^{(k)}, y_n^{(l)}). \tag{6.12}$$

In this case the transfer entropy reduces to zero. Indeed, TE is zero if transitions of X do not depend statistically on past values of Y, and is greater than zero otherwise, signaling dependence of the transition dynamics of X on Y. In our studies, we extended the original description of TE provided in Eq. (6.7) to the form

$$\begin{aligned} TE^*_{Y\to X|G} = &-\sum_{x\in X, y\in Y} p(x_{n+1}, x_n^{(k)}, y_n^{(k)}|g_{n+1} < \tilde{g}) \\ &\log_2 \frac{p(x_{n+1}|x_n^{(k)}, y_n^{(l)}, g_{n+1} < \tilde{g})}{p(x_{n+1}|x_n^{(k)}, g_{n+1} < \tilde{g})}. \end{aligned} \tag{6.13}$$

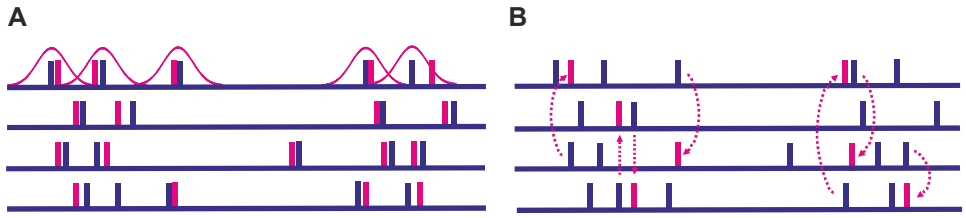

Figure 6.2: **Shuffling methods for null models.** (A) Schematic illustration of Monte Carlo interval *jitter* for different binary activity traces of individual neurons. Time correlations are removed while maintaining the temporal and spatial network modulation. (B) *swapping* technique, in which the inter–firing–interval distribution of individual neurons is preserved.

This description accounts for the conditioning of the fluorescence signal through $\tilde{g}$, and is called Generalized Transfer Entropy (GTE) [676]. Since the synaptic time constants of the neuronal network ($\simeq$ 1 ms) are much shorter than the acquisition times of the recording $\simeq$ 20 ms), we considered each discrete Markov process to have equal order $k \approx 2$, and with $k = l$. In this case, the derived connectivity matrix represents a weighted and direct graph.

6.2.3 Optimization and Testing

Once the connectivity matrices were obtained, we proceeded to analyze them to purge spurious connections. Weak and non–significant links were filtered out by using a *null model* of the connectivity matrices under inspection. The quality of reconstruction was assessed using simulated networks, contrasting the obtained connectivity matrices with the real, ground–truth structural matrix.

This analysis allowed us to choose the most appropriate reconstruction method and to select the optimal threshold to define the top ranked links, which finally represent the connectivity network.

Null model: Surrogates Data Testing

Null models were first proposed by Newmann et al. [519] as a generalization of surrogates data testing in the framework of graph theory. It is a methodology commonly used as a term of comparison to verify whether the graph of interest displays statistically significant features (i.e. non–random).

The null model consists of building a graph which matches a specific graph in some of its structural features, but that otherwise is taken to be an instance of a random graph. Surrogates matrices are hence generated by randomizing the specific features that one wants to study. Two different possibilities to generate surrogates are usually utilized: *a priori* one based on the original data, or *a posteriori* one based on the resultant matrix. In our case, the general recommendation is that surrogates must be generated from the original signals to preserve the structure of the data while destroying temporal correlations among neurons.

To identify statistically significant, non–random features of reconstructed topology, two shuffling methods are usually used in neuroscience [68, 591, 529], namely the *jittering method* and the *swapping method*, illustrated in Fig. 6.2. The former perturbs the timing of each spike by an amount drawn from a Gaussian distribution of mean zero and standard deviation matching the upper time delay between neurons (with typically $\sigma > 1$ ms). Because the perturbation has zero mean, the inter–spike–interval distribution is preserved along with the modulations in population activity. Additionally, the number of spikes per neuron remain invariant but the time correlation between neurons is removed. The latter method is a balanced rearrangement of spikes over the neurons. It retains the same number of spikes for each neuron, but they occur at different times. This method preserves both temporal and spatial population modulations, but fails at preserving the inter–spike–interval distribution of individual neurons.

Since we are interested in preserving the firings per neuron, we finally used the *jitter* method. For its construction we used Gaussian distributions of mean zero and a standard deviation of 20 ms centered at each spike.

In regard to number of surrogates to generate, we proceeded in the same way than in the previous Chapter. In practice, it is common to generate 10 to 100 surrogates of a given type to obtain a minimal significance requirement. Following Theiler *et al.* [699], for a two–side test we would generate $M = 2/\alpha - 1$ surrogates, resulting in a probability α that the data gives either smaller or the largest value. Then, for a minimal significance requirement of 98% we thus need at least 99 surrogate time series. Using more surrogates can increase the discrimination power but decreases the computational efficiency.

Once the surrogate were generated, noisy and non-causal connectivity scores are filtered by thresholding and normalizing the reconstructed network with respect to randomized matrices. We then computed the z-score Z_{ij} for the weight w_{ij} as

$$Z_{ij} = \frac{w_{ij} - \langle w_{ij}^s \rangle}{\sigma_{ij}^s}, \tag{6.14}$$

where $\langle w_{ij}^s \rangle$ is the mean weight between neuron i and neuron j provided for the 99 surrogates of the null model, and σ_{ij}^s the corresponding standard deviation. If we define $W_{ij} \equiv Z_{ij}$, then this matrix provides the effective connectivity between the neurons in the network. In order to compare the different experiments, we finally normalized $\tilde{W}_{ij} = W_{ij}^{(max)}$ to obtain $\tilde{W} \in [0, 1]$.

Reconstruction Matrix Testing and Threshold selection

In order to test the different approximations applied, we focused on the reconstruction of simulated networks based on synthetic fluorescence time series. We simulated the spiking dynamics of homogeneous networks formed by a sub–set of $N = 1000$ neurons, along a duration of 10 minutes. Calcium fluorescence time series were then produced on this spiking dynamics, resorting to a model introduced in Ref. [736] and described in Chapter 3. In a first analysis, the binary firing sequence of each neuron obtained from the simulation was sampled with different frame rates with a fixed signal–to–noise ratio (see Fig. 3.6B). In a second analysis, given a fixed frame rate of 50 fps, different signal–to–noise ratios were simulated in order to test the sensitivity of the different reconstruction methods explained above (Fig. 3.6A). Once the synthetic fluorescence time series were obtained,

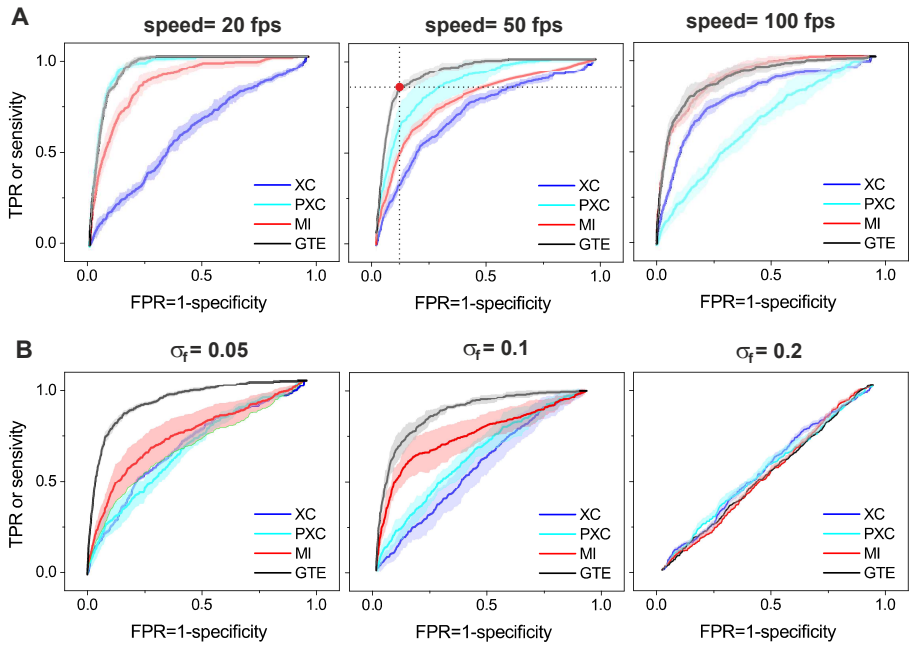

Figure 6.3: **Testing of the reconstruction matrix using ROC curves.** The plots show the ROC curves for the different similarity measures studied. (A) Considering different frame rates, with a fixed signal–to–noise ratio of $\sigma_f = 0.05$. (B) Considering different signal–to–noise ratios, with a fixed frame rate of 50 fps. The red dot shows the preset cut–off threshold for providing a quantification of the goodness of the reconstruction.

we proceeded to reconstruct the connectivity matrix with the techniques outlined above. With the aim of isolating potential spike events, synthetic fluorescence time series were discretized. XC, PCC, MI and GTE–reconstruction were then performed and contrasted with the ground–truth connectivity matrix of the simulated model.

To assess the quality of the reconstruction for the different methods, we computed standard *Receiver-Operator Characteristic* (ROC) curves. They are constructed through the comparison of the structural adjacency matrix $A^{(str)}$ and the dynamic one$A^{(dyn)}$, and by plotting the true positive rate (TPR or sensitivity) as a function of the false positive rate (FPR) at various equally spaced thresholds ranging from 0 to 1. We note that FPR = 1- *specificity*, with the latter being the true negative rate or TNR.

The higher threshold led to zero true positives and false positives and, hence, zero reconstructed links. At the other extreme, the lowest threshold provided both 100% of true and false positives, including the whole network. Then, the coordinate $(0, 1)$ of the ROC space is also called a *perfect classification*. Intermediate values of the threshold provides a smooth curve of true/false positives as a function of the threshold. A completely random guess would give points along the diagonal lines, also termed *line of no discrimination*, from the left–bottom to the top–right corners. Then, the accuracy of reconstruction can then be validated by measuring the degree of deviation of this curve from the diagonal.

The graph in Fig. 6.3 shows the ROC curves for the respective models, with different frame rates (top panels), or different signal–to–noise ratios with a fixed frame rate of $v = 50$ fps (bottom panels). Each curve represents the average of ten simulations with the

same topology where the shaded area corresponds to the error given by their corresponding standard deviation. Good reconstructions were obtained by the GTE method whose results appears to be independent of the frame rate applied. At the other extreme, worse tests are obtained with XC–reconstruction, although the results improve as the frame rate increase. Intermediate results are obtained with the MI– and PXC–reconstructions. Additionally, these set of analysis allows us to choose the optimum threshold value that minimizes the cost of reconstruction. This optimal cut–off is marked with a red circle in Fig. 6.3A. As an indicator for the quality of reconstruction we used the quantity $TE_{15\%}$ defined as the fraction of true positive for a 15% of false positives.

The analysis shows that PXC reconstruction achieves better results than XC–reconstruction. Indeed, unlike bi–variate methods such as XC coefficient, PXC is a multivariate method that provides simultaneous analysis of interdependences between three or more processes. So in this sense, XC–reconstruction was unable to distinguish direct and indirect connections falling short in reconstructing the network's topology. It is important to highlight this fact because of reconstructing specific topological motifs involves more than two nodes. Considering for example the *shared source motif* in which a node A was connected to a node B ($A \rightarrow B$) and to a node C ($A \rightarrow C$) but in which there was no direct connection between B and C. In consequence, the existence the one shared input A may lead to adding fictitious links such as the causal interactions between nodes B and C. Similarly, in the case of embedded chains, i.e. motifs in which a node A is connected to B, connected on its turn to C, but without a direct link from A to C ($A \rightarrow B \rightarrow C$). About a 20% of incorrect links ($A \rightarrow C$) were introduced by bi–variate measures like XC.

In contrast, an overall quality is obtained by MI and GTE reconstruction because both techniques are sensitive to both linear interaction and nonlinear correlations between any pair of neuronal activities.

6.3 Network properties

Once the network topology was reconstructed, we proceed to characterize it with different statistical descriptors. In the next subsections the different statistics of networks used in this thesis are briefly explained.

Degree and strength

The *degree* of a node i (k_i) is defined as the number of neighbors (links) connected to this node. In a directed network, k_i is defined as the sum of ingoing (in–degree, k_i^{in}) and outgoing (out–degree, k_i^{out}) links in node i. The weighted extension of degree is called the strength g, which is defined in the same way but taking into account the weight of the edge,

$$g_i = g_i^{out} + g^{in}, \tag{6.15}$$

where the out-strength g_i^{out} is given by th form,

$$g_i^{out} = \sum_{j \in N} w_{ij}, \tag{6.16}$$

and the in-strength g_i^{in} by,

$$g_i^{in} = \sum_{j \in N} w_{ji}, \tag{6.17}$$

where N is the total set of nodes and w_{ij} are the normalized weighted links, $0 \leq w_{ij} \leq 1$.

Characteristic path length and global efficiency

.

The *characteristic path length* (L) is defined as the mean of shortest paths for all the possible pairs of the network nodes, i.e.

$$L = \frac{1}{n} \sum_{i \in N} L_i = \frac{1}{n} \sum_{i \in N} \frac{\sum\limits_{j \in N, j \neq i} l_{ij}}{n-1}, \tag{6.18}$$

where N is the total set of nodes, n is the number of nodes, L_i is the average distance between the node i and all the others and the shortest paths l_{ij} are given by the following form,

$$l_{ij} = \sum_{g_{i \to j}} \left(\frac{1}{w_{ij}} \right), \tag{6.19}$$

where $g_{i \to j}$ is the direct shortest weighted path from i to j computed by the Dijkstra's algorithm [191]. The inverse of this measure determines the *global efficiency* E_{global} of the network [410, 16],

$$E_{global} = \frac{1}{n} \sum_{i \in N} G_{eff,i} = \frac{1}{n} \sum_{i \in N} \frac{\sum\limits_{j \in N, j \neq i} l_{ij}^{-1}}{n-1}, \tag{6.20}$$

where $G_{eff,i}$ is the efficiency of node i. Both quantities represent the global information flow or the mass transport on a network, and they are used to characterize the traffic transport of the network. However, the first parameter (L) provides a measure of the network's capacity for serial information transfer between nodes, whereas the second one (E_{global}) is a measure of the network's capacity for parallel information transfer between nodes. Since there are strong evidences suggesting that the brain supports massively parallel information processing, it seems conceptually preferable to adopt efficiency metrics. Notice that in a small–world network we will have E_{global} greater than a regular lattice but E_{global} smaller than a random network. The longest shortest path between any two nodes in the network defines the diameter of the network, which represent the longest geodesic.

Clustering and local efficiency

The *cluster coefficient* (CC) is a topological local property that is given by the number of triangles around an individual node i respect its maximum possible triangles [749],

$$CC = \frac{1}{N} \sum_{i \in N} CC_i = \frac{1}{n} \sum_{i \in N} \frac{t_i}{(g_i^{out} + g_i^{in})(g_i^{out} + g_i^{in} - 1) - 2 \sum\limits_{j \in N} w_{ij} w_{ji}}, \tag{6.21}$$

where CC_i is the clustering coefficient of node i and t_{ij} is the number of triangles given by the form,

$$t_i = \frac{1}{2} \sum_{j,k \in N} ((w_{ij} + w_{ji})(w_{ik} + w_{ki})(w_{jk} + w_{kj}))^{1/3}. \tag{6.22}$$

Hence, in this sense, it is an important local quantity that measures the number of loops (triangles) a node over all its possibilities and characterizes percolation properties of the network [627]. On the other hand, we can define the *local efficiency* as the average efficiency of the local subgraphs, G_i [410, 16]. Like the cluster coefficient, such a quantity plays a similar role, indicating how each subgraph exchanges information and can also be understood as a measure of the fault tolerance of the network.

Degree correlation and assortativity mixing

Degree correlation is a basic structural metric which calculates the likelihood that nodes attach to other nodes of similar or dissimilar nodal degree [473, 545, 733, 515, 516]. In the former case, the network presents a positive correlation and they are called *assortative*. Whereas,for the latter, the network is characterized by a negative correlation coefficient and they are so–called *disassortative*.

To study the dependence on k, one can calculate the average degree of the nearest neighbors of the nodes with degree k, denoted as $k_{nn}(k)$ [545]. Then the *average nearest neighbors degree* of a node i can be defined as

$$k_{nn,i} = \frac{1}{k_i} \sum_{j \in N_i} k_j = \frac{1}{k_i} \sum_{j=1}^{N} a_{ij} k_j, \tag{6.23}$$

where the sum runs over the nodes belonging to N_i, the set of first neighbors of i. By using this definition, the average of nearest neighbors of nodes with degree k can be expressed in terms of the conditional probability as,

$$k_{nn}(k) = \sum_{k'} k' P(k'|k). \tag{6.24}$$

When $k_{nn}(k)$ is independent of k and no degree correlation is presented, then Eq. (6.24) gives $k_{nn}(k) = \langle k^2 \rangle / \langle k \rangle$. Correlated graphs are *assortative* if $k_{nn}(k)$ is an increasing function of k, whereas they are referred to as *dissassortative* when $k_{nn}(k)$ is a decreasing function of k [515]. Degree correlation are usually quantified by reporting the numerical values of the slope of $k_{nn}(k)$ as a function of k or by calculating the Pearson correlation coefficient of the degree. In direct weighted network this coefficient can be defined as [517, 692]

$$\rho^{DW} = \frac{\sum_{i,j} w_{i,j} (g_i^{out} - \langle g^{out} \rangle_E)(g_j^{in} - \langle g^{in} \rangle_E)}{\sqrt{\sum_i g_i^{out} (g_i^{out} - \langle g^{out} \rangle_E)^2} \sqrt{\sum_j g_j^{in} (g_j^{in} - \langle g^{in} \rangle_E)^2}}, \tag{6.25}$$

where E computes all the links in the network, and

$$\langle g^{out} \rangle_E = \frac{1}{\sum_{(i,j) \in E} w_{ij}} \sum_{(i,j) \in E} w_{ij} g_i^{out}, \tag{6.26}$$

and

$$\left\langle g^{in} \right\rangle_E = \frac{1}{\sum\limits_{(i,j)\in E} w_{ij}} \sum_{(i,j)\in E} w_{ij} g_j^{in}. \tag{6.27}$$

Networks with high positive assortativity coefficient would indicate that nodes with the same degree tend to be interconnected. On the other hand, networks with negative assortative mixing (disassortative) tend to show high–degree nodes connected with low–degree ones, showing a democratic rules of connectivity. Since in diassortative networks the magnitude of the standard assortativity decreases with network size [434], usually the Pearson correlation is replaced by the Spearman rank correlation, ρ^{SW}. This coefficient is calculated in the same way as the Pearson correlation but substituting the strength of the nodes by their respective ranks, i.e. their position when the values are sorted in ascending order.

The estimation of the error in the assortativity value is computed through the bootstrap algorithm [207] considering 1000 random samples of the data.

Community and Modularity Index

Many complex networks often present different densely connected group of vertices, shaping the so–called *community structure*. This tightly–knot group with only sparser connections between this *modulus* or *structural motifs* gives rise to different subgraphs in the dynamical level, shaping the onset of neuronal functional motifs [1]. The concept of the motifs was originally introduced by Alon and coworkers [635, 487, 465, 486, 378], who studied small n motifs in biological and other networks. Indeed, finding the communities within a network is a suitable tool for understanding the functioning of the network, as well as for identifying a hierarchy of connections within a complex architecture.

The traditional method for extracting community structure from a network is using the *modularity index* Q [518]

$$Q = \frac{1}{2p} \sum_{i,j\in N} \left(w_{ij} - \frac{g_i^{out} g_j^{in}}{2p} \right) \delta_{m_i,m_j}, \tag{6.28}$$

where p is the total number of edges, m_i is the module containing node i and δ_{m_i,m_j} is the Kronecker delta. This measure quantifies the non–overlapping modules maximizing the number of links within the module while minimizing the number of inter–modular links.

Hubs and Centrality Measures

Connectivity in reconstructed networks is often heterogeneous and groups of nodes with tighter internal connectivity are often visually similar. These nodes with a number of links that greatly exceeds the average, usually termed *hubs*, in general play a crucial role in efficient integration of information across the network. A possible indicator of a node's

[1] Those building blocks are called 'motifs' in analogy to driving elements that are elaborated in musical theme or composition. In music, a motif or motive is a short music idea, a salient recurring figure which constitutes the smallest functional unit possessing thematic identity. Although in music, the motif may have harmonic, melodic and/or rhythmic aspects

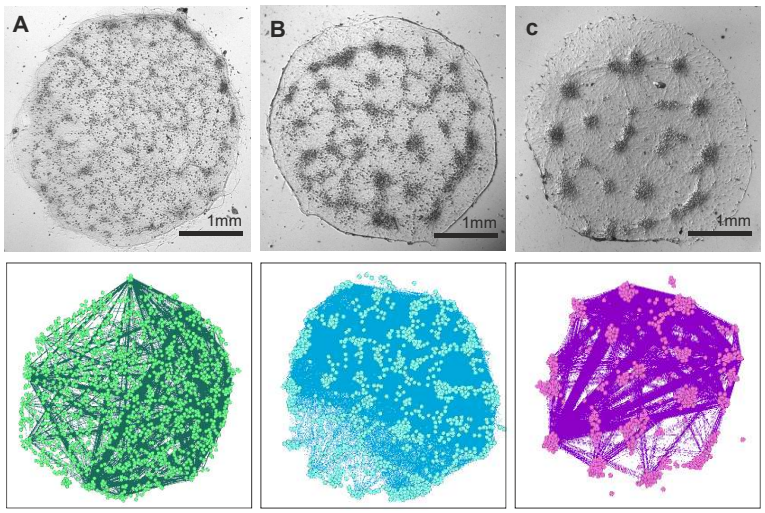

Figure 6.4: **GTE–reconstruction from [E+I]-networks with different degree of aggregation.** The top images show bright–field images of neuronal cultures with different degrees of aggregation. The bottom graphs show their corresponding reconstructed networks. In all cases, data corresponds to GTE–reconstructions of [E+I]–networks. (A) Homogeneous culture (DIV=15, $\lambda = 0.43$); (B) Semi–aggregated culture (DIV=14, $\lambda = 0.69$); and (C) Aggregated culture (DIV=14, $\lambda = 0.77$).

centrality in a network is the *betweenness centrality*. This measure quantifies the number of shortest paths that pass through a given node i,

$$b_i = \frac{1}{(n-1)(n-2)} \sum_{h,j \in N} \frac{l_{hj}(i)}{l_{hj}}, \tag{6.29}$$

where l_{hj} is the number of shortest path between h and j and $l_{hj}(i)$ is the number of shortest path between h and j that pass through i. A node with high betweenness centrality has a large influence in the network, asserting a control over the flow of information.

6.4 Case Study: Cortical Neuronal Cultures

Reconstruction analysis was carried out for the entire population of imaged neurons in the different contexts reported in Chapter 2. Although the degree of aggregation of the different cultures obtained presented a continuous range as a function of the spatial distribution of neurons, all the experiments were classified in the following three categories: aggregated cultures ($\lambda \in [1-0.7)$), semi–aggregated cultures ($\lambda \in [0.7-0.50)$) and homogeneous cultures ($\lambda \in (0.50-0]$) where λ is the aggregation coefficient. As discussed in previous sections, we examined the networks defined by the top 10% of GTE–ranked links and these results were matched with the null models where randomized networks were associated to an Erdös-Rényi model (ER–networks). Three examples of different GTE–reconstructions corresponding to [E+I]–networks with different degree of aggregation are pictured in Fig. 6.4.

6.4.1 Development experiments

Connectivity of the network

As seen in the previous Chapter, there is no activity during the first 5 days of development of a neuronal network. The gradual emergence of spontaneous activity occurs during the next few days, and as a consequence of the evolution and interplay between single–neuron dynamics and network connectivity. Hence, revealing the major characteristics of the culture connectivity can be a key piece to help us understanding such a complex developmental process.

In Tab. 6.1 we provide the different network statistics for the three network aggregation schemes, and as a function of age (DIV). The different levels of aggregation, measured through the aggregation coefficient λ, comprised the following ranges: $\lambda \in [0.21 - 0.43]$ for homogeneous networks, $\lambda \in [0.45 - 0.57]$ for semi–aggregated networks and $\lambda \in [0.71 - 0.81]$ for aggregated networks. In all the experiments, the neuronal cultures were confined in circular PDMS wells of 3 mm in diameter. In this way, all the neurons in the culture could be simultaneously imaged. Although all cultures presented the same nominal density upon plating, and similar total number of neurons $N \simeq 1000$ upon imaging, they exhibited important variations at a local scale due to aggregation. Indeed, homogeneous cultures provided $\rho \simeq 180$ neurons/mm^2 everywhere, but aggregated ones provided $\rho \simeq 120$ inside the aggregates and $\rho \simeq 90$ neurons/mm^2 outside. Interesting is the fact that aggregates usually presented the same size ($A = \pi r^2 \simeq 0.20$ mm^2 with radius $r \simeq 0.25$ mm) with the similar number of neurons, $N_a \simeq 100$. Considering this context, different outcomes can be taken into consideration in regard to the connectivity.

As the cultures mature, the average number of edges (and so, their density of wiring) increased in accordance with the development of connections. Before *GABA switch*, [E+I]-networks of young cultures ($DIV < 7 \pm 2$) presented low values of average degree $\overline{k}_{EI} \simeq [3 \pm 9 - 7 \pm 11]$ and average synaptic strength $\overline{g}_{EI} \simeq [7 \pm 10 - 7 \pm 8]$. At this early age, no substantial differences between $\overline{k}_{EI}$ and $\overline{g}_{EI}$ were observed. Low connectivity and weakness of the links predominate in the first days of growth. However, we note that the error associated with the computation of both parameters is too high to draw any conclusion.

Culture type	DIV	Nº Exp (n)	Aggreg. coeff. (γ)	Firing rate (min^{-1})	Average number of nodes	Average number of edges	Average degree			Average strength			Average path length			Clustering coefficient		
					GTE	GTE	GTE	PXC	ER*	GTE	PXC	ER*	GTE	PXC	ER*	GTE	PXC	ER*
A	5	2	0.71±0.07	1.4±0.3	1521±26	6716±413	7±11	12±12	8±7	7±8	25±7	9±9	1.0±0.5	0.7±0.3	0.8±0.3	0.12±0.06	0.09±0.08	0.01±0.09
A	7	6	0.80±0.04	3.6±0.4	1000±32	9301±512	32±14	37±23	26±5	68±11	78±12	28±6	1.8±0.4	1.2±0.4	0.2±0.4	0.34±0.09	0.11±0.07	0.04±0.07
A	8	2	0.73±0.03	2.9±0.2	803±41	13835±612	19±12	21±21	34±7	32±10	89±23	35±7	2.1±0.6	1.3±0.5	0.2±0.4	0.30±0.08	0.21±0.08	0.04±0.06
A	9	4	0.72±0.03	4.7±0.5	710±43	6534±441	21±13	29±16	21±8	22±14	47±27	25±8	2.1±0.3	0.8±0.3	0.3±0.1	0.21±0.05	0.13±0.06	0.03±0.07
A	12	3	0.71±0.05	5.2±0.4	1421±45	10121±656	76±14	31±25	14±7	98±12	102±21	31±6	2.5±0.4	1.2±0.6	0.5±0.2	0.35±0.07	0.24±0.09	0.01±0.08
A	14	4	0.76±0.04	4.2±0.3	947±52	35244±598	116±21	142±26	128±6	191±17	144±13	132±13	1.9±0.4	1.0±0.6	0.1±0.4	0.41±0.06	0.21±0.04	0.24±0.05
A	15	3	0.81±0.07	3.8±0.4	996±44	7620±614	94±15	105±24	20±4	156±16	211±29	47±9	2.3±0.2	1.0±0.7	0.4±0.3	0.37±0.07	0.20±0.08	0.02±0.06
					GTE	GTE	GTE	PXC	ER*	GTE	PXC	ER*	GTE	PXC	ER*	GTE	PXC	ER*
SA	5	4	0.57±0.04	0.9±0.5	961±42	4511±724	5±12	6±12	9±12	5±11	8±14	9±6	1.1±0.2	1.0±0.4	0.7±0.3	0.09±0.06	0.08±0.04	0.01±0.05
SA	7	4	0.55±0.06	2.4±0.3	1551±41	3587±689	6±13	8±14	13±9	17±17	21±16	10±5	1.8±0.2	1.0±0.4	0.4±0.5	0.12±0.02	0.11±0.05	0.02±0.07
SA	8	5	0.56±0.02	1.3±0.4	866±33	5984±213	7±9	14±23	13±6	12±18	11±17	14±7	2.1±0.6	0.9±0.4	0.5±0.6	0.34±0.07	0.20±0.08	0.01±0.06
SA	9	4	0.56±0.03	2.1±0.2	979±44	6959±781	18±15	21±22	14±5	9±14	14±15	12±9	2.3±0.4	2.1±0.4	0.5±0.5	0.31±0.05	0.13±0.07	0.01±0.05
SA	13	4	0.59±0.10	2.2±0.4	1001±33	5984±812	41±11	54±24	47±6	55±16	65±21	50±13	2.5±0.1	1.3±0.4	0.1±0.4	0.34±0.06	0.22±0.08	0.05±0.03
SA	14	2	0.45±0.01	2.5±0.4	1368±33	21812±672	70±11	88±18	18±5	40±17	56±14	22±14	2.3±0.2	2.0±0.4	0.4±0.7	0.18±0.04	0.25±0.09	0.02±0.02
SA	15	4	0.45±0.02	2.1±0.3	910±34	12710±812	62±12	95±19	18±8	89±15	98±16	32±17	2.5±0.1	1.6±0.4	0.4±0.3	0.25±0.01	0.18±0.07	0.02±0.05
					GTE	GTE	GTE	PXC	ER*	GTE	PXC	ER*	GTE	PXC	ER*	GTE	PXC	ER*
H	5	2	0.38±0.04	1.4±0.3	1556±36	5556±643	3±9	8±17	7±10	4±11	14±14	8±12	1.2±0.2	1.0±0.5	0.8±0.6	0.07±0.04	0.03±0.03	0.01±0.04
H	7	4	0.36±0.06	1.2±0.4	2109±32	9129±480	11±8	19±18	8±14	9±12	13±14	9±10	1.8±0.3	1.1±0.2	0.3±0.3	0.15±0.05	0.08±0.05	0.01±0.05
H	8	4	0.41±0.05	1.4±0.4	1330±34	6149±329	9±11	21±15	9±15	6±14	14.±11	11±7	2.2±0.9	1.3±0.9	0.5±0.3	0.07±0.05	0.05±0.04	0.01±0.03
H	9	6	0.43±0.01	1.1±0.4	1526±58	6580±555	10±7	22±16	8±14	9±15	24±7	9±8	2.3±0.7	0.9±0.8	0.6±0.5	0.09±0.04	0.04±0.03	0.01±0.04
H	12	2	0.21±0.01	2.3±0.5	973±49	16265±561	26±5	31±14	33±18	30±13	74±9	43±18	2.3±0.2	1.5±0.4	0.4±0.6	0.18±0.02	0.08±0.06	0.03±0.02
H	14	3	0.41±0.14	2.2±0.5	1028±51	34788±776	67±6	79±13	67±18	101±14	98±8	87±17	1.9±0.1	1.2±0.7	0.5±0.4	0.15±0.05	0.09±0.05	0.06±0.03
H	16	2	0.43±0.08	2.8±0.5	1265±47	27198±696	57±5	89±11	43±18	81±14	97±7	57±12	2.5±0.2	1.2±0.3	0.6±0.7	0.11±0.06	0.07±0.05	0.03±0.04

Table 6.1: **Network statistics of aggregated (A), semi-aggregated (SA) and homogeneous (H) cultures.** The table shows the different topological descriptors of GTE and PXC–reconstructions corresponding to aggregated (A), semi-aggregated (SA) and homogeneous (H) cultures in function of *day in vitro* (DIV) and aggregation degree (λ). The obtained values are one average of n experiments and the results are compared with the corresponding ER–surrogates.

On the other hand, mature cultures ($DIV \geq 7 \pm 2$) are characterized by an increase of connectivity ($\overline{k}_{EI} \simeq [6 \pm 13 - 116 \pm 21]$) and synaptic strength ($\overline{g}_{EI} \simeq [6 \pm 14 - 191 \pm 17]$). As the cultures ripen, the gap between $\overline{k}_{EI}$ and $\overline{g}_{EI}$ tends also to increase and $\overline{g}_{EI} > \overline{k}_{EI}$ showing a gain of the synaptic strength of the links of the network. Notice that the average degree $\overline{k}_{EI}$ refers to the mean number of connections per node, so for old cultures (DIV $\geq 14 \pm 2$) an average of $\overline{k}_{EI} \simeq 62 \pm 6$ and $\overline{k}_{EI} \simeq 66 \pm 12$ neighbors per neurons are computed for homogeneous and semi-aggregated networks, respectively. For heterogeneous networks, this average is increased $\overline{k}_{EI} \simeq 105 \pm 18$. Additionally, the average strength $\overline{g}_{EI}$ refers to the mean weight per node. Hence, for old cultures (DIV $\geq 14 \pm 2$) an average of $\overline{g}_{EI} \simeq 91 \pm 14$, $\overline{g}_{EI} \simeq 65 \pm 16$, $\overline{g}_{EI} \simeq 174 \pm 17$ strength per neurons is computed for homogeneous, semi-aggregated and aggregated networks respectively. Overall, aggregated cultures present values of average degree and synaptic strength slightly higher than homogeneous and semi–aggregated ones.

As the days go by, a greater number of neurons are activated and their connections get reinforced. In Fig. 6.5 we picture the fraction of neurons ϕ that show spontaneous activity as a function of the *day in vitro* (DIV). One can observe that the fraction of active neurons in the case of aggregated culture is slightly higher than the semi–aggregated and homogeneous cases. However, by rearranging the neuronal activity ϕ as a function of in-degree $\overline{k}_{EI}^{in}$, similar behavior is observed between the different topologies. Hence, despite the presence of aggregates, it seems that all the curves collapse showing a similar behavior. On the other hand, it is interesting to point out the fact that the emergence of neuronal activity in aggregated cultures is detected on a threshold around the value $\overline{k}_{EI}^{in} \simeq 4 \pm 7$, slightly higher than in semi-aggregated $\overline{k}_{EI}^{in} \simeq 2 \pm 6$ and homogeneous $\overline{k}_{EI}^{in} \simeq 1 \pm 4$ counterparts. That is, the number of the inputs to activate a neuron or a set of them is higher in the aggregated case than in the semi-aggregated and homogeneous cases. In consequence, in aggregated cultures the emergence of neuronal activity occurs slightly later than their counterparts. However, once the threshold is exceeded, the aggregated will be activated in greater proportion than their counterparts. However, high error values are associated in this analysis, making it difficult to interpret.

Finally, as will be analyzed later, in Tab. 6.1 one can also observe marked differences between GTE–reconstructions and their corresponding ER–surro-gates. Values similar to ER–surrogates were achieved with PXC–reconstruc-tions.

In Tab. 6.2 the network parameters obtained from simulated aggregated and homogeneous networks are attached. All the simulated networks were encapsulated with circular pattern of 3 mm in diameter. In the case of aggregated networks, all the islands densely populated were simulated with the same bi–color pattern as substrate in order to create the same topology as a function of their density. However, for each simulation n, the pattern of aggregated were randomized to obtain different topologies. We considered the size of networks in the range $N \in [1000 - 5000]$ neurons with densities of $\rho \in [142 \pm 25 - 707 \pm 32]$ neurons/mm^2. In this case, the density of each aggregated island is fixed by $\rho \simeq 107 \pm 12$ neurons/mm^2 while it is increased the density of the homogeneous subnetwork.

The network descriptors were computed from the structural adjacency matrix. Just as in experiments, the aggregated networks in the simulations presented average degrees $\overline{k}$, strengths $\overline{g}$ and clustering coefficients CC slightly higher than the homogeneous ones. Notice that the clustering coefficient for homogeneous networks is almost invariant since

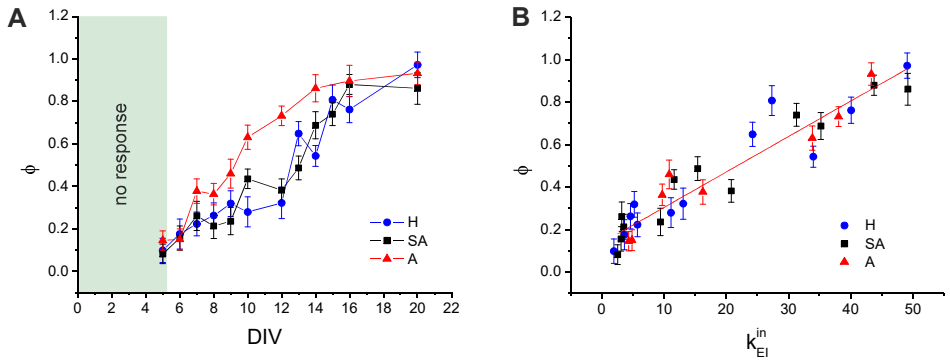

Figure 6.5: **Neuronal activity and connectivity**. (A) Fraction of neurons ϕ that spontaneously fired as a function of the *day in vitro* (DIV). (B) Average in–degree $\overline{k}_{EI}^{in}$ as a function of DIV. In both plots, the three different topologies of networks are considered. Neuronal activity ϕ is linearly fitted as $\phi = a\overline{k}_{EI}^{in} + b$ where $a = 0.016$, $b = 0.170$ and $r^2 = 0.911$. Data points are an average over $2 - 6$ experiments (see Tab. 6.1).

the growth rules are the same for each simulation n. In contrast, the average path length L is different, and depends on the density and the spatial arrangements considered.

With regard to the interplay between the connectivity and the topology of the simulated networks, different aspects should be considered. First, although homogeneous networks exhibit higher values of the average connectivity $\overline{k}$ and average strength $\overline{g}$, in this regime of density for any value of g_{AMPA}, g_{GABA} and g_{NMDA}, no collective bursting dynamics is achieved. Despite the singular firing rate is higher, the [E+I]- and [E-only]-networks simulated over this homogeneous topology are unable to achieve coherent collective dynamics. Indeed, a critical size of homogeneous network ($N \simeq 10,000$ neurons) is required to sustain the collective dynamics. In contrast, small simulated aggregated networks are already capable of generating this collective dynamics although they still need grater number of connections and greater synaptic strengths. Surprisingly, our small experimental cultures with few and weak connections already present the bursting dynamics at early ages. We conjecture that not only the number and strength of connections matter, but also how they are organized. We will revisit this issue later.

Topology retrieved through GTE-reconstruction

In order to characterize the typology of the networks we proceed to compare the network parameter obtained through the GTE–reconstructions with their randomized counterparts (ER–networks). Although we computed the ER–surrogates referenced in Sec. 6.2.3 and applied them to the GTE–reconstruction, *a posteriori* we also contrasted this analysis creating analytically ER–ensembles. The network parameters for the ER–ensembles were computed considering that for large N the distribution of the degree of any particular vertex is given by a Poisson distribution. Then, the shortest path length was analytically computed as $L^r \sim ln(|N|)/\langle k \rangle$, the clustering coefficient as $CC^r = \langle k \rangle / |N|$ and the average degree as $\langle k \rangle = (N-1)\rho(k)$ where the density of the links was calculated as $\rho(k) = 2p/(N^2 - N)$, with p the total number of edges. With the aim to characterize the

Culture type	DIV	Nº Exp (n)	Average aggreg. coefficient (γ)	Average assortativity Pearson (wh)			Average assortativity Spearman (wh)		
				GTE	PXC	ER*	GTE	PXC	ER*
A	5	2	0.71±0.07	0.511±0.043	0.302±0.067	0.021±0.032	0.507±0.057	0.325±0.084	0.021±0.032
A	7	6	0.80±0.04	0.363±0.065	0.201±0.032	0.089±0.018	0.356±0.032	0.272±0.053	0.089±0.018
A	8	2	0.73±0.03	0.352±0.067	0.137±0.042	-0.012±0.029	0.344±0.069	0.138±0.036	-0.012±0.029
A	9	4	0.72±0.03	0.488±0.089	0.298±0.056	0.035±0.025	0.483±0.045	0.252±0.076	0.035±0.025
A	12	3	0.71±0.05	0.643±0.036	0.143±0.087	-0.067±0.012	0.636±0.067	0.149±0.068	-0.067±0.012
A	14	4	0.76±0.04	0.465±0.044	-0.151±0.043	-0.076±0.010	0.460±0.052	-0.146±0.054	-0.076±0.010
A	15	3	0.81±0.07	0.603±0.071	0.451±0.056	-0.013±0.019	0.509±0.064	0.407±0.082	-0.013±0.019
				GTE	PXC	ER*	GTE	PXC	ER*
SA	5	4	0.57±0.04	0.124±0.017	0.105±0.013	0.041±0.005	0.115±0.014	0.117±0.011	0.038±0.006
SA	7	4	0.55±0.06	-0.161±0.009	-0.301±0.016	0.021±0.011	-0.168±0.006	-0.305±0.048	0.019±0.009
SA	8	5	0.56±0.02	-0.231±0.018	-0.245±0.015	-0.031±0.013	-0.236±0.005	-0.249±0.064	-0.039±0.011
SA	9	4	0.56±0.03	-0.029±0.013	0.187±0.012	0.029±0.009	-0.031±0.013	0.179±0.023	0.023±0.007
SA	13	4	0.59±0.10	0.121±0.027	0.111±0.018	-0.075±0.009	0.120±0.019	0.140±0.032	-0.071±0.007
SA	14	2	0.45±0.01	-0.236±0.012	-0.154±0.017	-0.049±0.008	-0.242±0.007	-0.152±0.010	-0.041±0.004
SA	15	4	0.45±0.02	-0.039±0.015	0.017±0.039	0.051±0.007	-0.040±0.008	0.021±0.059	0.045±0.005
				GTE	PXC	ER*	GTE	PXC	ER*
H	5	2	0.38±0.04	-0.275±0.009	0.139±0.009	0.010±0.007	-0.281±0.007	0.144±0.011	0.010±0.005
H	7	4	0.36±0.06	-0.280±0.011	0.080±0.008	-0.017±0.009	-0.285±0.005	0.076±0.017	-0.012±0.006
H	8	4	0.41±0.05	-0.277±0.007	-0.171±0.005	0.021±0.021	-0.286±0.012	-0.179±0.006	0.027±0.010
H	9	6	0.43±0.01	-0.294±0.006	-0.172±0.009	0.009±0.006	-0.300±0.005	-0.167±0.007	0.015±0.009
H	12	2	0.21±0.01	-0.402±0.008	0.204±0.010	-0.013±0.010	-0.406±0.006	0.201±0.015	-0.019±0.009
H	14	3	0.41±0.14	-0.171±0.012	0.071±0.007	-0.095±0.004	-0.173±0.010	0.069±0.003	-0.090±0.008
H	16	2	0.43±0.08	-0.213±0.009	-0.213±0.021	0.032±0.005	-0.223±0.009	-0.211±0.016	0.027±0.006

Table 6.2: **Network statistics for aggregated (A) and homogeneous (H) simulated networks.** The table shows the different topological descriptors from direct adjacency matrices corresponding to aggregated and homogeneous simulated networks as a function of the density. The simulated networks were encapsulated in circular patterns of 3 mm in diameter. In the case of aggregated networks the same bi–color pattern was used in the creation of the aggregated island for all of them. The obtained values of the network statistics are average over n simulations.

typology of our neuronal cultures, we focused on analyzing these three different network descriptors.

As one can observe in Tab. 6.1, a significant deviation of the GTE–reconstructed networks from ER–surrogates was detected. GTE–reconstruction detects clustering at a moderate level ($\overline{CC} \simeq 0.12 \pm 0.04$) in the case of homogeneous culture, increasing for the aggregated networks ($\overline{CC} \simeq 0.30 \pm 0.06$). Intermediate values are obtained in the semi–aggregated topologies ($\overline{CC} \simeq 0.23 \pm 0.04$). In contrast, no differences were detected in the average path length as a function of different topologies ($\overline{L} \simeq 2.0 \pm 0.3$).

The distribution of local clustering coefficient, in–degree and out–degree inferred by GTE-reconstruction are shown in Fig. 6.6 for an aggregated A and a homogeneous B example. In both cases, clear differences are observed between the GTE–reconstruction, the GTE–surrogates and the ER–ensembles. In contrast to distribution associated to ER–ensembles, the degree distribution inferred from GTE–reconstruction is characteristically broadened and distinctly right-skewed. This effect is more pronounced in the aggregated case. Distributions of local clustering coefficient reveal that aggregated networks present three different peaks, showing the effect of the different overlapped sub–networks. The first peak would correspond to the homogeneous sub–networks, while the remaining ones refer to the aggregated sub–networks. This effect causes an increase of the whole average clustering coefficient. Indeed, high values of $\overline{CC}$ were obtained for the aggregated

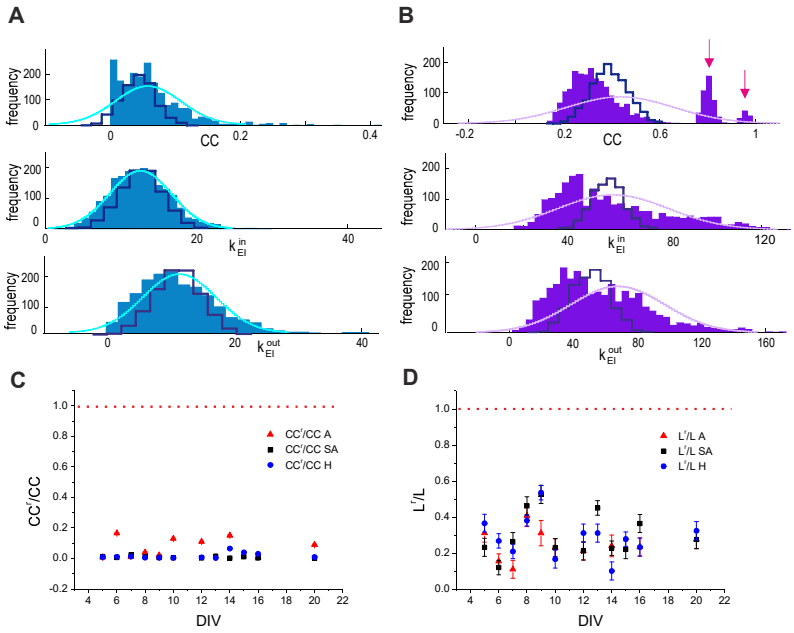

Figure 6.6: **Network characterization of GTE-reconstruction of aggregated and homogeneous neuronal cultures**. Properties of aggregated (A) and homogeneous (B) networks inferred from GTE–reconstruction method contrasted with their corresponding ER–surrogates and ER–ensembles. Results are compared with simulated networks. Only the 10% of GTE–ranked links is considered in order to perform the analysis. The ratio between the actual measures CC and L and their ER–ensembles in terms of DIV is also pictured in panels (C) and (D), respectively. A small–world network requires that $CC^r/CC \ll 1$ and $L^r/L \simeq 1$.

cases, while in the semi–aggregated and homogeneous cases these values were reduced. Aggregates are not only nucleation center for activity, but they also establishe a greater number of triangles in its immediate neighborhood.

To quantify the degree of SW–features presented in our neuronal cultures, we proceed in the following way. To properly compute SW–features, the first condition that must be satisfied is that the network under study must present an average degree that verifies $\langle k \rangle > log(N)$ [63, 105]. This condition implies that the sparseness of each networks was localized in the optimal range, namely that the density of links was within the ideal cost range (approximately $0.01-0.30$). So, we filtered all experiments ($\simeq 10\%$) which did not comply the aforesaid condition. Next, we checked the two necessary condition $CC^r/CC \ll 1$ and $L^r/L \sim 1$ to ensure the existence of SW–features [749, 497]. Both ratios can be observed in Fig. 6.6C and D respectively. Although the CC^r/CC is sufficiently smaller ($CC^r/CC \simeq 0.009 \pm 0.004$), the relatively high characteristic path length corresponds to smaller values of L^r/L ($L^r/L \simeq 0.25 \pm 0.03$), leading to a rejection of the SW–features hypothesis.

Culture type	DIV	Nº Exp (n)	Average aggreg. coefficient (γ)	Average assortativity Pearson (wh)			Average assortativity Spearman (wh)		
				GTE	PXC	ER*	GTE	PXC	ER*
A	5	2	0.71±0.07	0.511±0.043	0.302±0.067	0.021±0.032	0.507±0.057	0.325±0.084	0.021±0.032
A	7	6	0.80±0.04	0.363±0.065	0.201±0.032	0.089±0.018	0.356±0.032	0.272±0.053	0.089±0.018
A	8	2	0.73±0.03	0.352±0.067	0.137±0.042	-0.012±0.029	0.344±0.069	0.138±0.036	-0.012±0.029
A	9	4	0.72±0.03	0.488±0.089	0.298±0.056	0.035±0.025	0.483±0.045	0.252±0.076	0.035±0.025
A	12	3	0.71±0.05	0.643±0.036	0.143±0.087	-0.067±0.012	0.636±0.067	0.149±0.068	-0.067±0.012
A	14	4	0.76±0.04	0.465±0.044	-0.151±0.043	-0.076±0.010	0.460±0.052	-0.146±0.054	-0.076±0.010
A	15	3	0.81±0.07	0.603±0.071	0.451±0.056	-0.013±0.019	0.509±0.064	0.407±0.082	-0.013±0.019
				GTE	PXC	ER*	GTE	PXC	ER*
SA	5	4	0.57±0.04	0.124±0.017	0.105±0.013	0.041±0.005	0.115±0.014	0.117±0.011	0.038±0.006
SA	7	4	0.55±0.06	-0.161±0.009	-0.301±0.016	0.021±0.011	-0.168±0.006	-0.305±0.048	0.019±0.009
SA	8	5	0.56±0.02	-0.231±0.018	-0.245±0.015	-0.031±0.013	-0.236±0.005	-0.249±0.064	-0.039±0.011
SA	9	4	0.56±0.03	-0.029±0.013	0.187±0.012	0.029±0.009	-0.031±0.013	0.179±0.023	0.023±0.007
SA	13	4	0.59±0.10	0.121±0.027	0.111±0.018	-0.075±0.009	0.120±0.019	0.140±0.032	-0.071±0.007
SA	14	2	0.45±0.01	-0.236±0.012	-0.154±0.017	-0.049±0.008	-0.242±0.007	-0.152±0.010	-0.041±0.004
SA	15	4	0.45±0.02	-0.039±0.015	0.017±0.039	0.051±0.007	-0.040±0.008	0.021±0.059	0.045±0.005
				GTE	PXC	ER*	GTE	PXC	ER*
H	5	2	0.38±0.04	-0.275±0.009	0.139±0.009	0.010±0.007	-0.281±0.007	0.144±0.011	0.010±0.005
H	7	4	0.36±0.06	-0.280±0.011	0.080±0.008	-0.017±0.009	-0.285±0.005	0.076±0.017	-0.012±0.006
H	8	4	0.41±0.05	-0.277±0.007	-0.171±0.005	0.021±0.021	-0.286±0.012	-0.179±0.006	0.027±0.010
H	9	6	0.43±0.01	-0.294±0.006	-0.172±0.009	0.009±0.006	-0.300±0.005	-0.167±0.007	0.015±0.009
H	12	2	0.21±0.01	-0.402±0.008	0.204±0.010	-0.013±0.010	-0.406±0.006	0.201±0.015	-0.019±0.009
H	14	3	0.41±0.14	-0.171±0.012	0.071±0.007	-0.095±0.004	-0.173±0.010	0.069±0.003	-0.090±0.008
H	16	2	0.43±0.08	-0.213±0.009	-0.213±0.021	0.032±0.005	-0.223±0.009	-0.211±0.016	0.027±0.006

Table 6.3: **Assortativity measure for aggregated, semi–aggregated and homogeneous [E+I]–networks**. Pearson coefficient ρ^{PW} and Spearman rank correlation ρ^{SW} from GTE, PXC–reconstructions and ER-surrogates as a function of the DIV and the λ coefficient. The obtained values are an average over n experiments.

Assortativity Mixing

Tab. 6.3 summarizes the average of assortativity measures computed for different aggregated, semi-aggregated and homogeneous cultures. The parameter were inferred from GTE-reconstruction methods and contrasted from their respective ER-surrogates and PXC–reconstructions. In particular, we computed the Pearson coefficient ρ^{PW} and the Spearman rank correlation ρ^{SW} of the weight-to-weight data. Both coefficient provide values in the range of $[-1, 1]$. Positive Pearson coefficient $\overline{\rho}^{PW} \simeq 0.543 \pm 0.059$ and Spearman rank correlation, $\overline{\rho}^{SW} \simeq 0.530 \pm 0.055$ are obtained from aggregated cultures. Indeed, aggregated networks exhibited moderate and positive values of assortativity coefficients showing the preference for neurons to attach to others that present similar out–strength. On the contrary, homogeneous cultures displayed negative values of Pearson coefficient $\overline{\rho}^{PW} \simeq -0.273 \pm 0.012$ and of Spearman rank correlation $\overline{\rho}^{SW} \simeq -0.279 \pm 0.010$. In this way, homogeneous neuronal cultures show disassortative mixing or *dissortativity*, where high in–strength nodes tend to attach to low out–strength nodes. Uncorrelated networks are obtained with semi–aggregated networks: $\overline{\rho}^{PW} \simeq -0.064 \pm 0.015$ and $\overline{\rho}^{SW} \simeq -0.069 \pm 0.010$. Similar outlines are obtained with ER–surrogates where both parameters present values close to zero.

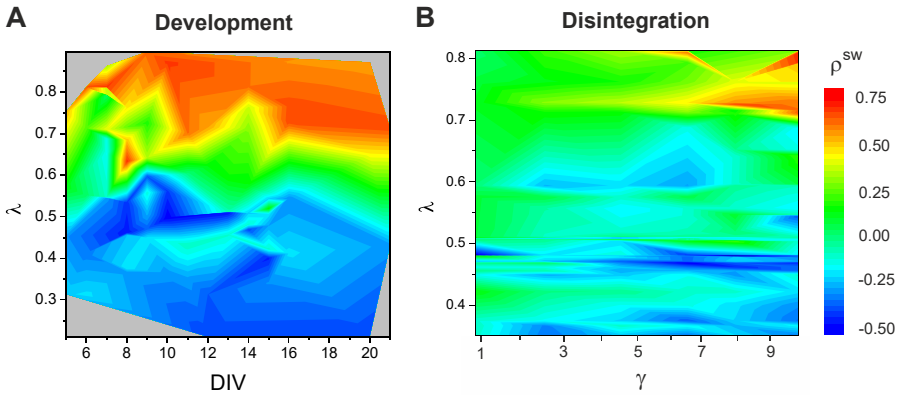

Figure 6.7: **Spearman rank correlation ρ^{SW} as a function of DIV, the aggregation coefficient λ and the disintegration coefficient** γ. (A) Dependence of ρ^{SW} on DIV and λ for [E+I]–networks. (B) Dependence of ρ^{SW} on γ and λ for [E]–only networks. The disintegration coefficient is defined as $\gamma = 1 + [CNQX]/K_d$ where $K_d = 300$ nM.

In Fig. 6.7A is pictured the Spearman rank correlation ρ^{SW} as a function of DIV and the aggregation coefficient λ. One can observe that both coefficients clearly depend on the degree of aggregation λ of the network. However, this parameter appears to be independent of the day of maturation of the network (DIV).

Comparing these results with the simulations (Tab. 6.2), one can observe that uncorrelated networks are obtained with simulated homogeneous networks, $\overline{\rho}^{PW} \simeq -0.011 \pm 0.010$ and $\overline{\rho}^{SW} \simeq 0.011 \pm 0.022$. In the aggregated cases, positive moderate values of both coefficients were gathered: $\overline{\rho}^{PW} \simeq 0.332 \pm 0.042$ and $\overline{\rho}^{SW} \simeq 0.323 \pm 0.038$. However, in contrast with the experimental ones, these values are slightly lower.

Functional connectivity hubs and Modularity

Epochs of synchronous bursting are associated to functional connectivity with a stronger degree of clustering [676]. The existence of hub nodes with an elevated degree of connection may have one important impact in the spatio–temporal organization of bursting dynamics. As a proxy within the network, hubs can help to redirect the information flow. The number, the weight and their distribution within the network could be the key to understanding how the information gets spread, as well as via wave or via avalanches. A wave produced in the experiment of a homogeneous culture is annexed in the Fig. 6.8A. The analysis of the times of firing is pictured in Fig. 6.8B. A wave is initiated in the upper right–hand corner of culture and spreads down towards the other end at the bottom of network. In general. two initiation regions were detected at the edges of the culture. Additionally the network analysis reveals different accumulation of hubs, forming two different components (C1 and C2, see Fig. 6.8C). In turn, C1 and C2 are linked by a third component C3, termed *bridge*, which balances the information flow from side to side of culture. No specific node is detected that acts in isolation as *hub* or *bridge*, but rather the networking of them seems crucial for ensuring that the different tasks are properly performed. By bundling hubs or bridges, the segregation or integration of information

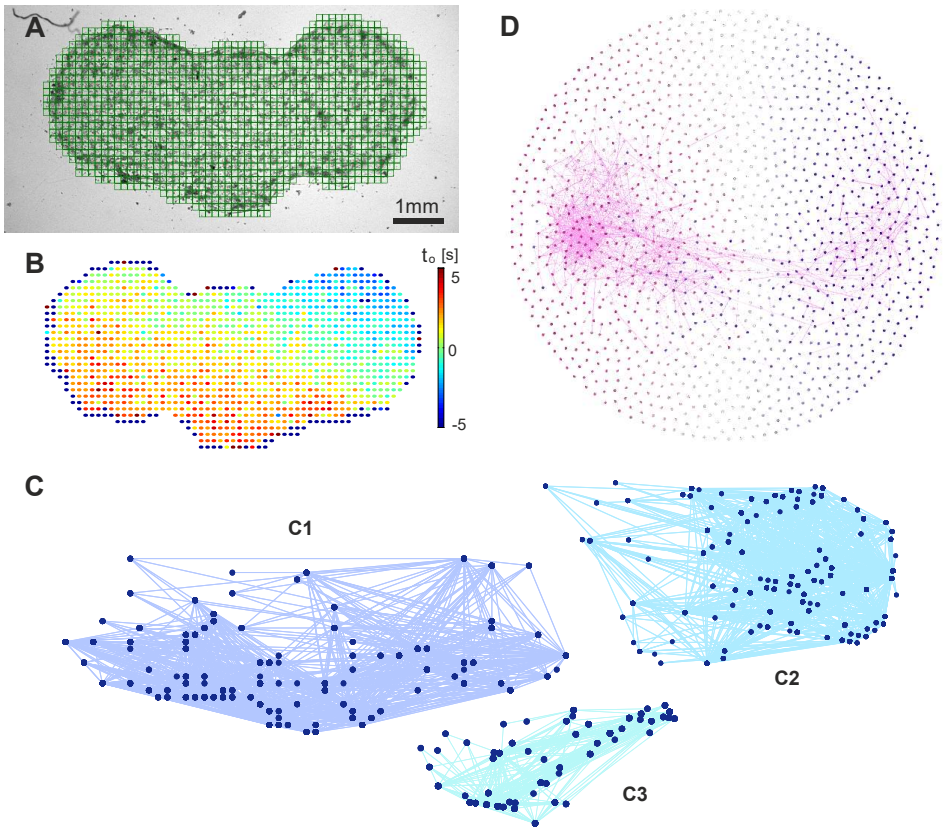

Figure 6.8: **Functional connectivity hubs and spatio–temporal organization of bursting dynamics**. (A) [E+I]-network from homogeneous mature culture (DIV=12, $\rho^{SW} = -0.422 \pm 0.012$). (B) The analysis of firing times reveals that the activity spreads as a waveform at a speed of $v \simeq 1$ mm/s from end to end of the culture. (C) Network analysis evidences different components (C1 and C2, *hubs zones*) constituted by high density of *hubs*, linked by a third component (C3, *bridges zone*) that balances the activity. (D) Fruchterman–Reingold algorithm [248] is applied in order to visualize graph clustering. The input parameters used are the followings: area of $A = 10.000$ mm^2, gravity of $g = 10$ mm/s^2 and speed $v = 1$ mm/s.

flows is enhanced respectively. The Fruchterman–Reingold algorithm [248] is applied in order to visualize the separation of C1 and C2, joined together by C3. The usage of this clustering model whose minimum energy drawings reveal these different *communities* of the drawn graph, as is pictured in the Fig. 6.8D.

Not only the direction of wave could be influenced by the position and importance of the *hubs* and *bridges* within the networks, but also its speed. Indeed, likewise, as we shall see in Sec. 6.4.2 nodes within the neighborhood of the same functional hubs provide the strongest mutual synchronization where the frequency of oscillation depends on the strength of the network. Notice that in these case hubs within the network are presented as integrating elements. However, depending on how these hubs are connected, segregation or integration will be prioritized. Indeed, in a dissortative network as seen in the Fig. 6.8 ($\rho^{SW} = -0.422 \pm 0.012$), the hubs will integrate the low–degree nodes, allowing better diffusion or dissemination of information flows. In this way, locally, all the nodes will be activated. Additionally, in homogeneous culture the same distribution of degree (or synaptic strength) will also benefit the network's coupling and the emergence of oscillations.

On the other hand, in assortative networks (as for aggregated cultures), hubs may also offer many other benefits. This effect is evidenced when we consider the analysis of the distribution of $\delta g = g_{EI}^{out} - g_{EI}^{in}$ and specifically their average $\overline{\delta g}$. Indeed, $\overline{\delta g}$ is a key fundamental to understanding the mechanisms to increase transport effectiveness [484]. Positive values of $\overline{\delta g}$ reflects that a fraction of neurons in the network exhibits more outputs than inputs and they have a tendency to act as a *sources* ($g_{EI}^{out} > g_{EI}^{in}$) rather as a *sinks* ($g_{EI}^{out} < g_{EI}^{in}$) of the connectivity. In Tab. 6.4 we provide the values of $\overline{\delta g}$ obtained from the different experiments. One can observe that this quantity is slightly higher in the case of aggregated cultures and has a slight tendency to increase during the development of them. The same effect is observed in the analysis of *modularity index* Q. Aggregated cultures exhibit a clear hierarchically modular network with higher modularity index than homogeneous ones. In aggregated cultures networks are partitioned in different communities.

6.4.2 Disintegration experiments

In this section we compared the change of activity between different topological networks during gradual weakening of neuronal connectivity. The weakening was achieved by progressive application of CNQX, an AMPA-glutamate receptor antagonist in excitatory neurons. As previously introduced, we define the disintegration coefficient as $\gamma = 1 + [CNQX]/K_d$ where $K_d = 300$ nM. In Fig. 6.9 we represent some examples of different GTE–reconstructions for disintegration experiments according to the different topologies: A homogeneous cultures (DIV=15, $\lambda = 0.43$ and $\rho^{SW} = -0.354 \pm 0.011$ (top), DIV=14, $\lambda = 0.48$ and $\rho^{SW} = -0.211 \pm 0.016$ (bottom)), in B semi–aggregated cultures (DIV=14, $\lambda = 0.58$ and $\rho^{SW} = -0.202 \pm 0.015$ (top), DIV=14, $\lambda = 0.63$ and $\rho^{SW} = 0.114 \pm 0.017$ (bottom)) and in C aggregated cultures (DIV=14, $\lambda = 0.77$ and $\rho^{SW} = 0.312 \pm 0.009$ (top), DIV=14, $\lambda = 0.81$ and $\rho^{SW} = 0.412 \pm 0.015$ (bottom)).

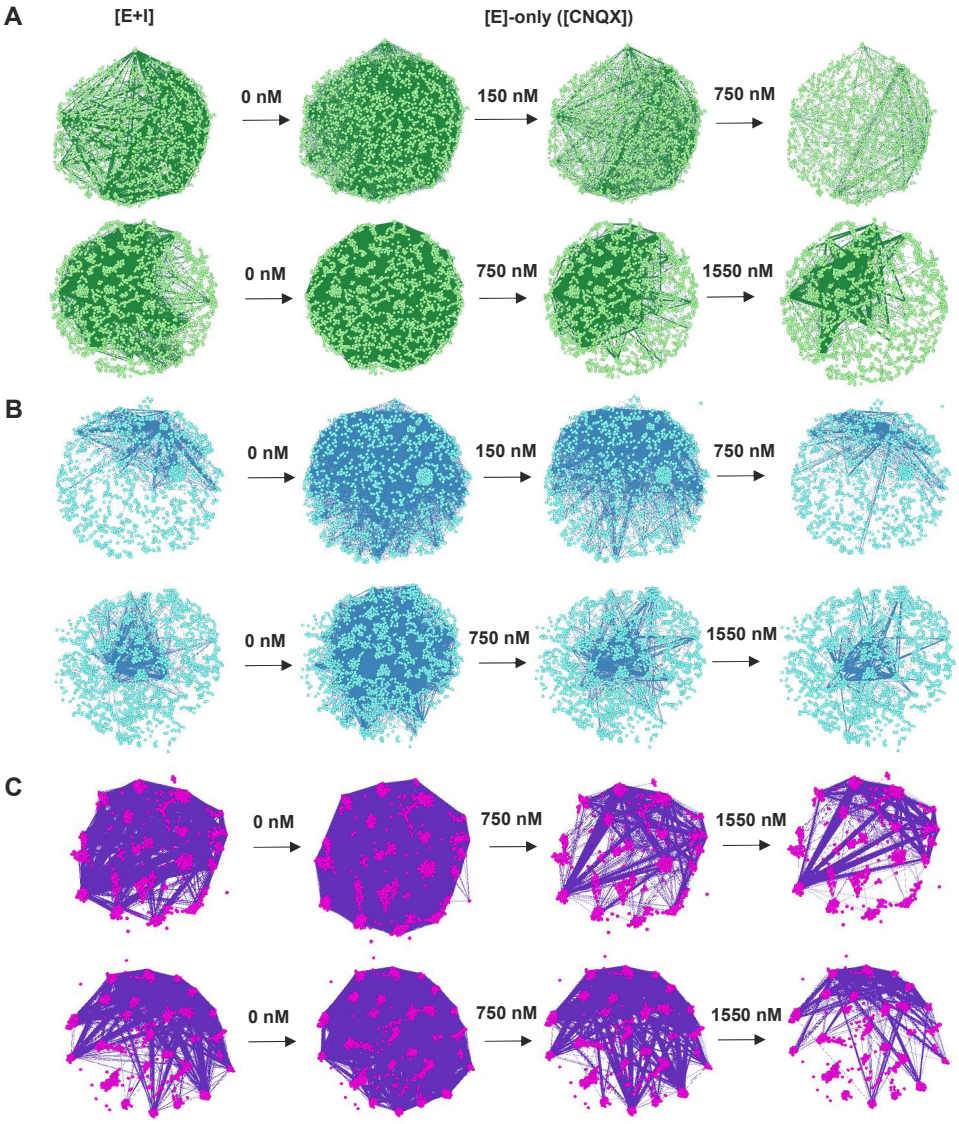

Figure 6.9: **GTE-reconstructions for disintegration experiments of different topologies**. (A) Homogeneous cultures: DIV=15, $\lambda = 0.43$ and $\rho^{SW} = -0.354 \pm 0.011$ (top), DIV=14, $\lambda = 0.48$ and $\rho^{SW} = -0.211 \pm 0.016$ (bottom). (B) Semi–aggregated cultures: DIV=14, $\lambda = 0.58$ and $\rho^{SW} = -0.202 \pm 0.015$ (top), DIV=14, $\lambda = 0.63$ and $\rho^{SW} = 0.114 \pm 0.017$ (bottom). (C) Aggregated cultures: DIV=14, $\lambda = 0.77$ and $\rho^{SW} = 0.312 \pm 0.009$ (top), DIV=14, $\lambda = 0.81$ and $\rho^{SW} = 0.412 \pm 0.015$ (bottom).

Culture type	DIV	N° Exp (n)	Aggreg. coefficient (γ)	Firing rate (min^{-1})	Average number of nodes (N)	Average number of edges (E)	Average of information flux (δg)			Modularity Index (Q)		
					GTE	GTE	GTE	PXC	ER*	GTE	PXC	ER*
A	5	2	0.71±0.07	1.4±0.6	1521±16	6716±413	0.07 ± 0.04	0.09 ± 0.05	0.04 ± 0.05	0.14 ± 0.03	0.11 ± 0.04	0.10 ± 0.05
A	7	6	0.80±0.04	3.6±0.5	1000±12	9301±512	0.10 ± 0.06	0.07 ± 0.06	0.05 ± 0.06	0.21 ± 0.05	0.17 ± 0.06	0.14 ± 0.04
A	8	2	0.73±0.03	2.8±0.5	803±21	13835±612	0.12 ± 0.04	0.06 ± 0.04	0.06 ± 0.03	0.30 ± 0.04	0.16 ± 0.06	0.08 ± 0.07
A	9	4	0.72±0.03	4.7±0.6	710±23	6534±441	0.10 ± 0.08	0.06 ± 0.04	0.08 ± 0.05	0.45 ± 0.05	0.21 ± 0.03	0.12 ± 0.08
A	12	3	0.71±0.05	5.2±0.7	1421±25	10121±656	0.14 ± 0.05	0.08 ± 0.03	0.07 ± 0.05	0.56 ± 0.04	0.25 ± 0.05	0.11 ± 0.06
A	14	4	0.76±0.04	4.2±0.7	947±32	35244±598	0.16 ± 0.07	0.07 ± 0.04	0.06 ± 0.04	0.24 ± 0.08	0.14 ± 0.05	0.15 ± 0.04
A	15	3	0.81±0.07	3.8±0.8	996±14	7620±614	0.15 ± 0.06	0.08 ± 0.07	0.07 ± 0.02	0.33 ± 0.09	0.28 ± 0.08	0.16 ± 0.07
					GTE	GTE	GTE	PXC	ER*	GTE	PXC	ER*
SA	5	4	0.57±0.04	0.9±0.5	961±32	4511±724	0.04 ± 0.05	0.06 ± 0.06	0.03 ± 0.04	0.13 ± 0.04	0.14 ± 0.05	0.14 ± 0.03
SA	7	4	0.55±0.06	2.4±0.3	1551±11	3587±689	0.06 ± 0.07	0.07 ± 0.04	0.02 ± 0.06	0.18 ± 0.06	0.21 ± 0.03	0.18 ± 0.05
SA	8	5	0.56±0.02	1.3±0.4	866±23	5984±213	0.09 ± 0.05	0.08 ± 0.05	0.01 ± 0.04	0.14 ± 0.07	0.17 ± 0.04	0.15 ± 0.08
SA	9	4	0.56±0.03	3.0±0.8	979±34	6959±781	0.08± 0.04	0.06 ± 0.05	0.04 ± 0.05	0.10± 0.05	0.18 ± 0.06	0.15 ± 0.08
SA	13	4	0.59±0.10	4.2±0.4	1001±23	5984±812	0.09 ± 0.04	0.04 ± 0.03	0.08 ± 0.03	0.14 ± 0.05	0.09 ± 0.04	0.17 ± 0.04
SA	14	3	0.45±0.01	2.5±0.5	1368±23	21812±672	0.10 ± 0.03	0.07 ± 0.08	0.08 ± 0.03	0.11 ± 0.04	0.14 ± 0.05	0.11 ± 0.05
SA	15	4	0.45±0.02	2.1±0.8	910±34	12710±812	0.08 ± 0.04	0.09 ± 0.04	0.09 ± 0.02	0.27 ± 0.08	0.19 ± 0.05	0.16 ± 0.03
					GTE	GTE	GTE	PXC	ER*	GTE	PXC	ER*
H	5	2	0.38±0.04	1.4±0.3	1556±26	5556±643	0.04 ± 0.04	0.05 ± 0.05	0.02 ± 0.04	0.13 ± 0.05	0.14 ± 0.06	0.13 ± 0.06
H	7	4	0.36±0.06	1.2±0.4	2109±32	9129±480	0.06 ± 0.04	0.07 ± 0.05	0.03 ± 0.04	0.17 ± 0.04	0.18 ± 0.04	0.13 ± 0.05
H	8	4	0.41±0.05	1.4±0.5	1330±24	6149±329	0.05 ± 0.04	0.06 ± 0.03	0.04 ± 0.04	0.15 ± 0.07	0.14 ± 0.04	0.17 ± 0.04
H	9	6	0.43±0.01	2.7±0.5	1526±28	6580±555	0.07 ± 0.05	0.04 ± 0.04	0.02 ± 0.05	0.18 ± 0.08	0.21 ± 0.05	0.16 ± 0.04
H	12	2	0.21±0.01	3.1±0.7	973±19	16265±561	0.08 ± 0.08	0.09 ± 0.02	0.04 ± 0.05	0.10 ± 0.06	0.11 ± 0.05	0.16 ± 0.06
H	14	3	0.41±0.14	2.2±0.7	1028±21	34788±776	0.09 ± 0.07	0.10 ± 0.02	0.02 ± 0.06	0.20 ± 0.04	0.19 ± 0.03	0.14 ± 0.05
H	16	2	0.43±0.08	2.8±0.8	1265±27	27198±696	0.08 ± 0.09	0.09 ± 0.04	0.01 ± 0.04	0.31 ± 0.07	0.27 ± 0.08	0.15 ± 0.05

Table 6.4: **Hierarchically modular network and presence of sinks in cultures.** The table shows the average of $\delta g = g_{EI}^{out} - g_{EI}^{in}$ and the *modularity index* Q of GTE and PXC–reconstructions corresponding to aggregated (A), semi-aggregated (SA) and homogeneous (H) cultures as a function of the *day in vitro* (DIV) and aggregation degree (λ). The obtained values are an average over n experiments and the results are compared with the corresponding ER–surrogates.

Giant Component Breakdown

In Fig. 6.10 we depict the change of activity of the network during the disintegration process. For simplicity, we only attach the results of the extreme case of homogeneous and aggregated cultures. Each curve is the average over $n = 4$ experiments recorded simultaneously. In Fig. 6.10A the average fraction of neurons $\overline{\phi}$ that exhibit spontaneous activity during the disintegration process is represented. During the three weeks of culture's maturation, one can observe that the $\overline{\phi}$ increases both for homogeneous and aggregated networks. In the case of homogeneous networks, this activity curves exhibit a monotonous decay, more or less abrupt as a function of the underlying specific connectivity. Additionally, one can distinguishe that in the homogeneous case the curve $\overline{\phi}$ decays faster than in aggregated ones. Indeed, the number of active neurons in aggregated cultures is slightly higher than in the homogeneous counterparts. Furthermore, the curve of $\overline{\phi}$ refers to aggregated cultures present interesting plateaus (pink star), markedly more pronounced for mature cultures (DIV=15). The emergence of these plateaus and their abrupt disintegration can be due to the aggregated sub–networks, more resilient to disintegration.

Similar behavior is observed when one analyzes the average of firing rate $\overline{\psi}$ as a function of λ during the disintegration process. In general, values of $\overline{\psi}$ for aggregated case are markedly higher than homogeneous counterparts. Moreover, homogeneous cultures

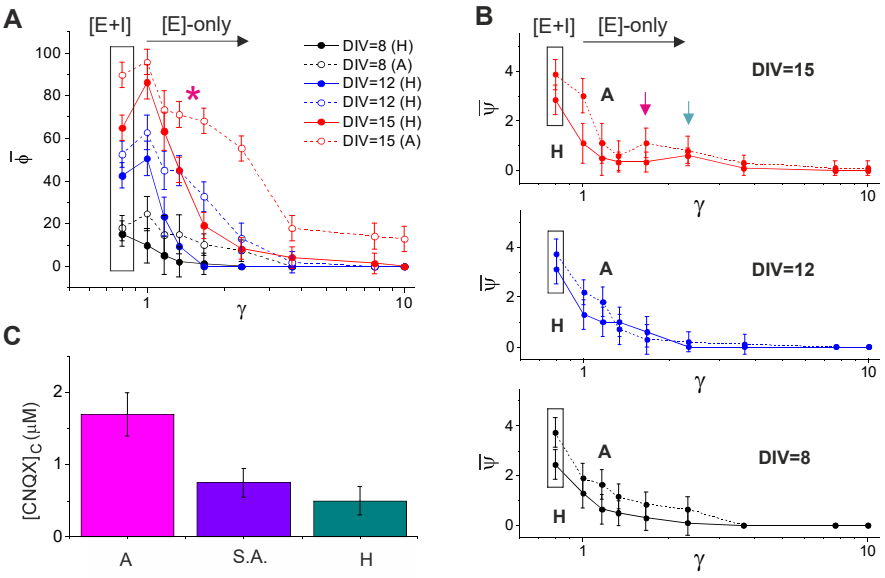

Figure 6.10: **Change of activity of the [E+I]–networks during three weeks of development for homogeneous and aggregated cultures**. Evolution of the average fraction of neurons $\overline{\phi}$ (A), and the average of firing rate $\overline{\psi}$ (B), as a function of the DIV and the disintegration coefficient γ for homogeneous and aggregated cultures. The concentration of $[\text{CNQX}]_C$ necessary to disintegrate the [E]–network is shown in (C). Each curve is an average of 4 cultures on the same recording.

turned almost silent for γ values lower than aggregated ones. Indeed, homogeneous cultures are in general broken down faster than their aggregated counterparts, as we can observed in Fig. 6.10C. As we have seen in previous Chapters, the analysis of $\overline{\psi}$ firing rate, reveals that in mature culture (DIV $\geq$ 14) an increase in their activity is detected for intermediate values of disintegration. This effect is detected independently of the degree of aggregation of the network (pink and green arrows). This rise of activity can be interpreted as a compensatory effect where the network respond in order to counterbalance the applied perturbation.

In regard of the above analysis, one can observe that above a critical connectivity there is a continuum of connected neurons that spans a significant fraction of the network. In the theory of percolation, a sudden jump in the fraction of neurons ϕ that spontaneously fired indicates the appearance of a single connected cluster, called *giant component* G_c [96, 660]. The number of neurons to spontaneously fire is the *order parameter* and the *transition point* where the giant component G_c emerges is termed *critical point*.

As we have already seen in the previous Chapters, when we are in the first stage of the disintegration ([CNQX]=0 nM, 'E–only' network), all neurons fire and the giant component spans across to the whole network. As the connectivity decreases, the number of excitatory inputs per neuron is reduced and a growing number of neurons with low in–degree get disconnected from the network. The size of giant component G_c then gradually shrinks. At a critical value of m^* the giant component is disintegrated and the network is comprised of isolated clusters. Shortly, for $m < m^*$ the network is connected through

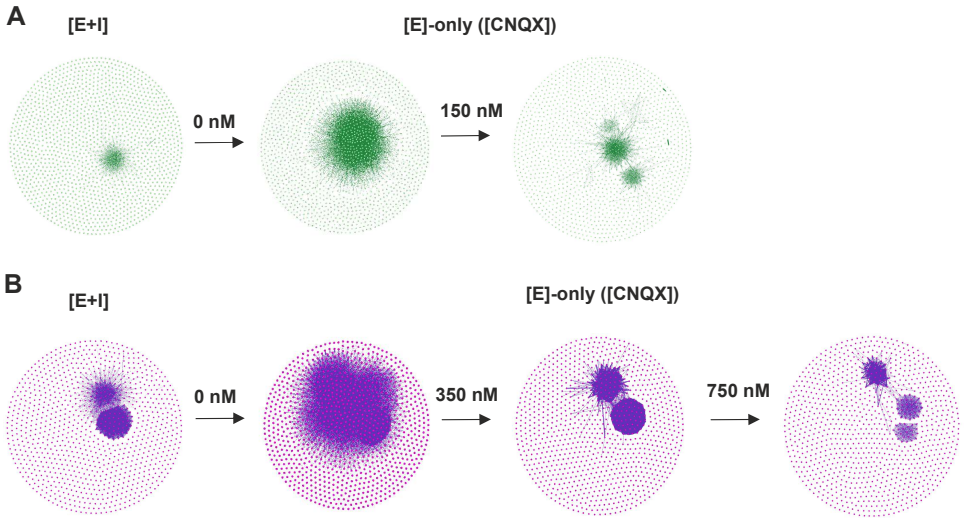

Figure 6.11: **Emergence of components in the disintegration process**. Rupture of the Giant Component G_C in the disintegration process for different topologies: (A) Homogeneous culture (DIV=15, $\lambda = 0.43$ and $\rho^{SW} = -0.354 \pm 0.011$), and (B) Aggregated culture ($\lambda = 0.77$ and $\rho^{SW} = 0.312 \pm 0.009$). The analysis was implemented through the Fruchterman–Reingold algorithm [248], with the following input parameters: $A = 10.000$ mm^2, $g = 80$ mm/s^2 and $v = 1$ mm/s.

the giant component G_c. For $m > m^*$ the network is broken down by isolated clusters or single neurons that erratically fire at the extreme of full blocking of the network. Then, to quantify this change in connectivity we used as *control parameter* which represents the average number of inputs m required for a neuron to fire, so $m^* \sim \overline{k}_E^{*in}$.

In Fig. 6.11 we picture the analysis of the different components that emerged during the disintegration process for a homogeneous (A) and an aggregated (B) culture. In the case of homogeneous culture, [E+I]–network present a small main component that grows by blocking the inhibitory current. However, after applying [CNQX]= 150 nM, this giant component G_c is broken, giving rise to two news components. In this stage of disintegration, the average in–degree $\overline{k}_E^{*in}$ computed is approximately of 17 ± 6. On the other hand, a more complex scenario appears with the aggregate cases. In the case considered in the Fig. 6.11B, the initial [E+I]–network is constituted by two components. The blockage of inhibitory current causes the union of them, giving rise to the emergence of the giant component G_C. In the same way, the progressive application of CNQX disintegrates the network into different components. However, in this case, two different transition are detected: one in [CNQX]=350 nM ($\overline{k}_E^{*in} = 31 \pm 11$) and the other in [CNQX]=750 nM ($\overline{k}_E^{*in} = 17 \pm 8$). The detailed analysis of each experiment reveals that the emergence of G_c is detected in aggregated culture around the value $\overline{k}_E^{*in} \simeq 27 \pm 7$, slightly higher than in semi–aggregated $\overline{k}_E^{*in} \simeq 21 \pm 7$ and homogeneous $\overline{k}_E^{*in} \simeq 18 \pm 9$ counterparts. Since aggregated cultures exhibit assortative mixing patterns, then it seems that assortativity increases the threshold of percolation when nodes are spatially segregated by their degree. However, experimentally, this *critical point* is very hard to

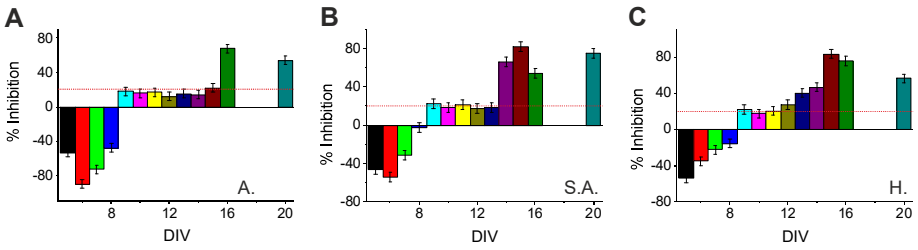

Figure 6.12: **Percentage of Inhibitory currents during the development for different topologies**. Evolution of inhibitory currents during the DIV for the different worked toplogies: (A) Aggregated cultures, (B) Semi–aggregated cultures, and (C) Homogeneous cultures. Inhibitory connectivity is described by a highly simplified model of 'substractive' inhibition. The horizontal, red, dashed line refers to the values obtained in the simulations.

detect and the associated error is extremely high.

Amount of Inhibition in the network

The study of disintegration of the network with CNQX provided information on the average connectivity of the network. In particular, it allows us to identify the emergence of inhibition during the development and quantify the fraction of inhibition currents present in the networks.

In the present analysis, inhibitory connectivity is described as a highly simplified model of 'substractive' inhibition. If $\overline{k}_I$ and $\overline{k}_E$ are the average number of inhibitory and excitatory inputs onto a neuron, then the net input connectivity is given by $\overline{k}_{EI} = \overline{k}_E - \overline{k}_I$. This relation assumes that excitatory and inhibitory synapses have similar strength and that the average EPSC and IPSC amplitudes are practically equivalent. This relation likewise deems that the role of inhibition in neural connectivity is to effectively reduce the amount of excitatory connections [96]. In the Fig. 6.12 is pictured the percentage of inhibitory currents as a function of DIV for aggregated (A), semi–aggregated (B) and homogeneous cultures (C). The emergence of inhibition is associated around the day 8 ± 2 when GABA–switch is produced, as explained in Chapter 4. One can observe that the fraction of inhibition arrived at levels around 20% in the second week of development, regardless of the considered topology. After the second week, extremely highly values are obtained for mature cultures. If one compares this values respect to the simulated ones (the horizontal, red, dashed line), one can conclude that the linear approximation assumed above is misleading. Indeed, in this referred regime ($DIV \geq 14 \pm 2$) a non–lineal model should be applied.

Assortativity and resilience

Global network disintegration experiments through photo–damage and chemical degradation showed that aggregated cultures exhibit a high resilience to damage as compared to homogeneous ones. In fact, networks with assortative mixing patterns show greater robustness against photo–damage and chemical degradation than disassortative ones. A illustrative example of disintegration of aggregated culture is displayed in Fig. 6.9B (top).

As one can see, during the process of disintegration, aggregated sub–networks are silenced later than the homogeneous ones. Indeed, aggregates appear to be more resistant to disintegration than homogeneous sub–networks. A possible cause could be that for entropic reasons since the receptor antagonist has more difficulty to act inside of the aggregates. For homogeneous cultures with some anomalous heterogeneity of neuronal density, the same behavior is detected. Indeed, regions of greater activity and hence, more connected to each other, have the tendency to deactivate later. Taking into account that receptor antagonist acts homogeneously on the whole of the network, this result does not seems striking. Nodes with lower degree are disconnected before those with higher degree. Since semi–aggregated cultures are made up by the superposition of two sub–nets, an aggregated and the other homogeneous, then interesting is the question of whether a disassortativity–assortativity transition is detected during the disintegration process.

In Fig. 6.7B we represented the Spearman rank correlation ρ^{SW} during the disintegration process for different cultures of different topology. No transition is observed. As the [E]–only networks are weakened, for homogeneous and aggregated cultures, both coefficients have a tendency to increase. Indeed, for disassortativite mixing patterns, one can observe that ρ^{SW} tends to take values close to zero, giving rise to uncorrelated networks. At the other extreme, for assortativite mixing patterns, ρ^{SW} presents also a slight tendency to increase, showing strong resistance on the part of aggregates during the disintegration process. We note that when the inhibition is blocked, in assortativite networks the ρ^{SW} decreases. Finally, in the case of semi–aggregated cultures or uncorrelated networks, the values computed for ρ^{SW} fluctuate around the zero when a chemical perturbation is applied.

Oscillations and functional connectivity hubs

Previously, in Chapter 4, we detected the emergence of collective oscillations modes in the networks of mature homogeneous cultures (DIV $\geq 14 \pm 2$) which were remarkably strong and spatially localized at particular regions of cultures. For example, in Fig. 6.13A is pictured the Gabor Transform for a homogeneous mature culture ($DIV = 16 \pm 2$) during the disintegration process. PSD analysis revealed the presence of peaks at frequencies f in the range of $5 - 10$ Hz. The detailed study of the fluorescence traces evidenced that the oscillatory modes originated from activity within the bursts themselves. The analysis of anatomical and functional connectivity showed us that these oscillations modes are markedly strong in localized communities, made up of functional connectivity hubs (Fig. 6.13B). As we saw in Chapter 5, simulations analysis showed that only homogeneous networks with a critical size ($N \geq 10000$ neurons) and high synaptic strengths ($g_{AMPA} \geq 9.50$, $g_{GABA} = -42$ and $g_{NMDA} = 1.3$) achieved the oscillatory regime. As on can observe in Fig 6.13, during the process of disintegration, the synaptic strengths of the [E]–only networks are weakened and the oscillations dampen. Additionally, the blockage of inhibition reinforce oscillatory modes. Indeed, it seems that the frequency of oscillations is tunned throughout the disintegration process. Thus, it would seem that the complete or gradual blockade of AMPA, NMDA and GABA receptors, which in turn determine the synaptic strength between the nodes of the network, could modulate the oscillatiory modes.

However, the emergence of these oscillatory modes could be due to the combined ef-

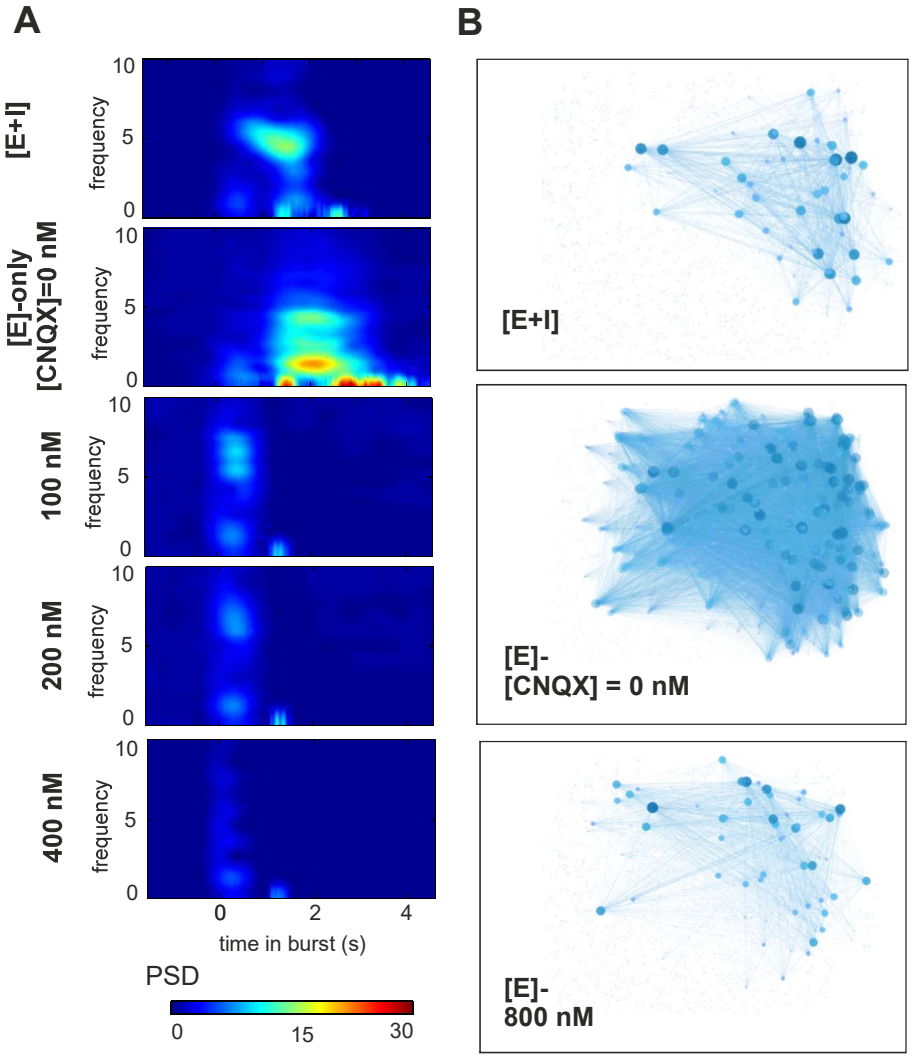

Figure 6.13: **Oscillations in Homogeneous cultures**. Emergence of oscillations in homogeneous mature culture ($DIV = 16 \pm 2$). (A) During the disintegration process of [E+I]–network, the analysis using Gabor Transform revealed the presence of peaks at frequencies f in the range of 5-10 Hz. The oscillatory mode emerges during the collective bursting of the network. (B) GTE–reconstructions for different stages of disintegration: [E+I]–network ($\overline{k}_E = 13 \pm 9$, $\overline{g}_E = 23 \pm 9$), [E]–only network for [CNQX]=0 nM ($\overline{k}_E = 64 \pm 14$, $\overline{g}_E = 86 \pm 21$) and [E]–only network for [CNQX]=800 nM ($\overline{k}_E = 21 \pm 8$, $\overline{g}_E = 24 \pm 8$).

fect of different causes, hindering its analysis. These oscillations could emerge as a result of recurrent activity within these communities. Likewise, functional connectivity hubs could also reflect foci of enhanced local bursting synchrony. Certainly, these oscillations seem to be inexistent in young cultures (or too weak to be detected), which strengthens the argument that strong coupling within the cell community is required for their generation. However the emergence of oscillations is a complex phenomenon and is not simply related to the presence of high degree nodes, but also depend on the properties of a diffusion process on the networks or their ability of transport of information flow. Indeed, a homogeneous distributions in the coupling of the nodes leads to great synchronization between the respective nodes than on heterogeneous ones. It is worth noting that only in homogeneous networks with disassortative mixing pattern we detected synchronization patterns. By contrast, in aggregated cultures no oscillatory modes were observed. Nevertheless, the lack of oscillatory modes in aggregated cultures in experimental and synthetic networks could be because we work with very small culture, with a maximum of 15 aggregates. Then, each aggregate may behave as a single entity. Perhaps it would be more correct to compare homogeneous and aggregated cultures with the same number of entities. Howver, each aggregate behaves differently than a neuron.

6.5 Discussion

Average connectivity of the networks

The previous outcomes aim to help better understanding the underlying connectivity of neuronal cultures. During the first days *in vitro* our neuronal cultures present a weak activity, making its grasp more difficult. After the GABA switch, for a youngest cultures low values of $\overline{k}_{EI}$ and $\overline{k}_{E}$ in the range of $3-15$ were obtained for homogeneous case. This results seems in accordance which the values reported by [93], indicating that a minimum value in the range of $5-10$ is required to excite one neuron in the cortex. Slightly higher values of $\overline{k}_{EI}$ and $\overline{k}_{E}$ in the range of $7-20$ were achieved in the aggregated one, either by the first days of development or by the last stage of chemical disintegration. Those findings lead one to think, that aggregates act rather as joint entities that in an individual and independent way. Rising the threshold would lead a later activation by aggregates although it would mean a substantial increase and modulation of latency of the network. In the same way, the network would gain in resilience and robustness. In mature culture, GTE-reconstructions predicted values of $\overline{k}_{EI}$ and $\overline{k}_{E}$ in the range of $15-150$ for our neuronal cultures, consistent with simulation findings. Similarly, the aggregate cases present slightly higher values than the homogeneous ones. In the framework of percolation, theoretical studies [660, 355, 142, 676] estimate an average number of excitatory inputs in the range of $\overline{k}_{E} \approx 75-150$ per neuron in cortical culture, depending on neuronal density. These values are about two orders of magnitude lower than the average connectivity in the brain, which is in the range of $1-8\text{x}10^{3}$ synaptic connections per neuron on average [527, 153, 588]. This discrepancy may be due to different reasons as well as the ability of neurons in the brain to use the third dimension for connections or the continuous refinement of connectivity, among others.

No evidence for scale free connectivity

The preceding results reveal highly nonrandom features of synaptic connectivity in local cortical circuits. Analysis of the degree distributions showed characteristically broad ones with a conspicuous right tail. No evidences of scale free distribution were detected in our neuronal cultures, in accordance with the results reported by [668, 676, 692]. However, several studies [657, 216] using networks of cortical neurons in developing rats identifies power law distributions in the functional connectivity which reflects the existence of a few nodes with very high degree and many with low degree. Scale–free topology was also identified in hippocampal developing networks in cultures [425] and slices [88] on the analysis of calcium activity. Both studies demonstrated the existence of functional hubs and suggested that these higher connected nodes, composed of a subpopulation of GABAergic interneurons, orchestrate spontaneous network synchronization, producing physiological or pathological network oscillations [109, 295]. In mature cultures, the existence of functional hubs and oscillations was also detected in our reconstructed maps, either in [E+I]-networks or even in [E]-only networks. Small subset of nodes dominates the activity of the synchronous peaks in local community, the frequency of them seemed to depend on the different stages of the network. However, even though network topology and the existence of functional hubs can significantly affect synchronous firing activity in a variety of network models [295], they are not the only factors involved, as we will see later.

Due to the existence of hubs nodes with very high- and low-degree, the connectivity maps derived from cultured neural assemblies can be best described in terms of SW-networks [370]. However, owing to the large uncertainty in the reconstruction and the high sensitive to error in the estimation of the average path length between nodes, is difficult to conclude such assertion. Although our networks share some traits with SW-networks, such as high clustering coefficient, we prefer to describe the reconstructed degree distribution just as 'exponential' or 'right–skewed' as a function of age and maturity of culture. However, several studies [633, 74, 195] showed that functional structure of cortical neuronal networks grown *in vitro* exhibit SW properties similar to those found *in vivo* at multiple scales over a range of species in both structural [749, 663] and functional [17, 670, 172, 126] networks. Existing literature revealed that the functional network properties of cortical cultures changed during maturation [134]. In particular, network obtained from young cultures display a random topology, which evolved to a SW architecture during maturation between the third and fourth week *in vitro* [195] (DIV $\simeq 28-35$). Indeed, the topology change was accompanied by an increase in clustering coefficient, by a change in the distribution of links lengths, from a clear dominance of long-range links (DIV ≥ 14), by an increase of the presence of highly connected areas (hubs) and finally, by a gain of network efficiency. This tendency was also observed in our neuronal cultures during the development stage, as has already been mentioned in the preceding lines.

Disassortativity in homogeneous cultures

Previous outcomes sowed that homogeneous cultures present disassortative mixing patterns in accordance with the studies in developing cortical networks on MEAs reported by [74]. Most of biological [35, 683, 767, 38], technological [641, 112, 342, 55] and information-related or linguistic networks [335] are preferably disassortativite in their degree-degree

correlation [748, 368, 743, 335, 545]. So far, it is not known why this matter, but different explanations have been proposed in the literature. Dissasortative features in metabolic and signalling pathways were found and explained by Maslov et al. [473]. For this biological networks the authors argued that this result may reflect the specificity and complementarity in interactions that is also observed on various levels. Indeed, complementarity is an essential mechanism for pattern recognition interactions which could clearly favor the preferential attachment between opposed degree nodes. This lock-and-key principle is underlying in most biological and biochemical processes as well as in genetic regulation, signal transduction in individual cells or symbiotic species in ecological networks. Indeed, such complementary mechanism seems to be the rule, not the exception of many interrelationships, in particular, at the molecular level, enabling fruitful and safe interaction.

However, being a mechanism that acts mainly at the molecular level, it is not clear what role can play at the mesoscopic scale. In neuronal brain, synaptic growth depend on concentrations of various molecules [372, 782] which can diffuse through large areas of tissue. Indeed, axons guidance or axons pathfinding, is usually mediated by gradients of target-derivated components [694] which could give rise whatever previously defined topology of the network. Indeed, in the brain, this directed mechanism would lead to any kind of network as one would like. However, our 2D-neuronal cultures lack such targets and consequently, at first sight one may think that the growth would have to be homogeneous or unguided giving rise to uncorrelated networks. Notice that simulated homogeneous cultures exhibit uncorrelated networks unlike its experimental counterparts which present disassortative mixing patterns.

It is important to point out that the development of neural tissue is a complex organizing process and a number of other factors are thought to be involved in its development. Indeed, neuronal wiring is mediated not only by the genome, but also by every sort of field interactions including electrical, neurotrophic factors, gradients of ionic and molecular concentrations and gravity. Effectively, for example, experimental neuroscience has shown that enhanced electric activity induces synaptic growth and dendritic arborization [416, 228, 389, 174]. Furthermore, another important property of brain development is their reviewed *synaptic pruning*. This large reduction in synaptic density undergone throughout infancy can mold a different topology of the network. Despite this highly biological complexity, different studies have suggest simple laws that govern the growth. Chechik *et al.* [128, 129] proposed that via an elimination of less needed synapses, this can reduce the energy consumed by the brain while maintaining near optimal memory performance.

Indeed, as Ramón y Cajal already pointed out, topology and structure of nervous system was constrained by three well-defined 'laws' of optimization [575]. First, space optimization: packing compactness. Second, matter optimization: each element must be of the right size. And third, time optimization: conduction time must be optimal. Hence, a consideration that is very interesting to analyze is if this optimization rules leads to a specific topology at the mesoscopic level, and hence one specific degree-degree mixing pattern at the network. Although this analysis goes out of scope of this research, it has to be mentioned. Notice that in our neuronal cultures the degree-degree pattern mixing doesn't seem to depend on the *day in vitro*, but rather of the heterogeneity of the network. It has to be remarked that aggregated cultures lose the specific morphology of individual neurons. The key question is whether such morphology has any impact at the

topology of the network and their degree-degree correlation.

Effectively, another explanation for the origin of disassortativite mixing has been proposed by different studies [474, 516, 543, 364]. Using computer simulations, Maslov et al. [474] demonstrated that on small networks, disassortative mixing is produced if one restricts the network topology to having at most one edge between any pair of vertices. Park and Newman analytically shown [543] how this analogue of the Pauli exclusion principle leads to the network present a disassortative mixing pattern. Indeed, if the edges follow Fermi statistics where double edge are forbidden and self–connections are not allowed, then graph ensembles with single edges have negative correlations. We note that directed networks usually have no double edge and hence duplicated links have been removed. Then, in these cases, the disassortative matching is caused by the topological restriction that no pair of nodes is allowed to have multiple connections in the ensemble of graphs with given (or expected) degree sequences. Homogeneous neuronal networks are clearly an example of directed networks where neurons have evolved as a device whose morphology is highly specialized to make selective directed connections. In contrast, such restrictions are not presented in the aggregated cultures where duplicated links are allowed.

Other interpretations have been provided by several studies [364, 365] by showing that the expected value of the mixing is usually disassortative for highly heterogeneous degree distributions such as those of the ubiquitous SF-networks. The authors argued that in absence of knowledge regarding the specific evolutionary forces at work, disassortativity should be considered the most likely state. In a seminal series of papers Bianconi [77, 78] showed by a statistical mechanics model that SF degree distribution are the most likely degree distribution at given small value of structural entropy while Poisson degree distribution are the most likely degree distribution of networks with maximal structural entropy. Consequently, SF-networks and disassortativity arise naturally when the total entropy is restricted to a small finite value and therefore larger amount of order.

It is worth noting that SF-networks can be classified into three groups: (i) pure fractal, (ii) pure SW and (iii) a mixture between fractal and SW. Recent researches [382, 772, 781] showed that self–similar fractal networks with SF features, with their skeleton composed by maximum spanning trees, are not assortative, and in this case, the qualitative feature of disassortativity is scale-invariant under renormalization. Conversely, structural analysis of complexes networks reveal that the emergence of SF fractal networks is mainly due to disassortativity or repulsion between hubs [655, 656]. In contrast, SF SW-networks can be generated with tunable assortative coefficient exhibiting either assortative or disassortative mixing patterns [302]. Noteworthy, that large-scale cortical network display SW attributes [749] as highly clustering and short path lengths [666, 318, 667, 603, 17] and SF properties [208]. Indeed, several studies reveal that cortical structures in the macro-scale level exhibit highly heterogeneously structure as well as distinct clusters [318, 319], hierarchical organization [320], a specific composition of of structural and functional motifs [664], short wiring length [133] and high complexity [666, 665].

However, the degre-degree correlation pattern is still a much debated issue and further analysis have to be performed. Although our homogeneous neuronal cultures appeared to be significantly disassortative in their mixing patterns, they did not seem to exhibit SF features, but rather Poisson or 'right-skewed' distributions with some traits of SW. But nevertheless, if one consider that disassortativity arises in a process of growth where the

total entropy is restricted to small finite value [77, 78], such argumentation could be valid to explain our disassortative mixing pattern. Cortical neurons exhibit a specific structure whit fractal morphology of dendrite and axonal tree [444, 753]. Although axons guidances are influenced by multiples factors, the degree of spatial occupancy and complexity of a dendritic tree is directly related to its potential as a synaptic target for growing axons [151]. Shape and function paradigm is treated by [151] showing the influence of the individual shape of neurons to the overall connectivity [163, 150] and several topological properties can be foreseen from the geometrical features of individual neurons [152]. However, no inference of degree-degree correlation is analyzed in these studies and, as the authors argue, many factors can influence the overall structure of the network and further analysis should be carried out to understand the problem.

Assortativity in aggregated cultures

On the other hand, aggregated cultures appear to be significantly assortative in their mixing patterns. The origin of obvious degree assortativity of aggregated cultures can be miscellaneous. In general, assortativity can be explained taking into account homophily [515] or modularity [520]. Indeed, a possible reason of assortative preferential attachment is due to entities are jointly associate by a similar affinity as well as real social networks [122, 513, 626, 581, 54]. In the case of information processing systems as neuronal brain, associations by similarity of semantic thematic seem to lead to patterns of assortativity. In this way, S. de Franciscis et al. [171] shown that assortative networks of simple model neurons are able to exhibit associative memory in the presence of levels of noise while that uncorrelated or disassortative networks cannot. Conversely, it is possible that the synaptic reinforcement mediated by Hebb learning rule [312] leads to the networks assortative mixing. Despite being a dynamical mechanism, perhaps, over time, this synaptic reinforcement has ended up giving shape the underlying topology of the network.

As pointed out by Holme et al. [327], another typical context where assortative mixing appears is in competitive areas such as scientific, actor, and business collaborations [177, 514, 298]. When the maintenance of different relationships or interactions (or links) required a continuous effort or cost and the resource are scarce, assortative mixing patterns seem to predominate. Evidence of this fact is seen, for example, in real-world social networks which exhibit significantly assortative mixing pattern [516] while that on-line social networks shown diverse degree correlation pattern, including disassortative, assortative or nearly neutral mixing [335]. Indeed, on-line social networks can shown assortativity-disassortativity transition [122, 335] being one overlap of real and virtual social subnetworks. Notice that the on-line interactions are exposed to less physical constrains than what is typically the case in most other real social interrelationships. In addition, the maintenance of on-line links doesn't involve any cost, just consist in a one-press operation. In contrast, in real life friendship require constant care, time and dedication. But, what happens to our aggregated cultures?

Until now we have seen that in hostile environments assortativity seems to be the norm. Indeed, assortativity tends to enhance network performance in bad conditions (low density of edges and high noise), whereas disassortative networks perform best in good conditions (high density of edges and low noise) [612, 613]. At this early stage, the cortical networks is presenting itself to us delicate, whit weak connections and whit

one poor and intermittent dynamic. In this sense, during the maturation of the network, bundling could be a mechanism to protect the *neuroblast* which still not developed their dendrites and axons [502, 260]. Additionally, as we had seen previously, the formation of the clusters is an efficient mechanism to transport the *neuroblasts* in the migration phase [502, 260]. However, the posterior evolution of these clusters is still an open issue but still unknown at the present. Some study [259] suggests that they end up being splitting up during the post-natal period, others researches [333, 502] argue that clusters can be the valuable key for a better understanding of cortical columns. As has been seen in the Chap.1, in primates, cortical columns contains $\sim$ 80 mini-columns of 50-60 μm in diameter and each mini-column contain $\sim$ 80-100 neurons, except for the striate cortex where the number is $\sim$ 2.5 times larger [438, 440, 503, 504, 338]. Curiously, notice that our aggregates and clusters present the same size ($\sim$ 50 μm) and they are also constituted by the same order of neurons ($\simeq$ 100 neurons). In addition, we have observed that assortative mixing patterns tend to break the network up into separate *communities*, then different set of aggregates or clusters could give rise to different *functional modulus*, similar to cortical columns [504]. In this sense, each aggregate or cluster could then be considered as the elementary functional units, similar to mini-column [503]. However, such assumptions are simply guesses and not evidence of this there are.

However, it is true that degree mixing pattern has profound effect on network structure and behaviors, such as the storage and retrieval of information [612, 171, 711, 363, 56], robustness of networks against intentional attack or random breakdown of their element[29, 143, 144, 114, 328, 84, 209, 83], percolation [525, 621, 114, 113], transport properties [766, 84, 732] and synchronization [125, 423]. In the following sections, these factors are analyzed in greater detail.

Degree correlation and information coding

If we consider that the information is encoded in the mean firing rate of the network [760, 268], the estimation of this quantity can then provide much insight. Previous analyzes show that networks with assortative degree correlation (aggregated networks) lead to firing patterns higher than those with uncorrelated (semi-aggregated networks) and disassortative (homogeneous networks) degree correlation of the semi-aggregated and homogeneous networks. In assortativite networks, firing rates of high-degree populations are raised and the ones of low-degree populations are lowered compared to their uncorrelated counterparts.

Within a generalized mean-field approach, high impact of correlations on the firing rates is also suggested in theoretical approaches by [612, 613]. The authors showed how heterogeneous networks with assortative degree correlations increases the ability of the network to transfer information I about sub-threshold signals. Firing rate of networks with assortativite mixing become slightly higher, even for sub-threshold inputs, where an uncorrelated network would not fire. Specifically, the authors found that I is optimized for networks with intermediate degree of assortativity $p \simeq 0.6$. Moderates values of assortativity degree were also detected in our aggregated cultures in accordance with [692]. Intermediate values of assortativity would help to a better integration between both subnetworks of high- and low-degree. A higher values would lead to a decoupling of both subnets, which would operate at two-speed and independently way from one

other. Moreover, the increase of assortativity adds up to a high level of noise entropy, reducing I even further. In contrast, moderate values of the assortativity provide a optimized balance between segregation and integration in the network, arising as a result of a detailed balance between network interactions.

These outcomes seem consistent with recent studies that suggest that assortativity enhances neuronal network memory in noisy conditions [171] and increases the information content of heterogeneous directed networks [557]. Highl levels of heterogeneity in the topology of the network can may be advantageous for the performance of certain tasks which require unstable behavior —such as pattern recognition, family discrimination and categorization [711, 363, 56]. Increasing the assortativity leads to a loss of stability in the dynamics of the network [95] while that the disassortative mixing seen in biological networks could be a consequence of evolutionary optimization of these networks to minimize the effect of dynamical fluctuations. Notice that for definition, the third and higher order correlation are related to the network assortativity. So, in this sense, assortative mixing by degree tends to severely destabilize the networks, meanwhile disassortative networks are more resistant to the effect of dynamical fluctuations [190].

Resilience and Percolation transition

Similar effects are observed as we weaken the strength of links in the disintegration process. In uncorrelated and disassortatives networks for low strength shown a sharp transition to sustain activity, whereas assortative networks are actives even for small strength of links. When total input current becomes weak, low in-degree neurons stop firing leading to a cascading failure of spiking of stronger connected neurons. In assortativite networks the failure of neurons with low in-degree only entail the failure of the low-degree subnetworks, whereas high-degree subnetworks (aggregates) sustain their recurrent activity. Indeed, aggregated cultures with assortativity mixing patterns seems to present more resilience to disintegration process in accordance with the results suggests by [29, 143, 144, 114, 328]. And this behavior is reminiscent of findings for percolation in complex theory where assortatives networks remain robust under random failure [515] in conditions of low densities of edges. In contrast, assortatives networks are highly sensitive to intentional attack or targeted deletion of aggregated network [144, 114, 692]. To this, one should add that particularly in disassortative networks, the detailed analysis of the internal connectivity of each burst, also reveal high redundant wiring of the functional neuronal network. This complex communication networks provides in turn to the network a surprising high degree of robustness and stability. This fact could be in accordance with the hypothesis that brain network maximize both the number and the diversity of functional motifs, while the repertoire of structural motifs remain small [664].

We note that the disintegration of our aggregated cultures does not present assortativity-disassortativity transition despite being the superposition of both subnetworks. This effect may be due to the fact that we work with very small networks and the homogeneous subnet percolate sooner that the aggregated one. Effectively, during the disintegration the natural tendency of the assortative coefficient is to increase, showing the highest resilience of the aggregates which persist to disintegration. However, it is observed that the disintegration of aggregates is achieved with higher thresholds than for individuals neurons. One one side, this fact shown us that the aggregates act as an entity of our own.

On the other hand, as we had seen previously, homogeneous cultures need a minimum network size to to reach the collective bursting regime. Above this, it would be interesting to analyze if the assortative networks percolate sooner than disassortative ones. So, it would be necessary to perform experiments on larger network.

Finally, it is important to highlight that degree correlations cannot be treated as an independent topological feature, but must be taken into account together with the spatial embedding of the networks. Indeed, in neuronal cultures the connections between spatially close nodes are often more probable than between distant nodes [607, 660], so spatial constraints impact significantly on topological features of functional networks. As is pointed out by Lie *et al.* [421] spatial constraints generally increase the percolation threshold and shift the percolation transition from the universality class of random graphs to the universality class of two-dimensional lattices. In this line, Schmeltzer *et al.* [613] shown the assortativity decrease the percolation threshold of spatial random graphs when nodes are distributed randomly in space, whereas assortativity increases percolation when nodes are spatially segregated by their degree. Hence, our aggregated cultures seem to fall in this second category.

Transport of information flow and Oscillations

The study of real networks usually serves a particular purpose which can be expressed in terms of flow problems, in particular in the context of transport between the nodes along links with restricted capacities. The preceding outcomes shown that the transport properties strongly depend of the structure of the medium, in particular to various aspects of connectedness. In fact, the traffic of information flow and the underlying topology are mutually correlated and it is very important to define appropriate quantities and measures capable of capturing how all these ingredients participate in the formation of complex networks [59]. Given the approximation of the individual neuronal behavior in a discrete Markov process of second order, special interest should be taken to the analysis of random walks over different topologies [442] as well as on regular networks [202, 57], SW-networks [33, 360, 768], SF-networks [526, 253, 21, 768] and ER-networks [658, 344, 768]. Notice that, in accordance the outcomes obtained in the previous Chapt, if the aggregates were treated as an own entity, they would have to model as in a discrete Markov process of k order where k would be in the range of $[15 - 30]$ approximately (if $\delta = k\tau$ then $\delta \simeq [0.3 - 0.6, \pm 0.1]$s if $\tau = 20$ms).

Transport properties in complex networks characterized p.e. by conductance or maximum flow is generally related to the degree distribution $P(k)$ of the different networks. Several studies [415, 118] obtain that in SF-networks where the degree k follows a power-law distribution $P_d(k) \sim k^{-\alpha}$ asymptotically, the maximum flow obeys a power-law distribution with the exponent $2\alpha - 1$ while in completely ER-networks it follows a Poisson distribution. The same asymptotic behavior for the conductance distribution in SF-network is reported by [437, 422]. In contrast, due to the exponential decay of degree distribution, ER-networks lacks of hubs and their properties (specifically transport), are controlled solely by the average degree $\overline{k}$ [87, 294].

As we highlighted several times, our analyses makes emphasis on collective properties of the population, and not on individual neurons. In this context, if the underlying physical connectivity is regular or random, we may then neglect spatial interactions and deal

simply with the temporal dynamics of the network [760]. In fact, physiological evidences [505, 339, 340] shown that neuronal population present a high degree of *redundancy*. Their findings indicate that even within relatively small volumes of cortical tissue there exist many cells with nearly identical responses to the same stimuli. It is just such local redundancy which allows us characterizing spatially localized neural populations by a single variable. Under this approximation, one can then consider that the information is encoded in the mean firing rate of the network, as was previously assumed. Notice that this implies that the relevant aspect of single cell activity is not the single spike but rather spike frequency [75]. Consequently, only the mean frequency of the population will need to be known in order to describe the encoded information of the network. However, when the network is heterogeneous and the degree of redundancy is low, this assumption may well be incomplete and other consideration will have to be taken into account.

In heterogeneous networks, in a transport process, each node does not contribute equally likely. Hence, the distribution of hubs, sinks, sources and bridges has a strong impact in the dynamics of the network. Furthermore, although stronger connections have a high impact for network dynamics, weaker connections need to be considered as well. Effectively, as we had seen recently over, a correct integration among all the parts is to be attained with a view to ensure the proper functioning of the network. In neurobiological literature, synaptic connections have been classified previously by their impact into 'drivers' and 'modulators' [637]. Indeed, firstly, we saw that hubs have an important impact in the spatio-temporal organization of bursting dynamics, redirecting the flow of information, by modulating and balancing the loading of speed. Hub regions are thought to play pivotal roles in the coordination of information flows in the brain networks [663]. Secondly, the analysis of time of firing of these strong-synchrony communities is also analyzed and ours findings suggest that functional hubs and related communities fire on average earlier than the rest of the culture. However the highest negative time delays are detected in the communities organized around its associated functional hubs and their communities, describing local burst initiation cores [216, 206].

Finally, besides this, we have seen that functional connectivity hubs reflect foci of enhanced local bursting synchrony [295, 676]. Indeed, SF- and SW-networks are knows to be more easily synchronized than regular or ER lattices [406, 250, 367, 329, 56, 744]. However, the emergence of oscillations patterns is not simply related to the node degree distribution and the prescence of functional hubs, but instead depends on the properties of a diffusion process on the networks or their ability of transport of information flow. This process is in turn influenced by how the coupling strengths are distributed. In general, homogeneous distributions in the coupling of the nodes leads to greater synchronization between the respective nodes than heterogeneous distributions. So, in this line, disassortative networks make for more synchronizable [95, 190] than assortativity ones. Indeed, in the brain, synchrony between local areas processing specific stimuli is desirable functionally [290] but where global or very large scale synchrony is considered pathological as in epilepsy [372]. Notice that synchronization of culture activity can be defined over a range of timescales, from synchronous busting [737], where areas of the network are synchronously active (usually within 100 ms), to precise synchronization between the spike times of two or more neural units [134] (usually within 10 ms or less). Unfortunately, due to experimental limitations of fluorescence technique, we can only analyze the former case.

The increasing prevalence of highly connected nodes in older cultures suggests that such hubs play a greater role in network activity as the cultures mature. Indeed, the energy-efficient routing becomes one of the most critical point for sustaining the overall network lifetime. In a directed networks, transport flow becomes more efficient if an optimal number of sources and sinks are correctly inserted and bridged [119]. Indeed, transport properties usually have been investigated in the context of the shipping between pairs of sources and sinks. Current could flow from the source node to the sink node via a number of paths more or less redundant. However, several researches [437, 415] shown that the quality of transport strongly depends on the degree of the sources and the sinks, whereas the rest of the network serves as an approximately resistance-free substrate for the transport process.

Communities and hierarchically modular network

Assortativity is an important parameter governing geometrical and transport properties of networks. Indeed, the diameter of the network and the clustering coefficient increase dramatically with the degree of assortativity [766]. In addition, similar mixing correlations between degree-degree nodes tend to break the network up into separate communities [85, 516]. Clustering and assortativity in network arise because the vertex are divide into groups and communities [520, 543] with a high density of edge between members of the same group. Implicitly, the assemblage by similarity could cause different stratifications in the network, giving rise one hierarchical organization. Notice that modular architecture no not always imply hierarchically organization. Evidences shows that the connectance for human brain is around 10^{-6} [636], which leads us to the question of how communication efficiency can remain high in such a sparsely connected network. It is possible that the more intricate hierarchical and modular structures found in the brains of higher organisms is a response to the above problem. Indeed, in information processing system, there are several general advantages to modular and hierarchically modular network organization, including greater robustness, adaptivity, and evolvability of network function [645]. As is pointed out by Simons [645], a 'nearly decomposable system built of multiple, sparsely inter-connected modules allows faster adaptation or evolution of the system in response to changing environmental conditions.

As we had previously seen, modular network topology of aggregated cultures is associated with a rich non-lineal dynamics. Modular networks tends to produce time-scale separation, where one can distinguish fast intra-modular processes and slow inter-modular processes [542]. Indeed, intra-components links are generally stronger than intercomponent linkages. This coexistence of segregated and integrated activity [629, 541], also so-called transient 'chimera' states [630], would drive the system to high dynamical complexity where synchronization and de-synchronization would be switched across the network. Formation of modules generally emerges in dynamical systems where network structure and function coevolve [297]. Neuronal networks with adaptive rewiring typically involve a reinforcement of links between synchronized units and a pruning of links between desynchronized ones. In turn, this continuous feedback between the dynamics and the structure of the network spontaneously drives the emergence of inhomogeneities and modules in networks.

On the other hand, from a functional point of view, modular networks is an optimal

organization for performing complex tasks in a changing environment [377]. Indeed, evolutionary pressure produces networks where modules specialize in these sub-problems and where rapid adaptation to each of the different goals is enhanced. In this way, the combination of these 'building functions' enable a rapid and efficient response to the need of the changing environment. In addition, during evolution this specialization by splitting of structures or brain growth by duplication of substructures seems to be a natural way to form hierarchical architectures. R.A. Robinson et al. [586] shown how hierarchical networks can simultaneously emerged by imposing topological constrain of networks as well as high clustering, short path lengths and low wiring costs. However, weak hierarchical modularity has been detected in our neuronal cultures, surely due the fact that our networks are very small in size. However, it is important to bear in mind several considerations in accordance to hierarchical structures, complex system and information processing system.

Indeed, complexity and hierarchy are two concepts closely linked. Hierarchy is one of the central structural schemes that the architect of complexity uses [644, 643]. In current language, this term has a narrower meaning and it has generally been used to refer to a complex system in which each of the subsystems is subordinated by an authority relation to the system it belongs to. However, in the complexity theory, the relation among of these subsystems can be more complex than a simple relation of subordination. So, in this context one tend to reserve the word hierarchy for a system that is divided into a small o moderate number of subsystems, each of which may be further subdivided or partitioned.

In his seminal paper, Simon gave at least three reasons for the existence of hierarchies in complex system. Firstly, as we have previously seen, hierarchical organization and modular structures are easier to be generated. In addition, hierarchical structures are being robustly stable under large scale reconnection of substructures and evolve far more quickly than non-hierarchic systems of comparable size [645]. In this sense, this organization structure enable the system to take better advantage of evolutionary opportunities. Secondly, hierarchical structures are more efficient in the transport of information. While it is true that hierarchical structure is the simplest kind of database and it is inflexible because the relationship is confined to a one-to-many links. However, despite their rigidity, hierarchies (or taxonomies) are a good way to help organizing vast amounts of information, establishing unambiguous routes of communication. And finally, in the third place, Simons suggested that hierarchical systems have significant redundancy, and that it is therefore possible to construct models of such systems that are simpler than the system itself. Moreover, in a information processing system, hierarchical structures can offer the idea that each architectural layers should correspond to different conceptual layers, with every entity in a given layer being at the same level of conceptual abstraction. So, different levels of abstractions are associated with the the different topological layers.

However, this notion of hierarchy seems contrary according to the arguments that complex systems do not have central control system. In this sense, the 'distributed' nature of the structure of the system seems more appropriate in order to describe self-organization and to obtain a dynamic and adaptable system, flexible and invariable. However, although it is recurrently found that optimal networks providing efficient transport are tree–like structures [53, 86, 200, 72]. In particular, optimal trees are generally found to be self-similar [589]. These results are only contingent on the assumption of a stationary

flow through the network. Effectively, when time variations or fluctuations are added, a different class of optimal structures arise which share the hierarchical organization of trees yet contain loops [149]. In certain contexts, the incorporation of loops could thereby have a beneficial impact in introducing a suitable measure of network redundancy, providing alternate routes to accommodate fluctuations. Indeed, hierarchical structures which contain loops can be understood as a compromise between transport efficiency and other requirements, such as tolerance to damage. In this sense, although hierarchies are need in order to generate frameworks of meaning in the system, they cannot be defined as rigid and permanent structures. Effectively, the vitality of the system lies in its ability to transform its hierarchies in a flexible and adaptable way to the demands of a constantly changing environment.

Chapter 7

SUMMARY: Conclusions and future lines of work

7.1 Conclusions

The present thesis has investigated the global and individual dynamics of a neuronal population and its interrelation with the underlying topology of the network. We combined experiments, numerical simulations and data analysis. As experimental platform, we used primary cultures of embryonic rat cortices, monitored through calcium imaging. For simulations, we considered a neuronal population consisting of a series of integrate–and–fire units (the neurons) interconnected in a two–dimensional space. For analysis, we used linear and nonlinear time series analyses techniques.

Linear analyses of experimental data:

To begin with, in order to characterize neuronal network dynamics and its structure, each time series was modeled as a linear autoregressive stochastic process and we focused on analyzing its energy and spectral distribution. In particular, special emphasis was placed on the characterization of its power spectrum (PSD) and the determination of its frequency exponent α. We observed that, during the first week of growth *in vitro*, the changes in the PSD were abrupt and with strong variability from culture to culture, showing the fragility of the networks. Over the first week in culture (DIV $\simeq 7 \pm 2$), we detected the emergence of inhibitory currents (GABA switch) and, as the neuronal cultures matured (DIV $\geq 10 \pm 2$), the global energy of the system stabilized. Indeed, during this stage (DIV $\leq 21 \pm 2$), we observed that all the PSDs collapsed, and followed a behavior of the form $P \sim f^{-\alpha}$, with $2.3 \leq \alpha \leq 2.8$.

In addition, the spatial analysis of spectral analysis reveled the richness in the distribution of energy across the network. This study revealed that, when network connectivity was gradually reduced through CNQX, PSD spatial distribution switched from a homogeneous configuration to a heterogeneous one. Specifically, in mature cultures (DIV $\geq 13 \pm 2$), this analysis uncovered the existence of strongly connected communities, which activated in quasi–synchronous oscillations, and with an activation frequency that strongly correlated with the degree of disintegration of the network.

Nonlinear analyses of experimental data:

Despite the success in describing neuronal collective behavior through linear analyses, neurons are inherently nonlinear units coupled in a nonlinear manner. Hence, the dynamics of the neuronal assembly cannot be fully addressed using linear approaches. To solve this difficult, we extended the above analysis to incorporate nonlinear embedding techniques [537, 689, 383].

Our goal was to reconstruct the underlying dynamics of the network in the state space and to study its internal recurrences. In particular, the method of delays (MOD) [689] was used for this end and special care was placed on the determination of its characteristic parameters, namely the embedding dimension m and the time delay δ. The former one rendered the number of independent variables needed to describe the network [381, 116, 262], whereas the latter defined the time window characterizing the two closest uncorrelated events [631, 230, 271].

With this information, we proceeded to calculate the distance matrix between the respective states through the construction of recurrence plots (RPs), and studied the different dynamical patterns that emerged. In particular, we analyzed the following dynamical structures: (i) the distribution of isolated single points, characteristic of stochastic dynamics; (ii) the distribution of diagonal lines, characteristic of two parallel and similar segments of orbits; and (iii) the distribution of vertical or horizontal lines, characteristic of rare, abrupt and unexpected events. These analyses were applied to two kinds of experimental data, *development experiments*, and *disintegration experiments*.

For *development experiments*, we first observed that, at the very initial stages of growth *in vitro*, i.e. over the first week of culturing (DIV $\sim 7\pm2$), neurons exhibit a highly stochastic behavior ($m > 8$ and $\delta > 5.0 \pm 0.4$ s) that reflects their weak interconnectivity and reduced capacity to exhibit strong collective phenomena. As maturation progressed, a collective and coherent regime begins to emerge, low–dimensional (m $\sim [3-4]$ and $\delta \sim 1.0 \pm 0.2$ s), characterized by quasi–periodic orbits and with the existence of a limit cycle in the state space. The synchrony and similarity of the orbits gradually grew, and by the second week (DIV $\simeq 13 \pm 2$), these properties started to decrease, possibly due to a pruning effect or the increase of inhibitory currents. For larger maturation stages (DIV $\geq 13 \pm 2$), two different dynamical behaviors of the [E+I]-networks were observed. On the one hand, just like young cultures, a first line of experiments with mature cultures presented low–dimensional dynamics with bursts of type I, characterized with a large amplitude of fluorescence and a quasi–periodic dynamic behavior ($m \sim 3$ and $\delta \sim 0.8 \pm 0.2$ s). In these conditions, %DET, L_{max}, %LAM and %TT increased. On the other, a second line of experiments with mature cultures showed a change of dynamics with burst of type II, with low amplitude of fluorescence and high firing rate. Indeed, these cultures showed high–dimensional dynamics (m $\in [5-12]$ and $\delta \simeq 0.9 \pm 0.3$ s) displaying collective orbits that were densely populated of micro–states, and folding onto themselves. Indeed, in this stage, the complexity of the dynamics increased and provided rich and colorful RPs, with %DET, L_{max}, %LAM and %TT diminishing.

For *disintegration experiments*, we considered mature cultures with inhibition blocked, and proceeded to gradually weaken the connectivity among neurons through CNQX. To be more precise, we monitored homogeneous cultures only at DIV $\geq 13 \pm 2$, and explored [E+I]-network's dynamics folowed bu E-only networks with gradually higher CNQX. The

results showed that the dynamics in these [E]-networks exhibited a return towards low–dimensionality for large CNQX (m $\sim$ 3 and $\delta \sim 0.9 \pm 0.3$ s) with bursts of type I, and reveling highly–synchronous states. %DET, L_{max} increased and %LAM and %TT decreased. These highly–synchronous states seemed to be dominant in homogeneous networks. They were indeed unobserved in aggregated ones.

These nonlinear analyses evinced that, despite the apparent simplicity of neuronal cultures, they offer a rich dynamics whose complexity depends on the connectivity among neurons. CNQX experiments in particular revealed substantial changes in the dynamics as disintegration progressed. These findings are in accordance with the studies of Refs. [277, 276], which rose the hypothesis that the dynamics of a healthy physiological system produces highly irregular and highly complex dynamics, with prominent variability and fluctuations. Diseased and even aging networks, on the contrary, exhibited a far less complexity and more regularity ('dynamical disease') [273, 274, 275, 458, 459, 488]. The loss of complexity was also detected in the disintegration and degradation process in our neuronal cultures. However, the nonlinear testing revealed that our systems still present a low–dimensional behavior showing small degree of nonlinearity.

Modeling *in vitro* networks through numerical simulations:

The use of simulation with RS–type spiking neurons helped us to elucidate certain unclear aspects of the experiments. The study of the collective dynamical regimen with different sizes of networks and various synaptic strengths, indicated that only a small region of the explored parameters was in accordance with the experimentally observed biological behavior.

In the case of homogeneous networks, we detected the emergence of collective bursting dynamics only for large populations (N $\gtrsim 8 \times 10^3$). In this case, two different dynamics were distinguished. A pure oscillatory dynamics ($m \simeq 2$ and $\delta \simeq 0.8 \pm 0.2$ s) was obtained for large [E+I] networks (N $\simeq 10^4$) and high synaptic strengths ($g_{GABA} = -42$, $g_{NMDA} = 0.4$, $g_{AMPA} \in [10.15 - 10.55]$). In the other instances, quasi–periodic dynamics (m $\simeq 2$ and $\delta \simeq 0.9 \pm 0.2$ s) with bursting type I, similar to the experimental behavior, was observed. Indeed, in homogeneous networks, a critical size was required to achieved the collective bursting dynamics. For small homogeneous networks (N $\lesssim 8 \times 10^3$), and although individual neurons displayed RS, the collective firing regime was impossible to be reached.

The addition of *aggregation* in the networks, in the form of small groups of highly packed neurons, changed the global network behavior. Indeed, the inclusion of small sets of grouped neurons enabled the network to achieve the collective regime with less neurons, and maintaining a similar density of connections as homogeneous networks. The incorporation of aggregates leaded to a boost in neuronal activity, increasing the clustering coefficient in its neighborhood, and generating regions that facilitated the topological amplification of small firing events that grew to trigger network–broad activity. Hence, similar to the experimental conditions, for small aggregated networks ($N \gtrsim 1 \times 10^3$), collective bursting dynamics emerged. For moderate sizes of [E+I] networks (N $\simeq 3 \times 10^3$) and high synaptic strengths ($g_{GABA} = -42$, $g_{NMDA} = 0.4$, $g_{AMPA} > 9.95$), unstable high–dimensional dynamics with bursting of type II was detected ($m \gtrsim 3$ and $\delta \simeq 1.5 \pm 0.3$ s). In the remaining cases, quasi–periodic dynamics with bursting type I were observed

($m \simeq 2$ and $\delta \simeq 0.7 \pm 0.2$ s).

From dynamics to connectivity reconstruction:

Since intrinsic neuronal dynamics and neuronal interconnectivity shaped dynamics, we wondered to what extreme we could predict the connectivity of the network solely from activity data. Thus, in order to *reconstruct* the underlying connectivity of different networks, we considered that two neurons were connected if they presented a statistical relationship based on the similarity between their activity traces. This relationship was quantified in different ways, and according to four descriptors: (i) cross–correlation (XC), (ii) partial correlation (PCC), (iii) mutual information (MI), and (iv) generalized transfer entropy (GTE). We tested these four methodologies through simulations, and concluded that best reconstruction was obtained through GTE. On this basis, GTE–reconstruction was applied to different experimental data in order to determine the physical connectivity of the networks, or at least a coarse description through key statistical parameters such as the average connectivity $\overline{k}$ or the degree of assortativity.

The different network's topological parameters obtained were the following. After GABA switch, very young cultures exhibited low values of $\overline{k}_{EI}$ and $\overline{k}_{E}$, in the range of $3-15$ for homogeneous networks and $7-20$ for aggregated ones, respectively. In mature cultures, GTE–reconstructions provided values of $\overline{k}_{EI}$ and $\overline{k}_{E}$ in the range of $15-150$ for homogeneous cultures. Similarly, the aggregate cases presented slightly higher values than the homogeneous ones in the range $20-180$.

We highlight that we did not see any evidence for a small–world (SW) network structure. Indeed, although our neuronal networks share some traits with SW–networks, in particular high clustering coefficients, we did not have sufficient evidences for a SW connectivity, in particular due to the high uncertainty in the values of average path lengths. We therefore preferred to describe the reconstructed degree distributions as just 'exponential' or 'right–skewed', and as a function of the age of the culture. Young cultures presented 'exponential' degree distributions while mature cultures had a tendency to show 'right–skewed' distributions. The latter result indicates that this mature cultures contained a larger number of highly connected areas (hubs). This trend was accentuated in aggregated networks, which exhibited high coefficients of modularity, accompanied by a hierarchical architecture and the presence of a greater number of sources and sinks. Such a combination of network measures indicates that the transport of information may be more efficient in aggregated networks [484].

The degree–degree correlation analysis reveled that homogeneous cultures exhibited negative values of Pearson coefficient ρ^{PW} and Spearman rank correlation ρ^{SW}, showing a disassortative mixing pattern. As the degree of aggregation increased, these coefficients gradually increased until they reached positives values ($\rho^{PW} \simeq \rho^{SW} \simeq 0.6$). Hence, we concluded that networks with some degree of aggregation have a tendency towards an assortative mixing pattern. According to different studies, such a result indicates that information transmission was more optimized in aggregated networks [612, 613].

We note that networks with extremely high assortativity values would lead to a decoupling between the high–degree and the low–degree subnets. In this case, the whole network would not be able to integrate and manage the information, which would become extremely inefficient, not adaptable and with a poor response to external stimuli.

Likewise, in heterogeneous directed networks immersed in a highly noise environment, assortativity would increase the ability to store information, enhancing the memory of the system by improving the number of meta–states in the state space [171, 557]. Instead, disassortative networks are more resistant to the effect of dynamical fluctuations [190].

Pivotal studies in the literature presented the idea that assortative networks are robust under random failure [515] in conditions of low densities of edges. Interestingly, in the context of the analyzed experimental data, aggregated networks presented a higher resilience against disintegration through CNQX than their disassortative counterparts. This results supports the observation that assortativity increases percolation threshold [613].

Moreover, unlike a disassortativite mixing pattern, assortativity would affect the system's ability to synchronize [40]. Strong–synchrony communities were detected in homogeneous networks with disassortativity mixing pattern in mature cultures, where its oscillatory frequency depends on the degree of disintegration of the network. In addition, these communities seem to be sustained around functional connectivity hubs which would reflect foci of enhanced local bursting synchrony [295, 676]. We note that the degree distribution of our mature cultures presented 'right–skewed' shapes and not 'exponential' ones. This fact is in accordance with the idea that scale–free, as well as small–worldness, are easier to synchronize than regular or Erdös–Rény lattices [406, 250, 367, 329, 56, 744].

Finally, in regard to degree–degree correlation, two other considerations are important to be made. As already argued, an assortative mixing pattern offers advantages for information processing. Interestingly, only assortative networks of simple model neurons are able to exhibit associative memory in the presence of levels of noise, while uncorrelated or disassortative networks cannot [171]. However, disassortativity could yield significant benefits as explained. We note that a possible argumentation for the existence of disassortativity in homogeneous networks [77, 78] could be that, although the spatial distribution of neurons is homogeneous, the intrinsic connectivity of neurons present a fine and refined metric structure, where dendrites and axons trees display a fractal and auto–similar structure [444, 753]. It can not be a coincidence the fact that neurons have only one axon [474, 516, 543, 364]. Indeed, this metric structure must be taken into account and it should certainly play an important role for a smooth and efficient functioning of the system. In summary, each one of the different topologies investigated offers different advantages and drawbacks to the system and, according to the context of our work, they could complement to one another when put together to shape very large neuronal circuits.

7.2 Limitations and future lines of work

Here we outline some of the difficulties and limitations of our research throughout this thesis and that may inspire future lines of work.

From an **experimental perspective**, different problems will have to be overcome.

Firstly, we worked with a two–dimensional (2D) monolayered cell culture systems, which reduces the complexity level both at the dynamics and the connectivity levels. Certainly, 2D cell culture systems do not accurately reproduce the structure, function, and physiology of living tissues and differ from a three-dimensional (3D) cell matrix [132,

19, 334, 509]. Thus, the combination of microfluidics technology with 3D cell culturing would offer a great potential for *in vivo*–like tissue–based applications [426].

Secondly, ours networks are too small. Taking into account that highly dense aggregates exhibited very interesting dynamics, having solely $5 - 10$ in the field of view greatly reduced our ability to understand complex spatio–temporal dynamics. Although the optical system can be tuned, networks 4 times larger (or more) would be preferable and, clearly, much more experiments are required to better understand our networks.

Thirdly, the slow dynamics of the fluorescence marker masks the fast individual dynamics of neurons. This is a major problem. Indeed, individual dynamics represent inter–neuronal correlations of the networks and their identification is crucial in order to reconstruct the underlying anatomical connectivity. In this context, an analysis comparing MEAs [587, 651] and calcium image fluorescence [703, 761, 296] would be really useful to the community.

Fourthly, the application of electric fields for stimulating or interrogating the circuit would be also important [546, 222, 660]. Such experiments could provide clues on the behavior of the cultures when they receive stimuli, and could be interesting to compare the degree of complexity and nonlinearity with and without stimulation.

And finally, fifthly, a line very interesting to investigate would be the following. A week after plating an aggregated culture, new neurons could be added to the initial network and observe their integration into the old network. Although this line was explored for some months, it was discarded due to the technical difficulty of maintaining populations that require very different culture media. Preliminary results, however, indicated that the incorporation of young tissue did not seem to damage the network, but rather reinforced it. Nevertheless, a more accurate study would have to be carried out and be contrasted with the behavior of young tissue over homogeneous old networks.

In regard to simulations, different considerations are worth mentioning. First of all, our simulations do not embrace all the shades of complexity and richness of our neuronal cultures. Experimentally, small homogeneous cultures which disassortative mixing patterns reach a collective activity regime, whilst their simulated ones do not. In our case, simulated homogeneous networks exhibit uncorrelated degree–degree correlation. Hence, the study of the emergence of collective bursting dynamics in small homogeneous synthetic networks with disassortative mixing patterns is a problem that could be investigated. Perhaps our meso–scale approximation that ommitts the specific morphology of single–neuron is too restrictive, and may have a significant impact in the overall blueprint of the network [151, 163, 150]. Secondly, a more careful simulation of aggregated networks could be done. We lack a good model for the formation and constitution of aggregated networks, and such a development would be very interesting [502, 260, 622, 34, 333]. Thirdly, although the choice of the dynamic model [354, 351, 352, 353] allows to simulate the network and its development along DIV, we could not study the effect of synaptic reinforcement in the activity, which certainly occurs. And finally, fourthly, we only used the RS–type spiking neuron for simplicity, but single neurons display a wide spectrum of individual dynamics [351, 352, 353]. We note that the selection of this dynamical model provided relatively easy simulations, with only four important parameters at play. However, although the implementation of different dynamics is not difficult, its interpretation may be too complex. Indeed, in such a case, the role of network structure on global dynamics could be much more difficult to carry out.

Referring to data **processing and analysis**, further improvements could be achieved. Firstly, although the combination of linear and nonlinear approaches provided interesting insights, we considered most of the time as main data the average over the network population. These tools are so complex and computationally demanding that they are unfeasible to extent to *individual* $\simeq 3000$ neurons. Additionally, our data has poor signal-to-noise ratio, which would make even more difficult the analysis. Secondly, once the collective orbit of population is reconstructed, the extraction of the nullclines could be very interesting [428]. Indeed, this fact would allow us to link the experimental findings with some population–based theoretical model. Although mature cultures present complex dynamics, such analysis could perhaps be carried out with young cultures. And finally, thirdly, in reference to decode the underlying connectivity, the GTE–reconstruction could be extended to multivariate methods using incremental conditional TE measurements [435, 217, 681] or considering not only the temporal correlations but also the topological ones [757, 521, 576, 628].

Bibliography

[1] http://www.treestoolbox.org/download.html. pages 43, 44

[2] https://github.com/orlandi/neurongen. pages 47

[3] https://github.com/orlandi/neurondyn. pages 47

[4] https://gephi.org. pages 49

[5] http://www.mpipks-dresden.mpg.de/~tisean/. pages 90, 101, 102

[6] http://www.physik3.gwdg.de/tstool/. pages 90, 104

[7] http://tocsy.pik-potsdam.de/commandline-rp.php. pages 90

[8] http://www.mathworks.com/matlabcentral/fileexchange/3102-optimal-embedding-parameters. pages 104, 105

[9] https://es.mathworks.com/matlabcentral/fileexchange/10922-matlabbgl. pages 150

[10] https://github.com/orlandi/te-causality. pages 150

[11] https://github.com/orlandi/connectomicsPCV. pages 150

[12] A. Abbott. Solving the brain. *Nature*, 499(7458):272, 2013. pages 17

[13] L. Abbott and R. Rohrkemper. A simple growth model constructs critical avalanche networks. *Progress in brain research*, 165:13–19, 2007. pages 11

[14] L. Abbott and C. van Vreeswijk. Asynchronous states in networks of pulse-coupled oscillators. *Physical Review E*, 48(2):1483, 1993. pages 145

[15] L. Abbott, J. Varela, K. Sen, and S. Nelson. Synaptic depression and cortical gain control. *Science*, 275(5297):221–224, 1997. pages 56

[16] S. Achard and E. Bullmore. Efficiency and cost of economical brain functional networks. *PLoS Comput Biol*, 3(2):e17, 2007. pages 159, 160

[17] S. Achard, R. Salvador, B. Whitcher, J. Suckling, and E. Bullmore. A resilient, low-frequency, small-world human brain functional network with highly connected association cortical hubs. *The Journal of neuroscience*, 26(1):63–72, 2006. pages 6, 181, 183

[18] J. Acimovic, T. Mki-Marttunen, and M.-L. Linne. The effects of neuron morphology on graph theoretic measures of network connectivity: The analysis of a two-level statistical model. *Frontiers in Neuroanatomy*, 9:76, 2015. pages 47

[19] S. Agastin, U.-B. T. Giang, Y. Geng, L. A. DeLouise, and M. R. King. Continuously perfused microbubble array for 3d tumor spheroid model. *Biomicrofluidics*, 5(2):024110, 2011. pages 198

[20] G. Aghajanian and F. Bloom. The formation of synaptic junctions in developing rat brain: a quantitative electron microscopic study. *Brain research*, 6(4):716–727, 1967. pages 5

[21] E. Agliari and R. Burioni. Random walks on deterministic scale-free networks: Exact results. *Physical Review E*, 80(3):031125, 2009. pages 187

[22] H. Agmon-Snir, C. E. Carr, and J. Rinzel. The role of dendrites in auditory coincidence detection. *Nature*, 393(6682):268–272, 1998. pages 43, 48

[23] M. Ahissar, E. Ahissar, H. Bergman, and E. Vaadia. Encoding of sound-source location and movement: activity of single neurons and interactions between adjacent neurons in the monkey auditory cortex. *Journal of Neurophysiology*, 67(1):203–215, 1992. pages 3

[24] R. Ahrons. Superconductive associative memories. *RCA REVIEW*, 24(3):325–354, 1963. pages 9

[25] B. Akgün. *Identification of periodic autoregressive moving average models*. METU, 2003. pages 61

[26] A. Albano, N. Abraham, G. De Guzman, M. Tarroja, D. Bandy, R. Gioggia, P. Rapp, I. Zimmerman, N. Greenbaun, and T. Bashore. Lasers and brains: complex systems with low-dimensional attractors. In *Dimensions and entropies in chaotic systems*, pages 231–240. Springer, 1986. pages 14

[27] A. M. Albano, J. Muench, C. Schwartz, A. Mees, and P. Rapp. Singular-value decomposition and the grassberger-procaccia algorithm. *Physical Review A*, 38(6):3017, 1988. pages 99, 109

[28] R. Albert and A.-L. Barabási. Statistical mechanics of complex networks. *Reviews of modern physics*, 74(1):47, 2002. pages 8

[29] R. Albert, H. Jeong, and A.-L. Barabási. Error and attack tolerance of complex networks. *nature*, 406(6794):378–382, 2000. pages 185, 186

[30] M. Alegre, I. Gurtubay, A. Labarga, J. Iriarte, M. Valencia, and J. Artieda. Frontal and central oscillatory changes related to different aspects of the motor process: a study in go/no-go paradigms. *Experimental Brain Research*, 159(1):14–22, 2004. pages 14

[31] M. Alegre, A. Labarga, I. Gurtubay, J. Iriarte, A. Malanda, and J. Artieda. Movement-related changes in cortical oscillatory activity in ballistic, sustained and negative movements. *Experimental Brain Research*, 148(1):17–25, 2003. pages 14

[32] A. P. Alivisatos, M. Chun, G. M. Church, R. J. Greenspan, M. L. Roukes, and R. Yuste. The brain activity map project and the challenge of functional connectomics. *Neuron*, 74(6):970–974, 2012. pages 17

[33] E. Almaas, R. Kulkarni, and D. Stroud. Scaling properties of random walks on small-world networks. *Physical Review E*, 68(5):056105, 2003. pages 187

[34] G. Almazan, P. Honegger, J.-M. Matthieu, and B. Guentert-Lauber. Epidermal growth factor and bovine growth hormone stimulate differentiation and myelination of brain cell aggregates in culture. *Developmental Brain Research*, 21(2):257–264, 1985. pages 23, 198

[35] U. Alon, M. G. Surette, N. Barkai, and S. Leibler. Robustness in bacterial chemotaxis. *Nature*, 397(6715):168–171, 1999. pages 181

[36] E. Alvarez-Lacalle and E. Moses. Slow and fast pulses in 1-d cultures of excitatory neurons. *Journal of computational neuroscience*, 26(3):475–493, 2009. pages 41, 47, 53, 56

[37] B. Amirikian and A. P. Georgopoulos. Modular organization of directionally tuned cells in the motor cortex: is there a short-range order? *Proceedings of the National Academy of Sciences*, 100(21):12474–12479, 2003. pages 6

[38] D. J. Amit. *Modeling brain function: The world of attractor neural networks*. Cambridge University Press, 1992. pages 181

[39] R. G. Andrzejak, K. Lehnertz, F. Mormann, C. Rieke, P. David, and C. E. Elger. Indications of nonlinear deterministic and finite-dimensional structures in time series of brain electrical activity: Dependence on recording region and brain state. *Physical Review E*, 64(6):061907, 2001. pages 14, 147

[40] A. Arenas, A. Díaz-Guilera, J. Kurths, Y. Moreno, and C. Zhou. Synchronization in complex networks. *Physics Reports*, 469(3):93–153, 2008. pages 197

[41] J. Argyris, H. Maria, and G. Faust. *An exploration of chaos*. North-Holland, 1994. pages 110

[42] J. Argyris, H. Maria, and G. Faust. *An exploration of chaos*. North-Holland, 1994. pages 116

[43] M. Armstrong-James and R. Johnson. Quantitative studies of postnatal changes in synapses in rat superficial motor cerebral cortex. *Zeitschrift für Zellforschung und mikroskopische Anatomie*, 110(4):559–568, 1970. pages 5

[44] G. A. Ascoli, J. L. Krichmar, R. Scorcioni, S. J. Nasuto, S. L. Senft, and G. Krichmar. Computer generation and quantitative morphometric analysis of virtual neurons. *Anatomy and Embryology*, 204(4):283–301, 2001. pages 43

[45] F. Auger, P. Flandrin, P. Gonçalvès, and O. Lemoine. Time-frequency toolbox. *CNRS France-Rice University*, page 46, 1996. pages 61, 66

[46] A. Babloyantz. Strange attractors in the dynamics of brain activity. In *Complex systemsOperational approaches in neurobiology, physics, and computers*, pages 116–122. Springer, 1985. pages 14

[47] A. Babloyantz and A. Destexhe. Low-dimensional chaos in an instance of epilepsy. *Proceedings of the National Academy of Sciences*, 83(10):3513–3517, 1986. pages 14, 17, 147

[48] A. Babloyantz and A. Destexhe. Strange attractors in the human cortex. In *Temporal disorder in human oscillatory systems*, pages 48–56. Springer, 1987. pages 14

[49] A. Babloyantz and A. Destexhe. The creutzfeld-jakob disease in the hierarchy of chaotic attractors. In *From chemical to biological organization*, pages 307–316. Springer, 1988. pages 14, 147

[50] A. Babloyantz, J. Salazar, and C. Nicolis. Evidence of chaotic dynamics of brain activity during the sleep cycle. *Physics Letters A*, 111(3):152–156, 1985. pages 14, 147

[51] P. Bak et al. How nature works: the science of self-organized criticality. *Nature*, 383(6603):772–773, 1996. pages 11

[52] P. Bak, C. Tang, and K. Wiesenfeld. Self-organized criticality: An explanation of the 1/f noise. *Physical review letters*, 59(4):381, 1987. pages 11

[53] J. R. Banavar, F. Colaiori, A. Flammini, A. Maritan, and A. Rinaldo. Topology of the fittest transportation network. *Physical Review Letters*, 84(20):4745, 2000. pages 190

[54] A.-L. Barabási and R. Albert. Emergence of scaling in random networks. *science*, 286(5439):509–512, 1999. pages 184

[55] A.-L. Barabási, R. Albert, and H. Jeong. Mean-field theory for scale-free random networks. *Physica A: Statistical Mechanics and its Applications*, 272(1):173–187, 1999. pages 181

[56] M. Barahona and L. M. Pecora. Synchronization in small-world systems. *Physical review letters*, 89(5):054101, 2002. pages 185, 186, 188, 197

[57] M. N. Barber and B. Ninham. Random walks and restricted walks. *Gordon and Breach, New York*, 1970. pages 187

[58] W. A. Barnett, A. R. Gallant, M. J. Hinich, J. A. Jungeilges, D. T. Kaplan, and M. J. Jensen. A single-blind controlled competition among tests for nonlinearity and chaos. *Journal of econometrics*, 82(1):157–192, 1997. pages 128

[59] A. Barrat, A. Barabasi, G. Caldarelli, P. De los Rios, A. Erzan, B. Kahng, R. Mantegna, J. Mendes, R. Pastor-Satorras, A. Vespignani, et al. Virtual round table on ten leading questions for network research. *European Physical Journal B*, 38(EPFL-ARTICLE-147435):143–145, 2004. pages 187

[60] E. Bartfeld and A. Grinvald. Relationships between orientation-preference pinwheels, cytochrome oxidase blobs, and ocular-dominance columns in primate striate cortex. *Proceedings of the National Academy of Sciences*, 89(24):11905–11909, 1992. pages 3

[61] E. Basar, C. Basar-Eroglu, J. Roschke, and J. Schult. Chaos-and alpha-preparation in brain function. 1989. pages 14

[62] E. Başar, C. Başar-Eroglu, J. Röschke, and J. Schult. Strange attractor eeg as sign of cognitive function. In *Machinery of the Mind*, pages 91–114. Springer, 1990. pages 15

[63] D. S. Bassett and E. Bullmore. Small-world brain networks. *The neuroscientist*, 12(6):512–523, 2006. pages 168

[64] J. Bastian and J. Nguyenkim. Dendritic modulation of burst-like firing in sensory neurons. *Journal of Neurophysiology*, 85(1):10–22, 2001. pages 45

[65] C. Beaulieu. Numerical data on neocortical neurons in adult rat, with special reference to the gaba population. *Brain research*, 609(1):284–292, 1993. pages 22

[66] C. Beaulieu and M. Colonnier. The number of neurons in the different laminae of the binocular and monocular regions of area 17 in the cat. *Journal of Comparative Neurology*, 217(3):337–344, 1983. pages 22

[67] J. M. Beggs and D. Plenz. Neuronal avalanches in neocortical circuits. *The Journal of neuroscience*, 23(35):11167–11177, 2003. pages 11

[68] J. M. Beggs and D. Plenz. Neuronal avalanches are diverse and precise activity patterns that are stable for many hours in cortical slice cultures. *The Journal of neuroscience*, 24(22):5216–5229, 2004. pages 156

[69] J. M. Bekkers and C. F. Stevens. Chapter two different ways evolution makes neurons larger. *Progress in brain research*, 83:37–45, 1990. pages 5

[70] Y. Ben-Ari. Excitatory actions of gaba during development: the nature of the nurture. *Nature Reviews Neuroscience*, 3(9):728–739, 2002. pages 22, 71

[71] H. Berger. Über das elektrenkephalogramm des menschen. *European Archives of Psychiatry and Clinical Neuroscience*, 87(1):527–570, 1929. pages 12

[72] M. Bernot, V. Caselles, and J.-M. Morel. *Optimal transportation networks: models and theory*, volume 1955. Springer Science & Business Media, 2009. pages 190

[73] N. Bertschinger and T. Natschläger. Real-time computation at the edge of chaos in recurrent neural networks. *Neural computation*, 16(7):1413–1436, 2004. pages 10

[74] L. M. Bettencourt, G. J. Stephens, M. I. Ham, and G. W. Gross. Functional structure of cortical neuronal networks grown in vitro. *Physical Review E*, 75(2):021915, 2007. pages 181

[75] R. L. Beurle. Properties of a mass of cells capable of regenerating pulses. *Philosophical Transactions of the Royal Society of London B: Biological Sciences*, 240(669):55–94, 1956. pages 188

[76] G.-q. Bi and M.-m. Poo. Distributed synaptic modification in neural networks induced by patterned stimulation. *Nature*, 401(6755):792–796, 1999. pages 23

[77] G. Bianconi. The entropy of randomized network ensembles. *EPL (Europhysics Letters)*, 81(2):28005, 2007. pages 183, 184, 197

[78] G. Bianconi. Entropy of network ensembles. *Physical Review E*, 79(3):036114, 2009. pages 183, 184, 197

[79] D. K. Bilkey and P. A. Schwartzkroin. Variation in electrophysiology and morphology of hippocampal ca3 pyramidal cells. *Brain research*, 514(1):77–83, 1990. pages 45

[80] A. Björklund and F. H. Gage. Neural grafting in animal models of neurodegenerative diseases. *Annals of the New York Academy of Sciences*, 457(1):53–81, 1985. pages 22

[81] A. G. Blankenship and M. B. Feller. Mechanisms underlying spontaneous patterned activity in developing neural circuits. *Nature Reviews Neuroscience*, 11(1):18–29, 2010. pages 17

[82] S. Boccaletti, V. Latora, Y. Moreno, M. Chavez, and D.-U. Hwang. Complex networks: Structure and dynamics. *Physics reports*, 424(4):175–308, 2006. pages 8

[83] M. Boguná and R. Pastor-Satorras. Epidemic spreading in correlated complex networks. *Physical Review E*, 66(4):047104, 2002. pages 185

[84] M. Boguná, R. Pastor-Satorras, and A. Vespignani. Absence of epidemic threshold in scale-free networks with degree correlations. *Physical review letters*, 90(2):028701, 2003. pages 185

[85] M. Boguná, R. Pastor-Satorras, and A. Vespignani. Epidemic spreading in complex networks with degree correlations. *arXiv preprint cond-mat/0301149*, 1, 2003. pages 189

[86] S. Bohn and M. O. Magnasco. Structure, scaling, and phase transition in the optimal transport network. *Physical review letters*, 98(8):088702, 2007. pages 190

[87] B. Bollobás. Random graphs. In *Modern Graph Theory*, pages 215–252. Springer, 1998. pages 187

[88] P. Bonifazi, M. Goldin, M. A. Picardo, I. Jorquera, A. Cattani, G. Bianconi, A. Represa, Y. Ben-Ari, and R. Cossart. Gabaergic hub neurons orchestrate synchrony in developing hippocampal networks. *Science*, 326(5958):1419–1424, 2009. pages 181

[89] J. Born, B. Rasch, and S. Gais. Sleep to remember. *The Neuroscientist*, 12(5):410–424, 2006. pages 17

[90] S. E. Boustani and A. Destexhe. Does brain activity stem from high-dimensional chaotic dynamics? evidence from the human electroencephalogram, cat cerebral cortex and artificial neuronal networks. *arXiv preprint arXiv:0904.4217*, 2009. pages 15, 16

[91] J. M. Bower and D. Beeman. *The book of GENESIS: exploring realistic neural models with the GEneral NEural SImulation System*. Springer Science & Business Media, 2012. pages 43, 45

[92] G. E. Box and G. M. Jenkins. Series analysis forecasting and control. *Holden-Day, San Francisco*, page 575, 1976. pages 60

[93] V. Braitenberg and A. Schüz. Anatomy of the cortex: Statistics and geometry (vol. 18), 1991. pages 180

[94] V. Braitenberg and A. Schüz. *Cortex: statistics and geometry of neuronal connectivity*. Springer Science & Business Media, 2013. pages 5

[95] M. Brede and S. Sinha. Assortative mixing by degree makes a network more unstable. *arXiv preprint cond-mat/0507710*, 2005. pages 186, 188

[96] I. Breskin, J. Soriano, E. Moses, and T. Tlusty. Percolation in living neural networks. *Physical review letters*, 97(18):188102, 2006. pages 24, 175, 177

[97] S. L. Bressler. Large-scale cortical networks and cognition. *Brain Research Reviews*, 20(3):288–304, 1995. pages 3

[98] S. L. Bressler and W. J. Freeman. Frequency analysis of olfactory system eeg in cat, rabbit, and rat. *Electroencephalography and clinical neurophysiology*, 50(1):19–24, 1980. pages 8

[99] W. A. Brock. Distinguishing random and deterministic systems: Abridged version. *Journal of economic theory*, 40(1):168–195, 1986. pages 125

[100] P. J. Brockwell and R. A. Davis. Introduction. In *Introduction to Time Series and Forecasting*, pages 1–42. Springer, 1996. pages 88

[101] D. Broomhead and G. P. King. Extracting qualitative dynamics from experimental data. *Physica D: Nonlinear Phenomena*, 20(2):217–236, 1986. pages 88, 92, 99, 106, 108, 110

[102] P. Brown. Oscillatory nature of human basal ganglia activity: relationship to the pathophysiology of parkinson's disease. *Movement Disorders*, 18(4):357–363, 2003. pages 14

[103] J. F. Brugge and M. M. Merzenich. Response of neurons in auditory cortex of the macaque monkey to monaural and binaural stimulation. *Journal of Neurophysiology*, 1973. pages 3

[104] E. Bullmore and O. Sporns. Complex brain networks: graph theoretical analysis of structural and functional systems. *Nature Reviews Neuroscience*, 10(3):186–198, 2009. pages 17

[105] E. T. Bullmore and D. S. Bassett. Brain graphs: graphical models of the human brain connectome. *Annual review of clinical psychology*, 7:113–140, 2011. pages 168

[106] A. B. Butler and W. Hoods. Brain structures.(book reviews: Comparative vertebrate neuroanatomy. evolution and adaptation.). *Science*, 274:521–522, 1996. pages 4

[107] G. Buzsáki. Two-stage model of memory trace formation: a role for noisy brain states. *Neuroscience*, 31(3):551–570, 1989. pages 17

[108] G. Buzsáki and A. Draguhn. Neuronal oscillations in cortical networks. *science*, 304(5679):1926–1929, 2004. pages 12

[109] G. Buzsáki, C. Geisler, D. A. Henze, and X.-J. Wang. Interneuron diversity series: circuit complexity and axon wiring economy of cortical interneurons. *Trends in neurosciences*, 27(4):186–193, 2004. pages 181

[110] A. Q. Cai, K. A. Landman, and B. D. Hughes. Modelling directional guidance and motility regulation in cell migration. *Bulletin of mathematical biology*, 68(1):25–52, 2006. pages 43

[111] R. Y. Cajal. Histologie du système nerveux de l'homme et des vertébrés. *Journal of Neuropathology and Experimental Neurology*, 57(9):883–883, 1998. pages 1, 4, 5, 7, 43, 45

[112] G. Caldarelli, R. Marchetti, and L. Pietronero. The fractal properties of internet. *EPL (Europhysics Letters)*, 52(4):386, 2000. pages 181

[113] D. S. Callaway, J. E. Hopcroft, J. M. Kleinberg, M. E. Newman, and S. H. Strogatz. Are randomly grown graphs really random? *Physical Review E*, 64(4):041902, 2001. pages 185

[114] D. S. Callaway, M. E. Newman, S. H. Strogatz, and D. J. Watts. Network robustness and fragility: Percolation on random graphs. *Physical review letters*, 85(25):5468, 2000. pages 185, 186

[115] E. M. Callaway and L. C. Katz. Emergence and refinement of clustered horizontal connections in cat striate cortex. *The Journal of Neuroscience*, 10(4):1134–1153, 1990. pages 6

[116] L. Cao. Practical method for determining the minimum embedding dimension of a scalar time series. *Physica D: Nonlinear Phenomena*, 110(1):43–50, 1997. pages 102, 103, 133, 194

[117] J. Caputo, B. Malraison, and P. Atten. Determination of attractor dimension and entropy for various flows: An experimentalists viewpoint. In *Dimensions and Entropies in Chaotic Systems*, pages 180–190. Springer, 1986. pages 109

[118] S. Carmi, Z. Wu, S. Havlin, and H. E. Stanley. Transport in networks with multiple sources and sinks. *EPL (Europhysics Letters)*, 84(2):28005, 2008. pages 187

[119] S. Carmi, Z. Wu, S. Havlin, and H. E. Stanley. Transport in networks with multiple sources and sinks. *EPL (Europhysics Letters)*, 84(2):28005, 2008. pages 189

[120] M. Casdagli. Recurrence plots revisited. *Physica D: Nonlinear Phenomena*, 108(1-2):12–44, 1997. pages 116

[121] M. Casdagli, S. Eubank, J. D. Farmer, and J. Gibson. State space reconstruction in the presence of noise. *Physica D: Nonlinear Phenomena*, 51(1):52–98, 1991. pages 90, 97, 110

[122] M. Catanzaro, G. Caldarelli, and L. Pietronero. Assortative model for social networks. *Physical Review E*, 70(3):037101, 2004. pages 184

[123] B. Cessac. A discrete time neural network model with spiking neurons. *Journal of Mathematical Biology*, 56(3):311–345, 2008. pages 146

[124] B. Cessac and T. Viéville. On dynamics of integrate-and-fire neural networks with conductance based synapses. *arXiv preprint arXiv:0709.4370*, 2007. pages 146

[125] M. Chavez, D.-U. Hwang, J. Martinerie, and S. Boccaletti. Degree mixing and the enhancement of synchronization in complex weighted networks. *Physical Review E*, 74(6):066107, 2006. pages 185

[126] M. Chavez, M. Valencia, V. Latora, and J. Martinerie. Complex networks: new trends for the analysis of brain connectivity. *International Journal of Bifurcation and Chaos*, 20(06):1677–1686, 2010. pages 181

[127] M. Chavez, M. Valencia, V. Navarro, V. Latora, and J. Martinerie. Functional modularity of background activities in normal and epileptic brain networks. *Physical review letters*, 104(11):118701, 2010. pages 17

[128] G. Chechik, I. Meilijson, and E. Ruppin. Synaptic pruning in development: a computational account. *Neural computation*, 10(7):1759–1777, 1998. pages 182

[129] G. Chechik, I. Meilijson, and E. Ruppin. Neuronal regulation: A mechanism for synaptic pruning during brain maturation. *Neural Computation*, 11(8):2061–2080, 1999. pages 182

[130] B. L. Chen, D. H. Hall, and D. B. Chklovskii. Wiring optimization can relate neuronal structure and function. *Proceedings of the National Academy of Sciences of the United States of America*, 103(12):4723–4728, 2006. pages 5

[131] D.-M. Chen, S. Wu, A. Guo, and Z. Yang. Self-organized criticality in a cellular automaton model of pulse-coupled integrate-and-fire neurons. *Journal of physics A: mathematical and general*, 28(18):5177, 1995. pages 11

[132] S.-Y. C. Chen, P. J. Hung, and P. J. Lee. Microfluidic array for three-dimensional perfusion culture of human mammary epithelial cells. *Biomedical microdevices*, 13(4):753–758, 2011. pages 197

[133] C. Cherniak, Z. Mokhtarzada, R. Rodriguez-Esteban, and K. Changizi. Global optimization of cerebral cortex layout. *Proceedings of the National Academy of Sciences of the United States of America*, 101(4):1081–1086, 2004. pages 6, 183

[134] M. Chiappalone, M. Bove, A. Vato, M. Tedesco, and S. Martinoia. Dissociated cortical networks show spontaneously correlated activity patterns during in vitro development. *Brain research*, 1093(1):41–53, 2006. pages 85, 181, 188

[135] M. Chicurel. Databasing the brain. *Nature*, 406(6798):822–825, 2000. pages 17

[136] D. B. Chklovskii, T. Schikorski, and C. F. Stevens. Wiring optimization in cortical circuits. *Neuron*, 34(3):341–347, 2002. pages 5

[137] A. Church. An unsolvable problem of elementary number theory. *American journal of mathematics*, 58(2):345–363, 1936. pages ii, 10

[138] H. T. Cline. Dendritic arbor development and synaptogenesis. *Current opinion in neurobiology*, 11(1):118–126, 2001. pages 48

[139] D. Cohen and M. Segal. Network bursts in hippocampal microcultures are terminated by exhaustion of vesicle pools. *Journal of neurophysiology*, 106(5):2314–2321, 2011. pages 56, 73

[140] E. Cohen, M. Ivenshitz, V. Amor-Baroukh, V. Greenberger, and M. Segal. Determinants of spontaneous activity in networks of cultured hippocampus. *Brain research*, 1235:21–30, 2008. pages 21

[141] L. Cohen. *Time-frequency analysis*, volume 778. Prentice Hall PTR Englewood Cliffs, NJ:, 1995. pages 67, 68

[142] O. Cohen, A. Keselman, E. Moses, M. R. Martínez, J. Soriano, and T. Tlusty. Quorum percolation in living neural networks. *EPL (Europhysics Letters)*, 89(1):18008, 2010. pages 24, 180

[143] R. Cohen, K. Erez, D. Ben-Avraham, and S. Havlin. Resilience of the internet to random breakdowns. *Physical review letters*, 85(21):4626, 2000. pages 185, 186

[144] R. Cohen, K. Erez, D. Ben-Avraham, and S. Havlin. Breakdown of the internet under intentional attack. *Physical review letters*, 86(16):3682, 2001. pages 185, 186

[145] S. A. Colamarino and M. Tessier-Lavigne. The axonal chemoattractant netrin-1 is also a chemorepellent for trochlear motor axons. *Cell*, 81(4):621–629, 1995. pages 51

[146] M. A. Colicos and N. I. Syed. Neuronal networks and synaptic plasticity: understanding complex system dynamics by interfacing neurons with silicon technologies. *Journal of experimental biology*, 209(12):2312–2319, 2006. pages 21

[147] J. Collins, T. T. Imhoff, and P. Grigg. Noise-mediated enhancements and decrements in human tactile sensation. *Physical Review E*, 56(1):923, 1997. pages 16

[148] J. J. Collins, T. T. Imhoff, and P. Grigg. Noise-enhanced information transmission in rat sa1 cutaneous mechanoreceptors via aperiodic stochastic resonance. *Journal of Neurophysiology*, 76(1):642–645, 1996. pages 16

[149] F. Corson. Fluctuations and redundancy in optimal transport networks. *Physical Review Letters*, 104(4):048703, 2010. pages 191

[150] L. d. F. Costa. Actively-induced percolation: An effective approach to multiple-object systems characterization. *arXiv preprint cond-mat/0404310*, 2004. pages 184, 198

[151] L. d. F. Costa. Morphological complex networks: Can individual morphology determine the general connectivity and dynamics of networks? *arXiv preprint q-bio/0503041*, 2005. pages 184, 198

[152] L. d. F. Costa and M. S. Barbosa. An analytical approach to neuronal connectivity. *The European Physical Journal B-Condensed Matter and Complex Systems*, 42(4):573–580, 2004. pages 184

[153] B. Cragg. The density of synapses and neurones in the motor and visual areas of the cerebral cortex. *Journal of Anatomy*, 101(Pt 4):639, 1967. pages 180

[154] B. G. Cragg. The density of synapses and neurons in normal, mentally defective ageing human brains. *Brain: a journal of neurology*, 98(1):81–90, 1975. pages 5

[155] B. G. Cragg. The development of synapses in the visual system of the cat. *Journal of Comparative Neurology*, 160(2):147–166, 1975. pages 5

[156] J. D. Cryer and N. Kellet. *Time series analysis*, volume 101. Springer, 1986. pages 60

[157] H. Cuntz. The dendritic density field of a cortical pyramidal cell. *Frontiers in Neuroanatomy*, 6:2, 2012. pages 47

[158] H. Cuntz, A. Borst, and I. Segev. Optimization principles of dendritic structure. *Theoretical Biology and Medical Modelling*, 4(1):1, 2007. pages 43, 45

[159] H. Cuntz, F. Forstner, A. Borst, and M. Häusser. One rule to grow them all: a general theory of neuronal branching and its practical application. *PLoS Comput Biol*, 6(8):e1000877, 2010. pages 43, 45

[160] H. Cuntz, F. Forstner, A. Borst, and M. Häusser. The trees toolboxprobing the basis of axonal and dendritic branching. *Neuroinformatics*, 9(1):91–96, 2011. pages 43

[161] H. Cuntz, F. Forstner, J. Haag, and A. Borst. The morphological identity of insect dendrites. *PLoS Comput Biol*, 4(12):e1000251, 2008. pages 43, 45

[162] L. da Fontoura Costa and R. C. Coelho. Growth-driven percolations: the dynamics of connectivity in neuronal systems. *The European Physical Journal B-Condensed Matter and Complex Systems*, 47(4):571–581, 2005. pages 43

[163] L. da Fontoura Costa and E. T. M. Manoel. A percolation approach to neural morphometry and connectivity. *Neuroinformatics*, 1(1):65–80, 2003. pages 184, 198

[164] F. L. Da Silva, J. Pijn, D. Velis, and P. Nijssen. Alpha rhythms: noise, dynamics and models. *International Journal of Psychophysiology*, 26(1):237–249, 1997. pages 147

[165] A. R. Damasio. The brain binds entities and events by multiregional activation from convergence zones. *Neural Computation*, 1(1):123–132, 1989. pages 6

[166] A. R. Damasio. Synchronous activation in multiple cortical regions: a mechanism for recall. 1990. pages 6

[167] A. R. Damasio. Time-locked multiregional retroactivation: a systems-level proposal for the neural substrates of recall and recognition, neurobiology of cognition, 1990. pages 6

[168] A. R. Damasio and H. Damasio. Brain and language. *Scientific American*, 267(3):88–95, 1992. pages 6

[169] E. Dauce, M. Quoy, B. Cessac, B. Doyon, and M. Samuelides. Self-organization and dynamics reduction in recurrent networks: stimulus presentation and learning. *Neural networks*, 11(3):521–533, 1998. pages 15

[170] L. de Arcangelis, C. Perrone-Capano, and H. J. Herrmann. Self-organized criticality model for brain plasticity. *Physical review letters*, 96(2):028107, 2006. pages 11

[171] S. de Franciscis, S. Johnson, and J. J. Torres. Enhancing neural-network performance via assortativity. *Physical Review E*, 83(3):036114, 2011. pages 184, 185, 186, 197

[172] W. de Haan, Y. A. Pijnenburg, R. L. Strijers, Y. van der Made, W. M. van der Flier, P. Scheltens, and C. J. Stam. Functional neural network analysis in frontotemporal dementia and alzheimer's disease using eeg and graph theory. *BMC neuroscience*, 10(1):1, 2009. pages 181

[173] R. L. de Nó. *La corteza cerebral del ratón:(Primera contribución.-La corteza acústica)*. Tipografía Artística, 1922. pages ii, 7

[174] M. De Roo, P. Klauser, P. Mendez, L. Poglia, and D. Muller. Activity-dependent psd formation and stabilization of newly formed spines in hippocampal slice cultures. *Cerebral cortex*, 18(1):151–161, 2008. pages 182

[175] E. De Schutter. *Computational neuroscience: realistic modeling for experimentalists*. CRC Press, 2000. pages 43

[176] E. De Schutter and J. M. Bower. An active membrane model of the cerebellar purkinje cell. i. simulation of current clamps in slice. *Journal of neurophysiology*, 71(1):375–400, 1994. pages 45

[177] D. J. de Solla Price. The pattern of bibliographic references indicates the nature of the scientific research front. *Social Networks: Critical Concepts in Sociology*, 4:328, 2002. pages 184

[178] D. Debanne. Information processing in the axon. *Nature Reviews Neuroscience*, 5(4):304–316, 2004. pages 43, 48

[179] D. Debanne, B. H. Gähwiler, and S. M. Thompson. Long-term synaptic plasticity between pairs of individual ca3 pyramidal cells in rat hippocampal slice cultures. *The Journal of Physiology*, 507(1):237–247, 1998. pages 7

[180] G. Deco, V. K. Jirsa, and A. R. McIntosh. Emerging concepts for the dynamical organization of resting-state activity in the brain. *Nature Reviews Neuroscience*, 12(1):43–56, 2011. pages 17

[181] K. R. Delaney, R. S. Zucker, and D. W. Tank. Calcium in motor nerve terminals associated with posttetanic potentiation. *The Journal of Neuroscience*, 9(10):3558–3567, 1989. pages 31

[182] W. Denk, J. H. Strickler, and W. W. Webb. Two-photon laser scanning fluorescence microscopy. *Science*, 248(4951):73–76, 1990. pages 31

[183] E. W. Dent and F. B. Gertler. Cytoskeletal dynamics and transport in growth cone motility and axon guidance. *Neuron*, 40(2):209–227, 2003. pages 51

[184] B. Derrida. Dynamical phase transition in nonsymmetric spin glasses. *Journal of Physics A: Mathematical and General*, 20(11):L721, 1987. pages 11

[185] B. Derrida, E. Gardner, and A. Zippelius. An exactly solvable asymmetric neural network model. *EPL (Europhysics Letters)*, 4(2):167, 1987. pages 11

[186] B. Derrida and Y. Pomeau. Random networks of automata: a simple annealed approximation. *EPL (Europhysics Letters)*, 1(2):45, 1986. pages 11

[187] A. Destexhe. *Nonlinear dynamics of the rhythmical activity of the brain*. PhD thesis, Doctoral Dissertation, Free University of Brussels, Belgium, 1992. pages 16

[188] A. Destexhe and M. Rudolph. Extracting information from the power spectrum of synaptic noise. *Journal of computational neuroscience*, 17(3):327–345, 2004. pages 84

[189] A. Destexhe, J. Sepulchre, and A. Babloyantz. A comparative study of the experimental quantification of deterministic chaos. *Physics letters A*, 132(2-3):101–106, 1988. pages 17, 147

[190] M. di Bernardo, F. Garofalo, and F. Sorrentino. Synchronizability and synchronization dynamics of weighed and unweighed scale free networks with degree mixing. *arXiv preprint cond-mat/0504335*, 2005. pages 186, 188, 197

[191] E. W. Dijkstra. A note on two problems in connexion with graphs. *Numerische mathematik*, 1(1):269–271, 1959. pages 159

[192] C. Diks. *Nonlinear time series analysis: methods and applications*, volume 4. World Scientific, 1999. pages 90

[193] C. Diks, J. Van Houwelingen, F. Takens, and J. DeGoede. Reversibility as a criterion for discriminating time series. *Physics Letters A*, 201(2):221–228, 1995. pages 127

[194] J. Douglass, L. Wilkens, E. Pantazelou, and F. Moss. Stochastic resonance: noise-enhanced information transfer in crayfish mechanoreceptors. *Nature*, 365:337, 1993. pages 16

[195] J. H. Downes, M. W. Hammond, D. Xydas, M. C. Spencer, V. M. Becerra, K. Warwick, B. J. Whalley, and S. J. Nasuto. Emergence of a small-world functional network in cultured neurons. *PLoS Comput Biol*, 8(5):e1002522, 2012. pages 181

[196] L. Dugan, V. Bruno, S. Amagasu, and R. Giffard. Glia modulate the response of murine cortical neurons to excitotoxicity: glia exacerbate ampa neurotoxicity. *The Journal of neuroscience*, 15(6):4545–4555, 1995. pages 22

[197] J. Duijnhouwer, M. W. Remme, A. Van Ooyen, and J. van Pelt. Influence of dendritic topology on firing patterns in model neurons. *Neurocomputing*, 38:183–189, 2001. pages 43

[198] A. Dunaevsky, A. Tashiro, A. Majewska, C. Mason, and R. Yuste. Developmental regulation of spine motility in the mammalian central nervous system. *Proceedings of the National Academy of Sciences*, 96(23):13438–13443, 1999. pages 45

[199] S. B. Dunnett and A. Björklund. *Functional neural transplantation II: novel cell therapies for CNS disorders*. Elsevier, 2000. pages 22

[200] M. Durand. Structure of optimal transport networks subject to a global constraint. *Physical Review Letters*, 98(8):088701, 2007. pages 190

[201] I. Dvorak, J. Siska, J. Wackermann, L. Hrudova, and C. Dostalek. Evidence for interpretation of the eeg as a deterministic chaotic process with a low dimension. *Activitas Nervosa Superior*, 28(3):228–231, 1986. pages 14

[202] A. Dvoretzky and P. Erdös. Some problems on random walk in space. In *Proc. 2nd Berkeley Symp*, pages 353–367, 1951. pages 187

[203] T. Ebendal and C.-O. Jacobson. Tissue explants affecting extension and orientation of axons in cultured chick embryo ganglia. *Experimental cell research*, 105(2):379–387, 1977. pages 51

[204] J.-P. Eckmann, O. Feinerman, L. Gruendlinger, E. Moses, J. Soriano, and T. Tlusty. The physics of living neural networks. *Physics Reports*, 449(1):54–76, 2007. pages 18, 21, 84, 89

[205] J.-P. Eckmann, S. O. Kamphorst, and D. Ruelle. Recurrence plots of dynamical systems. *Europhys. Lett*, 4(9):973–977, 1987. pages 110, 111, 113, 117

[206] J.-P. Eckmann, E. Moses, O. Stetter, T. Tlusty, and C. Zbinden. Leaders of neuronal cultures in a quorum percolation model. *arXiv preprint arXiv:1009.5355*, 2010. pages 188

[207] B. Efron. Computers and the theory of statistics: thinking the unthinkable. *SIAM review*, 21(4):460–480, 1979. pages 161

[208] V. M. Eguiluz, D. R. Chialvo, G. A. Cecchi, M. Baliki, and A. V. Apkarian. Scale-free brain functional networks. *Physical review letters*, 94(1):018102, 2005. pages 6, 183

[209] V. M. Eguiluz and K. Klemm. Epidemic threshold in structured scale-free networks. *Physical Review Letters*, 89(10):108701, 2002. pages 185

[210] S. El Boustani, O. Marre, S. Béhuret, P. Baudot, P. Yger, T. Bal, A. Destexhe, and Y. Frégnac. Network-state modulation of power-law frequency-scaling in visual cortical neurons. *PLoS Comput Biol*, 5(9):e1000519, 2009. pages 84

[211] T. Elbert, W. Lutzenberger, B. Rockstroh, P. Berg, and R. Cohen. Physical aspects of the eeg in schizophrenics. *Biological psychiatry*, 32(7):595–606, 1992. pages 14, 147

[212] T. Elbert, W. J. Ray, Z. J. Kowalik, J. E. Skinner, K. E. Graf, and N. Birbaumer. Chaos and physiology: deterministic chaos in excitable cell assemblies. *Physiological Reviews*, 74(1):1–47, 1994. pages 14

[213] P. Erdi. Structures, forms, patterns and perception: A brain-theoretic point of view. In *Symmetries in Science IV*, pages 29–52. Springer, 1990. pages 52

[214] G. B. Ermentrout and N. Kopell. Parabolic bursting in an excitable system coupled with a slow oscillation. *SIAM Journal on Applied Mathematics*, 46(2):233–253, 1986. pages 46

[215] C. W. Eurich, J. M. Herrmann, and U. A. Ernst. Finite-size effects of avalanche dynamics. *Physical review E*, 66(6):066137, 2002. pages 11

[216] D. Eytan and S. Marom. Dynamics and effective topology underlying synchronization in networks of cortical neurons. *The Journal of neuroscience*, 26(33):8465–8476, 2006. pages 181, 188

[217] L. Faes, G. Nollo, and A. Porta. Information-based detection of nonlinear granger causality in multivariate processes via a nonuniform embedding technique. *Physical Review E*, 83(5):051112, 2011. pages 199

[218] P. Faure and H. Korn. A new method to estimate the kolmogorov entropy from recurrence plots: its application to neuronal signals. *Physica D: Nonlinear Phenomena*, 122(1):265–279, 1998. pages 113

[219] S. Feldt, P. Bonifazi, and R. Cossart. Dissecting functional connectivity of neuronal microcircuits: experimental and theoretical insights. *Trends in neurosciences*, 34(5):225–236, 2011. pages 17

[220] D. J. Felleman and D. C. Van Essen. Distributed hierarchical processing in the primate cerebral cortex. *Cerebral cortex*, 1(1):1–47, 1991. pages 6

[221] I. Ferezou, S. Bolea, and C. C. Petersen. Visualizing the cortical representation of whisker touch: voltage-sensitive dye imaging in freely moving mice. *Neuron*, 50(4):617–629, 2006. pages 17

[222] R. D. Fields, E. A. Neale, and P. G. Nelson. Effects of patterned electrical activity on neurite outgrowth from mouse sensory neurons. *Journal of Neuroscience*, 10(9):2950–2964, 1990. pages 198

[223] B. L. Finlay and R. B. Darlington. Linked regularities in the development and evolution of mammalian brains. *Science*, 268(5217):1578, 1995. pages 5

[224] M. Fischer, S. Kaech, D. Knutti, and A. Matus. Rapid actin-based plasticity in dendritic spines. *Neuron*, 20(5):847–854, 1998. pages 45

[225] J. Fiser, P. Berkes, G. Orbán, and M. Lengyel. Statistically optimal perception and learning: from behavior to neural representations. *Trends in cognitive sciences*, 14(3):119–130, 2010. pages 17

[226] M. Fitzgerald, G. C. Kwiat, J. Middleton, and A. Pini. Ventral spinal cord inhibition of neurite outgrowth from embryonic rat dorsal root ganglia. *Development*, 117(4):1377–1384, 1993. pages 51

[227] R. FitzHugh. Mathematical models of threshold phenomena in the nerve membrane. *The bulletin of mathematical biophysics*, 17(4):257–278, 1955. pages 46

[228] E. Frank. Synapse elimination–for nerves it's all or nothing. *Science*, 275(5298):324–325, 1997. pages 182

[229] G. Frank, T. Lookman, M. Nerenberg, C. Essex, J. Lemieux, and W. Blume. Chaotic time series analyses of epileptic seizures. *Physica D: Nonlinear Phenomena*, 46(3):427–438, 1990. pages 17, 147

[230] A. M. Fraser and H. L. Swinney. Independent coordinates for strange attractors from mutual information. *Physical review A*, 33(2):1134, 1986. pages 99, 133, 153, 194

[231] W. Freeman. Dynamics of image formation by nerve cell assemblies. In *Synergetics of the brain*, pages 102–121. Springer, 1983. pages 14

[232] W. Freeman. On the problem of anomalous dispersion in chaoto-chaotic phase transitions of neural masses, and its significance for the management of perceptual information in brains. In *Synergetics of cognition*, pages 126–143. Springer, 1990. pages 14

[233] W. Freeman. *Neurodynamics: an exploration in mesoscopic brain dynamics*. Springer Science & Business Media, 2012. pages 15

[234] W. Freeman and C. Skarda. A perspective on brain theory: nonlinear dynamics of neural masses. *Brain Res. Rev*, 10:147–175, 1985. pages 14

[235] W. J. Freeman. Eeg analysis gives model of neuronal template-matching mechanism for sensory search with olfactory bulb. *Biological Cybernetics*, 35(4):221–234, 1979. pages 14

[236] W. J. Freeman. The physiological basis of mental images. *Biological Psychiatry*, 1983. pages 8, 14

[237] W. J. Freeman. Petit mal seizure spikes in olfactory bulb and cortex caused by runaway inhibition after exhaustion of excitation. *Brain Research Reviews*, 11(3):259–284, 1986. pages 8

[238] W. J. Freeman. How the olfactory system generates its chaotic background spontaneous electroencephalographic and unit activity. *Annals of the New York Academy of Sciences*, 510(1):304–306, 1987. pages 14

[239] W. J. Freeman. Simulation of chaotic eeg patterns with a dynamic model of the olfactory system. *Biological cybernetics*, 56(2-3):139–150, 1987. pages 8, 14

[240] W. J. Freeman. Perceptual processing using oscillatory chaotic dynamics. In *Engineering in Medicine and Biology Society, 1989. Images of the Twenty-First Century., Proceedings of the Annual International Conference of the IEEE Engineering in*, pages 2–AP. IEEE, 1989. pages 8, 14

[241] W. J. Freeman. *How brains make up their minds*. Columbia University Press, 2000. pages 15

[242] W. J. Freeman. A proposed name for aperiodic brain activity: stochastic chaos. *Neural Networks*, 13(1):11–13, 2000. pages 15

[243] W. J. Freeman, L. J. Rogers, M. D. Holmes, and D. L. Silbergeld. Spatial spectral analysis of human electrocorticograms including the alpha and gamma bands. *Journal of neuroscience methods*, 95(2):111–121, 2000. pages 12

[244] W. J. Freeman and C. A. Skarda. Spatial eeg patterns, non-linear dynamics and perception: the neo-sherringtonian view. *Brain Research Reviews*, 10(3):147–175, 1985. pages 8, 14

[245] W. J. Freeman, Y. Yao, and B. Burke. Central pattern generating and recognizing in olfactory bulb: a correlation learning rule. *Neural Networks*, 1(4):277–288, 1988. pages 8

[246] K. J. Fristen. Imaging cognitive anatomy. *Trends in cognitive sciences*, 1(1):21–27, 1997. pages 3

[247] R. C. Froemke, M.-m. Poo, and Y. Dan. Spike-timing-dependent synaptic plasticity depends on dendritic location. *Nature*, 434(7030):221–225, 2005. pages 7

[248] T. M. Fruchterman and E. M. Reingold. Graph drawing by force-directed placement. *Software: Practice and experience*, 21(11):1129–1164, 1991. pages 171, 172, 176

[249] P. Gabbott and P. Somogyi. Quantitative distribution of gaba-immunoreactive neurons in the visual cortex (area 17) of the cat. *Experimental Brain Research*, 61(2):323–331, 1986. pages 22

[250] P. M. Gade and C.-K. Hu. Synchronous chaos in coupled map lattices with small-world interactions. *Physical Review E*, 62(5):6409, 2000. pages 188, 197

[251] F. H. Gage. Neurogenesis in the adult brain. *The Journal of Neuroscience*, 22(3):612–613, 2002. pages 22

[252] D. J. Galas, M. Nykter, G. W. Carter, N. D. Price, and I. Shmulevich. Biological information as set-based complexity. *IEEE Transactions on Information Theory*, 56(2):667–677, 2010. pages 8

[253] L. K. Gallos. Random walk and trapping processes on scale-free networks. *Physical Review E*, 70(4):046116, 2004. pages 187

[254] K. Ganguly, A. F. Schinder, S. T. Wong, and M.-m. Poo. Gaba itself promotes the developmental switch of neuronal gabaergic responses from excitation to inhibition. *Cell*, 105(4):521–532, 2001. pages 22, 71

[255] C. Gantert, J. Honerkamp, and J. Timmer. Analyzing the dynamics of hand tremor time series. *Biological cybernetics*, 66(6):479–484, 1992. pages 125

[256] F.-B. Gao. Molecular and cellular mechanisms of dendritic morphogenesis. *Current opinion in neurobiology*, 17(5):525–532, 2007. pages 48

[257] J. Gao. Recurrence time statistics for chaotic systems and their applications. *Physical Review Letters*, 83(16):3178, 1999. pages 111

[258] J. Gao and Z. Zheng. Direct dynamical test for deterministic chaos and optimal embedding of a chaotic time series. *Physical review E*, 49(5):3807, 1994. pages 111

[259] W.-Q. Gao, N. Heintz, and M. E. Hatten. Cerebellar granule cell neurogenesis is regulated by cell-cell interactions in vitro. *Neuron*, 6(5):705–715, 1991. pages 23, 185

[260] B. B. Garber and A. Moscona. Reconstruction of brain tissue from cell suspensions: Ii. specific enhancement of aggregation of embryonic cerebral cells by supernatant from homologous cell cultures. *Developmental biology*, 27(2):235–243, 1972. pages 23, 185, 198

[261] E. Garcia-Perez, D. C. Lo, and J. F. Wesseling. Kinetic isolation of a slowly recovering component of short-term depression during exhaustive use at excitatory hippocampal synapses. *Journal of neurophysiology*, 100(2):781–795, 2008. pages 56

[262] T. Gautama, D. P. Mandic, and M. M. Van Hulle. A differential entropy based method for determining the optimal embedding parameters of a signal. In *Acoustics, Speech, and Signal Processing, 2003. Proceedings.(ICASSP'03). 2003 IEEE International Conference on*, volume 6, pages VI–29. IEEE, 2003. pages 104, 105, 109, 111, 133, 194

[263] T. Gautama, D. P. Mandic, and M. M. Van Hulle. The delay vector variance method for detecting determinism and nonlinearity in time series. *Physica D: Nonlinear Phenomena*, 190(3):167–176, 2004. pages 128

[264] T. Gautama, M. M. Van Hulle, D. P. Mandic, and K. Leuven. On the characterisation of the deterministic/stochastic and linear/nonlinear nature of time series. *Technical Report DPM-04-5, Imperial College London*, 2004. pages 142

[265] K. R. Gee, K. Brown, W. U. Chen, J. Bishop-Stewart, D. Gray, and I. Johnson. Chemical and physiological characterization of fluo-4 ca 2+-indicator dyes. *Cell calcium*, 27(2):97–106, 2000. pages 33

[266] A. P. Georgopoulos, R. Caminiti, J. F. Kalaska, and J. T. Massey. Spatial coding of movement: a hypothesis concerning the coding of movement direction by motor cortical populations. *Exp Brain Res Suppl*, 7(32):336, 1983. pages 4

[267] A. P. Georgopoulos, M. Taira, and A. Lukashin. Cognitive neurophysiology of the motor cortex. *SCIENCE-NEW YORK THEN WASHINGTON-*, 260:47–47, 1993. pages 4

[268] W. Gerstner and W. M. Kistler. *Spiking neuron models: Single neurons, populations, plasticity*. Cambridge university press, 2002. pages 185

[269] W. Gerstner and J. L. van Hemmen. Associative memory in a network of spikingneurons. *Network: Computation in Neural Systems*, 3(2):139–164, 1992. pages 145

[270] A. Gevins and S. Bressler. Functional topography of the human brain. *Functional brain imaging*, pages 99–116, 1988. pages 6

[271] J. F. Gibson, J. D. Farmer, M. Casdagli, and S. Eubank. An analytic approach to practical state space reconstruction. *Physica D: Nonlinear Phenomena*, 57(1):1–30, 1992. pages 92, 97, 98, 99, 100, 101, 106, 108, 109, 110, 133, 194

[272] E. D. Gireesh and D. Plenz. Neuronal avalanches organize as nested theta-and beta/gamma-oscillations during development of cortical layer 2/3. *Proceedings of the National Academy of Sciences*, 105(21):7576–7581, 2008. pages 11

[273] L. Glass. Synchronization and rhythmic processes in physiology. *Nature*, 410(6825):277–284, 2001. pages 15, 195

[274] L. Glass and M. C. Mackey. Pathological conditions resulting from instabilities in physiological control systems. *Annals of the New York Academy of Sciences*, 316(1):214–235, 1979. pages 15, 147, 195

[275] A. L. Goldberger. Fractal variability versus pathologic periodicity: complexity loss and stereotypy in disease. *Perspectives in Biology and Medicine*, 40(4):543–561, 1997. pages 15, 147, 195

[276] A. L. Goldberger, D. R. Rigney, B. J. West, et al. Chaos and fractals in human physiology. *Sci Am*, 262(2):42–49, 1990. pages 15, 147, 195

[277] A. L. Goldberger and B. J. West. Chaos in physiology: health or disease? In *Chaos in biological systems*, pages 1–4. Springer, 1987. pages 15, 147, 195

[278] D. Goldin and P. Wegner. The church-turing thesis: Breaking the myth. In *Conference on Computability in Europe*, pages 152–168. Springer, 2005. pages 10

[279] P. Goldman-Rakic, M. Chafee, and H. Friedman. Allocation of function in distributed circuits. *Brain mechanisms of perception and memory: From neuron to behavior*, pages 445–456, 1993. pages 6

[280] P. S. Goldman-Rakic. Topography of cognition: parallel distributed networks in primate association cortex. *Annual review of neuroscience*, 11(1):137–156, 1988. pages 6

[281] P. S. Goldman-Rakic. Regional and cellular fractionation of working memory. *Proceedings of the National Academy of Sciences*, 93(24):13473–13480, 1996. pages 6

[282] D. Golomb and Y. Amitai. Propagating neuronal discharges in neocortical slices: computational and experimental study. *Journal of neurophysiology*, 78(3):1199–1211, 1997. pages 56

[283] G. J. Goodhill, M. Gu, and J. S. Urbach. Predicting axonal response to molecular gradients with a computational model of filopodial dynamics. *Neural computation*, 16(11):2221–2243, 2004. pages 43

[284] K. Graf and T. Elbert. Dimensional analysis of the waking eeg. In *Brain dynamics*, pages 174–191. Springer, 1989. pages 14, 17

[285] C. W. Granger. Investigating causal relations by econometric models and cross-spectral methods. *Econometrica: Journal of the Econometric Society*, pages 424–438, 1969. pages 153

[286] E. Grannan, D. Kleinfeld, and H. Sompolinsky. Stimulus-dependent synchronization of neuronal assemblies. *Neural computation*, 5(4):550–569, 1993. pages 145

[287] P. Grassberger. Do climatic attractors exist? *Nature*, 323(6089):609–612, 1986. pages 125

[288] P. Grassberger and I. Procaccia. On the characterization of strange attractors. *Physical review letters*, 50(5):346, 1983. pages 113, 120

[289] P. Grassberger and I. Procaccia. Measuring the strangeness of strange attractors. In *The Theory of Chaotic Attractors*, pages 170–189. Springer, 2004. pages 113, 120

[290] C. M. Gray, P. König, A. K. Engel, W. Singer, et al. Oscillatory responses in cat visual cortex exhibit inter-columnar synchronization which reflects global stimulus properties. *Nature*, 338(6213):334–337, 1989. pages 188

[291] W. T. Greenough and F.-L. F. Chang. Dendritic pattern formation involves both oriented regression and oriented growth in the barrels of mouse somatosensory cortex. *Developmental Brain Research*, 43(1):148–152, 1988. pages 45

[292] P. E. Greenwood, L. M. Ward, D. F. Russell, A. Neiman, and F. Moss. Stochastic resonance enhances the electrosensory information available to paddlefish for prey capture. *Physical Review Letters*, 84(20):4773, 2000. pages 16

[293] C. Grienberger and A. Konnerth. Imaging calcium in neurons. *Neuron*, 73(5):862–885, 2012. pages 29

[294] G. Grimmett and H. Kesten. Random electrical networks on complete graphs. *Journal of the London Mathematical Society*, 2(1):171–192, 1984. pages 187

[295] G. Grinstein and R. Linsker. Synchronous neural activity in scale-free network models versus random network models. *Proceedings of the National Academy of Sciences of the United States of America*, 102(28):9948–9953, 2005. pages 181, 188, 197

[296] G. W. Gross. Simultaneous single unit recording in vitro with a photoetched laser deinsulated gold multimicroelectrode surface. *Biomedical Engineering, IEEE Transactions on*, (5):273–279, 1979. pages 22, 28, 198

[297] T. Gross and B. Blasius. Adaptive coevolutionary networks: a review. *Journal of the Royal Society Interface*, 5(20):259–271, 2008. pages 189

[298] J. W. Grossman and P. D. Ion. On a portion of the well-known collaboration graph. *Congressus Numerantium*, pages 129–132, 1995. pages 184

[299] Y. Grossman, I. Parnas, and M. Spira. Differential conduction block in branches of a bifurcating axon. *The Journal of physiology*, 295:283, 1979. pages 43, 48

[300] A. Grossmann and J. Morlet. Decomposition of hardy functions into square integrable wavelets of constant shape. *SIAM journal on mathematical analysis*, 15(4):723–736, 1984. pages 69

[301] R. Gundersen and J. Barrett. Neuronal chemotaxis: chick dorsal-root axons turn toward high concentrations of nerve growth factor. *Science*, 206(4422):1079–1080, 1979. pages 51

[302] Q. Guo, T. Zhou, J.-G. Liu, W.-J. Bai, B.-H. Wang, and M. Zhao. Growing scale-free small-world networks with tunable assortative coefficient. *Physica A: Statistical Mechanics and its Applications*, 371(2):814–822, 2006. pages 183

[303] C. Hafner. *Nonlinear time series analysis with applications to foreign exchange rate volatility*. Springer Science & Business Media, 2013. pages 90

[304] D. Halliday, J. Rosenberg, A. Amjad, P. Breeze, B. Conway, and S. Farmer. A framework for the analysis of mixed time series/point process datatheory and application to the study of physiological tremor, single motor unit discharges and electromyograms. *Progress in biophysics and molecular biology*, 64(2-3):237–278, 1995. pages 66

[305] P. Hamilton. A language to describe the growth of neurites. *Biological cybernetics*, 68(6):559–565, 1993. pages 43

[306] F. Han, N. Caporale, and Y. Dan. Reverberation of recent visual experience in spontaneous cortical waves. *Neuron*, 60(2):321–327, 2008. pages 17

[307] A. Hanlon. Content-addressable and associative memory systems a survey. *IEEE Transactions on Electronic Computers*, (4):509–521, 1966. pages 9

[308] D. Hansel, G. Mato, and C. Meunier. Synchrony in excitatory neural networks. *Neural computation*, 7(2):307–337, 1995. pages 145

[309] R. M. Harris and T. A. Woolsey. Dendritic plasticity in mouse barrel cortex following postnatal vibrissa follicle damage. *Journal of Comparative Neurology*, 196(3):357–376, 1981. pages 45

[310] J. M. Hausdorff, S. L. Mitchell, R. Firtion, C.-K. Peng, M. E. Cudkowicz, J. Y. Wei, and A. L. Goldberger. Altered fractal dynamics of gait: reduced stride-interval correlations with aging and huntingtons disease. *Journal of applied physiology*, 82(1):262–269, 1997. pages 17

[311] D. O. Hebb. *The organization of behavior: A neuropsychological approach*. John Wiley & Sons, 1949. pages 7

[312] D. O. Hebb. *The organization of behavior: A neuropsychological theory*. Psychology Press, 2005. pages 184

[313] C. D. Heffner, A. Lumsden, and D. O'leary. Target control of collateral extension and directional axon growth in the mammalian brain. *Science*, 247(4939):217–220, 1990. pages 51

[314] R. Hegger, H. Kantz, and T. Schreiber. Practical implementation of nonlinear time series methods: The tisean package. *Chaos: An Interdisciplinary Journal of Nonlinear Science*, 9(2):413–435, 1999. pages 90

[315] M. Heideman, D. Johnson, and C. Burrus. Gauss and the history of the fast fourier transform. *IEEE ASSP Magazine*, 1(4):14–21, 1984. pages 63

[316] H. Hentschel and A. Van Ooyen. Models of axon guidance and bundling during development. *Proceedings of the Royal Society of London B: Biological Sciences*, 266(1434):2231–2238, 1999. pages 43

[317] A. Hierlemann, U. Frey, S. Hafizovic, and F. Heer. Growing cells atop microelectronic chips: interfacing electrogenic cells in vitro with cmos-based microelectrode arrays. *Proceedings of the IEEE*, 99(2):252–284, 2011. pages 32

[318] C.-C. Hilgetag, G. A. Burns, M. A. O'Neill, J. W. Scannell, and M. P. Young. Anatomical connectivity defines the organization of clusters of cortical areas in the macaque and the cat. *Philosophical Transactions of the Royal Society of London B: Biological Sciences*, 355(1393):91–110, 2000. pages 6, 183

[319] C. C. Hilgetag and M. Kaiser. Clustered organization of cortical connectivity. *Neuroinformatics*, 2(3):353–360, 2004. pages 6, 183

[320] C.-C. Hilgetag, M. A. O'Neill, and M. P. Young. Hierarchical organization of macaque and cat cortical sensory systems explored with a novel network processor. *Philosophical Transactions of the Royal Society of London B: Biological Sciences*, 355(1393):71–89, 2000. pages 6, 183

[321] J. Hindmarsh and R. Rose. A model of neuronal bursting using three coupled first order differential equations. *Proceedings of the Royal Society of London B: Biological Sciences*, 221(1222):87–102, 1984. pages 46

[322] N. Hiratani and T. Fukai. Interplay between short-and long-term plasticity in cell-assembly formation. *PloS one*, 9(7):e101535, 2014. pages 7

[323] K. Hlaváčková-Schindler, M. Paluš, M. Vejmelka, and J. Bhattacharya. Causality detection based on information-theoretic approaches in time series analysis. *Physics Reports*, 441(1):1–46, 2007. pages 153

[324] A. L. Hodgkin and A. F. Huxley. A quantitative description of membrane current and its application to conduction and excitation in nerve. *The Journal of physiology*, 117(4):500, 1952. pages 45, 87

[325] K. Hoffman and B. McNaughton. Coordinated reactivation of distributed memory traces in primate neocortex. *Science*, 297(5589):2070–2073, 2002. pages 17

[326] R. G. Hohlfeld and N. Cohen. Self-similarity and the geometric requirements for frequency independence in antennae. *Fractals*, 7(01):79–84, 1999. pages 8

[327] P. Holme, C. R. Edling, and F. Liljeros. Structure and time evolution of an internet dating community. *Social Networks*, 26(2):155–174, 2004. pages 184

[328] P. Holme, B. J. Kim, C. N. Yoon, and S. K. Han. Attack vulnerability of complex networks. *Physical Review E*, 65(5):056109, 2002. pages 185, 186

[329] H. Hong, M.-Y. Choi, and B. J. Kim. Synchronization on small-world networks. *Physical Review E*, 65(2):026139, 2002. pages 188, 197

[330] J. J. Hopfield. Neural networks and physical systems with emergent collective computational abilities. *Proceedings of the national academy of sciences*, 79(8):2554–2558, 1982. pages 8

[331] J. J. Hopfield. Neurons with graded response have collective computational properties like those of two-state neurons. *Proceedings of the national academy of sciences*, 81(10):3088–3092, 1984. pages 8

[332] F. C. Hoppensteadt and E. M. Izhikevich. *Weakly connected neural networks*, volume 126. Springer Science & Business Media, 2012. pages 46

[333] J. Hsiang, S. Price, A. Heller, P. Hoffmann, and B. Wainer. Ultrastructural evidence for hippocampal target cell-mediated trophic effects on septal cholinergic neurons in reaggregating cell cultures. *Neuroscience*, 26(2):417–431, 1988. pages 23, 185, 198

[334] A. Y. Hsiao, Y.-s. Torisawa, Y.-C. Tung, S. Sud, R. S. Taichman, K. J. Pienta, and S. Takayama. Microfluidic system for formation of pc-3 prostate cancer co-culture spheroids. *Biomaterials*, 30(16):3020–3027, 2009. pages 198

[335] H.-B. Hu and X.-F. Wang. Disassortative mixing in online social networks. *EPL (Europhysics Letters)*, 86(1):18003, 2009. pages 181, 182, 184

[336] N. E. Huang, Z. Shen, S. R. Long, M. C. Wu, H. H. Shih, Q. Zheng, N.-C. Yen, C. C. Tung, and H. H. Liu. The empirical mode decomposition and the hilbert spectrum for nonlinear and non-stationary time series analysis. In *Proceedings of the Royal Society of London A: Mathematical, Physical and Engineering Sciences*, volume 454, pages 903–995. The Royal Society, 1998. pages 92

[337] N. E. Huang, Z. Wu, S. R. Long, K. C. Arnold, X. Chen, and K. Blank. On instantaneous frequency. *Advances in adaptive data analysis*, 1(02):177–229, 2009. pages 92

[338] D. H. Hubel and T. N. Wiesel. Receptive fields, binocular interaction and functional architecture in the cat's visual cortex. *The Journal of physiology*, 160(1):106–154, 1962. pages 3, 185

[339] D. H. Hubel and T. N. Wiesel. Receptive fields of cells in striate cortex of very young, visually inexperienced kittens. *J. neurophysiol*, 26(994):1002, 1963. pages 188

[340] D. H. Hubel and T. N. Wiesel. Receptive fields and functional architecture in two nonstriate visual areas (18 and 19) of the cat. *Journal of neurophysiology*, 28(2):229–289, 1965. pages 188

[341] D. H. Hubel and T. N. Wiesel. Receptive fields and functional architecture of monkey striate cortex. *The Journal of physiology*, 195(1):215–243, 1968. pages 3, 6

[342] B. A. Huberman and L. A. Adamic. Internet: growth dynamics of the world-wide web. *Nature*, 401(6749):131–131, 1999. pages 181

[343] J. E. Huettner and R. W. Baughman. Primary culture of identified neurons from the visual cortex of postnatal rats. *The Journal of neuroscience*, 6(10):3044–3060, 1986. pages 23

[344] B. D. Hughes. Random walks and random environments. 1996. pages 187

[345] L. Iasemidis, A. Barreto, R. Gilmore, B. Uthman, S. Roper, and J. Sackellares. Spatiotemporal evolution of dynamical measures precedes onset of mesial temporal lobe seizures. *Epilepsia*, 35(Suppl 8):133, 1994. pages 17, 147

[346] L. Iasemidis, J. Principe, J. Czaplewski, R. Gilmore, S. Roper, and J. Sackellares. Spatiotemporal transition to epileptic seizures: a nonlinear dynamical analysis of scalp and intracranial eeg recordings. *Spatiotemporal models in biological and artificial systems*, pages 81–88, 1997. pages 17, 147

[347] L. D. Iasemidis and J. C. Sackellares. The evolution with time of the spatial distribution of the largest lyapunov exponent on the human epileptic cortex. *Measuring chaos in the human brain*, pages 49–82, 1991. pages 147

[348] L. D. Iasemidis, J. C. Sackellares, H. P. Zaveri, and W. J. Williams. Phase space topography and the lyapunov exponent of electrocorticograms in partial seizures. *Brain topography*, 2(3):187–201, 1990. pages 17, 147

[349] M. S. Idelson, E. Ben-Jacob, and Y. Hanein. Innate synchronous oscillations in freely-organized small neuronal circuits. *PloS one*, 5(12):e14443, 2010. pages 26, 84, 85, 86

[350] S. Ito, F.-C. Yeh, E. Hiolski, P. Rydygier, D. E. Gunning, P. Hottowy, N. Timme, A. M. Litke, and J. M. Beggs. Large-scale, high-resolution multielectrode-array recording depicts functional network differences of cortical and hippocampal cultures. *PloS one*, 9(8):e105324, 2014. pages 32

[351] E. M. Izhikevich. Which model to use for cortical spiking neurons? *IEEE transactions on neural networks*, 15(5):1063–1070, 2004. pages 198

[352] E. M. Izhikevich. *Dynamical systems in neuroscience*. MIT press, 2007. pages 41, 46, 47, 53, 198

[353] E. M. Izhikevich. Hybrid spiking models. *Philosophical Transactions of the Royal Society of London A: Mathematical, Physical and Engineering Sciences*, 368(1930):5061–5070, 2010. pages 198

[354] E. M. Izhikevich et al. Simple model of spiking neurons. *IEEE Transactions on neural networks*, 14(6):1569–1572, 2003. pages 41, 46, 47, 53, 54, 198

[355] S. Jacobi, J. Soriano, M. Segal, and E. Moses. Bdnf and nt-3 increase excitatory input connectivity in rat hippocampal cultures. *European Journal of Neuroscience*, 30(6):998–1010, 2009. pages 36, 180

[356] D. B. Jaffe, W. N. Ross, J. E. Lisman, N. Lasser-Ross, H. Miyakawa, and D. Johnston. A model for dendritic ca2+ accumulation in hippocampal pyramidal neurons based on fluorescence imaging measurements. *Journal of Neurophysiology*, 71(3):1065–1077, 1994. pages 45

[357] B. Jelles, J. Van Birgelen, J. Slaets, R. Hekster, E. Jonkman, and C. Stam. Decrease of non-linear structure in the eeg of alzheimer patients compared to healthy controls. *Clinical Neurophysiology*, 110(7):1159–1167, 1999. pages 147

[358] J. Jeong, J.-H. Chae, S. Y. Kim, and S.-H. Han. Nonlinear dynamic analysis of the eeg in patients with alzheimers disease and vascular dementia. *Journal of Clinical Neurophysiology*, 18(1):58–67, 2001. pages 147

[359] H. Jerison. Evolution of the brain and intelligence. *New York*, 1973. pages 4

[360] S. Jespersen, I. Sokolov, and A. Blumen. Relaxation properties of small-world networks. *Physical Review E*, 62(3):4405, 2000. pages 187

[361] Y. Jimbo, T. Tateno, and H. Robinson. Simultaneous induction of pathway-specific potentiation and depression in networks of cortical neurons. *Biophysical Journal*, 76(2):670–678, 1999. pages 23

[362] H. Jing and M. Takigawa. Topographic analysis of dimension estimates of eeg and filtered rhythms in epileptic patients with complex partial seizures. *Biological cybernetics*, 83(5):391–397, 2000. pages 147

[363] S. Johnson, J. Marro, and J. J. Torres. Functional optimization in complex excitable networks. *EPL (Europhysics Letters)*, 83(4):46006, 2008. pages 185, 186

[364] S. Johnson, J. J. Torres, J. Marro, and M. A. Munoz. Entropic origin of disassortativity in complex networks. *Physical review letters*, 104(10):108702, 2010. pages 183, 197

[365] S. Johnson, J. J. Torres, J. Marro, and M. A. M. NOZ. Shannon entropy and degree correlations in complex networks. In *Proceedings of the 10th WSEAS international conference on Wavelet analysis and multirate systems*, pages 31–35. World Scientific and Engineering Academy and Society (WSEAS), 2010. pages 183

[366] D. Jones and A. M. Cullen. A quantitative investigation of some presynaptic terminal parameters during synaptogenesis. *Experimental neurology*, 64(2):245–259, 1979. pages 5

[367] J. Jost and M. P. Joy. Spectral properties and synchronization in coupled map lattices. *Physical Review E*, 65(1):016201, 2001. pages 188, 197

[368] B. H. Junker and F. Schreiber. *Analysis of biological networks*, volume 2. John Wiley & Sons, 2011. pages 182

[369] J. H. Kaas. Why is brain size so important: Design problems and solutions as neocortex gets biggeror smaller. *Brain and Mind*, 1(1):7–23, 2000. pages 4

[370] M. Kaiser. A tutorial in connectome analysis: topological and spatial features of brain networks. *Neuroimage*, 57(3):892–907, 2011. pages 181

[371] H. Kamioka, E. Maeda, Y. Jimbo, H. P. Robinson, and A. Kawana. Spontaneous periodic synchronized bursting during formation of mature patterns of connections in cortical cultures. *Neuroscience letters*, 206(2):109–112, 1996. pages 85

[372] E. R. Kandel, J. H. Schwartz, T. M. Jessell, S. A. Siegelbaum, and A. Hudspeth. *Principles of neural science*, volume 4. McGraw-hill New York, 2000. pages 182, 188

[373] H. Kantz and T. Schreiber. Nonlinear time series analysis, vol. 7 of cambridge nonlinear science series, 1997. pages 101, 116, 128, 133

[374] H. Kantz and T. Schreiber. *Nonlinear time series analysis*, volume 7. Cambridge university press, 2004. pages 90, 126

[375] D. T. Kaplan. Exceptional events as evidence for determinism. *Physica D: Nonlinear Phenomena*, 73(1-2):38–48, 1994. pages 128

[376] D. T. Kaplan and R. J. Cohen. Is fibrillation chaos? *Circulation Research*, 67(4):886–892, 1990. pages 125

[377] N. Kashtan and U. Alon. Spontaneous evolution of modularity and network motifs. *Proceedings of the National Academy of Sciences of the United States of America*, 102(39):13773–13778, 2005. pages 190

[378] N. Kashtan, S. Itzkovitz, R. Milo, and U. Alon. Efficient sampling algorithm for estimating subgraph concentrations and detecting network motifs. *Bioinformatics*, 20(11):1746–1758, 2004. pages 161

[379] T. Kenet, D. Bibitchkov, M. Tsodyks, A. Grinvald, and A. Arieli. Spontaneously emerging cortical representations of visual attributes. *Nature*, 425(6961):954–956, 2003. pages 17

[380] M. B. Kennel and H. D. Abarbanel. False neighbors and false strands: A reliable minimum embedding dimension algorithm. *Physical review E*, 66(2):026209, 2002. pages 101, 128

[381] M. B. Kennel, R. Brown, and H. D. Abarbanel. Determining embedding dimension for phase-space reconstruction using a geometrical construction. *Physical review A*, 45(6):3403, 1992. pages 101, 128, 133, 194

[382] J. Kim, B. Kahng, and D. Kim. Disassortativity of random critical branching trees. *Physical Review E*, 79(6):067103, 2009. pages 183

[383] G. P. King, R. Jones, and D. Broomhead. Phase portraits from a time series: a singular system approach. *Nuclear Physics B-Proceedings Supplements*, 2:379–390, 1987. pages 99, 194

[384] W. Kinzel. 2. phys. e, 58,229 (1985) and references therein; e. domany and w. kinzel. *Phys. Rev. Lett*, 53:311, 1984. pages 11

[385] P. Kirsch, C. Besthorn, S. Klein, J. Rindfleisch, and R. Olbrich. Indications of nonlinear deterministic and finite-dimensional structures in time series of brain electrical activity: Dependence on recording region and brain state. *Brain Topogr*, 2:187, 1990. pages 147

[386] S. C. Kleene. General recursive functions of natural numbers. *Mathematische annalen*, 112(1):727–742, 1936. pages 10

[387] S. C. Kleene. Introduction to metamathematics. 1952. pages 10

[388] W. Kliemann. A stochastic dynamical model for the characterization of the geometrical structure of dendritic processes. *Bulletin of mathematical biology*, 49(2):135–152, 1987. pages 43

[389] A. Y. Klintsova and W. T. Greenough. Synaptic plasticity in cortical systems. *Current opinion in neurobiology*, 9(2):203–208, 1999. pages 182

[390] T. Knöpfel. Genetically encoded optical indicators for the analysis of neuronal circuits. *Nature Reviews Neuroscience*, 13(10):687–700, 2012. pages 29

[391] C. Koch and E. d. Schutter. Biophysics of computation: Information processing in single neurons. *Nature*, 398(6729):678–678, 1999. pages 7, 43

[392] C. Koch and I. Segev. Methods in neural modeling, 1989. pages 45

[393] C. Koch and I. Segev. *Methods in neuronal modeling: from ions to networks*. MIT press, 1998. pages 43

[394] M. Koebbe and G. Mayer-Kress. Use of recurrence plots in the analysis of time-series data. In *SANTA FE INSTITUTE STUDIES IN THE SCIENCES OF COMPLEXITY-PROCEEDINGS VOLUME-*, volume 12, pages 361–361. Citeseer, 1992. pages 112

[395] L. Korbo, B. Pakkenberg, O. Ladefoged, H. J. G. Gundersen, P. Arlien-Søborg, and H. Pakkenberg. An efficient method for estimating the total number of neurons in rat brain cortex. *Journal of neuroscience methods*, 31(2):93–100, 1990. pages 22

[396] H. Korn and P. Faure. Is there chaos in the brain? ii. experimental evidence and related models. *Comptes rendus biologies*, 326(9):787–840, 2003. pages 14

[397] S. M. Kosslyn, G. Ganis, and W. L. Thompson. Neural foundations of imagery. *Nature Reviews Neuroscience*, 2(9):635–642, 2001. pages 17

[398] D. J. Kraemer, C. N. Macrae, A. E. Green, and W. M. Kelley. Musical imagery: sound of silence activates auditory cortex. *Nature*, 434(7030):158–158, 2005. pages 17

[399] G. Kreiman, C. Koch, and I. Fried. Imagery neurons in the human brain. *Nature*, 408(6810):357–361, 2000. pages 17

[400] A. R. Kriegstein and M. A. Dichter. Morphological classification of rat cortical neurons in cell culture. *The Journal of Neuroscience*, 3(8):1634–1647, 1983. pages 23

[401] J. K. Krottje and A. Van Ooyen. A mathematical framework for modeling axon guidance. *Bulletin of mathematical biology*, 69(1):3–31, 2007. pages 43

[402] D. Kugiumtzis. State space reconstruction parameters in the analysis of chaotic time seriesthe role of the time window length. *Physica D: Nonlinear Phenomena*, 95(1):13–28, 1996. pages 110

[403] S. Kullback. *Information theory and statistics*. Courier Corporation, 1997. pages 154

[404] S. Kullback and R. A. Leibler. On information and sufficiency. *The annals of mathematical statistics*, 22(1):79–86, 1951. pages 153

[405] J. Kurths and H. Herzel. An attractor in a solar time series. *Physica D: Nonlinear Phenomena*, 25(1-3):165–172, 1987. pages 125

[406] L. F. Lago-Fernández, R. Huerta, F. Corbacho, and J. A. Sigüenza. Fast response and temporal coherent oscillations in small-world networks. *Physical Review Letters*, 84(12):2758, 2000. pages 188, 197

[407] E. Lamm and R. Unger. *Biological computation*. CRC Press, 2011. pages ii

[408] C. G. Langton. *ALife*. Addison-Wesley, 1990. pages 10, 11

[409] L. Lapicque. Recherches quantitatives sur lexcitation électrique des nerfs traitée comme une polarisation. *J. Physiol. Pathol. Gen*, 9(1):620–635, 1907. pages 46

[410] V. Latora and M. Marchiori. Efficient behavior of small-world networks. *Physical review letters*, 87(19):198701, 2001. pages 8, 159, 160

[411] V. Latora and M. Marchiori. Economic small-world behavior in weighted networks. *The European Physical Journal B-Condensed Matter and Complex Systems*, 32(2):249–263, 2003. pages 8

[412] S. Layne, G. Mayer-Kress, and J. Holzfuss. Problems associated with dimensional analysis of electroencephalogram data. In *Dimensions and entropies in chaotic systems*, pages 246–256. Springer, 1986. pages 14

[413] M. Le Van Quyen, J. Martinerie, C. Adam, and F. J. Varela. Unstable periodic orbits in human epileptic activity. *Physical Review E*, 56(3):3401, 1997. pages 14

[414] C. Lee and M. Paull. A content addressable distributed logic memory with applications to information retrieval. *Proceedings of the IEEE*, 51(6):924–932, 1963. pages 9

[415] D.-S. Lee and H. Rieger. Maximum flow and topological structure of complex networks. *EPL (Europhysics Letters)*, 73(3):471, 2005. pages 187, 189

[416] K. S. Lee, F. Schottler, M. Oliver, and G. Lynch. Brief bursts of high-frequency stimulation produce two types of structural change in rat hippocampus. *Journal of Neurophysiology*, 44(2):247–258, 1980. pages 182

[417] K. Lehnertz, R. G. Andrzejak, J. Arnhold, T. Kreuz, F. Mormann, C. Rieke, G. Widman, and C. E. Elger. Nonlinear eeg analysis in epilepsy: Its possible use for interictal focus localization, seizure anticipation, and. *Journal of Clinical Neurophysiology*, 18(3):209–222, 2001. pages 17

[418] K. Lehnertz and C. Elger. Spatio-temporal dynamics of the primary epileptogenic area in temporal lobe epilepsy characterized by neuronal complexity loss. *Electroencephalography and clinical Neurophysiology*, 95(2):108–117, 1995. pages 17, 147

[419] P. C. Letourneau. Cell-to-substratum adhesion and guidance of axonal elongation. *Developmental biology*, 44(1):92–101, 1975. pages 26

[420] M. S. Lewicki. A review of methods for spike sorting: the detection and classification of neural action potentials. *Network: Computation in Neural Systems*, 9(4):R53–R78, 1998. pages 32

[421] D. Li, G. Li, K. Kosmidis, H. Stanley, A. Bunde, and S. Havlin. Percolation of spatially constraint networks. *EPL (Europhysics Letters)*, 93(6):68004, 2011. pages 187

[422] G. Li, L. A. Braunstein, S. V. Buldyrev, S. Havlin, and H. E. Stanley. Transport and percolation theory in weighted networks. *Physical Review E*, 75(4):045103, 2007. pages 187

[423] P. Li, K. Zhang, X. Xu, J. Zhang, and M. Small. Reexamination of explosive synchronization in scale-free networks: The effect of disassortativity. *Physical Review E*, 87(4):042803, 2013. pages 185

[424] W. Li. Mutual information functions versus correlation functions. *Journal of statistical physics*, 60(5-6):823–837, 1990. pages 153

[425] X. Li, G. Ouyang, A. Usami, Y. Ikegaya, and A. Sik. Scale-free topology of the ca3 hippocampal network: a novel method to analyze functional neuronal assemblies. *Biophysical journal*, 98(9):1733–1741, 2010. pages 181

[426] X. J. Li, A. V. Valadez, P. Zuo, and Z. Nie. Microfluidic 3d cell culture: potential application for tissue-based bioassays. 2012. pages 198

[427] W. Liebert and H. Schuster. Proper choice of the time delay for the analysis of chaotic time series. *Physics Letters A*, 142(2):107–111, 1989. pages 99

[428] D. Linaro, M. Storace, and M. Mattia. Inferring network dynamics and neuron properties from population recordings. *Frontiers in computational neuroscience*, 5:43, 2011. pages 199

[429] A. Lindenmayer. Mathematical models for cellular interactions in development i. filaments with one-sided inputs. *Journal of theoretical biology*, 18(3):280–299, 1968. pages 43

[430] A. Litke, N. Bezayiff, E. Chichilnisky, W. Cunningham, W. Dabrowski, A. Grillo, M. Grivich, P. Grybos, P. Hottowy, S. Kachiguine, et al. What does the eye tell the brain?: Development of a system for the large-scale recording of retinal output activity. *Nuclear Science, IEEE Transactions on*, 51(4):1434–1440, 2004. pages 32

[431] W. Little and G. L. Shaw. A statistical theory of short and long term memory. *Behavioral biology*, 14(2):115–133, 1975. pages 8

[432] W. A. Little. The existence of persistent states in the brain. *Mathematical Biosciences*, 19:101–120, 1974. pages 8

[433] W. A. Little. Analytic study of the memory storage capacity of a neural network. *Mathematical Biosciences*, 39:281–290, 1978. pages 8

[434] N. Litvak and R. Van Der Hofstad. Uncovering disassortativity in large scale-free networks. *Physical Review E*, 87(2):022801, 2013. pages 161

[435] J. Lizier, M. Rubinov, et al. Multivariate construction of effective computational networks from observational data. 2012. pages 199

[436] M. London and M. Häusser. Dendritic computation. *Annu. Rev. Neurosci.*, 28:503–532, 2005. pages 43, 48

[437] E. López, S. V. Buldyrev, S. Havlin, and H. E. Stanley. Anomalous transport in scale-free networks. *Physical review letters*, 94(24):248701, 2005. pages 187, 189

[438] D. LORENTE. N6, r., studies on the structure of the cerebral cortex. i. the area entorhinalis. *J. Psychol. Neurol.(Lpz.)*, 45:381–438, 1933. pages 3, 185

[439] R. Lorente de Nó. Studies on the structure of the cerebral cortex. ii. continuation of the study of the ammonic system. *Journal für Psychologie und Neurologie*, 1934. pages ii, 7

[440] R. Lorente de Nó. Architectonics and structure of the cerebral cortex. *Physiology of the nervous system*, pages 291–330, 1938. pages 3, 185

[441] E. N. Lorenz. Deterministic nonperiodic flow. *Journal of the atmospheric sciences*, 20(2):130–141, 1963. pages ii

[442] L. Lovász. Random walks on graphs. *Combinatorics, Paul erdos is eighty*, 2:1–46, 1993. pages 187

[443] S. Lowel and W. Singer. Selection of intrinsic horizontal connections in the visual cortex by correlated neuronal activity. *Science*, 255(5041):209, 1992. pages 7

[444] A. Luczak. Spatial embedding of neuronal trees modeled by diffusive growth. *Journal of neuroscience methods*, 157(1):132–141, 2006. pages 1, 7, 43, 184, 197

[445] A. Luczak and J. N. MacLean. Default activity patterns at the neocortical microcircuit level. *Frontiers in integrative neuroscience*, 6:30, 2012. pages 17

[446] J. Lumley and R. Meyer. Transition and turbulence. *Academic Press, New York*, pages 215–242, 1981. pages 99

[447] A. G. Lumsden and J. Dodd. Chemotropic guidance of developing axons in the mammalian central nervous system. *Nature*, 336:22, 1988. pages 51

[448] J. S. Lund, T. Yoshioka, and J. B. Levitt. Comparison of intrinsic connectivity in different areas of macaque monkey cerebral cortex. *Cerebral Cortex*, 3(2):148–162, 1993. pages 5

[449] A. R. Luria. *Higher cortical functions in man*. Springer Science & Business Media, 2012. pages 6

[450] J. Lurito, T. Georgakopoulos, and A. Georgopoulos. Cognitive spatial-motor processes. *Experimental Brain Research*, 87(3):562–580, 1991. pages 4

[451] W. Lutzenberger, N. Birbaumer, H. Flor, B. Rockstroh, and T. Elbert. Dimensional analysis of the human eeg and intelligence. *Neuroscience Letters*, 143(1):10–14, 1992. pages 14

[452] W. Lutzenberger, T. Elbert, N. Birbaumer, W. J. Ray, and H. Schupp. The scalp distribution of the fractal dimension of the eeg and its variation with mental tasks. *Brain topography*, 5(1):27–34, 1992. pages 14

[453] M.-E. Lynall, D. S. Bassett, R. Kerwin, P. J. McKenna, M. Kitzbichler, U. Muller, and E. Bullmore. Functional connectivity and brain networks in schizophrenia. *Journal of Neuroscience*, 30(28):9477–9487, 2010. pages 17

[454] W. Maass, R. A. Legenstein, and N. Bertschinger. Methods for estimating the computational power and generalization capability of neural microcircuits. In *Advances in neural information processing systems*, pages 865–872, 2004. pages 10

[455] W. Maass and A. M. Zador. Dynamic stochastic synapses as computational units. *Neural Computation*, 11(4):903–917, 1999. pages 54

[456] R. B. Maccioni, J. P. Muñoz, and L. Barbeito. The molecular bases of alzheimer's disease and other neurodegenerative disorders. *Archives of medical research*, 32(5):367–381, 2001. pages 17

[457] A. Macieira-Coelho and S. Avrameas. Variations in cell overlapping and growth depending on the substratum. *Experimental Biology and Medicine*, 139(4):1374–1378, 1972. pages 26

[458] M. C. Mackey, L. Glass, et al. Oscillation and chaos in physiological control systems. *Science*, 197(4300):287–289, 1977. pages 15, 195

[459] M. C. Mackey and J. G. Milton. Dynamical diseases. *Annals of the New York Academy of Sciences*, 504(1):16–32, 1987. pages 15, 195

[460] W. Mader, M. Mader, J. Timmer, M. Thiel, and B. Schelter. Networks: On the relation of bi-and multivariate measures. *Scientific reports*, 5, 2015. pages 153

[461] Z. F. Mainen and T. J. Sejnowski. Influence of dendritic structure on firing pattern in model neocortical neurons. *Nature*, 382(6589):363–366, 1996. pages 43, 45

[462] T. Mäki-Marttunen, J. Acimovic, M. Nykter, J. Kesseli, K. Ruohonen, O. Yli-Harja, and M.-L. Linne. Information diversity in structure and dynamics of simulated neuronal networks. *Frontiers in computational neuroscience*, 5:26, 2011. pages 8

[463] T. Mäki-Marttunen, J. Kesseli, and M. Nykter. Balance between noise and information flow maximizes set complexity of network dynamics. *PloS one*, 8(3):e56523, 2013. pages 16

[464] R. Mañé. On the dimension of the compact invariant sets of certain non-linear maps. In *Dynamical Systems and Turbulence, Warwick 1980*, pages 230–242. Springer, 1981. pages 91

[465] S. Mangan and U. Alon. Structure and function of the feed-forward loop network motif. *Proceedings of the National Academy of Sciences*, 100(21):11980–11985, 2003. pages 161

[466] Y. Manor, C. Koch, and I. Segev. Effect of geometrical irregularities on propagation delay in axonal trees. *Biophysical Journal*, 60(6):1424, 1991. pages 43, 48

[467] H. Markram. The blue brain project. *Nature Reviews Neuroscience*, 7(2):153–160, 2006. pages 43

[468] J. Martinerie, A. M. Albano, A. Mees, and P. Rapp. Mutual information, strange attractors, and the optimal estimation of dimension. *Physical Review A*, 45(10):7058, 1992. pages 99

[469] N. Marwan. *Untersuchung der Klimavariabilität in NW Argentinien mit Hilfe der quantitativen Analyse von Recurrence Plots*. Norbert Marwan, 1999. pages 112

[470] N. Marwan, M. C. Romano, M. Thiel, and J. Kurths. Recurrence plots for the analysis of complex systems. *Physics Reports*, 438(5):237–329, 2007. pages 113

[471] N. Marwan, N. Wessel, U. Meyerfeldt, A. Schirdewan, and J. Kurths. Recurrence-plot-based measures of complexity and their application to heart-rate-variability data. *Physical review E*, 66(2):026702, 2002. pages 89, 116, 120

[472] S. Maskery and T. Shinbrot. Deterministic and stochastic elements of axonal guidance. *Annu. Rev. Biomed. Eng.*, 7:187–221, 2005. pages 43

[473] S. Maslov and K. Sneppen. Specificity and stability in topology of protein networks. *Science*, 296(5569):910–913, 2002. pages 160, 182

[474] S. Maslov, K. Sneppen, and A. Zaliznyak. Pattern detection in complex networks: Correlation profile of the internet. *arXiv preprint cond-mat/0205379*, 2002. pages 183, 197

[475] A. Mason and A. Larkman. Correlations between morphology and electrophysiology of pyramidal neurons in slices of rat visual cortex. ii. electrophysiology. *The Journal of Neuroscience*, 10(5):1415–1428, 1990. pages 45

[476] G. Mayer-Kress and J. Holzfuss. Analysis of the human electroencephalogram with methods from nonlinear dynamics. In *Temporal disorder in human oscillatory systems*, pages 57–68. Springer, 1987. pages 14

[477] G. Mayer-Kress and S. P. Layne. Dimensionality of the human electroencephalogram. *Ann NY Acad Sci*, 504(1):62–87, 1987. pages 14

[478] G. Mayer-Kress, F. E. Yates, L. Benton, M. Keidel, W. Tirsch, S. Pöppl, and K. Geist. Dimensional analysis of nonlinear oscillations in brain, heart, and muscle. *Mathematical Biosciences*, 90(1-2):155–182, 1988. pages 14, 147

[479] S. K. McConnell. Development and decision-making in the mammalian cerebral cortex. *Brain Research Reviews*, 13(1):1–23, 1988. pages 22

[480] S. K. McConnell. Constructing the cerebral cortex: neurogenesis and fate determination. *Neuron*, 15(4):761–768, 1995. pages 22

[481] B. W. Mel. Synaptic integration in an excitable dendritic tree. *Journal of neurophysiology*, 70(3):1086–1101, 1993. pages 43

[482] M. M. Merzenich and J. F. Brugge. Representation of the cochlear partition on the superior temporal plane of the macaque monkey. *Brain research*, 50(2):275–296, 1973. pages 3

[483] M. Mesulam et al. Large-scale neurocognitive networks and distributed processing for attention, language, and memory. *Annals of neurology*, 28(5):597–613, 1990. pages 6

[484] D. Meunier, R. Lambiotte, and E. T. Bullmore. Modular and hierarchically modular organization of brain networks. *Frontiers in neuroscience*, 4:200, 2010. pages 172, 196

[485] M. Migliore, E. Cook, D. Jaffe, D. Turner, and D. Johnston. Computer simulations of morphologically reconstructed ca3 hippocampal neurons. *Journal of neurophysiology*, 73(3):1157–1168, 1995. pages 45

[486] R. Milo, S. Itzkovitz, N. Kashtan, R. Levitt, S. Shen-Orr, I. Ayzenshtat, M. Sheffer, and U. Alon. Superfamilies of evolved and designed networks. *Science*, 303(5663):1538–1542, 2004. pages 161

[487] R. Milo, S. Shen-Orr, S. Itzkovitz, N. Kashtan, D. Chklovskii, and U. Alon. Network motifs: simple building blocks of complex networks. *Science*, 298(5594):824–827, 2002. pages 161

[488] J. Milton and D. Black. Dynamic diseases in neurology and psychiatry. *Chaos: An Interdisciplinary Journal of Nonlinear Science*, 5(1):8–13, 1995. pages 15, 195

[489] G. M. Mindlin and R. Gilmore. Topological analysis and synthesis of chaotic time series. *Physica D: Nonlinear Phenomena*, 58(1):229–242, 1992. pages 112

[490] A. Minta and R. Y. Tsien. Fluorescent indicators for cytosolic sodium. *Journal of Biological Chemistry*, 264(32):19449–19457, 1989. pages 29

[491] M. Mitchell. Biological computation. 2010. pages ii

[492] M. Mitra and J. E. Skinner. Low-dimensional chaos maps learning in a model neuropil (olfactory bulb). *Integrative physiological and behavioral science*, 27(4):304–322, 1992. pages 14

[493] A. Miyawaki, J. Llopis, R. Heim, J. M. McCaffery, J. A. Adams, M. Ikura, and R. Y. Tsien. Fluorescent indicators for ca2+ based on green fluorescent proteins and calmodulin. *Nature*, 388(6645):882–887, 1997. pages 31

[494] M. H. Mohajerani, D. A. McVea, M. Fingas, and T. H. Murphy. Mirrored bilateral slow-wave cortical activity within local circuits revealed by fast bihemispheric voltage-sensitive dye imaging in anesthetized and awake mice. *Journal of Neuroscience*, 30(10):3745–3751, 2010. pages 17

[495] M. Molnár and J. E. Skinner. Low-dimensional chaos in event-related brain potentials. *International Journal of Neuroscience*, 1992. pages 14

[496] R. J. Montoro and R. Yuste. Gap junctions in developing neocortex: a review. *Brain research reviews*, 47(1):216–226, 2004. pages 23

[497] J. M. Montoya and R. V. Solé. Small world patterns in food webs. *Journal of theoretical biology*, 214(3):405–412, 2002. pages 168

[498] A. Morel, P. Garraghty, and J. Kaas. Tonotopic organization, architectonic fields, and connections of auditory cortex in macaque monkeys. *Journal of Comparative Neurology*, 335(3):437–459, 1993. pages 3

[499] F. Mormann, R. G. Andrzejak, C. E. Elger, and K. Lehnertz. Seizure prediction: the long and winding road. *Brain*, 130(2):314–333, 2007. pages 147

[500] F. Mormann, T. Kreuz, R. G. Andrzejak, P. David, K. Lehnertz, and C. E. Elger. Epileptic seizures are preceded by a decrease in synchronization. *Epilepsy research*, 53(3):173–185, 2003. pages 147

[501] F. Mormann, T. Kreuz, C. Rieke, R. G. Andrzejak, A. Kraskov, P. David, C. E. Elger, and K. Lehnertz. On the predictability of epileptic seizures. *Clinical neurophysiology*, 116(3):569–587, 2005. pages 147

[502] A. Moscona. Cell aggregation: properties of specific cell-ligands and their role in the formation of multicellular systems. *Developmental biology*, 18(3):250–277, 1968. pages 23, 185, 198

[503] V. Mountcastle. An organizing principle for cerebral function: the unit model and the distributed system. 1978. pages 3, 185

[504] V. B. Mountcastle. The columnar organization of the neocortex. *Brain*, 120(4):701–722, 1997. pages 3, 185

[505] V. B. Mountcastle et al. Modality and topographic properties of single neurons of cats somatic sensory cortex. *J neurophysiol*, 20(4):408–434, 1957. pages 3, 188

[506] K. Mulchandani. *Morphological modeling of neurons*. PhD thesis, Texas A&M University, 1995. pages 43

[507] V. Müller, W. Lutzenberger, F. Pulvermüller, B. Mohr, and N. Birbaumer. Investigation of brain dynamics in parkinson's disease by methods derived from nonlinear dynamics. *Experimental brain research*, 137(1):103–110, 2001. pages 147

[508] K. Muramoto, M. Ichikawa, M. Kawahara, K. Kobayashi, and Y. Kuroda. Frequency of synchronous oscillations of neuronal activity increases during development and is correlated to the number of synapses in cultured cortical neuron networks. *Neuroscience letters*, 163(2):163–165, 1993. pages 85

[509] K. Musick, D. Khatami, and B. C. Wheeler. Three-dimensional micro-electrode array for recording dissociated neuronal cultures. *Lab on a Chip*, 9(14):2036–2042, 2009. pages 198

[510] J. Nagumo, S. Arimoto, and S. Yoshizawa. An active pulse transmission line simulating nerve axon. *Proceedings of the IRE*, 50(10):2061–2070, 1962. pages 46

[511] X. Nan and X. Jinghua. The fractal dimension of eeg as a physical measure of conscious human brain activities. *Bulletin of Mathematical Biology*, 50(5):559–565, 1988. pages 14

[512] J.-L. Nandrino, L. Pezard, J. Martinerie, F. El Massioui, B. Renault, R. Jouvent, J.-F. Allilaire, and D. Widlöcher. Decrease of complexity in eeg as a symptom of depression. *Neuroreport*, 5(4):528–530, 1994. pages 17, 18, 147

[513] M. E. Newman. The structure of scientific collaboration networks. *Proceedings of the National Academy of Sciences*, 98(2):404–409, 2001. pages 184

[514] M. E. Newman. The structure of scientific collaboration networks. *Proceedings of the National Academy of Sciences*, 98(2):404–409, 2001. pages 184

[515] M. E. Newman. Assortative mixing in networks. *Physical review letters*, 89(20):208701, 2002. pages 160, 184, 186, 197

[516] M. E. Newman. Mixing patterns in networks. *Physical Review E*, 67(2):026126, 2003. pages 8, 160, 183, 184, 189, 197

[517] M. E. Newman. The structure and function of complex networks. *SIAM review*, 45(2):167–256, 2003. pages 160

[518] M. E. Newman. Modularity and community structure in networks. *Proceedings of the national academy of sciences*, 103(23):8577–8582, 2006. pages 161

[519] M. E. Newman and M. Girvan. Finding and evaluating community structure in networks. *Physical review E*, 69(2):026113, 2004. pages 155

[520] M. E. Newman and J. Park. Why social networks are different from other types of networks. *Physical Review E*, 68(3):036122, 2003. pages 184, 189

[521] J. Nichols, S. Trickey, and M. Seaver. Damage detection using multivariate recurrence quantification analysis. *Mechanical Systems and Signal Processing*, 20(2):421–437, 2006. pages 199

[522] E. Niedermeyer and F. L. da Silva. *Electroencephalography: basic principles, clinical applications, and related fields*. Lippincott Williams & Wilkins, 2005. pages 18

[523] C. M. Niell and S. J. Smith. Functional imaging reveals rapid development of visual response properties in the zebrafish tectum. *Neuron*, 45(6):941–951, 2005. pages 48

[524] S. C. Noctor, V. Martínez-Cerdeño, L. Ivic, and A. R. Kriegstein. Cortical neurons arise in symmetric and asymmetric division zones and migrate through specific phases. *Nature neuroscience*, 7(2):136–144, 2004. pages 22

[525] J. D. Noh. Percolation transition in networks with degree-degree correlation. *Physical Review E*, 76(2):026116, 2007. pages 185

[526] J. D. Noh and H. Rieger. Random walks on complex networks. *Physical review letters*, 92(11):118701, 2004. pages 187

[527] J. O'Kusky and M. Colonnier. A laminar analysis of the number of neurons, glia, and synapses in the visual cortex (area 17) of adult macaque monkeys. *Journal of Comparative Neurology*, 210(3):278–290, 1982. pages 5, 180

[528] T. Opitz, A. D. De Lima, and T. Voigt. Spontaneous development of synchronous oscillatory activity during maturation of cortical networks in vitro. *Journal of neurophysiology*, 88(5):2196–2206, 2002. pages 85

[529] M. Oram, M. Wiener, R. Lestienne, and B. Richmond. Stochastic nature of precisely timed spike patterns in visual system neuronal responses. *Journal of neurophysiology*, 81(6):3021–3033, 1999. pages 156

[530] J. G. Orlandi, J. Soriano, E. Alvarez-Lacalle, S. Teller, and J. Casademunt. Noise focusing and the emergence of coherent activity in neuronal cultures. *Nature Physics*, 9(9):582–590, 2013. pages 18, 47, 48, 86

[531] R. E. Ornstein and R. F. Thompson. *The amazing brain*. Houghton Mifflin Harcourt, 1991. pages 1

[532] A. Osborne, A. Kirwan, A. Provenzale, and L. Bergamasco. A search for chaotic behavior in large and mesoscale motions in the pacific ocean. *Physica D: Nonlinear Phenomena*, 23(1):75–83, 1986. pages 125

[533] A. R. Osborne and A. Provenzale. Finite correlation dimension for stochastic systems with power-law spectra. *Physica D: Nonlinear Phenomena*, 35(3):357–381, 1989. pages 124

[534] E. Ott. Chaos in dynamical systems, 1993. *Cambridge, New York*, 1993. pages 110

[535] N. Packard, J. Kelso, A. Mandell, and M. Shlesinger. Dynamic patterns in complex systems. *ed. JA Kelso, AJ Mandell and MF Shlesinger, World Scientific*, page 293, 1988. pages 10

[536] N. H. Packard. *Adaptation toward the edge of chaos*. University of Illinois at Urbana-Champaign, Center for Complex Systems Research, 1988. pages 10

[537] N. H. Packard, J. P. Crutchfield, J. D. Farmer, and R. S. Shaw. Geometry from a time series. *Physical review letters*, 45(9):712, 1980. pages 88, 91, 92, 194

[538] G. Palm. On associative memory. *Biological cybernetics*, 36(1):19–31, 1980. pages 8

[539] G. Palm. On the storage capacity of an associative memory with randomly distributed storage elements. *Biological Cybernetics*, 39(2):125–127, 1981. pages 8

[540] M. Paluš. Nonlinearity in normal human eeg: cycles, temporal asymmetry, nonstationarity and randomness, not chaos. *Biological cybernetics*, 75(5):389–396, 1996. pages 147

[541] R. K. Pan, N. Chatterjee, and S. Sinha. Mesoscopic organization reveals the constraints governing caenorhabditis elegans nervous system. *PloS one*, 5(2):e9240, 2010. pages 189

[542] R. K. Pan and S. Sinha. Modularity produces small-world networks with dynamical time-scale separation. *EPL (Europhysics Letters)*, 85(6):68006, 2009. pages 189

[543] J. Park and M. E. Newman. Origin of degree correlations in the internet and other networks. *Physical Review E*, 68(2):026112, 2003. pages 183, 189, 197

[544] V. Pasquale, P. Massobrio, L. Bologna, M. Chiappalone, and S. Martinoia. Self-organization and neuronal avalanches in networks of dissociated cortical neurons. *Neuroscience*, 153(4):1354–1369, 2008. pages 18

[545] R. Pastor-Satorras, A. Vázquez, and A. Vespignani. Dynamical and correlation properties of the internet. *Physical review letters*, 87(25):258701, 2001. pages 160, 182

[546] N. Patel and M.-M. Poo. Orientation of neurite growth by extracellular electric fields. *Journal of Neuroscience*, 2(4):483–496, 1982. pages 198

[547] M. Penttonen and G. Buzsáki. Natural logarithmic relationship between brain oscillators. *Thalamus & Related Systems*, 2(02):145–152, 2003. pages 12

[548] T. Petermann, T. C. Thiagarajan, M. A. Lebedev, M. A. Nicolelis, D. R. Chialvo, and D. Plenz. Spontaneous cortical activity in awake monkeys composed of neuronal avalanches. *Proceedings of the National Academy of Sciences*, 106(37):15921–15926, 2009. pages 11

[549] L. Pezard, R. Jech, and E. Růžička. Investigation of non-linear properties of multichannel eeg in the early stages of parkinson's disease. *Clinical Neurophysiology*, 112(1):38–45, 2001. pages 147

[550] J. Pijn. Quantitative evaluation of eeg signals in epilepsy. *University of Amsterdam, Amsterdam*, 1990. pages 17, 147

[551] J. P. M. Pijn, D. N. Velis, M. J. van der Heyden, J. DeGoede, C. W. van Veelen, and F. H. L. da Silva. Nonlinear dynamics of epileptic seizures on basis of intracranial eeg recordings. *Brain topography*, 9(4):249–270, 1997. pages 17, 147

[552] S. M. Pincus, T. R. Cummins, and G. G. Haddad. Heart rate control in normal and aborted-sids infants. *American Journal of Physiology-Regulatory, Integrative and Comparative Physiology*, 264(3):R638–R646, 1993. pages 147

[553] J. Pine. Recording action potentials from cultured neurons with extracellular microcircuit electrodes. *Journal of neuroscience methods*, 2(1):19–31, 1980. pages 22

[554] A. Pini. Chemorepulsion of axons in the developing mammalian central nervous system. *Science*, 261(5117):95–98, 1993. pages 51

[555] P. F. Pinsky and J. Rinzel. Intrinsic and network rhythmogenesis in a reduced traub model for ca3 neurons. *Journal of computational neuroscience*, 1(1-2):39–60, 1994. pages 45

[556] D. J. Pinto, S. L. Patrick, W. C. Huang, and B. W. Connors. Initiation, propagation, and termination of epileptiform activity in rodent neocortex in vitro involve distinct mechanisms. *The Journal of neuroscience*, 25(36):8131–8140, 2005. pages 18

[557] M. Piraveenan, M. Prokopenko, and A. Zomaya. Assortative mixing in directed biological networks. *IEEE/ACM Transactions on Computational Biology and Bioinformatics (TCBB)*, 9(1):66–78, 2012. pages 186, 197

[558] D. Plenz and T. C. Thiagarajan. The organizing principles of neuronal avalanches: cell assemblies in the cortex? *Trends in neurosciences*, 30(3):101–110, 2007. pages 11

[559] A. Polsky, B. W. Mel, and J. Schiller. Computational subunits in thin dendrites of pyramidal cells. *Nature neuroscience*, 7(6):621–627, 2004. pages 43, 48

[560] R. Porter, S. Ghosh, G. D. Lange, and T. Smith. A fractal analysis of pyramidal neurons in mammalian motor cortex. *Neuroscience letters*, 130(1):112–116, 1991. pages 47

[561] M. I. Posner and M. K. Rothbart. Constructing neuronal theories of mind. *Large-scale neuronal theories of the brain*, pages 183–199, 1994. pages 6

[562] S. M. Potter and T. B. DeMarse. A new approach to neural cell culture for long-term studies. *Journal of neuroscience methods*, 110(1):17–24, 2001. pages 23

[563] T. Powell. Certain aspects of the intrinsic organization of the cerebral cortex. *Brain mechanisms and perceptual awareness*, pages 1–19, 1981. pages 5

[564] R. C. Prim. Shortest connection networks and some generalizations. *Bell system technical journal*, 36(6):1389–1401, 1957. pages 43, 45

[565] W. S. Pritchard, D. W. Duke, and K. K. Krieble. Dimensional analysis of resting human eeg ii: Surrogate-data testing indicates nonlinearity but not low-dimensional chaos. *Psychophysiology*, 32(5):486–491, 1995. pages 147

[566] M. Prokopenko, F. Boschetti, and A. J. Ryan. An information-theoretic primer on complexity, self-organization, and emergence. *Complexity*, 15(1):11–28, 2009. pages ii

[567] M. Rabinovich and H. Abarbanel. The role of chaos in neural systems. *Neuroscience*, 87(1):5–14, 1998. pages 15

[568] P. Rakic. Contact regulation of neuronal migration. *The Cell in Contact: Adhesions and Junctions as Morphogenetic Determinants*, pages 67–91, 1985. pages 22

[569] P. Rakic. Specification of cerebral cortical areas. *Science*, 241(4862):170–176, 1988. pages 22

[570] P. Rakic. Radial versus tangential migration of neuronal clones in the developing cerebral cortex. *PROCEEDINGS-NATIONAL ACADEMY OF SCIENCES USA*, 92:11323–11327, 1995. pages 5

[571] P. Rakic, J.-P. Bourgeois, M. F. Eckenhoff, N. Zecevic, and P. S. Goldman-Rakic. Concurrent overproduction of synapses in diverse regions of the primate cerebral cortex. *Science*, 232(4747):232–235, 1986. pages 5

[572] W. Rall. Branching dendritic trees and motoneuron membrane resistivity. *Experimental neurology*, 1(5):491–527, 1959. pages 43

[573] W. Rall. Theoretical significance of dendritic trees for neuronal input-output relations. *Neural theory and modeling*, pages 73–97, 1964. pages 43

[574] S. Ramn y Cajal. La rtine des vertbrs. *La Cellule*, 9:121–255, 1892. pages 51

[575] S. Ramn y Cajal. *Textura del Sistema Nervioso del Hombre y de los Vertebrados*, volume 2. Madrid Nicolas Moya, 1904. pages ii, 1, 182

[576] D. Rangaprakash. Connectivity analysis of multichannel eeg signals using recurrence based phase synchronization technique. *Computers in biology and medicine*, 46:11–21, 2014. pages 199

[577] T. S. Rao and M. Gabr. *An introduction to bispectral analysis and bilinear time series models*, volume 24. Springer Science & Business Media, 2012. pages 126

[578] P. Rapp, I. Zimmerman, A. Albano, G. Deguzman, and N. Greenbaun. Dynamics of spontaneous neural activity in the simian motor cortex: The dimension of chaotic neurons. *Physics Letters A*, 110(6):335–338, 1985. pages 14

[579] P. Rapp, I. Zimmerman, A. Albano, N. Greenbaun, T. Bashore, et al. Experimental studies of chaotic neural behavior: cellular activity and electroencephalographic signals. In *Nonlinear oscillations in biology and chemistry*, pages 175–205. Springer, 1986. pages 14

[580] W. Ray, R. Wells, T. Elbert, W. Lutzenberger, and N. Birbaumer. Eeg and chaos: Dimensional estimation of sensory and hypnotic processes. *Measuring Chaos in the Human Brain, edited by D. Duke and W. Pritchard. Singapore: World Scientific*, pages 199–215, 1991. pages 14

[581] S. Redner. How popular is your paper? an empirical study of the citation distribution. *The European Physical Journal B-Condensed Matter and Complex Systems*, 4(2):131–134, 1998. pages 184

[582] J. Ren, Y. Aika, C. Heizmann, and T. Kosaka. Quantitative analysis of neurons and glial cells in the rat somatosensory cortex, with special reference to gabaergic neurons and parvalbumin-containing neurons. *Experimental brain research*, 92(1):1–14, 1992. pages 22

[583] M. Rey and P. Guillemant. Apport des mathématiques non-linéaires (théorie du chaos) à l'analyse de l'eeg. *Neurophysiologie Clinique/Clinical Neurophysiology*, 27(5):406–428, 1997. pages 14

[584] K. A. Richardson, T. T. Imhoff, P. Grigg, and J. J. Collins. Using electrical noise to enhance the ability of humans to detect subthreshold mechanical cutaneous stimuli. *Chaos: An Interdisciplinary Journal of Nonlinear Science*, 8(3):599–603, 1998. pages 16

[585] J. L. Ringo, R. W. Doty, S. Demeter, and P. Y. Simard. Time is of the essence: a conjecture that hemispheric specialization arises from interhemispheric conduction delay. *Cerebral Cortex*, 4(4):331–343, 1994. pages 5

[586] P. Robinson, J. Henderson, E. Matar, P. Riley, and R. Gray. Dynamical reconnection and stability constraints on cortical network architecture. *Physical review letters*, 103(10):108104, 2009. pages 190

[587] N. L. Rochefort, H. Jia, and A. Konnerth. Calcium imaging in the living brain: prospects for molecular medicine. *Trends in molecular medicine*, 14(9):389–399, 2008. pages 28, 198

[588] A. Rockel, R. W. Hiorns, and T. Powell. The basic uniformity in structure of the neocortex. *Brain: a journal of neurology*, 103(2):221–244, 1980. pages 5, 180

[589] I. Rodríguez-Iturbe and A. Rinaldo. *Fractal river basins: chance and self-organization*. Cambridge University Press, 2001. pages 190

[590] B. Roerig and M. B. Feller. Neurotransmitters and gap junctions in developing neural circuits. *Brain research reviews*, 32(1):86–114, 2000. pages 23

[591] J. D. Rolston, D. A. Wagenaar, and S. M. Potter. Precisely timed spatiotemporal patterns of neural activity in dissociated cortical cultures. *Neuroscience*, 148(1):294–303, 2007. pages 156

[592] S. Rombouts, R. Keunen, and C. Stam. Investigation of nonlinear structure in multichannel eeg. *Physics Letters A*, 202(5):352–358, 1995. pages 147

[593] B. Rörig and B. Sutor. Regulation of gap junction coupling in the developing neocortex. *Molecular neurobiology*, 12(3):225–249, 1996. pages 23

[594] J. Röschke. *Eine Analyse der nichtlinearen EEG-Dynamik*. na, 1986. pages 15

[595] J. Röschke and E. Basar. Is eeg a simple noise or a strange attractor. *Pflügers Arch*, 405(2):R45, 1985. pages 15

[596] J. Röschke and E. Başar. The eeg is not a simple noise: strange attractors in intracranial structures. In *Dynamics of sensory and cognitive processing by the brain*, pages 203–216. Springer, 1988. pages 15

[597] J. Röschke and E. Başar. Correlation dimensions in various parts of cat and human brain in different states. In *Chaos in brain function*, pages 92–109. Springer, 1990. pages 15

[598] E. F. Ryder, L. Bullard, J. Hone, J. Olmstead, and M. O. Ward. Graphical simulation of early development of the cerebral cortex. *Computer methods and programs in biomedicine*, 59(2):107–114, 1999. pages 43

[599] J. Sackellares, L. Iasemidis, H. Zaveri, and W. Williams. Measurement of chaos to localize seizure onset. *Epilepsia*, 30(5):663, 1989. pages 147

[600] J. Sackellares, L. Iasemidis, H. Zaveri, W. Williams, and T. Hood. Inference on the chaotic behavior of the epileptogenic focus. In *Epilepsia*, volume 29, pages 682–682. LIPPINCOTT-RAVEN PUBL 227 EAST WASHINGTON SQ, PHILADELPHIA, PA 19106, 1988. pages 17, 147

[601] S. Sadaghiani, G. Hesselmann, K. J. Friston, and A. Kleinschmidt. The relation of ongoing brain activity, evoked neural responses, and cognition. *Frontiers in systems neuroscience*, 4:20, 2010. pages 17

[602] K. Saermark, J. Lebech, C. Bak, and A. Sabers. Magnetoencephalography and attractor dimension: normal subjects and epileptic patients. In *Brain Dynamics*, pages 149–157. Springer, 1989. pages 14, 147

[603] R. Salvador, J. Suckling, M. R. Coleman, J. D. Pickard, D. Menon, and E. Bullmore. Neurophysiological architecture of functional magnetic resonance images of human brain. *Cerebral cortex*, 15(9):1332–1342, 2005. pages 6, 183

[604] A. V. Samsonovich and G. A. Ascoli. Statistical determinants of dendritic morphology in hippocampal pyramidal neurons: a hidden markov model. *Hippocampus*, 15(2):166–183, 2005. pages 43

[605] D. C. Samuels, H. Hentschel, and A. Fine. The origin of neuronal polarization: a model of axon formation. *Philosophical Transactions of the Royal Society B: Biological Sciences*, 351(1344):1147–1156, 1996. pages 43

[606] M. V. Sanchez-Vives and D. A. McCormick. Cellular and network mechanisms of rhythmic recurrent activity in neocortex. *Nature neuroscience*, 3(10):1027–1034, 2000. pages 23

[607] L. Sander, C. Warren, I. Sokolov, C. Simon, and J. Koopman. Percolation on heterogeneous networks as a model for epidemics. *Mathematical biosciences*, 180(1):293–305, 2002. pages 187

[608] S. Sarbadhikari and K. Chakrabarty. Chaos in the brain: a short review alluding to epilepsy, depression, exercise and lateralization. *Medical engineering & physics*, 23(7):447–457, 2001. pages 14

[609] T. Sasaki, N. Takahashi, N. Matsuki, and Y. Ikegaya. Fast and accurate detection of action potentials from somatic calcium fluctuations. *Journal of neurophysiology*, 100(3):1668–1676, 2008. pages 85, 110

[610] T. Sauer. Reconstruction of dynamical systems from interspike intervals. *Physical Review Letters*, 72(24):3811, 1994. pages 88, 91

[611] T. Sauer, J. A. Yorke, and M. Casdagli. Embedology. *Journal of statistical Physics*, 65(3-4):579–616, 1991. pages 88, 91, 96

[612] C. Schmeltzer, A. H. Kihara, I. M. Sokolov, and S. Rüdiger. Degree correlations optimize neuronal network sensitivity to sub-threshold stimuli. *PloS one*, 10(6):e0121794, 2015. pages 184, 185, 196

[613] C. Schmeltzer, J. Soriano, I. Sokolov, and S. Rüdiger. Percolation of spatially constrained erdős-rényi networks with degree correlations. *Physical Review E*, 89(1):012116, 2014. pages 184, 185, 187, 196, 197

[614] A. Schnitzler and J. Gross. Normal and pathological oscillatory communication in the brain. *Nature reviews neuroscience*, 6(4):285–296, 2005. pages 14

[615] T. Schreiber. Measuring information transfer. *Physical review letters*, 85(2):461, 2000. pages 153, 154

[616] T. Schreiber and A. Schmitz. Improved surrogate data for nonlinearity tests. *Physical Review Letters*, 77(4):635, 1996. pages 124, 126

[617] T. Schreiber and A. Schmitz. Discrimination power of measures for nonlinearity in a time series. *Physical Review E*, 55(5):5443, 1997. pages 126

[618] T. Schreiber and A. Schmitz. Surrogate time series. *Physica D: Nonlinear Phenomena*, 142(3):346–382, 2000. pages 105, 124

[619] D. Schubert, J. F. Staiger, N. Cho, R. Kötter, K. Zilles, and H. J. Luhmann. Layer-specific intracolumnar and transcolumnar functional connectivity of layer v pyramidal cells in rat barrel cortex. *The Journal of Neuroscience*, 21(10):3580–3592, 2001. pages 45

[620] A. Schüz and G. Palm. Density of neurons and synapses in the cerebral cortex of the mouse. *Journal of Comparative Neurology*, 286(4):442–455, 1989. pages 5

[621] N. Schwartz, R. Cohen, D. Ben-Avraham, A.-L. Barabási, and S. Havlin. Percolation in directed scale-free networks. *Physical Review E*, 66(1):015104, 2002. pages 185

[622] N. Seeds. Cell-cell recognition events influence neuronal maturation in brain cell reaggregates. *International Journal of Developmental Neuroscience*, 1(3):195, 1983. pages 23, 198

[623] W. W. Seeley, R. K. Crawford, J. Zhou, B. L. Miller, and M. D. Greicius. Neurodegenerative diseases target large-scale human brain networks. *Neuron*, 62(1):42–52, 2009. pages 17

[624] I. Segev and E. Schneidman. Axons as computing devices: basic insights gained from models. *Journal of Physiology-Paris*, 93(4):263–270, 1999. pages 43, 48

[625] R. Segev, Y. Shapira, M. Benveniste, and E. Ben-Jacob. Observations and modeling of synchronized bursting in two-dimensional neural networks. *Physical Review E*, 64(1):011920, 2001. pages 23

[626] P. O. Seglen. The skewness of science. *Journal of the American Society for Information Science*, 43(9):628, 1992. pages 184

[627] M. Á. Serrano and M. Boguná. Clustering in complex networks. ii. percolation properties. *Physical Review E*, 74(5):056115, 2006. pages 160

[628] R. Shalbaf, H. Behnam, J. W. Sleigh, D. A. Steyn-Ross, and M. L. Steyn-Ross. Frontal-temporal synchronization of eeg signals quantified by order patterns cross recurrence analysis during propofol anesthesia. *IEEE Transactions on Neural Systems and Rehabilitation Engineering*, 23(3):468–474, 2015. pages 199

[629] M. Shanahan. Dynamical complexity in small-world networks of spiking neurons. *Physical Review E*, 78(4):041924, 2008. pages 189

[630] M. Shanahan. Metastable chimera states in community-structured oscillator networks. *Chaos: An Interdisciplinary Journal of Nonlinear Science*, 20(1):013108, 2010. pages 189

[631] R. Shaw. The dripping faucet as a model chaotic system. 1984. pages 99, 133, 194

[632] B. W. Sheasby and J. F. Fohlmeister. Impulse encoding across the dendritic morphologies of retinal ganglion cells. *Journal of neurophysiology*, 81(4):1685–1698, 1999. pages 45

[633] O. Shefi, I. Golding, R. Segev, E. Ben-Jacob, and A. Ayali. Morphological characterization of in vitro neuronal networks. *Physical Review E*, 66(2):021905, 2002. pages 181

[634] D. Shelton. Membrane resistivity estimated for the purkinje neuron by means of a passive computer model. *Neuroscience*, 14(1):111–131, 1985. pages 43

[635] S. S. Shen-Orr, R. Milo, S. Mangan, and U. Alon. Network motifs in the transcriptional regulation network of escherichia coli. *Nature genetics*, 31(1):64–68, 2002. pages 161

[636] G. M. Shepherd. *The synaptic organization of the brain*. Oxford University Press, 2003. pages 46, 189

[637] S. M. Sherman and R. Guillery. On the actions that one nerve cell can have on another: distinguishing drivers from modulators. *Proceedings of the National Academy of Sciences*, 95(12):7121–7126, 1998. pages 188

[638] T. Shinbrot. Simulated morphogenesis of developmental folds due to proliferative pressure. *Journal of theoretical biology*, 242(3):764–773, 2006. pages 43

[639] R. Shirasaki, A. Tamada, R. Katsumata, and F. Murakami. Guidance of cerebellofugal axons in the rat embryo: directed growth toward the floor plate and subsequent elongation along the longitudinal axis. *Neuron*, 14(5):961–972, 1995. pages 51

[640] D. Shoham, M. Hübener, S. Schulze, A. Grinvald, and T. Bonhoeffer. Spatio–temporal frequency domains and their relation to cytochrome oxidase staining in cat visual cortex. *Nature*, 385(6616):529–533, 1997. pages 3

[641] G. Siganos, M. Faloutsos, P. Faloutsos, and C. Faloutsos. Power laws and the as-level internet topology. *IEEE/ACM Transactions on Networking (TON)*, 11(4):514–524, 2003. pages 181

[642] C. Silva, I. R. Pimentel, A. Andrade, J. P. Foreid, and E. Ducla-Soares. Correlation dimension maps of eeg from epileptic absences. *Brain topography*, 11(3):201–209, 1999. pages 17, 147

[643] H. Simon and H. H. Pattee. Hierarchy theory: The challenge of complex systems. *Hierarchy Theory: The Challenge of Complex Systems*, 1973. pages 190

[644] H. A. Simon. The architecture of complexity. *General systems*, 10(1965):63–76, 1965. pages 190

[645] H. A. Simon. The architecture of complexity. In *Facets of systems science*, pages 457–476. Springer, 1991. pages 189, 190

[646] E. Simonotto, M. Riani, C. Seife, M. Roberts, J. Twitty, and F. Moss. Visual perception of stochastic resonance. *Physical review letters*, 78(6):1186, 1997. pages 16

[647] C. A. Skarda and W. J. Freeman. How brains make chaos in order to make sense of the world. *Behavioral and brain sciences*, 10(02):161–173, 1987. pages 14

[648] J. E. Skinner, A. L. Goldberger, G. Mayer-Kress, and R. E. Ideker. Chaos in the heart: implications for clinical cardiology. *Nature Biotechnology*, 8(11):1018–1024, 1990. pages 147

[649] J. E. Skinner, M. Molnar, T. Vybiral, and M. Mitra. Application of chaos theory to biology and medicine. *Integrative Physiological and Behavioral Science*, 27(1):39–53, 1992. pages 14

[650] M. Small. *Applied nonlinear time series analysis: applications in physics, physiology and finance*, volume 52. World Scientific, 2005. pages 90

[651] D. Smetters, A. Majewska, and R. Yuste. Detecting action potentials in neuronal populations with calcium imaging. *Methods*, 18(2):215–221, 1999. pages 28, 198

[652] J. Snider, A. Pillai, and C. F. Stevens. A universal property of axonal and dendritic arbors. *Neuron*, 66(1):45–56, 2010. pages 41, 47, 52

[653] F. Solomon. Specification of cell morphology by endogenous determinants. *The Journal of cell biology*, 90(3):547–553, 1981. pages 23

[654] P. Somogyi, G. Tamas, R. Lujan, and E. H. Buhl. Salient features of synaptic organisation in the cerebral cortex. *Brain research reviews*, 26(2):113–135, 1998. pages 6

[655] C. Song, S. Havlin, and H. A. Makse. Fractal growth of complex networks: repulsion between hubs. *arXiv preprint cond-mat/0507216*, 2005. pages 183

[656] C. Song, S. Havlin, and H. A. Makse. Origins of fractality in the growth of complex networks. *Nature Physics*, 2(4):275–281, 2006. pages 183

[657] S. Song, P. J. Sjöström, M. Reigl, S. Nelson, and D. B. Chklovskii. Highly nonrandom features of synaptic connectivity in local cortical circuits. *PLoS Biol*, 3(3):e68, 2005. pages 181

[658] V. Sood, S. Redner, and D. Ben-Avraham. First-passage properties of the erdős–renyi random graph. *Journal of Physics A: Mathematical and General*, 38(1):109, 2004. pages 187

[659] A. C. Soong and C. I. Stuart. Evidence of chaotic dynamics underlying the human alpha-rhythm electroencephalogram. *Biological cybernetics*, 62(1):55–62, 1989. pages 14, 147

[660] J. Soriano, M. R. Martínez, T. Tlusty, and E. Moses. Development of input connections in neural cultures. *Proceedings of the National Academy of Sciences*, 105(37):13758–13763, 2008. pages 21, 22, 24, 35, 36, 69, 71, 85, 175, 180, 187, 198

[661] R. Sorkin, T. Gabay, P. Blinder, D. Baranes, E. Ben-Jacob, and Y. Hanein. Compact self-wiring in cultured neural networks. *Journal of neural engineering*, 3(2):95, 2006. pages 26

[662] H. Soula, G. Beslon, and O. Mazet. Spontaneous dynamics of asymmetric random recurrent spiking neural networks. *Neural Computation*, 18(1):60–79, 2006. pages 15

[663] O. Sporns, C. J. Honey, and R. Kötter. Identification and classification of hubs in brain networks. *PloS one*, 2(10):e1049, 2007. pages 181, 188

[664] O. Sporns and R. Kötter. Motifs in brain networks. *PLoS Biol*, 2(11):e369, 2004. pages 6, 183, 186

[665] O. Sporns and G. Tononi. Classes of network connectivity and dynamics. *Complexity*, 7(1):28–38, 2001. pages 6, 183

[666] O. Sporns, G. Tononi, and G. M. Edelman. Theoretical neuroanatomy: relating anatomical and functional connectivity in graphs and cortical connection matrices. *Cerebral Cortex*, 10(2):127–141, 2000. pages 6, 183

[667] O. Sporns and J. D. Zwi. The small world of the cerebral cortex. *Neuroinformatics*, 2(2):145–162, 2004. pages 6, 183

[668] K. V. Srinivas, R. Jain, S. Saurav, and S. K. Sikdar. Small-world network topology of hippocampal neuronal network is lost, in an in vitro glutamate injury model of epilepsy. *European Journal of Neuroscience*, 25(11):3276–3286, 2007. pages 181

[669] R. Srinivasan, D. P. Russell, G. M. Edelman, and G. Tononi. Increased synchronization of neuromagnetic responses during conscious perception. *The Journal of Neuroscience*, 19(13):5435–5448, 1999. pages 3

[670] C. Stam, B. Jones, G. Nolte, M. Breakspear, and P. Scheltens. Small-world networks and functional connectivity in alzheimer's disease. *Cerebral cortex*, 17(1):92–99, 2007. pages 17, 181

[671] C. Stam, J. Pijn, P. Suffczynski, and F. L. Da Silva. Dynamics of the human alpha rhythm: evidence for non-linearity? *Clinical Neurophysiology*, 110(10):1801–1813, 1999. pages 147

[672] C. J. Stam. Chaos, continuous eeg, and cognitive mechanisms: a future for clinical neurophysiology. *American journal of electroneurodiagnostic technology*, 43(4):211–227, 2003. pages 14

[673] C. J. Stam. Nonlinear dynamical analysis of eeg and meg: review of an emerging field. *Clinical neurophysiology*, 116(10):2266–2301, 2005. pages 87, 147

[674] C. J. Stam, T. Van Woerkom, and R. Keunen. Non-linear analysis of the electroencephalogram in creutzfeldt-jakob disease. *Biological cybernetics*, 77(4):247–256, 1997. pages 147

[675] A. Stepanyants, J. A. Hirsch, L. M. Martinez, Z. F. Kisvárday, A. S. Ferecskó, and D. B. Chklovskii. Local potential connectivity in cat primary visual cortex. *Cerebral Cortex*, 18(1):13–28, 2008. pages 43

[676] O. Stetter, D. Battaglia, J. Soriano, and T. Geisel. Model-free reconstruction of excitatory neuronal connectivity from calcium imaging signals. *PLoS Comput Biol*, 8(8):e1002653, 2012. pages 85, 151, 155, 170, 180, 181, 188, 197

[677] C. F. Stevens. How cortical interconnectedness varies with network size. *Neural computation*, 1(4):473–479, 1989. pages 5

[678] D. B. C. C. F. Stevens. Wiring optimization in the brain. In *Advances in Neural Information Processing Systems 12: Proceedings of the 1999 Conference*, volume 12, page 103. MIT Press, 2000. pages 4, 5

[679] C. V. Stewart and D. Plenz. Inverted-u profile of dopamine–nmda-mediated spontaneous avalanche recurrence in superficial layers of rat prefrontal cortex. *The Journal of neuroscience*, 26(31):8148–8159, 2006. pages 11

[680] C. Stosiek, O. Garaschuk, K. Holthoff, and A. Konnerth. In vivo two-photon calcium imaging of neuronal networks. *Proceedings of the National Academy of Sciences*, 100(12):7319–7324, 2003. pages 29

[681] S. Stramaglia, G.-R. Wu, M. Pellicoro, and D. Marinazzo. Expanding the transfer entropy to identify information circuits in complex systems. *Physical Review E*, 86(6):066211, 2012. pages 199

[682] G. Strang. Wavelets. *American Scientist*, 82(3):250–255, 1994. pages 63

[683] G. M. Süel, J. Garcia-Ojalvo, L. M. Liberman, and M. B. Elowitz. An excitable gene regulatory circuit induces transient cellular differentiation. *Nature*, 440(7083):545–550, 2006. pages 181

[684] Q. Sun. The missing piece in the"use it or lose it"puzzle: Is inhibition regulated by activity or does it act on its own accord? *Reviews in the Neurosciences*, 18(3/4):295, 2007. pages 7

[685] B. Sutor. Gap junctions and their implications for neurogenesis and maturation of synaptic circuitry in the developing neocortex. In *Cortical Development*, pages 53–73. Springer, 2002. pages 23

[686] L. O. Svaasand and R. Ellingsen. Optical properties of human brain. *Photochemistry and photobiology*, 38(3):293–299, 1983. pages 31

[687] J. Symanzik, G. A. Ascoli, S. D. Washington, and J. L. Krichmar. Visual data mining of brain cells. In *Computing Science and Statistics*. Citeseer, 1999. pages 45

[688] B. Szende and E. Tyihák. Effect of formaldehyde on cell proliferation and death. *Cell biology international*, 34(12):1273–1282, 2010. pages 36

[689] F. Takens. *Detecting strange attractors in turbulence*. Springer, 1981. pages 88, 90, 91, 95, 96, 194

[690] D. W. Tank, M. Sugimori, J. A. Connor, and R. R. Llinas. Spatially resolved calcium dynamics of mammalian purkinje cells in cerebellar slice. *Science*, 242(4879):773–777, 1988. pages 31

[691] C. M. Teeter and C. F. Stevens. A general principle of neural arbor branch density. *Current Biology*, 21(24):2105–2108, 2011. pages 41, 47, 52

[692] S. Teller, C. Granell, M. De Domenico, J. Soriano, S. Gómez, and A. Arenas. Emergence of assortative mixing between clusters of cultured neurons. *PLoS Comput Biol*, 10(9):e1003796, 2014. pages 160, 181, 185, 186

[693] J.-n. Teramae and T. Fukai. Local cortical circuit model inferred from power-law distributed neuronal avalanches. *Journal of computational neuroscience*, 22(3):301–312, 2007. pages 11

[694] M. Tessier-Lavigne and C. S. Goodman. The molecular biology of axon guidance. *Science*, 274(5290):1123, 1996. pages 50, 182

[695] C. Tetzlaff, S. Okujeni, U. Egert, F. Wörgötter, and M. Butz. Self-organized criticality in developing neuronal networks. *PLoS Comput Biol*, 6(12):e1001013, 2010. pages 18

[696] J. Theiler. Spurious dimension from correlation algorithms applied to limited time-series data. *Physical review A*, 34(3):2427, 1986. pages 111, 120

[697] J. Theiler. Estimating fractal dimension. *JOSA A*, 7(6):1055–1073, 1990. pages 120

[698] J. Theiler. On the evidence for low-dimensional chaos in an epileptic electroencephalogram. *Physics Letters A*, 196(1):335–341, 1994. pages 17, 147

[699] J. Theiler, S. Eubank, A. Longtin, B. Galdrikian, and J. D. Farmer. Testing for nonlinearity in time series: the method of surrogate data. *Physica D: Nonlinear Phenomena*, 58(1-4):77–94, 1992. pages 124, 125, 126, 127, 128, 156

[700] J. Theiler and D. Prichard. Constrained-realization monte-carlo method for hypothesis testing. *Physica D: Nonlinear Phenomena*, 94(4):221–235, 1996. pages 124

[701] J. P. Theiler. Quantifying chaos: practical estimation of the correlation dimension. Technical report, California Inst. of Tech., Pasadena, CA (USA), 1988. pages 125

[702] M. Thiel, M. C. Romano, J. Kurths, R. Meucci, E. Allaria, and F. T. Arecchi. Influence of observational noise on the recurrence quantification analysis. *Physica D: Nonlinear Phenomena*, 171(3):138–152, 2002. pages 112, 113

[703] C. Thomas, P. Springer, G. Loeb, Y. Berwald-Netter, and L. Okun. A miniature microelectrode array to monitor the bioelectric activity of cultured cells. *Experimental cell research*, 74(1):61–66, 1972. pages 28, 198

[704] S. Thurner, C. Windischberger, E. Moser, P. Walla, and M. Barth. Scaling laws and persistence in human brain activity. *Physica A: Statistical Mechanics and its Applications*, 326(3):511–521, 2003. pages 84

[705] E. Tibau, C. Bendiksen, S. Teller, N. Amigo, J. Soriano, P. L. Garrido, J. Marro, J. J. Torres, and J. Cortés. Interplay activity-connectivity: dynamics in patterned neuronal cultures. In *AIP Conference Proceedings*, volume 1510, pages 54–63. AIP, 2013. pages 84

[706] J. Timmer, C. Gantert, G. Deuschl, and J. Honerkamp. Characteristics of hand tremor time series. *Biological cybernetics*, 70(1):75–80, 1993. pages 127

[707] H. Tong. *Non-linear time series: a dynamical system approach*. Oxford University Press, 1990. pages 90

[708] G. Tononi, G. M. Edelman, and O. Sporns. Complexity and coherency: integrating information in the brain. *Trends in cognitive sciences*, 2(12):474–484, 1998. pages 3

[709] G. Tononi, O. Sporns, and G. M. Edelman. A measure for brain complexity: relating functional segregation and integration in the nervous system. *Proceedings of the National Academy of Sciences*, 91(11):5033–5037, 1994. pages 3

[710] M. G. Toro, J. S. Ruiz, J. A. Talavera, and C. Blanco. Chaos theories and therapeutic commonalities among depression, parkinson's disease, and cardiac arrhythmias. *Comprehensive psychiatry*, 40(3):238–244, 1999. pages 17, 147

[711] J. J. Torres, M. A. Munoz, J. Marro, and P. Garrido. Influence of topology on the performance of a neural network. *Neurocomputing*, 58:229–234, 2004. pages 185, 186

[712] R. D. Traub, J. Jefferys, R. Miles, M. Whittington, and K. Toth. A branching dendritic model of a rodent ca3 pyramidal neurone. *The Journal of Physiology*, 481(Pt 1):79, 1994. pages 45

[713] R. D. Traub, R. Wong, R. Miles, and H. Michelson. A model of a ca3 hippocampal pyramidal neuron incorporating voltage-clamp data on intrinsic conductances. *Journal of Neurophysiology*, 66(2):635–650, 1991. pages 45

[714] L. Trulla, A. Giuliani, J. Zbilut, and C. Webber. Recurrence quantification analysis of the logistic equation with transients. *Physics Letters A*, 223(4):255–260, 1996. pages 89, 117, 119

[715] Y. Tsau, L. Guan, and J.-Y. Wu. Initiation of spontaneous epileptiform activity in the neocortical slice. *Journal of neurophysiology*, 80(2):978–982, 1998. pages 18

[716] R. Y. Tsien. A non-disruptive technique for loading calcium buffers and indicators into cells. 1981. pages 31

[717] M. Tsodyks, T. Kenet, A. Grinvald, and A. Arieli. Linking spontaneous activity of single cortical neurons and the underlying functional architecture. *Science*, 286(5446):1943–1946, 1999. pages 17

[718] M. Tsodyks, A. Uziel, H. Markram, et al. Synchrony generation in recurrent networks with frequency-dependent synapses. *J Neurosci*, 20(1):825–835, 2000. pages 56

[719] M. V. Tsodyks and H. Markram. The neural code between neocortical pyramidal neurons depends on neurotransmitter release probability. *Proceedings of the National Academy of Sciences*, 94(2):719–723, 1997. pages 56

[720] D. Turner, X.-G. Li, G. Pyapali, A. Ylinen, and G. Buzsaki. Morphometric and electrical properties of reconstructed hippocampal ca3 neurons recorded in vivo. *Journal of Comparative Neurology*, 356(4):580–594, 1995. pages 45

[721] P. J. Uhlhaas and W. Singer. Neuronal dynamics and neuropsychiatric disorders: toward a translational paradigm for dysfunctional large-scale networks. *Neuron*, 75(6):963–980, 2012. pages 17

[722] A. Van Ooyen, J. Duijnhouwer, M. W. Remme, and J. van Pelt. The effect of dendritic topology on firing patterns in model neurons. *Network: Computation in neural systems*, 13(3):311–325, 2002. pages 43

[723] A. van Ooyen and D. J. Willshaw. Competition for neurotrophic factor in the development of nerve connections. *Proceedings of the Royal Society of London B: Biological Sciences*, 266(1422):883–892, 1999. pages 43

[724] J. Van Pelt, M. Corner, P. Wolters, W. Rutten, and G. Ramakers. Longterm stability and developmental changes in spontaneous network burst firing patterns in dissociated rat cerebral cortex cell cultures on multielectrode arrays. *Neuroscience letters*, 361(1):86–89, 2004. pages 22, 85

[725] J. van Pelt, M. Kamermans, C. N. Levelt, A. van Ooyen, G. J. Ramakers, and P. Roelfsema. *Development, Dynamics and Pathology of Neuronal Networks: From Molecules to Functional Circuits: Proceedings of the 23rd International Summer*

School of Brain Research, Held at the Royal Netherlands Academy of Arts and Sciences, Amsterdam, The Netherland, 25-29 August 2003. Elsevier, 2005. pages 43

[726] J. van Pelt and A. van Ooyen. Estimating neuronal connectivity from axonal and dendritic density fields. *Frontiers in computational neuroscience*, 7:160, 2013. pages 47

[727] J. Van Pelt and R. Verwer. The exact probabilities of branching patterns under terminal and segmental growth hypotheses. *Bulletin of mathematical biology*, 45(2):269–285, 1983. pages 43

[728] J. van Pelt, P. S. Wolters, M. A. Corner, W. L. Rutten, and G. J. Ramakers. Long-term characterization of firing dynamics of spontaneous bursts in cultured neural networks. *IEEE Transactions on Biomedical Engineering*, 51(11):2051–2062, 2004. pages 22, 84, 85

[729] C. van Vreeswijk. Partial synchronization in populations of pulse-coupled oscillators. *Physical Review E*, 54(5):5522, 1996. pages 145

[730] F. Varela, J.-P. Lachaux, E. Rodriguez, and J. Martinerie. The brainweb: phase synchronization and large-scale integration. *Nature reviews neuroscience*, 2(4):229–239, 2001. pages 14

[731] R. Vautard, P. Yiou, and M. Ghil. Singular-spectrum analysis: A toolkit for short, noisy chaotic signals. *Physica D: Nonlinear Phenomena*, 58(1):95–126, 1992. pages 109

[732] A. Vazquez. Spreading dynamics on small-world networks with connectivity fluctuations and correlations. *Physical Review E*, 74(5):056101, 2006. pages 185

[733] A. Vázquez, R. Pastor-Satorras, and A. Vespignani. Large-scale topological and dynamical properties of the internet. *Physical Review E*, 65(6):066130, 2002. pages 160

[734] G. Viana di Prisco and W. J. Freeman. Odor-related bulbar eeg spatial pattern analysis during appetitive conditioning in rabbits. *Behavioral neuroscience*, 99(5):964, 1985. pages 14

[735] J. L. Vincent, G. H. Patel, M. D. Fox, A. Z. Snyder, J. T. Baker, D. C. Van Essen, J. M. Zempel, L. H. Snyder, M. Corbetta, and M. E. Raichle. Intrinsic functional architecture in the anaesthetized monkey brain. *Nature*, 447(7140):83–86, 2007. pages 17

[736] J. T. Vogelstein, B. O. Watson, A. M. Packer, R. Yuste, B. Jedynak, and L. Paninski. Spike inference from calcium imaging using sequential monte carlo methods. *Biophysical journal*, 97(2):636–655, 2009. pages 56, 156

[737] T. Voigt, T. Opitz, and A. D. de Lima. Activation of early silent synapses by spontaneous synchronous network activity limits the range of neocortical connections. *The Journal of neuroscience*, 25(18):4605–4615, 2005. pages 188

[738] V. Volman, I. Baruchi, and E. Ben-Jacob. Manifestation of function-follow-form in cultured neuronal networks. *Physical biology*, 2(2):98, 2005. pages 18

[739] J. Von Neumann and R. Kurzweil. *The computer and the brain*. Yale University Press, 2012. pages 1

[740] G. Vrensen, D. De Groot, and J. Nunes-Cardozo. Postnatal development of neurons and synapses in the visual and motor cortex of rabbits: a quantitative light and electron microscopic study. *Brain research bulletin*, 2(6):405–416, 1977. pages 5

[741] D. A. Wagenaar, Z. Nadasdy, and S. M. Potter. Persistent dynamic attractors in activity patterns of cultured neuronal networks. *Physical Review E*, 73(5):051907, 2006. pages 84

[742] D. A. Wagenaar, J. Pine, and S. M. Potter. An extremely rich repertoire of bursting patterns during the development of cortical cultures. *BMC neuroscience*, 7(1):11, 2006. pages 18, 84, 85

[743] W.-X. Wang, B.-H. Wang, B. Hu, G. Yan, and Q. Ou. General dynamics of topology and traffic on weighted technological networks. *Physical review letters*, 94(18):188702, 2005. pages 182

[744] X. F. Wang and G. Chen. Synchronization in small-world dynamical networks. *International Journal of Bifurcation and Chaos*, 12(01):187–192, 2002. pages 188, 197

[745] S. D. Washington, G. A. Ascoli, and J. L. Krichmar. A statistical analysis of dendritic morphology's effect on neuron electrophysiology of ca3 pyramidal cells. *Neurocomputing*, 32:261–269, 2000. pages 45

[746] R. Watt and S. R. Hameroff. Phase space electroencephalography (eeg): a new mode of intraoperative eeg analysis. *International journal of clinical monitoring and computing*, 5(1):3–13, 1988. pages 14

[747] R. C. Watt and S. R. Hameroff. Phase space analysis of human eeg during general anesthesia. *Annals of the New York Academy of Sciences*, 504(1):286–288, 1987. pages 14

[748] D. J. Watts. *Small worlds: The dynamics of networks between order and randomness*. Princeton University Press, 2001. pages 182

[749] D. J. Watts and S. H. Strogatz. Collective dynamics of small-worldnetworks. *nature*, 393(6684):440–442, 1998. pages 6, 8, 159, 168, 181, 183

[750] C. L. Webber and J. P. Zbilut. Dynamical assessment of physiological systems and states using recurrence plot strategies. *Journal of applied physiology*, 76(2):965–973, 1994. pages 89, 116

[751] P. Welch. The use of fast fourier transform for the estimation of power spectra: a method based on time averaging over short, modified periodograms. *IEEE Transactions on audio and electroacoustics*, 15(2):70–73, 1967. pages 66

[752] M. Weliky, W. H. Bosking, and D. Fitzpatrick. A systematic map of direction preference in primary visual cortex. 1996. pages 3

[753] Q. Wen, A. Stepanyants, G. N. Elston, A. Y. Grosberg, and D. B. Chklovskii. Maximization of the connectivity repertoire as a statistical principle governing the shapes of dendritic arbors. *Proceedings of the National Academy of Sciences*, 106(30):12536–12541, 2009. pages 1, 7, 41, 43, 49, 52, 184, 197

[754] B. C. Wheeler and G. J. Brewer. Designing neural networks in culture. *Proceedings of the IEEE*, 98(3):398–406, 2010. pages 84

[755] H. Whitney. Differentiable manifolds. *Annals of Mathematics*, pages 645–680, 1936. pages 87, 90

[756] J. Whittaker. *Graphical models in applied multivariate statistics*. Wiley Publishing, 2009. pages 153

[757] M. Wibral, N. Pampu, V. Priesemann, F. Siebenhühner, H. Seiwert, M. Lindner, J. T. Lizier, and R. Vicente. Measuring information-transfer delays. *PloS one*, 8(2):e55809, 2013. pages 199

[758] N. Wiener. The theory of prediction. *Modern mathematics for engineers*, 1:125–139, 1956. pages 149

[759] D. J. Willshaw, O. P. Buneman, and H. C. Longuet-Higgins. Non-holographic associative memory. *Nature*, 1969. pages 8

[760] H. R. Wilson and J. D. Cowan. Excitatory and inhibitory interactions in localized populations of model neurons. *Biophysical journal*, 12(1):1, 1972. pages 145, 185, 188

[761] K. D. Wise and J. B. Angell. A low-capacitance multielectrode probe for use in extracellular neurophysiology. *Biomedical Engineering, IEEE Transactions on*, (3):212–219, 1975. pages 28, 198

[762] S. Wise, J. Fleshman, and E. Jones. Maturation of pyramidal cell form in relation to developing afferent and efferent connections of rat somatic sensory cortex. *Neuroscience*, 4(9):1275–1297, 1979. pages 45

[763] S. Wolfram. Statistical mechanics of cellular automata. *Reviews of modern physics*, 55(3):601, 1983. pages 10, 11

[764] S. Wolfram. Statistical mechanics of cellular automata. *Reviews of modern physics*, 55(3):601, 1983. pages 99

[765] C. N. Woolsey and E. M. Walzl. Topical projection of nerve fibers from local regions of the cochlea to the cerebral cortex of the cat. *Bull Johns Hopkins Hosp*, 71(315-344):127, 1942. pages 3

[766] R. Xulvi-Brunet and I. Sokolov. Construction and properties of assortative random networks. *arXiv preprint cond-mat/0405095*, 2004. pages 185, 189

[767] S. R. y Cajal. *Histology of the nervous system of man and vertebrates*, volume 1. Oxford University Press, USA, 1995. pages 181

[768] S.-J. Yang. Exploring complex networks by walking on them. *Physical Review E*, 71(1):016107, 2005. pages 187

[769] Y. Yao and W. J. Freeman. Model of biological pattern recognition with spatially chaotic dynamics. *Neural networks*, 3(2):153–170, 1990. pages 15

[770] E. Yavin and Z. Yavin. Attachment and culture of dissociated cells from rat embryo cerebral hemispheres on polylysine-coated surface. *The Journal of cell biology*, 62(2):540–546, 1974. pages 26

[771] O. Yizhar, L. E. Fenno, M. Prigge, F. Schneider, T. J. Davidson, D. J. OShea, V. S. Sohal, I. Goshen, J. Finkelstein, J. T. Paz, et al. Neocortical excitation/inhibition balance in information processing and social dysfunction. *Nature*, 477(7363):171–178, 2011. pages 17

[772] S.-H. Yook, F. Radicchi, and H. Meyer-Ortmanns. Self-similar scale-free networks and disassortativity. *Physical Review E*, 72(4):045105, 2005. pages 183

[773] G. U. Yule. Why do we sometimes get nonsense-correlations between time-series?–a study in sampling and the nature of time-series. *Journal of the royal statistical society*, pages 1–63, 1926. pages 60

[774] G. U. Yule. On a method of investigating periodicities in disturbed series, with special reference to wolfer's sunspot numbers. *Philosophical Transactions of the Royal Society of London. Series A, Containing Papers of a Mathematical or Physical Character*, pages 267–298, 1927. pages 60

[775] R. Yuste, W. Denk, et al. Dendritic spines as basic functional units of neuronal integration. *Nature*, 375(6533):682–684, 1995. pages 31

[776] J. P. Zbilut, A. Giuliani, and C. L. Webber. Detecting deterministic signals in exceptionally noisy environments using cross-recurrence quantification. *Physics Letters A*, 246(1):122–128, 1998. pages 89

[777] J. P. Zbilut, M. Koebbe, H. Loeb, and G. Mayer-Kress. Use of recurrence plots in the analysis of heart beat intervals. In *Computers in Cardiology 1990, Proceedings.*, pages 263–266. IEEE, 1990. pages 112

[778] J. P. Zbilut, N. Thomasson, and C. L. Webber. Recurrence quantification analysis as a tool for nonlinear exploration of nonstationary cardiac signals. *Medical engineering & physics*, 24(1):53–60, 2002. pages 112, 113

[779] J. P. Zbilut and C. L. Webber. Embeddings and delays as derived from quantification of recurrence plots. *Physics letters A*, 171(3-4):199–203, 1992. pages 89, 116

[780] J. P. Zbilut and C. L. Webber. Embeddings and delays as derived from quantification of recurrence plots. *Physics letters A*, 171(3):199–203, 1992. pages 112

[781] Z.-Z. Zhang, S.-G. Zhou, and T. Zou. Self-similarity, small-world, scale-free scaling, disassortativity, and robustness in hierarchical lattices. *The European Physical Journal B*, 56(3):259–271, 2007. pages 183

[782] F. Zubler and R. Douglas. A framework for modeling the growth and development of neurons and networks. *Frontiers in computational neuroscience*, 3:25, 2009. pages 182